

High-Resolution Terahertz Gas Spectroscopy



UNIVERSITY OF LEEDS

Nicholas North

Submitted in accordance with the requirements for the degree of
Doctor of Philosophy

University of Leeds
School of Electronic and Electrical Engineering
April 2024

Declaration

The candidate confirms that the work submitted is his own and that appropriate credit has been given where reference has been made to the work of others. This copy has been supplied on the understanding that it is copyright material and that no quotation from this work may be published without proper acknowledgement. ©The University of Leeds and Nicholas Kenneth North.

All Quantum-Cascade Lasers (QCLs) described in this work were designed and fabricated by Iman Kundu and Mohammed Salih in the University of Leeds cleanroom. The wafers for all QCLs in this thesis were grown by Lianhe Li. Integrating QCLs into metallic waveguide blocks was done by RAL space and characterisation of the block integrated devices was done by Eleanor Nuttall.

All of the TeraFET detectors used in this work are part of the Interest collaboration with Goethe University Frankfurt. All of the TeraFET detectors were designed and provided by Jakob Holstein, Alvydas Lisauskas and Hartmut Roskos. The detector characterisation in Section 2.4 was done with Jakob Holstein and Harry Godden under the supervision of Michael Horbury. The code to characterise the gate voltage of a TeraFET and the simulated channel resistance of the TeraFET was provided by Jakob Holstein. The rapid scan FTIR experiment shown in Section 2.5.3 was taken with the assistance of Sanchit Kondawar.

The gas spectroscopy work in Chapter 3 was done under the supervision of Michael Horbury. The scripts to run gas spectroscopy measurements in Chapter 3, for beam profiling and Fourier Transform Infrared (FTIR) characterisation in Chapter 2 were written by Michael Horbury. The methanol (MeOH) and D₂O spectra shown in Section 3.2.2 were taken with the help of Michael Horbury. The cider experimental data in Section 3.4.1 and time-resolved measurements taken in Section 3.5 were taken by Michael Horbury.

The Herriott cell design in Chapter 4 was done under the supervision of Julia Lehman. Neil Macleod from RAL Space provided the first Herriott mirrors, mirror mounts and a concept design for the Herriott cell.

The Racetrack Resonator (RTR) in Chapter 5 was designed and fabricated by Iman Kundu. Characterisation of the RTR device was done with Sanchit Kondawar and the power lock result from Figure 5.8 was taken by Sanchit Kondawar.

Dedicated to Grandad, who always asked how I was doing at university but
never saw how far I'd go.

Acknowledgements

I want to thank Dr Alexander Valavanis, my supervisor who helped me throughout this project and allowed me to study in this field. I would also like to thank my co-supervisors Dr Julia Lehman and Dr Daniel Stone for supporting me with their knowledge of the field of chemistry.

Thank you to the THz space research group - Elly and Mitch for teaching me the world of THz gas spectroscopy, Sanchit for always being there when the QCL was misbehaving, Harry for always being eager to lend a hand whenever he could and Mohammed for helping support our project by providing QCLs.

Thank you to our collaborators at Goethe University, Professor Hartmut Roskos and Professor Alvydas Lisauskas who changed the outlook of my work with the wonderful TeraFET detectors. I would also like to thank Jakob Holstein, a collaborator and a friend, for his support in using these detectors and for making memorable lab visits when he came to the UK.

I want to thank Connor for being a close friend from moving in together during freshers week, to finishing our PhDs together. A special thank you Jac and JT for keeping things in high spirits over lockdown and sharing the ups and downs of research. Additionally, I would like to thank the Anti Posers - Adam, Arran, Charlotte, Grace, Joe, Nicolle and Shane for the best times at gigs and festivals.

Most of all, thank you to my family who supported me through my undergraduate degree and PhD. Without the help and company from my Mum and Dad, none of this would have been possible and I will always be grateful.

Finally, I would like to thank the Fenton, for being the best pub in Leeds.

Abstract

Earth's climate is governed by the atmosphere which is a complex multi-phase system with natural and anthropogenic contributions. One of the greatest challenges scientists of this generation face is better understanding the many factors which influence Earth's climate and weather. Complex reactions take place in Earth's upper atmosphere which is dominated by Ultraviolet (UV) radiation where highly reactive radicals such as atomic oxygen are created by photolysis of ozone and carry chemical potential energy before releasing heat in exothermic reactions [1].

Atomic oxygen was not directly observable using field-based systems until recently due to its spectral features lying within the Terahertz (THz) range and instead intermediates in the exothermic reactions have been tracked to assume the concentrations [2]. The THz spectrum was known historically for difficulties in fabricating coherent sources and detectors, but in recent decades the development of THz Quantum Cascade Laser (QCL) sources has made the spectrum attractive for many technologies including astronomy and Earth observation.

Laboratory experiments in the THz region allow us to sample the spectrum of a molecule and track the kinetics of a reaction by controlling parameters. Fast and sensitive THz detection is needed to ensure that any short-lived or low-concentration intermediate states are accurately recorded.

This project aims to further develop an already existing THz gas spectrometer which uses a QCL source and focuses on atmospheric gases. This work was carried out by characterising a 3.4 THz QCL, measuring errors within the system, characterising a fast THz detector and developing a multi-pass gas cell to increase the minimum detection concentration.

The characterisation of a 3.4 THz QCL is presented which includes the Light-Current (LI) characteristic and spectral information from Michelson interferometry. The results from the interferometry are then compared to known spectral features from methanol (MeOH) spectra in the THz region to accurately acquire the QCL emission frequency. A fast room temperature THz detector using Field-Effect Transistor (FET) technology (TeraFET) is characterised which is part of the Interest collaboration between the University of Leeds and Goethe University Frankfurt. A QCL measured the noise characteristic of an array of FET detectors and tested the modulation bandwidth which exceeded 100 Megahertz (MHz) modulation bandwidth. This chapter demonstrated the first investigation into fast modulation of THz signals utilising an

array TeraFET detector.

Gas spectroscopy results taken throughout this thesis have been used to calibrate and benchmark the system throughout development. MeOH and D₂O were used as calibration gases to obtain the lasing frequency and test the lowest detectable concentration. Using a TeraFET detector allowed a high number of averages and reduced noise floor, revealing previously undocumented MeOH absorption features. After static measurements, deuterated methanol (MeOD) was sampled in the gas cell which is an undocumented species in this spectrum. The first spectra of MeOH and deuterated methanol at 3.4 THz are presented in this work along with the first observation of a H/D exchange in methanol in the 3.4 THz spectrum.

A multi-pass Herriott cell has been designed and fabricated to improve the sensitivity of the spectrometer. By increasing the number of passes, low-concentration gases such as intermediates in a chemical reaction will be easier to track due to an increased absorption strength. Additionally, the multi-pass optics are set up for future photolysis experiments by including a path for UV radiation.

A Photonic Integrated Circuit (PIC) approach to stabilise the output power of a QCL is presented. The device is a Racetrack Resonator (RTR) which was designed and fabricated by Iman Kundu for QCL power modulation. The RTR work in this thesis shows a control loop using both Proportional Integral (PI) and Proportional Integral Derivative (PID) control to stabilise the power of a 3.4 THz QCL for over 10 minutes, which is longer than a typical Earth observation integration period. Utilising a PIC reduces weight and complexity in a space mission where weight is critical in a satellite, this approach shows a simple power modulation system without the need for additional optics.

Publications

The work in this thesis has been presented in the following journal papers and conference proceedings:

Peer-reviewed journal papers

- J. Holstein, **N. K. North**, M. D. Horbury, S. S. Kondawar, I. Kundu, A. Krysl, L. Li, E. H. Linfield, J. R. Freeman, A. Valavanis, A. Lisauskas, and H. G. Roskos. "8×8 patch-antenna-coupled TeraFET detector array for rapid analysis of terahertz quantum-cascade laser emission". in IEEE Transactions on Terahertz Science and Technology, vol 14, p. 799-807, August 2024.
- S. S. Kondawar, **N. K. North**, Y. Han, D. Pardo, N. Brewster, M. D. Horbury, M. Salih, L. Li, P. Dean, J. R. Freeman, B. N. Ellison, I. Kundu, and A. Valavanis. "Power stabilization of a terahertz-frequency quantum cascade laser using a photonic-integrated modulator" in Optics Express, vol 32, p. 30017-30026, August 2024.
- **N. K. North**, M. D. Horbury J. Holstein, E. Nuttall, H. Godden, L. H. Li, E. H. Linfield, H. G. Roskos, A. Lisauskas and A. Valavanis. "Terahertz Transmission Spectroscopy of Deuterium Exchange between Methanol and Deuterated Water in the Gas-Phase". To be submitted.

Conference proceedings

- J. Holstein, M. D. Horbury, **N. North**, H. Godden, A. Krysl, A. Lisauskas, L. H. Li, A. Valavanis, J. R. Freeman, E. H. Linfield, and H. G. Roskos. "Implementation of a multi-element detector consisting of an 8×8 network of patch-antenna-coupled TeraFETs for gas spectroscopy with THz-QCLs" in Proceedings of 2023 48th International Conference on Infrared, Millimeter, and Terahertz Waves (IRMMW-THz).
- M. D. Horbury, **N. K. North**, J. Holstein, H. Godden, L. H. Li, J. R. Freeman, E. H. Linfield, H. Roskos, A. Lisauskas, and A. Valavanis. "Real-Time Terahertz Absorption Spectroscopy of Methanol and DeuteratedMethanol Vapour, using a TeraFET Detector Array" in Proceedings

of 2023 48th International Conference on Infrared, Millimeter, and Terahertz Waves (IRMMW-THz).

- S. S. Kondawar, **N. K. North**, Y. Han, D. Pardo, N. Brewster, M. Salih, M. D. Horbury, L. H. Li, P. Dean, B. N. Ellison, I. Kundu, and A. Valavanis. "Amplitude Stabilization of a THz Quantum-Cascade Laser using a Photonic Integrated Circuit." in Proceedings of 2023 48th International Conference on Infrared, Millimeter, and Terahertz Waves (IRMMW-THz).
- **N. K. North**, J. Holstein, M. D. Horbury, H. Godden, L. H. Li, J. R. Freeman, E. H. Linfield, H. Roskos, A. Lisauskas, and A. Valavanis. "Real-Time Analysis of THz Quantum-Cascade Laser Signals using a Field Effect Transistor Array" in Proceedings of 2023 48th International Conference on Infrared, Millimeter, and Terahertz Waves (IRMMW-THz).
- E. Nuttall, Y. J. Han, D. Pardo, M. D. Horbury, S. S. Kondawar, **N. K. North**, I. Kundu, O. Auriacombe, T. Rawlings, N. Brewster, M. Oldfield, M. Salih, L. H. Li, E. Zafar, A. G. Davies, E. H. Linfield, E. Saenz, H. Wang, B. N. Ellison and A. Valavanis. "Waveguide integrated terahertz quantum-cascade laser systems" in Proceedings of 2021 46th International Conference on Infrared, Millimeter and Terahertz Waves (IRMMW-THz).

Contents

List of Figures	xi
Abbreviations	xvii
1 Introduction	1
1.1 Terahertz Radiation	2
1.1.1 Terahertz Imaging and Communications	3
1.1.2 Terahertz Astronomy and Earth Observation	4
1.2 Spectrometers	8
1.2.1 Dispersive Spectrometer	8
1.2.2 Fourier Transform Infrared Spectroscopy	9
1.2.3 Error Correction	11
1.2.4 Time-Resolved FTIR	12
1.2.5 Terahertz Time-Domain Spectroscopy	13
1.3 Terahertz Sources	15
1.3.1 Electronic Sources	15
1.3.2 Photoconductive Antennas	16
1.3.3 Photomixers	17
1.3.4 Quantum Cascade Laser	18
1.4 THz Detectors	24
1.5 Gas Spectroscopy	26
1.5.1 Gas Spectroscopy Instrumentation	26
1.5.2 THz Gas Spectroscopy Instrumentation	28
1.5.3 Spectroscopy Catalogues	29
1.5.4 Aims and Objectives	30
1.6 Thesis layout	31
2 Terahertz Instrumentation	33
2.1 Closed-cycle Cryocooler	33
2.2 Quantum Cascade Laser Optical Characteristics	37
2.2.1 Beam Profiles	40
2.3 FTIR Results	44
2.3.1 Frequency Calibration	48
2.4 Fast THz Detection	58

2.4.1	Modulation Techniques	58
2.4.2	Thermal Detector Noise	59
2.5	TeraFET Detectors	62
2.5.1	Gate Voltage Sweep	65
2.5.2	Modulation Results	66
2.5.3	Rapid Scan FTIR	71
2.6	Summary	73
3	Single Pass Gas Spectroscopy	76
3.1	Molecular Absorptions	76
3.1.1	Beer-Lambert Law	79
3.2	Experimental Setup	81
3.2.1	Gas Manifold	81
3.2.2	Single Pass Cell	83
3.3	Static Measurements	84
3.3.1	Metal Gas Cell Methanol and D ₂ O Study	85
3.3.2	Glass Gas Cell Methanol and D ₂ O Study	90
3.3.3	Detection Limit	99
3.4	Mixture Measurements	102
3.4.1	Food Safety Applications	106
3.5	Time-Resolved Measurements	109
3.6	Conclusion	111
4	Multi-Pass Cell	114
4.1	White Cell Background	115
4.2	Herriott Cell Background	116
4.2.1	Herriott Cell Theory	117
4.2.2	Optical Interference Fringes	119
4.2.3	Cavity Enhanced Techniques	120
4.3	Ray Tracing	121
4.3.1	Sequential Ray Tracing	121
4.3.2	Non-Sequential Ray Tracing	123
4.4	Herriott Mirrors	123
4.4.1	Entry Optics	125
4.4.2	Herriott Cell Simulation	129
4.4.3	Performance Improvement	132
4.5	Purge Box	133
4.5.1	Purge Box Fabrication	138
4.6	Optical Alignment	140
4.7	Summary	143
5	QCL Power Stabilisation	145
5.1	QCL Stability	145
5.1.1	Proportional Integral Derivative Control	146
5.1.2	Power Locking	147
5.1.3	Frequency Stabilisation	148

5.1.4	Phase Locking	149
5.1.5	Injection Lock	150
5.2	Racetrack Resonator	151
5.3	Control Loop	153
5.3.1	PI Lock Box	154
5.3.2	Field Programmable Gate array	154
5.4	Experimental Setup	154
5.5	Characterisation	156
5.6	Power Locking Results	157
5.6.1	PID Results	158
5.7	Summary	160
6	Conclusion	161
6.1	Future Work	163
7	Bibliography	165

List of Figures

1.1	An illustration of each spectrum's frequency and wavelength. . .	2
1.2	(a) THz image of a leaf examining the water content as it dries. (b) THz image of an Integrated Circuit (IC), inspecting the electrical contacts through epoxy packaging. Figure from [13]. . . .	3
1.3	THz image of a skin sample before (Left) and after a burn (Right). Image adapted from [17].	4
1.4	An illustration comparing atmospheric attenuation of the observatory on Mauna Kea (13,803 ft elevation) to SOFIA (43,000 ft elevation). Figure taken from [33].	7
1.5	Illustration of a simple dispersion spectrometer. The incoming radiation has three wavelengths and by using the diffraction and slit, λ_2 has been separated.	8
1.6	Illustration of a Michelson interferometer. (1) Light is split at the beam splitter. (2) Light is reflected in the mirrors. (3) The detector observes an interferogram. (4) Some light is reflected to the source.	10
1.7	An example of the interferogram and FFT of monochromatic light.	11
1.8	A drawing of the cosine angle error.	11
1.9	Illustration of time resolution.	13
1.10	Diagram of a transmission THz TDS spectrometer.	14
1.11	A THz TDS measurement with no sample in a purged atmosphere. Data provided by Harry Godden.	15
1.12	A simple illustration of a THz PCA.	16
1.13	A simple illustration of a THz Photomixer. The mixer uses the principle of generating a THz wave by the difference frequency of two lasers.	17
1.14	A two energy level model of laser emission showing the three interactions (a) Absorption. (b) Spontaneous Emission. (c) Stimulated emission.	18
1.15	A three energy level model of laser emission showing the three interactions. (a) Electrons are pumped to the third state E_3 and relax to a stable state E_2 . (b) Stimulated emission causes the electrons to transition to E_1 and emits in-phase light.	19

1.16	(a) An illustration showing modes of the standing wave inside a laser cavity. (b) The resulting spectrum of the integer modes and the gain bandwidth.	20
1.17	Illustration of a quantum well structure. Materials A and B are semiconductors with different band gap energies.	21
1.18	A simple diagram of a QCL structure showing one period of the heterostructure.	22
1.19	Diagrams of the different active region designs taken from [69].	23
1.20	Simple diagram of a heterodyne receiver.	25
1.21	Diagram of the spectrometer.	31
2.1	Illustration of the bias tee QCL modulation experiment.	34
2.2	Illustration of the cryocooler.	36
2.3	LI characteristics of the QCL.	37
2.4	LI data of the QCL operating at a cryostat temperature of 35 K.	39
2.5	Schematic of the beam profiling system.	40
2.6	Two-dimensional view of the beam profile at a poor focus. The X and Y-axes are stage positions.	41
2.7	Side view of the beam profile at focus. The uneven beam pattern can be seen here.	41
2.8	2D view of the beam profile 0.3 mm before focus.	42
2.9	Side view of the beam profile before focus.	42
2.10	2D view of the beam profile at a detector position of 106 mm.	43
2.11	Full Width Half Maximum (FWHM) plot of the detector passing through focus.	43
2.12	Spectral data of Mode 1 at a QCL temperature of 31 K.	45
2.13	Spectral data of Mode 2 at a QCL temperature of 31 K.	46
2.14	Spectral data of Mode 3 at a QCL temperature of 31 K.	47
2.15	Scatter of the Mode 2 FFT peaks compared to the QCL bias current (blue). A polynomial fit of the points (red).	48
2.16	The LI characteristic of the laser with a methanol sample introduced into the gas cell at a QCL temperature of 50 K.	51
2.17	Comparison of the frequency of an observed spectrum vs the JPL.	52
2.18	The error of the peak positions compared to the catalogues JPL peak positions.	53
2.19	Heatmap of the QCL spectrum at a temperature of 31 K. Where the current is on the Y-axis in milliamps and frequency in THz on the X-axis.	54
2.20	Heatmap of the QCL spectrum at a temperature of 35 K. Where the current is on the Y-axis in milliamps and frequency in THz on the X-axis.	54
2.21	Heatmap of the QCL spectrum at a temperature of 40 K. Where the current is on the Y-axis in milliamps and frequency in THz on the X-axis.	55

2.22	Heatmap of the QCL spectrum at a temperature of 45 K. Where the current is on the Y-axis in milliamps and frequency in THz on the X-axis.	55
2.23	Heatmap of the QCL spectrum at a temperature of 48 K. Where the current is on the Y-axis in milliamps and frequency in THz on the X-axis.	56
2.24	Heatmap of the QCL spectrum at a temperature of 50 K. Where the current is on the Y-axis in milliamps and frequency in THz on the X-axis.	56
2.25	Heatmap of the QCL spectrum at a temperature of 55 K. Where the current is on the Y-axis in milliamps and frequency in THz on the X-axis.	57
2.26	Self-mixing noise experimental data.	60
2.27	Overnight thermal noise experiment.	61
2.28	Histograms of the chopper thermal drift experiments.	61
2.29	Illustration of the TeraFET THz detection process. The detector signal is the Drain-Source signal and the FET must be operated above the threshold.	63
2.30	Images of an array TeraFET detector.	64
2.31	Results from the Gate sweep experiment using an array TeraFET.	66
2.32	Illustration of the bias tee QCL modulation experiment.	67
2.33	The comparison of the normalised amplitude of a bolometer, 200 kHz Array and the 20 MHz Array.	68
2.34	A comparison of the normalised amplitude of the 20 MHz Array using a 3.4 THz QCL and a 2.9 THz QCL.	69
2.35	Modulation bandwidth of the 3.4 THz QCL. The red arrow indicates a possible resonance at 20 MHz.	70
2.36	Diagram of the optical ports available for the Bruker FTIR. The optical path can either exit through the bolometer port or port B.	71
2.37	FTIR spectra taken from a 3.4 THz multi-mode QCL.	72
2.38	H ₂ O absorption compared to the FTIR characterisation of the multi-mode QCL.	73
3.1	(Top) An illustration of a simple direct absorption measurement. (Bottom) The light intensity compared to distance as it passes through the sample.	79
3.2	(a) Current sweep of the QCL with a vacuum blank gas cell. (b) Current sweep of the QCL with MeOH in the gas cell. (c) Transmission as a percentage through the sample. (d) The absorbance of the sample.	80
3.3	Photo of the gas manifold with two MFCs. The second MFC is off-camera perpendicular to the gas in MFC.	82
3.4	Diagram of the time-resolved gas manifold.	83
3.5	A picture of the glass gas cell used in this work.	84
3.6	A picture of the metal gas cell used in this work.	84
3.7	A flow diagram of the data acquisition and data processing.	85

3.8	Two MeOH experiments taken during different cooldown cycles using the same QCL bias to frequency calibration. (a) MeOH at a gas cell pressure of 0.5 Torr. (b) MeOH sample at a gas cell pressure of 1 Torr. The spectral features are approximately 10 GHz offset.	86
3.9	Simulated data from the JPL catalogue ranging 3380 GHz to 3450 GHz.	87
3.10	Mode 1 experimental data and JPL data showing the same peaks.	87
3.11	Experimental data showing MeOH absorptions in Mode 2 compared to simulated data in the JPL catalogue.	88
3.12	Experimental data showing MeOH absorption and D ₂ O overlap in Mode 3.	89
3.13	MeOH and D ₂ O absorptions in Mode 3 taken from the JPL catalogue.	89
3.14	Methanol spectra taken at a 0.5 Torr, QCL Mode 1.	92
3.15	Methanol spectra taken at a 0.5 Torr, QCL Mode 2.	93
3.16	Methanol spectra taken at a 0.5 Torr, QCL Mode 3.	94
3.17	D ₂ O spectra taken at a 0.5 Torr using QCL Mode 1.	97
3.18	D ₂ O spectra taken at a 0.5 Torr using QCL Mode 2.	98
3.19	D ₂ O spectra taken at a 0.5 Torr using QCL Mode 3.	98
3.20	Experimental data of one D ₂ O peak as the gas cell pressure is reduced.	100
3.21	Results from Mode 1.	103
3.22	Results from Mode 2.	103
3.23	Results from Mode 3.	104
3.24	Mode 1 comparing MeOD to a 1:1 mixture of MeOH and D ₂ O.	105
3.25	Mode 2 comparing MeOD to a 1:1 mixture of MeOH and D ₂ O.	105
3.26	Mode 3 comparing MeOD to a 1:1 mixture of MeOH and D ₂ O.	106
3.27	The QCL observing cider and a 90% cider, 10% MeOH mixture.	107
3.28	The MeOH peak observed by QCL.	110
3.29	Experimental data of the detector signal as MeOH is introduced into the gas cell.	110
4.1	Diagram of a White cell. The beam enters at point 1, reflects off M2 and exits at point 5 after being reflected off M3.	115
4.2	Two Herriott cell designs which maintain the optical axis.	116
4.3	Drawing of a Herriott cell with an addition optic to couple radiation into the side.	116
4.4	Drawing of four passes between the two mirrors on one plane. X represents spots on the far mirror and O represents spots on the near mirror.	117
4.5	Drawing of a simple CRDS system.	121
4.6	An example of sequential ray tracing in Zemax. An optical laser is defined in POP launched through a lens (Left) and focused on a detector (Right).	122
4.7	Non-sequential simulation of the Herriott mirrors.	123

4.8	Pictures of the Herriott mirrors loaned from RAL in mounts. . .	124
4.9	A CAD design and photo of the redesigned Herriott mirrors. . .	125
4.10	Optical layout of the proposed THz path for multi-pass spectroscopy.	126
4.11	Zemax simulation of the first coupling optic design.	127
4.12	Zemax simulation of the final optical design.	128
4.13	Pictures of the optical path through the entry and exit optics. . .	129
4.14	The ZBF from the Herriott cell POP simulation.	131
4.15	Interpolated ray trace of the Herriott cell.	132
4.16	CAD drawing provided by Dr Neil Macleod from RAL.	133
4.17	Middle of the multi-pass gas cell made from ISO-LF standard parts. .	134
4.18	The first CAD designs of the Herriott cell purge boxes.	135
4.19	CAD model of the half nipple.	136
4.20	The final CAD designs of the Herriott cell purge boxes.	136
4.21	CAD models of the mirror assemblies.	137
4.22	Pictures of the purge boxes with the mirror assembly mounted inside.	139
4.23	A picture of the front Herriott mirror aligned with four passes in the cell.	140
4.24	A picture of the Herriott cell aligned with the mirrors facing forward ($N = 18$) giving an elliptical pattern.	141
4.25	Visible alignment after adjusting the off-axis tilt of the Herriott mirrors ($N = 30$).	142
4.26	A side view of the Herriott cell aligned with a HeNe laser.	142
5.1	Block diagram of a parallel PID controller, a common PID configuration.	146
5.2	QCL emission (Black spot) on the side of a frequency feature. A change in the laser frequency results in a detected shift in amplitude, this shift creates an error signal inside the controller.	149
5.3	A simple block diagram of a Phase Lock Loop. The microwave source and control systems have various components such as amplifiers and filters to condition the signal.	150
5.4	3D image of a RTR coupled to a QCL ridge. Black rings show the bonding pads. Figure taken from [175].	151
5.5	(Left) 3D model of the device integrated into a waveguide block. (Right) Microscope image showing the gap between the resonator and QCL ridge inside a waveguide block.	152
5.6	Diagrams of how the QCL emission is coupled into the RTR as it is biased.	153
5.7	A block diagram of the power locking experimental set-up using the New Focus PI controller.	155
5.8	(Left) the LIV characteristics of the THz QCL. (Right) The effect of the RTR bias on the QCL power.	156

5.9	(a) RTR was off and QCL current increased. (b) Peak frequency vs bias current for QCL sweep. (c) QCL at a constant current and RTR bias increased. (d) Peak frequency vs bias current for RTR sweep.	157
5.10	Results from the power locking experiments showing the signal detected with a lock-in amplifier. (Top) The QCL is free-running. (Bottom) The QCL signal with the control loop active, quantisation effects are due to the lock-in sensitivity.	158
5.11	(Top) Results from the FPGA experiments showing the signal detected with a lock-in amplifier while free-running. (Bottom) Detector signal with the control loop active.	159

Abbreviations

3D 3 Dimensional

AC Alternating Current

BPP Beam Parameter Product

BTC Bound To Continuum

BWO Backward Wave Oscillator

CAD Computer Aided Design

CMOS Complementary Metal-Oxide Semiconductor

CRDS Cavity Ring Down Spectroscopy

CSL Chirped Superlattice

CW Continuous Wave

DAQ Data Acquisition

DC Direct Current

EM Electromagnetic

FEM Finite Element Method

FET Field-Effect Transistor

FFT Fast Fourier Transform

FPGA Field-Programmable Gate Array

fs Femtosecond

FSR Free Spectral Range

FTIR Fouier Transfer Infrared

FWHM Full Width Half Maximum

GaAs Gallium Arsenide

GHz Gigahertz

HDPE High-Density Polyethylene

HEBM Hot Electron Bolometer Mixer

HeNe Helium-Neon

HITRAN High-Resolution Transmission Molecular Absorption Database

IC Integrated Circuit

IF Intermediate Frequency

IMPATT Impact avalanche transit time

IR Infrared Radiation

IRMMW-THz Infrared Millimeter Wave and Terahertz

ITQW Infrared Terahertz Quantum Workshop

JPL Jet Propulsion Laboratory

LED Light Emitting Diode

LFGL Low Frequency Gain Limit

LI Light-Current

LIV Light-Current-Voltage

LO Local Oscillator

LOCUS Low-Cost Upper-Atmosphere Sounder

LT-GaAs Low-Temperature Grown Gallium Arsenide

MBE Molecular Beam Epitaxy

MFC Mass Flow Controller

MHz Megahertz

MLS Microwave Limb Sounder

MLT Mesosphere and Lower Thermosphere

NASA National Aeronautics and Space Administration
NEP Noise Equivalent Power
NIR Near Infrared
NMR Nuclear Magnetic Resonance
NSC Non-Sequential Component

OAP Off-Axis Parabolic
OPD Optical Path Difference
OSAS-B Oxygen Spectrometer for Atmospheric Science from a Balloon

PCA Photo-Conductive Antenna
PI Proportional Integral
PIC Photonic Integrated Circuit
PID Proportional Integral Derivative
PLL Phase-Locked Loop
POP Physical Optics Propagation
PV Process Variable
PYZDE Python Zemax Dynamic Data Exchange

QAM Quadrature Amplitude Modulation
QCL Quantum Cascade Laser

RAL Rutherford Appleton Laboratory
RC Resistor-Capacitor
RF Radio Frequency
RP Resonant Phonon
RTD Resonant Tunneling Diode
RTR Racetrack Resonator

SABER Sounding of the Atmosphere using Broadband Emission Radiometry
SM Self-Mixing
SNR Signal-To-Noise Ratio

SOFIA Stratospheric Observatory for Infrared Astronomy

STO Stratospheric THz Observatory

SV Set-point Variable

TDS Time-Domain Spectroscopy

THz Terahertz

TIMED Thermosphere, Ionosphere, Mesosphere Energetics and Dynamics

TPX Polymethyl Pentene

TSMC Taiwan Semiconductor Manufacturing Company

UV Ultraviolet

VOC Volatile Organic Compound

ZOPD Zero Optical Path Difference

Chapter 1

Introduction

Earth's atmosphere is a complex multi-phase system consisting of solids, liquids and gasses with natural and anthropogenic contributions. One of the greatest challenges scientists face in this generation is understanding the many factors which influence the climate and weather. Complex reactions are influenced by solar radiation, such as the generation of reactive radicals such as atomic oxygen [O] and hydroxyl [OH] generated by Ultraviolet (UV) radiation. These radicals are difficult to observe due to their altitude, absorption cross-sections and low concentration which translates to difficulties in accurately modelling Earth's climate. The concentrations of O have been measured in the field to be on the order of magnitude $1 \times 10^{11} \text{cm}^{-3}$ [3]. The difficulty in creating new accurate climate models to understand the changing climate has motivated the development of instrumentation which can carry out in situ measurements of the atmosphere to better allow us to model the planet's climate [4]. The need for sensitivity and selectivity in instrumentation is universal for analytical chemistry and drives the development of new systems and models.

A solution to help fill the gaps in atmospheric chemistry is Terahertz (THz) spectroscopy which has been under-utilised due to the historic difficulty in generating and detecting radiation at this frequency. The invention of the THz Quantum Cascade Laser (QCL) has created a new field in the world of THz technology as now the potential of having compact solid-state sources with high optical powers comes closer to realisation. THz QCLs currently operate under cryogenic conditions and use cooling equipment. Still, technology has advanced to where these lasers can be inside compact cryocoolers and used for remote sensing in satellites or balloon missions.

This research has developed a THz gas spectrometer capable of detecting low-concentration gas phase samples through improved detection speed and sensitivity. A THz QCL was characterised as an instrument for fast, sensitive measurements used to examine methanol (MeOH) and Heavy water (D₂O) to demonstrate the system's capability for in-field measurements.

1.1 Terahertz Radiation

The THz band is a range of frequencies in the electromagnetic spectrum spanning 0.1 THz to 10 THz ($\lambda = 1\text{mm} - 300\mu\text{m}$, $E = 0.414 - 41.36\text{ meV}$), which lies between the Electronic (Microwave and RF) and Photonic (Infrared and Visible) ranges. The sources of THz radiation are discussed in Section 1.3. However, conventional electronic and photonic sources typically fail to operate in this band, for common reasons. In the electronic region, devices such as the Gunn Diode Oscillator or transistors are used as high-frequency sources. When increasing frequency from electronic technology, the parasitic impedances inside devices can be thought of as a ladder of Resistor-Capacitor (RC) circuits with individual rise and fall times where T is time, C is capacitance and L is inductance.

$$T = R \times C \quad (1.1)$$

$$T = \frac{L}{R} \quad (1.2)$$

The parasitic impedances of circuits are small and typically do not affect the performance of everyday electronics. Increasing the operating frequency of a device into the THz range will reach a limit where the period of the signals falls below the rise and fall times introduced by the parasitic impedance inside of a semiconductor device and limit the bandwidth [5].

$$\hbar\omega_0 \simeq E_g \quad (1.3)$$

In Photonic technology, the wavelength of a diode laser is determined by electron transitions in the band gap of the gain medium, Equation 1.3 shows the relationship between band gap E_g , photon wavelength ω_0 and Plank's constant \hbar . This relationship shows that a narrow band gap corresponds to lower photon energy and a larger wavelength. A lack of narrow band gap semiconductors limits the lower frequency of diode lasers to the range of tens of THz [6].

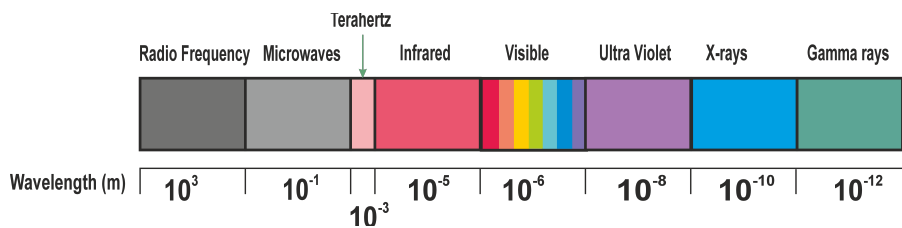


Figure 1.1: An illustration of each spectrum's frequency and wavelength.

Due to the slow development of devices, few systems using THz technology have been used commercially. THz radiation is non-ionising due to the low photon energies the THz spectrum's position in the Electromagnetic (EM) spectrum

is shown in Figure 1.1. The low photon energy in the THz band offers unique and attractive opportunities for imaging, sensing and non-destructive testing.

1.1.1 Terahertz Imaging and Communications

The first THz images were produced by T. S. Hartwick, et al. in 1976 using optically pumped lasers ranging and a helium-cooled Gallium Arsenide (GaAs) detector [7]. The information gathered from THz imaging differs from X-ray images or microwaves which can be used as complementary information of a sample. Using THz imaging alone for testing has advantages over other frequencies, the shorter wavelength allows smaller objects to be resolved but at a loss to the superior material penetration of microwaves [8].

THz waves penetrate most dry, nonmetallic and non-polar objects such as plastics, paper and fabrics. Conversely, Metals are opaque due to their reflectance and water strongly absorbs this frequency range. These material qualities alongside the low photon energy make THz an attractive frequency for non-destructive testing or security. In industrial applications, THz can penetrate the packaging of an integrated circuit and examine the reflective conductors inside of the devices an example of this as well as moisture detection within a leaf is shown in Figure 1.2 [8] [9] [10] [11] [12].

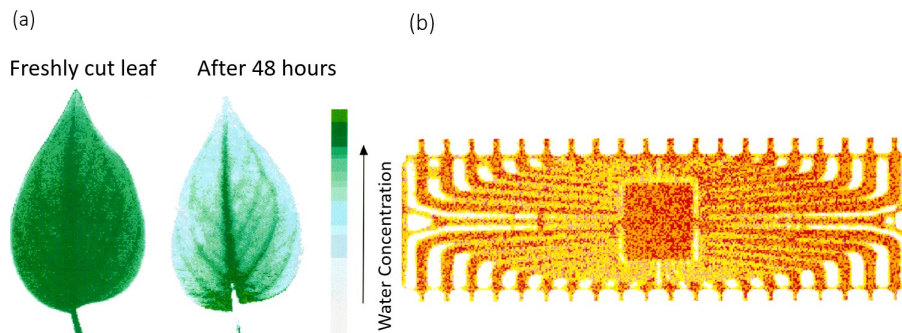


Figure 1.2: (a) THz image of a leaf examining the water content as it dries. (b) THz image of an Integrated Circuit (IC), inspecting the electrical contacts through epoxy packaging. Figure from [13].

In the medical field, non-invasive methods are a way to examine a patient without opening the body in surgery. Medical imaging may be used in non-invasive methods such as Magnetic Resonance Imaging (MRI) or X-ray radiography which have unique purposes in the medical field. Numerous non-polar liquids are fairly transparent in the THz region whereas polar molecules such as alcohols or water have strong THz responses. Additionally, most dry fabric dressings a patient wears would also be transparent to THz. Water absorption tends to be a problem in THz technology but in some applications, it is advantageous such as medical imaging. A change in water content in cells can be

used for detecting cancerous cells or burns in patients. Burns in a skin sample imaged by THz radiation can be seen in Figure 1.3 [14] [15] [16] [17].

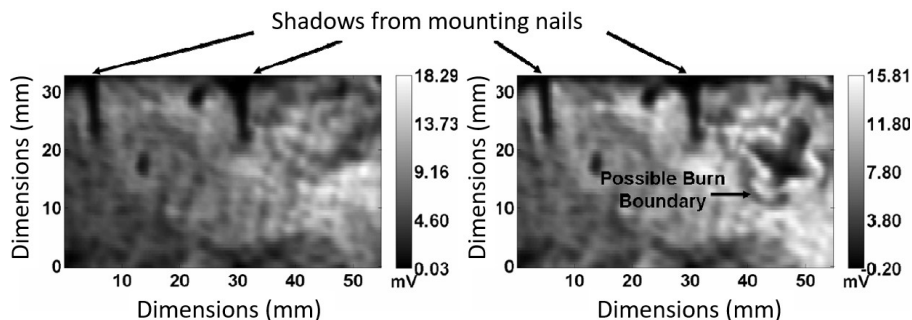


Figure 1.3: THz image of a skin sample before (Left) and after a burn (Right). Image adapted from [17].

THz radiation has great potential for other purposes such as wireless communications. Cisco predicted that by 2023 there will be 5.3 billion internet users representing 66% of the global population, a growth from 2018 when there were 3.9 billion users in 2018 [18]. With this growth comes an increase in data traffic and demand for faster bit rates to transfer the large quantities of data being passed daily. Since the first microwave wireless communication link system was demonstrated by Guglielmo Marconi in 1896, the carrier frequencies for communications have been increasing to meet bandwidth demands [19]. Wireless systems like WiFi operate at carrier frequencies below 5 Gigahertz (GHz), where the limited bandwidth at this range demands high spectral efficiency. New parts of the spectrum must be found with a higher frequency to keep up with the increase in demand, but this becomes problematic as the usable spectrum around the microwave region is crowded. A solution to this wireless communication in the terahertz range [20].

The bandwidths available in the THz gap are suitable to modulate at high bit rates with a carrier frequency capable of transmitting data in the terabit per second range. The first THz communication link was demonstrated at a carrier frequency up to 3 THz over a short distance using photoconductive antennas to transmit audio [21]. Digital encoded THz communication links have also been demonstrated using Quadrature Amplitude Modulation (QAM), resulting in 1 Tb/s bit rates over a distance of 3.1 m [22].

1.1.2 Terahertz Astronomy and Earth Observation

In this work, the instrumentation will focus on the gaseous atmospheric particles and targeting low-concentration species in the future. Radicals are intermediates in reactions, are low in concentration and are the main drivers in atmospheric chemistry for example hydroxyl [OH] controls the oxidising power of the atmo-

sphere [23]. [O] is an important radical in the chemistry of the atmosphere, it plays a role in the energy transfer of the Mesosphere and Lower Thermosphere (MLT). Atomic oxygen can be found 80 to 300 km above the Earth's surface with 90% concentrated between 85 to 125 km. Atomic oxygen has fine structure transitions in the THz region at approximately 4.7 THz and 2.06 THz [24].

The sensitivity requirements in atmospheric research instrumentation depend on the target species as the volumes of molecules can range from parts per billion to parts per quadrillion (1 in 10^{15}). Atmospheric studies also have additional requirements for in situ instrumentation [25]:

1. Sensitivity and time resolution. Atmospheric composition can change rapidly, the instrument must have adequate sensitivity and time resolution to capture dispersion and any chemical changes.
2. Instrument size. The size of an instrument is a strict requirement for in situ measurements as these are typically done on aircraft or a satellite where weight and size are limited. Where weight requirements span small satellites (<500 kg) and nanosats (1 kg to 15 kg) are common in government, academia and industry [26].
3. Calibration. Ease of calibration is important due to the difficulty in recalibrating a system which is on a satellite or balloon mission.
4. Stability to environmental changes. Systems used in the field don't have environmental control which is seen in research labs, so an instrument must be stable concerning changes in ambient temperature. If the instrument is flying, it must also be stable to changes in pressure.

Mesosphere and Lower Thermosphere

The heat exchange for Earth is not a simple process as when radiation is absorbed in the upper atmosphere it is either observable as airglow, where an absorbing species cools and emits radiation, or when photolysis occurs, the energy is transferred to the chemical potential energy of a product species. An example is when UV radiation from the sun is absorbed by O_2 or O_3 and [O] is generated. The reactive [O] carries the potential energy into various exothermic chemical reactions in the MLT and the heating from exothermic reactions exceeds the heating from direct UV absorption in this atmospheric region. Therefore the monitoring of oxygen concentrations in this region is important to help model heating mechanisms in the upper atmosphere [1] [27].

The altitude of the MLT makes it difficult to observe due to the height being above the altitude of balloon missions and below the orbit of satellites. Therefore, the only instruments which can collect samples from within the MLT are flown on sounding rocket missions, previous sounding rocket missions used mid IR and far IR spectrometers to target vibrational modes of CO_2 , O_3 , H_2O and NO [28].

An alternative to flying sounding rockets through the MLT is observing the region through high-altitude missions and satellites. Satellite instrumentation has also targeted the MLT, an example of this is the Thermosphere, Ionosphere, Mesosphere Energetics and Dynamics (TIMED) satellite mission which was launched in 2001 with four instruments to study the upper climates of Earth’s atmosphere. This satellite used UV photometers to measure solar radiation, a UV spectrograph to image temperature profiles of the upper atmosphere, a Doppler interferometer to measure wind profiles in the MLT and a multi-channel IR radiometer to measure the heat and airglow from cooling molecules [29]. As [O] is not directly observable, to track the concentrations in the atmosphere, indirect means are applied. An example is the IR radiometer in TIMED that is called Sounding of the Atmosphere using Broadband Emission Radiometry (SABER) which in the daytime tracks ozone concentrations to derive the concentration [O] and O₃. At night, [OH] is tracked in the IR region and used to derive [O] concentrations [30].

Particles within the atmosphere vary in size from aerosols and radicals on the scale of 10⁻⁹m or 10⁻⁴m for dust and debris, even larger particles such as gravel or raindrops are present but the weight leads to a short lifetime in the atmosphere.

THz Missions

The previously discussed missions indirectly track [O] through assumptions in photochemical models, using THz to measure radicals in their excited states as a means of direct measurement. Earth observation and Radio Astronomy have both driven THz technology as the visibility of functional groups and rotational states in molecules. In Radio observations, the content of interstellar clouds lets us understand the evolution of the Universe. The ability for THz radiation to penetrate interstellar dust clouds is useful in understanding the formation of stars. Approximately half of the stellar energy in The Milky Way is absorbed by gas and dust which radiates back as black body radiation which is observable THz radiation carrying spectral information from the radiating body [31]. Molecules in the atmosphere such as water have strong attenuation and can limit THz observations to atmospheric windows where there is no strong water attenuation. Taking measurements during a high-altitude mission broadens the atmospheric windows by elevating the instrument to an atmosphere with lower water content. One such balloon mission was the Stratospheric THz Observatory (STO) which operated in the 1-2 THz range to target Nitrogen and carbon bonds in Interstellar Medium [32]. Stratospheric Observatory for Infrared Astronomy (SOFIA) was an observation platform fitted inside a Boeing 747 which was a joint mission between the National Aeronautics and Space Administration (NASA) and German Space Agency (DLR). SOFIA used THz heterodyne receivers to target a fine structure transition of atomic oxygen at 4.7 THz. SOFIA operated at an altitude of 43,000 ft and was flown at night, Figure 1.4 demonstrates the impact atmospheric absorption has on THz observations [33].

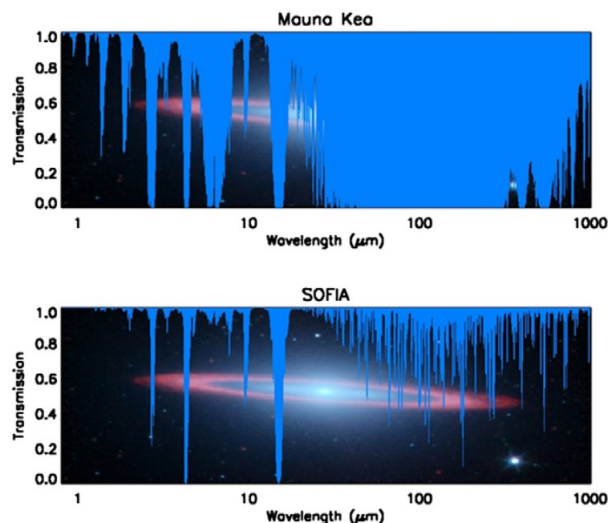


Figure 1.4: An illustration comparing atmospheric attenuation of the observatory on Mauna Kea (13,803 ft elevation) to SOFIA (43,000 ft elevation). Figure taken from [33].

As THz technology progresses, more satellite and balloon missions are being developed to further observe [O] and [OH] in the MLT. The Low-Cost Upper-Atmosphere Sounder (LOCUS) satellite payload is a THz system which aims to be deployed in low orbit and use four frequency bands spanning 0.8 - 4.7 THz to directly target (O, O₂, O₃, OH, HO₂O, HO₂, NO and CO) [34] [35]. Aura is a successful satellite mission which was launched to observe Volatile Organic Compound (VOC)s and monitor ozone in the atmosphere. Microwave Limb Sounder (MLS) is a payload on the Aura mission which spans 118 GHz to 2.5 THz and in 2001 was able to target water vapour in Earth's upper troposphere [36] [37]. The Oxygen Spectrometer for Atmospheric Science from a Balloon (OSAS-B) is a 4.7 THz heterodyne spectrometer which is flown on a stratospheric balloon and has the benefit of flying higher than SOFIA. OSAS-B is a spectrometer flown by the DLR and has the benefit of being able to be flown in the day as well as night due to the higher altitude reducing background noise [38].

The THz and IR regions have also proved useful in interstellar observations as well as Earth Observations. The Planck mission was a satellite with two payloads, the Low-Frequency instrument and the High-Frequency instrument. The High-Frequency instrument spanned 0.1 to 1 THz and was designed to measure the cosmic background radiation. The shorter wavelength in millimetre waves provided high-resolution observations of the cosmic background radiation compared to previous observations [39] [40].

1.2 Spectrometers

It is also highly desirable to develop lab-based instruments to complement satellite observations. These remove the size, weight and power constraints experienced by satellite payloads and allow finely controlled studies of the reactions of interest, allowing us to further explore this spectral region. This is the focus of the present work and typical lab-based spectroscopy techniques are introduced in the following section.

Spectroscopy is the study of electromagnetic radiation interacting with matter and by examining wavelength and intensity changes. After an interaction, information about matter is carried on the radiation. The first spectrometer can be traced back to Joseph Fraunhofer who in 1817 placed a prism at the eyepiece of a telescope and observed the resulting spectrum from sunlight. Various dark lines appeared in the spectrum of varying thickness these were the spectral information carried from the sun. From this discovery, the field of spectroscopy became a science and methods to examine matter through electromagnetic interaction became a field of study.

1.2.1 Dispersive Spectrometer

Dispersive spectrometers build upon the principle observed in 1817 by using an optical element to spatially separate frequencies of the electromagnetic spectrum. To sample the individual frequencies, an optical component scans each spatially separated mode individually. A dispersion spectrometer comprises multiple parts which condition the light, the main components being a source, a dispersion optic, a slit to separate the frequencies and a detector. A simple diagram of a dispersion spectrometer is shown in Figure 1.5.

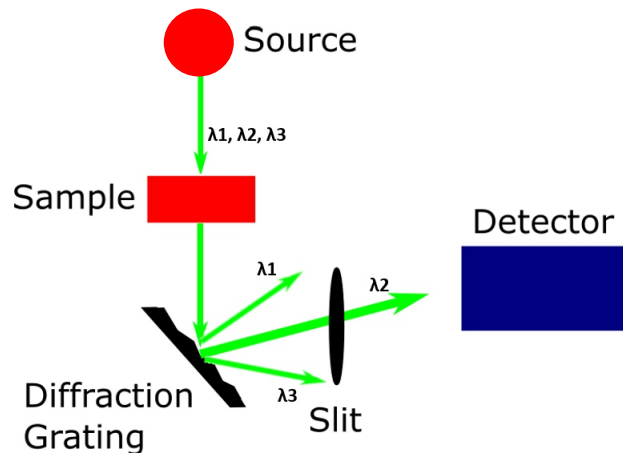


Figure 1.5: Illustration of a simple dispersion spectrometer. The incoming radiation has three wavelengths and by using the diffraction and slit, λ_2 has been separated.

Dispersive spectrometers can be categorised as a Monochromator or Spectrograph. Monochromators use a single detection element and a slit to select the frequencies, Spectrographs have multiple spatially separated detectors which sample all frequencies at once. The resolution of a spectrometer is the ability of the device to resolve small features by separating wavelengths and is given by:

$$R = \frac{\lambda}{\Delta\lambda} \quad (1.4)$$

Where R is Resolution, λ is wavelength and $\Delta\lambda$ is the Full Width Half Maximum (FWHM) of the smallest resolvable spectral feature. The reciprocal of the diffraction multiplied by the slit size sets the resolution of a Monochromator, where a narrower slit results in a higher resolution. A trade-off with the higher resolution is a lower optical intensity on the detector, lowering instrument Signal-To-Noise Ratio (SNR). In a Spectrograph, smaller pixels sampling the separated spectrum are analogous to changing the slit size [41].

1.2.2 Fourier Transform Infrared Spectroscopy

A Fourier Transfer Infrared (FTIR) spectrometer is an instrument which first found use in the IR spectrum. FTIR uses the principle of interferometry and can also be used in THz frequencies to obtain spectral data. Discussions about FTIR spectroscopy in this work refer to the technique in the THz frequencies.

A FTIR spectrometer has high acquisition speeds and SNR when compared to a dispersion system. These spectrometers work by using a Michelson Interferometer which was invented by A. A. Michelson in 1881 who used the device in an attempt to measure the speed of the earth compared to the hypothetical ether by measuring the interference of radiation to calculate distance [42].

Michelson interferometers use constructive and destructive interference and consist of three parts: beam splitter, fixed mirror and moving mirror. The interference pattern of monochromatic radiation causes a periodic interference pattern. The intensity of fringes depends on the radiation wavelength and by counting the fringes distance can be measured. The time domain signal from an interferometer is called an interferogram and applying a Fast Fourier Transform (FFT) to the resulting interferogram gives the frequency spectrum of the light. Unlike a dispersion spectrometer which examines wavelengths individually, the FTIR observes all frequencies simultaneously during measurement.

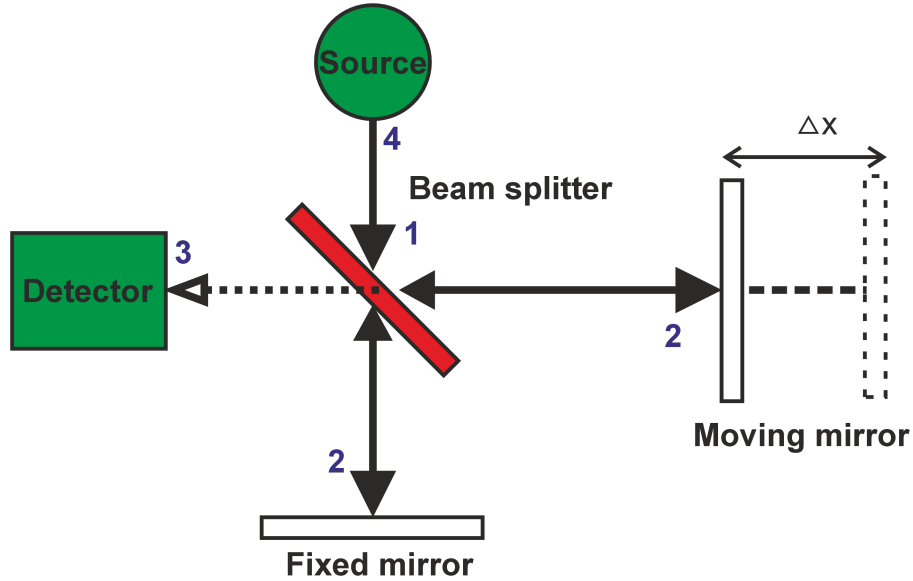


Figure 1.6: Illustration of a Michelson interferometer. (1) Light is split at the beam splitter. (2) Light is reflected in the mirrors. (3) The detector observes an interferogram. (4) Some light is reflected to the source.

Light in an interferometer takes multiple paths which are illustrated in Figure 1.6. Light emitted by the source is split among the two arms (1). The beams are reflected by the mirrors (2) and recombined at the splitter, the resulting interferogram is split to the detector (3) and source (4). The low-intensity light reflected to the source is negligible and is ignored in most cases.

The interferogram is the time domain function of intensity related to mirror position and wavelength. When the Optical Path Difference (OPD) is equal, radiation is in phase and experiences constructive interference and the detector observes a signal maximum, this is called Zero Optical Path Difference (ZOPD). As the mirror moves away from ZOPD a phase shift is introduced and after a distance of $\frac{\lambda}{2}$ the signal experiences destructive interference. If the mirror is moving at a constant speed a sinusoidal interferogram with a period of $\frac{\lambda}{2}$ is observed [41]. An example of an interferogram of monochromatic light is shown in Figure 1.7.

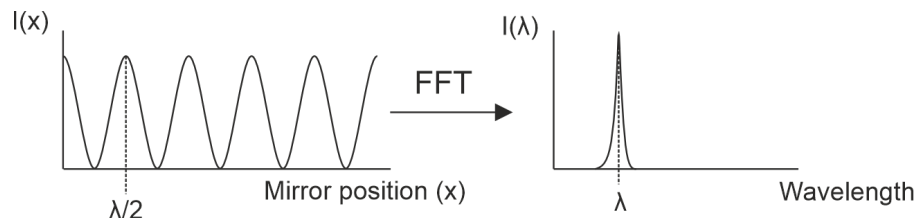


Figure 1.7: An example of the interferogram and FFT of monochromatic light.

The beam divergence and mirror distance determine the resolution of a FTIR spectrometer. In a typical commercial FTIR such as the Bruker Invenio the resolution is 0.085 cm^{-1} , or in high-resolution systems developed for research such as the Bruker IFS 125HR, resolutions can be as low as 0.0009 cm^{-1} . An aperture is typically used in commercial FTIR systems to reduce beam divergence, in laser systems it is assumed that the beam is perfectly collimated leaving the resolution defined Equation 1.5, where Δx is the distance travelled by the moving mirror and R is the resolution of the spectrometer.

$$R = \frac{1}{\Delta x} \quad (1.5)$$

1.2.3 Error Correction

Misalignment in the interferometer shifts the frequency of the spectrum, an example of this is the $\cos(\theta)$ error. The distance measured by the interferometer compared to the real distance of the optic can be expressed as 1.6 where: L_{meas} = Distance measured by the interferometer, L = the real distance of the optic, θ = the angle of the misalignment. Figure 1.8 is an illustration of $\cos(\theta)$ error in an interferometer.

$$L_{meas} = L \times \cos(\theta) \quad (1.6)$$

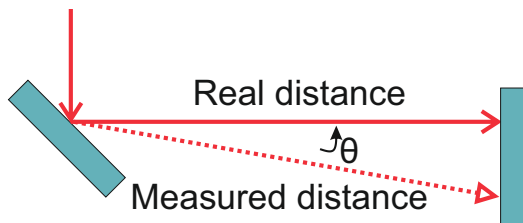


Figure 1.8: A drawing of the cosine angle error.

Commercial FTIR spectrometers correct this error through a stable laser which aligns the interferometer. This stable laser will collinearly pass through the interferometer with the probe beam and be detected by a second detector. The stable laser frequency can be used to correct for misalignment, as the peaks in the interferogram can be compared to the reported mirror distance and correct for errors.

Post-processing can also be applied to atmospheric absorption inside the IR and THz regions as water absorption can cause attenuation in these spectral regions. Typically, the software driving a commercial FTIR will have a library of known peaks which can be assigned to output spectra. The library of known absorption features can also be used to correct and subtract common atmospheric species such as water and CO₂. This process takes a background spectrum with no sample in the spectrometer and creates an envelope assigned to water absorption.

When running a scan or many scans to be averaged, the intensity of the spectrum may change over time due to environmental changes or inherent drifts in the radiation source. Baseline correction is a post-processing technique employed to reduce this long-term drift by fitting functions such as a polynomial to the baseline spectrum and subtracting from the experimental data, resulting in a flat baseline.

1.2.4 Time-Resolved FTIR

Time-resolved measurements are a method to sample signals rapidly changing in the time domain such as the switch on dynamics and settling of a laser's intensity. FTIR spectrometers can be operated in step-scan or rapid-scan modes for time-resolved measurements. Time-resolved FTIR is useful within the scope of this work as it is a method to probe intermediate states within a chemical reaction such as monitoring the concentration of [O] generated in photolysis experiments. Another technique enabled by time-resolved FTIR is to rapidly examine the changing dynamics of a laser to simultaneously study a sample and characterise the frequency of a source. Figure 1.9 is an illustration of a signal $g(t)$ as a function of time and intensity. In this example, each step in time is a time-resolved measurement.

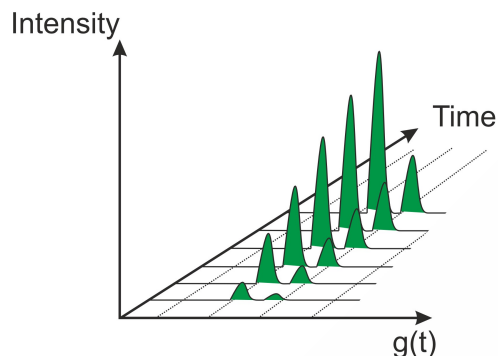


Figure 1.9: Illustration of time resolution.

In step-scan, the mirror is stopped at even intervals and the experiment is repeated. The stepped mirror positions relate to an optical delay and stepped position in time relative to the signal. Step-scan measurements require a process which is easy to repeat or reverse due to a large number of repetitions to obtain a full spectrum [43]. The step-scan method takes longer than regular averaged acquisitions or rapid scans but has the benefit of giving spectra in the time domain without the equipment necessary to rapidly sweep a mirror. Commercial FTIR spectrometers achieve a time resolution on the order of milliseconds in step-scan operation.

An alternative is Rapid-scan FTIR which involves scanning the mirror rapidly over the the experimental time. Rapid-scan techniques cannot reach small time resolutions as seen in step-scan as the mirror is moving the full distance of the interferometer. When choosing a time-resolved method the experimental time must be considered alongside time resolution.

1.2.5 Terahertz Time-Domain Spectroscopy

Previous sections have discussed spectroscopic techniques which work in the frequency domain by utilising FFT, there are time domain methods which allow the time domain and frequency domain characteristics of a sample to be measured. In the THz spectroscopy field, perhaps the most established and popular technique is THz Time-Domain Spectroscopy (TDS). A TDS system utilises coherent radiation and detection through a pair of Photo-Conductive Antenna (PCA) devices pumped by a Femtosecond (fs) laser. The PCA will be discussed in more detail in the following Section 1.3. The combination of broadband emission and coherent detection makes TDS a powerful tool for sampling the properties of a material in both the time and frequency domain.

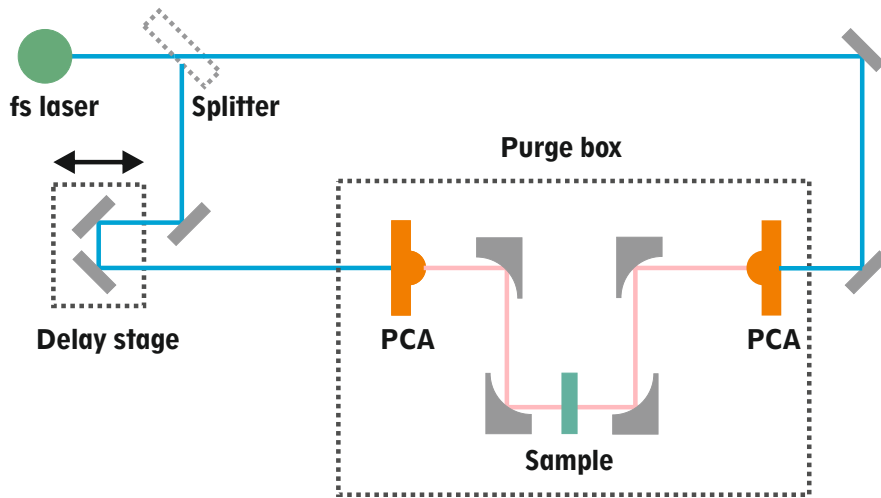


Figure 1.10: Diagram of a transmission THz TDS spectrometer.

Figure 1.10 shows a diagram of a typical transition TDS system where blue lines represent the fs pulse and pink is THz. A common pump laser used is a mode-locked Ti:sapphire laser generating Near IR pulse trains on the order of 100 fs. The pulses are divided by a 50:50 beam splitter down two optical paths before hitting the PCA emitters at different times. The optical delay stage is what enables the time-domain aspect of this method, as when the delay is increased the difference between the pulses arriving at the PCA emitters is altered. The PCAs in this system are biased by a voltage and stimulated by the fs laser, because a PCA is a coherent detection method that detects the THz field rather than intensity. By moving the stage, the measurements become a function of time against the THz electric field. This method of measurement contains real and complex information about the optical sample such as the refractive index and dielectric constants [44] [45].

Figure 1.11 shows a reference sample taken by a THz TDS system in the University of Leeds by Harry Godden, this reference trace had no sample and was in a purged atmosphere. The usable bandwidth of the PCA in this system is 6 THz. The THz pulse can be seen in the time domain in Figure 1.11a, the X-axis is a delay in picoseconds which correlates to a distance the delay stage has moved and the frequency domain in Figure 1.11b. When looking at the frequency domain trace, there is a dip in amplitude around the 8 THz region, this is due to the GaAs within the PCA absorbing the THz radiation.

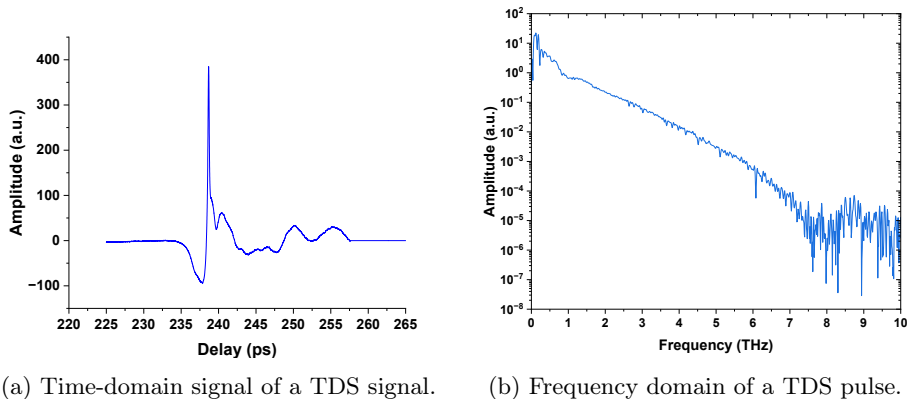


Figure 1.11: A THz TDS measurement with no sample in a purged atmosphere. Data provided by Harry Godden.

1.3 Terahertz Sources

In this section, a range of THz generation technologies will be discussed with a focus on the THz QCL. THz radiation is emitted as part of the black body spectrum so a simple means of emitting THz radiation is a thermal source. The need for coherent light sources has moved research away from thermal sources and towards photonic or microwave-based solutions to bridging the THz gap [46].

1.3.1 Electronic Sources

Below the range of 100 GHz, solid-state electronics such as transistors and oscillators can deliver significant power in the range of Watts. Finding THz sources which have an output power over the range of milliwatts requires approaches from microwave technology. One such device is the Backward Wave Oscillator (BWO) that has been reported to operate at 1.4 THz with a power of 2 mW [47]. The BWO operates by focusing an electron beam generated by a Cathode through a decelerating surface onto an Anode. As a result of this deceleration, THz radiation is produced in the opposite direction which is coupled out of the oscillator [48].

Schottky diode multipliers are an alternative low-power generation method compared to free electron generation, being compact and having a stable frequency, Schottky diodes see wide use in THz instrumentation. Frequency multipliers are non-linear devices designed to optimise power transfer from the fundamental frequency to a higher-order harmonic [49]. The devices consist of matching networks to couple a microwave circuit into multipliers and amplifiers to get a THz output in the range of 1 to 2 THz with powers up to hundreds of milliwatts [50].

Weak parasitic impedances in Schottky diodes make them an ideal choice for use in multiplier circuits in the THz region, the low parasitic parameters in a Schottky diode are a result of the vertical structure of Schottky devices. Unlike typical diodes which are fabricated along a horizontal plane, a Schottky diode is constructed of vertical layers which reduce the parasitic impedances seen within the device [51]. In both BWO and Schottky multiplier, impedances within the system limit usable power to the frequency to the 2 THz range. Another electronic THz source is the Gunn diode, which has been simulated to operate up to frequencies of 700 GHz and practical devices have been reported operating at output powers of 10 mW at 400 GHz [52]. Another diode THz emitter is a Resonant Tunneling Diode (RTD) which operates in frequencies between 0.1 to 2 THz with reported powers in the ranges of 2 mW to 10^{-6} mW [53]. Impact avalanche transit time (IMPATT) oscillators are a solid state device which typically operates at optical powers in the range of 1 W in the microwave region. These devices have been designed to operate at frequencies towards the 1 THz point, but suffer from large losses giving optical power in the 1 mW range. Although these devices seem to be restricted to lower frequencies, using Molecular Beam Epitaxy (MBE) to grow precise structures could see an improved output power from these devices in the mm-wave region [54].

1.3.2 Photoconductive Antennas

Room temperature THz sources are an attractive technology due to the reduced cost and complexity when compared to a cryogenic system. The THz PCA, sometimes called a photoconductive switch is an optically pumped device which can be used as an emitter or detector. These antennas were first reported by P. R. Smith, et al, in 1988, with an antenna bandwidth spanning < 100 GHz to > 2 THz. These devices are fabricated on GaAs which is grown in an MBE process [55]. Antenna design in a PCA is important and a field of study itself for example nao antenna arrays can improve device efficiency [56]. A simple PCA design is shown in Figure 1.12.

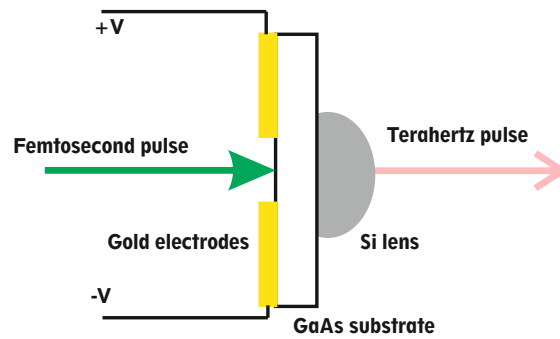


Figure 1.12: A simple illustration of a THz PCA.

PCAs typically consists of a substrate with simple gold electrodes patterned which are under bias. A THz pulse is generated when an incident fs pulse illuminates the gap in the electrodes whilst they are under bias. The substrate absorbs photons from the incident light and excites carriers from the valence band to the conduction band. The conductor bias accelerates these carriers and generates a photocurrent. The rapid change in photocurrent density is on the picosecond timescale and generates electromagnetic radiation in the THz frequency. GaAs is commonly used as a substrate due to its direct band gap and band gap energy of 1.42 eV, which optimises the absorption of 800 nm (1.55 eV) Ti:sapphire lasers [57]. A PCA is an attractive source for THz spectroscopy and is commonly used in TDS, but the need for external pumping lasers increases a system footprint. A low optical conversion efficiency sees low THz power with typical optical pump powers ranging from 1 - 50 W and PCA common conversion efficiencies ranging 0.01% to 0.1% [58]. The broadband emission of a PCA is attractive in many situations involving solids and liquids. However, in gas spectroscopy, the broadband emission results in difficulty obtaining high-resolution gas spectra and lineshapes which a tuneable narrow-band source can provide.

1.3.3 Photomixers

A popular photonic approach to THz generation is using two diode lasers with a difference frequency in the THz range and a Photomixer. The Photomixer is a non-linear device which operates in a heterodyne system where the two lasers are focused onto the mixer and the result is a beat frequency which can be tuned by changing the frequency of the lasers [59]. A THz photomixer generates continuous wave THz radiation unlike a PCA. Photomixers suffer from low conversion efficiency where the typical performance is around the 0.1% region [60].

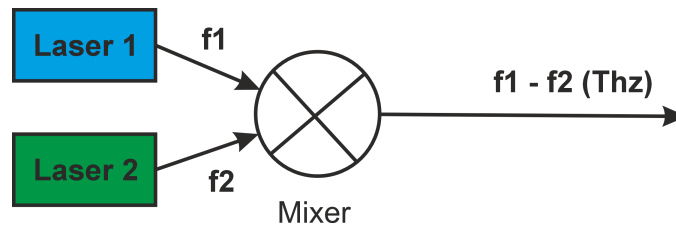


Figure 1.13: A simple illustration of a THz Photomixer. The mixer uses the principle of generating a THz wave by the difference frequency of two lasers.

The Photomixer is a device which consists of electrodes patterned onto a semiconductor which can produce carriers fast enough to match the beating of the input lasers, an example of this is shown in Figure 1.13. In the case of THz Photomixers, Low-Temperature Grown Gallium Arsenide (LT-GaAs) is a common substrate due to the carrier recombination time being in the order of picoseconds, allowing THz radiation being emitted. Operating as a CW source for THz experiments, Photomixers have a broadband emission capable of reaching powers in the order of microwatts and up to frequencies of 3.8 THz [61].

1.3.4 Quantum Cascade Laser

An electron inside of an atom can be excited from one energy level E_1 to a higher level E_2 by an absorbed photon, this simple two-level energy model can be used to explain the emission in a laser and is shown in 1.14.

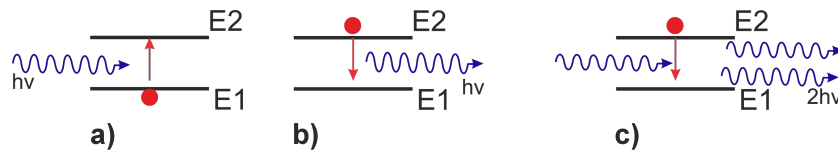


Figure 1.14: A two energy level model of laser emission showing the three interactions (a) Absorption. (b) Spontaneous Emission. (c) Stimulated emission.

An electron can be thought of as having three interactions:

1. Absorption where the electron is excited from E_1 to E_2 .
2. Spontaneous emission where an electron falls from E_2 to E_1 and a photon with energy $h\nu = E_2 - E_1$ where h is Planck's constant and ν is the frequency. In spontaneous emission, the electron falls randomly and the photon is emitted in a random direction.
3. Stimulated emission is how a laser achieves amplification. A photon stimulates the electron to transit from E_2 to E_1 and the emitted photon is in phase and travelling in the same direction as the stimulating electron.

Laser is an acronym for Light Amplification by Stimulated Emission of Radiation and to use stimulated emission for light amplification, population inversion must be achieved. Population inversion is the state where the upper energy level E_2 has more electrons than the lower E_1 this is done by pumping the electrons to a higher state. This is important to ensure more stimulated emission than absorption when a photon enters the laser. Population inversion cannot be achieved in a two-level energy system like Figure 1.14 because incoming pump photons would cause stimulated emission. Figure 1.15 shows a three-level model where the electrons are first pumped to E_3 before dropping into a more stable state E_2 where stimulated emission causes in-phase photons to be emitted [62].

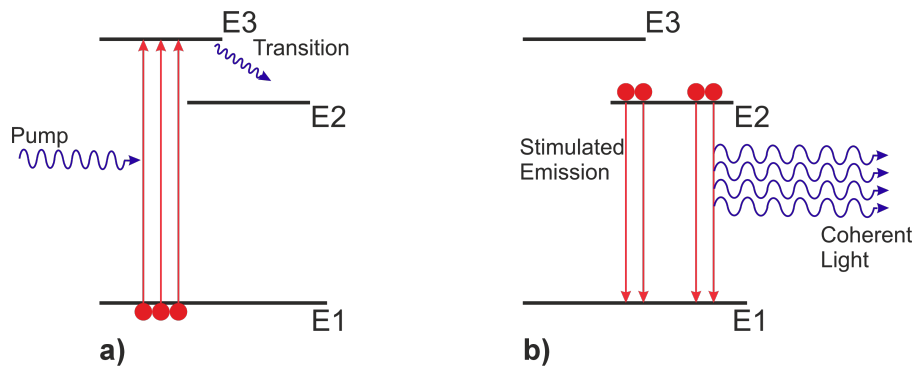


Figure 1.15: A three energy level model of laser emission showing the three interactions. (a) Electrons are pumped to the third state E_3 and relax to a stable state E_2 . (b) Stimulated emission causes the electrons to transition to E_1 and emits in-phase light.

The gain medium of a laser is inside a Fabry-Perot cavity which consists of two highly reflective mirrors forming a cavity. This cavity reflects the stimulated photons through the gain medium, further stimulating emission and amplifying the light. An integer number of standing waves called modes exist inside the laser cavity because of constructive and destructive interference. The spectrum of a laser consists of a sum of these modes inside its spectrum and the bandwidth is typically decided by the bandwidth of the gain medium. Figure 1.16 shows a laser cavity's standing wave and resulting spectrum.

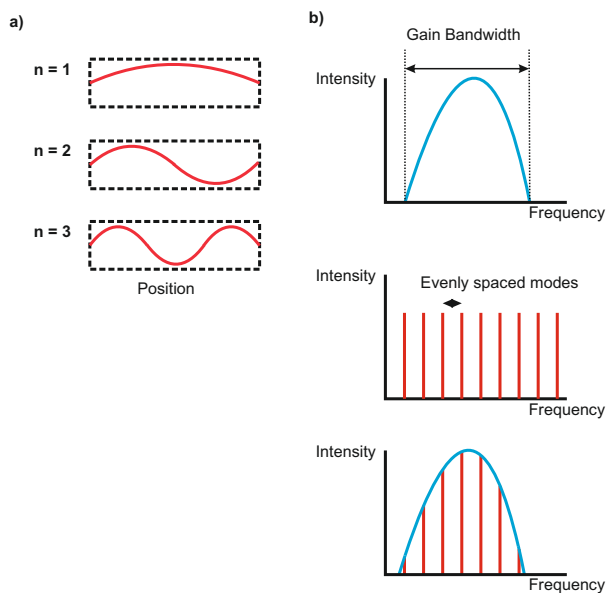


Figure 1.16: (a) An illustration showing modes of the standing wave inside a laser cavity. (b) The resulting spectrum of the integer modes and the gain bandwidth.

The wavelength of a diode laser depends on the separation of the band gap in the semiconductor and in the THz range the photons are low in energy (0.41 meV - 41 meV). This is a material limitation when making THz diode lasers due to a lack of narrow bandgap semiconductors. Narrow band gap semiconductors have been grown which are lead salt lasers. These materials require cryogenic cooling and emit radiation in the mid IR region (3-30 μm), these lasers historically have been used mostly for spectroscopy due to the wavelength falling within the region of IR spectrum where atmospheric gasses are visible. These devices are known for their difficulty producing and being in relative infancy compared to GaAs [63].

An alternative to interband stimulation is to have the energy levels within a semiconductor's conduction band. This can be realised by a heterostructure which uses two semiconductors with different band gaps. Having a thin layer (< 50 nm) between two wider band gap materials gives quantum well, plotting this as potential against position gives Figure 1.17. In Figure 1.17 the energy levels E_e and E_h are minibands formed in the quantum well which can be engineered to produce low-energy photons when the electrons move between the mini bands.

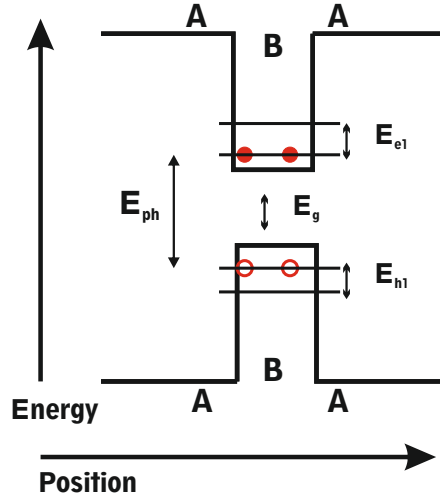


Figure 1.17: Illustration of a quantum well structure. Materials A and B are semiconductors with different band gap energies.

Any charge carriers in the system will try to lower their energy, electrons (filled) by going down into the valence band and holes (circle) by going to the conduction band. This attempt to lower the overall energy results in the carriers gathering in a quantum well and creating a set of energy levels within the quantum well. The energy levels within a quantum well are quantised energy levels, this is found through the infinite potential well model, where a particle is confined within a potential well with infinite walls. The potential walls mean a particle must be inside the potential well, resulting in a quantised number of allowable levels. When applied to a practical quantum well, the generalised equation becomes 1.7 which shows in a simple model, that the separation of energy levels E_{en} in these subbands can be adjusted by the length (L) or effective mass m_e^* as the other values are constants [62] [64].

$$E_{en} = \frac{\hbar^2 \pi^2 n^2}{2m_e^* L^2} \quad (1.7)$$

In 1994 a laser structure was fabricated using a periodic structure of quantum wells inside the conduction band of GaAs with a fundamental band gap of 1.519 eV to engineer the first QCL reported by J. Faist [65]. This design of laser was further used to develop the first THz QCL in 2002 and was reported by A. Tredicucci [66]. The QCL is fabricated from a periodic structure of quantum wells which are grown in MBE where the thickness of material layers can be controlled to get the desired material properties. QCLs get their name from the cascading effect of electrons through quantum wells that occurs when a bias is applied to the device. Figure 1.18 shows a simple structure with a bias applied.

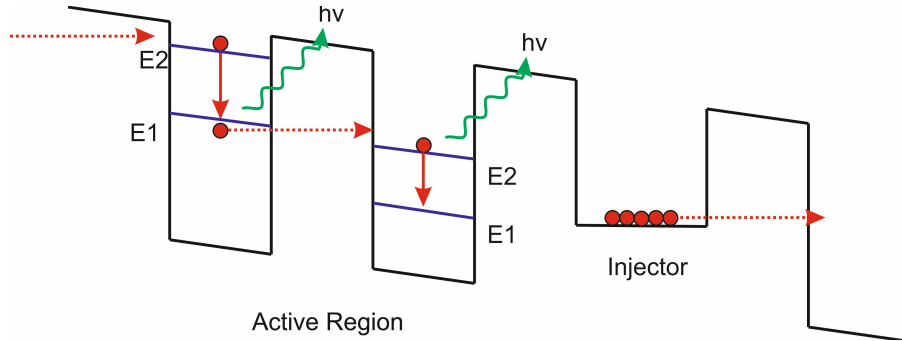


Figure 1.18: A simple diagram of a QCL structure showing one period of the heterostructure.

Lasing occurs inside the QCL in the gain medium known as the active region and population inversion is achieved through the injector regions where electrons are usually injected into the top energy levels of quantum wells through quantum tunneling. From the injector, an electron enters the top energy level of a quantum well, relaxes into the lower state and emits a photon before being transported to the top energy level of the adjacent quantum well. Now a single electron can emit multiple photons as it passes through the periodic structure of quantum wells inside the active region, which efficiently uses electrons within the system.

The frequency of photons emitted in the QCL depends on the thickness of the quantum well, which sets the energy level separation within a quantum well. The active region designs are designed in complex simulations and fabricated using the MBE process.

Different active region designs exist for a QCL and are used depending on the desired QCL properties. There are four main designs, the first THz QCL used a Chirped Superlattice (CSL) design [66]. In a CSL active region when a bias is applied a series of minibands are formed and lasing takes place as an electron falls from E_2 to E_1 in the miniband rather than between quantum wells. The Bound To Continuum (BTC) design is based on CSL, where emission is through transitions through minibands. The design differs slightly as a thin well is introduced near the injector creating a small minigap, the electron relaxing then moves in a diagonal direction to E_2 rather than a vertical relaxation. The BTC design offers greater temperature performance and higher output powers than that seen in CSL designs [67].

An alternative mechanism to superlattice designs utilises a non-radiative transition called LO phonon scatter. Transitions between energy levels can be radiative, or non-radiative where the energy is released through lattice vibrations within the crystal. Phonons can be classified by direction, either longitudinal (LO) phonons or transversal phonons (TO), inside a QCL only LO phonons are considered as TO phonons have minimal effects [68]. This process depopulates the lower energy state into the injector region.

The Resonant Phonon (RP) design uses quantum wells which bring the lower state E_1 into resonance with the top of the injector region which quickly scatters the electron into the next radiative state E_2 . This design has a lower chance of thermal excitation, these designs typically require high-bias currents and are mostly used in pulsed operation due to heating within the active region. Hybrid designs combining the RP and superlattice active regions which use both LO-phonon scattering within a superlattice and are popular in long wavelength operation, the operation of a hybrid active region is complex and covered in literature [69] [70]. The emission bandwidth of THz QCLs spend 1 - 5 THz and the output powers from QCLs have been reported up to 130 mW in CW and 1 W peak power in pulsed operation [71]. QCLs have been reported with a tuning range up to approximately 20% tuning range (660 GHz) in a 3.47 THz QCL [72]. The intrinsic linewidth of a QCL is in the range of 100 Hz and the operating temperature of a QCL ranges from 4 K to high-temperature designs operating at low pulsed duty cycles reported as high as 250 K [73] [74]. Band diagrams of four different QCL active region designs are shown in Figure 1.19 which is taken from [69].

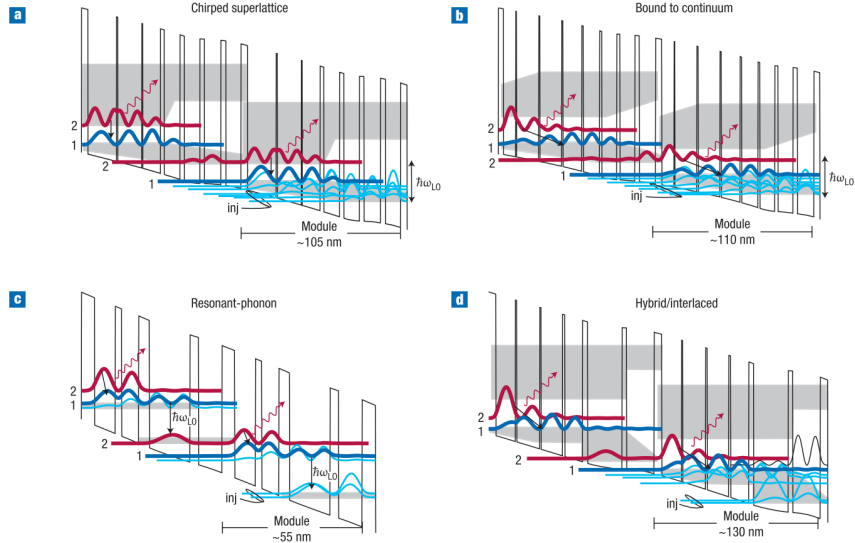


Figure 1.19: Diagrams of the different active region designs taken from [69].

The optical mode inside of a THz QCL should be confined within the active region for better performance [75]. Higher order optical modes within a device often have large diffraction losses and within a QCL, suppressing these through high mode confinement leads to a higher optical output. A high mode confinement also reduces the gain threshold which results in lower waveguide losses in lasers operating in the THz range [76] [77]. The first THz QCL used a single metal semiconductor layer as a waveguide which confined the THz field. The design uses surface plasmons at the metal-semiconductor contact inside the

QCL [78]. An alternate design to the surface plasmon waveguide is a double-metal design. The double-metal waveguide uses a metal-semiconductor-metal waveguide where the plasmon is confined within the structure and there is a near unity confinement factor ($\Gamma \approx 0.98$) [79] compared to surface plasmon designs ($\Gamma \approx 0.2 - 0.5$) [68]. Double metal waveguide QCLs typically have higher power performance and temperature performances, but sacrifice the beam pattern which tends to be poor compared to a surface plasmon device and requires complex fabrication techniques [69].

1.4 THz Detectors

The first THz detectors were thermal detectors which work on the principle of incident radiation heating an element and detecting a change related to radiation intensity. Thermal detectors are incoherent, where no phase information from the incoming radiation is recorded. An example of thermal detection is a bolometer which is a sensitive and broadband detector, the sensitivity of these detectors can often be improved through cryogenic operation. A bolometer has a resistive element with a small thermal capacity and a large temperature coefficient, incident radiation correlates to a change in element resistance. The change in resistance is measured so there is no direct photon-electron interaction, unlike a photodiode. An example of a helium-cooled bolometer is the QMC Instruments QNbTES/X which is a composite germanium bolometer. This detector has a specified range of 100 GHz to 20 THz, Noise Equivalent Power (NEP) of $< 2 \times 10^{-12} \text{ W Hz}^{1/2}$ and a modulation bandwidth to 1 kHz. An example of a room-temperature thermal detector is the pyroelectric detector, which uses two electrodes perpendicular to a capacitive element. When radiation hits the capacitor, a charge is generated between the plates which causes current to flow between the electrodes [80]. Pyroelectric detectors are less sensitive than a bolometer but have the advantage of being compact, room temperature and require less maintenance. An alternative room temperature detection method uses a Field-Effect Transistor (FET) as a detection element, the operating principle of these devices and performance will be discussed in Chapter 2.

The mixing principle can be used to produce and detect THz radiation. Heterodyne receivers are commonly used in remote sensing systems and operate using a mixer and THz Local Oscillator (LO). The LO converts the THz to an intermediate frequency which is either the sum or the difference of the RF signal and LO. The difference is filtered out and can be examined at lower frequencies using RF devices such as a spectrum analyser. A block diagram of a mixer being used as a detector is shown in Figure 1.20.

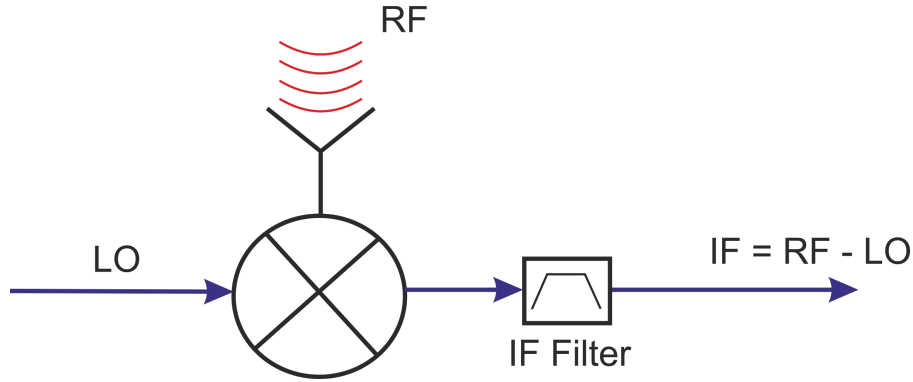


Figure 1.20: Simple diagram of a heterodyne receiver.

The Hot Electron Bolometer Mixer (HEBM) is an example of a sensitive THz mixer, these use a thin superconducting film as a detector element. HEBMs have been used in multiple astronomical missions such as the Herschel Space telescope operating up to 1.7 THz or on SOFIA which used HEBM mixers up to 4.7 THz [81]. Schottky diode mixers can also be used to down-convert THz signals. They are attractive for satellite-based missions because of their small size and ability to work at room temperature or cryogenic temperatures. Schottky diode mixers have been reported to operate up to 2 THz which would allow them to target [O] [82]. When using mixers in a heterodyne receiver in remote sensing, these detectors often are the most sensitive systems. Heterodyne receivers have a high resolving power, typically in the order of $R > 10^6$ and can resolve gas dynamics from the cold interstellar medium through Doppler shift. With sensitivities in HEBM systems reaching the physical limit for coherent detection which is given in Equation 1.8, where $T_{RX,SSB}$ is the receiver noise temperature given in kelvin and $h\nu$ is Plank's constant multiplied by the frequency [83].

$$T_{RX,SSB} \geq \frac{h\nu}{k_b} \quad (1.8)$$

Golay cells are common THz gas sensors and are used in astronomical detection. These are room-temperature devices which contain a gas chamber, one side of the chamber is an absorber and the other is a flexible mirror, to ensure any light is reflected away from the cell. When taking a measurement, a Light Emitting Diode (LED) is focused onto the mirror and reflected onto a photodiode. When THz radiation interacts with the chamber it heats the gas which causes it to expand, this expansion deforms the mirror and changes the intensity of the detected LED light [84] [85]. An example of a commercial Golay cell is a Tydex GC-1P which has a specified NEP of $1.4 \times 10^{-10} \text{ W Hz}^{1/2}$, a modulation bandwidth up to peak modulation response of 15 Hz and a detection bandwidth from 37.5 GHz to 20 THz.

1.5 Gas Spectroscopy

Instrumentation for chemical analysis is vast and spans centuries as humans have always found new ways to perform analytical chemistry. This section will briefly discuss the mechanism behind spectral features and why they occur in certain frequency ranges and review instrumentation used for chemical analysis.

Features in molecular spectroscopy are a result of absorption, emission or scattering of photons as they interact with a molecule. The properties of a molecule dictate where there is a spectral feature due to an oscillating dipole at a given frequency, these properties are called selection rules. Gross selection rules are the general features of a molecule to exhibit spectral lines at a frequency, specific selection rules describe whether a transition is allowed through the change in a molecule's quantum number. For example, the gross selection rule of a purely rotational spectrum is the molecule must have a permanent electric dipole and purely rotational spectral features are associated with the THz and microwave range. The selection rules and quantum numbers are described in more detail in Chapter 3.

In IR spectroscopy, vibrational states are present. A molecule can experience harmonic oscillations, where the vibrations can be categorised as either changes in the length of the molecular bonds through stretching or changes to the angle of the molecular bond through bending. The gross selection rule for vibration transitions is the electric dipole moment of the molecule must change when the atoms in the molecule are displaced, these vibrations are infrared active. Some vibrations do not affect the dipole moment and do not absorb or generate radiation, these are infrared inactive vibrations. The THz spectrum of a molecule shows fundamental rotational and vibrational transitions and fine-line electronic transitions of some atoms are also present in the THz region [86] [87].

1.5.1 Gas Spectroscopy Instrumentation

Chromatography is a method of separating components of a mixture into components and gas chromatography is perhaps one of the most popular methods for analysing mixtures in the gas phase. Chromatography separates a mixture into two phases: the stationary phase and the mobile phase. The stationary phase has a large surface area and when the mobile phase is introduced, the different components within the mixture of the mobile phase will react with the stationary at different rates. The difference in reaction rates allows each component of the mobile phase to be examined separately as it passes through the stationary phase [88]. The sample under test is lost in a gas chromatography system after analysis, making it unattractive in situations where the sample must be preserved.

There is no formal definition for fast gas chromatography, the speeds of a gas chromatography system are set by the separation speed of the sample and various methods are employed to improve the separation speed. Reducing the resolution of the measurements is a popular method to increase experimental time into the sub-second range. Increasing the gas pressure of the sample, the

temperature of the sample or using capillary columns with reduced volume all reduce the separation time seen in a gas chromatography system. A disadvantage to gas chromatography is the reliance on volatile compounds as the species under test must be able to be evaporated without decomposing to be sampled by the instrument [89].

A popular analytical method is Nuclear Magnetic Resonance (NMR) which is a powerful tool, when paired with other experimental methods such as IR analyses it can find the full information of a sample. NMR operates on the principle of nuclear spin where a nucleus has an observable angular spin momentum. NMR uses alternating magnetic fields to examine the spin moments of a particle and observing the transitions of the spin moments, the structure of a sample can be deduced. Not all molecules have an observable magnetic moment in NMR such as common atmospheric gasses including oxygen and carbon [90]. A NMR instrument can be split into two categories, low field and high field. Low field NMR use permanent magnets and operate at frequencies ranging 40-80 MHz, these are often referred to as benchtop spectrometers. High field NMR spectrometers use large superconducting magnets and typically span the ranges of 200 to 600 MHz. If a reaction can take place inside of the sample tube of a NMR spectrometer, then the option for in situ monitoring of reactions is possible, but due to the size and complexity of a high field NMR this is rarely done using flow reactors [91]. NMR can be used to track isotopes of common species such as carbon-13 (^{13}C) to track the flow of minerals which is particularly useful in metabolic studies. A lack in sensitivity of NMR is considered the main drawback of this technology, the limit of detection is often defined as the amount of sample required to give a Signal-To-Noise Ratio (SNR) of 3:1. This value is often orders of magnitude above other spectroscopic methods. For example, a benchtop Bruker Fourier 80 NMR is quoted as having a 180:1 ^1H sensitivity. Still with the sensitivity limitation, NMR tends to be one of the most used analytical techniques [92].

When looking for a system which has a small footprint and can be used in the field, NMR spectrometers are unsuitable. The large superconducting magnets found in high field instruments require cryogenic cooling and have high power consumption. Due to the large size and high power consumption when compared to other technologies, NMR spectrometers are unsuitable for in-situ measurements [93].

A popular technique for gas sensing is tunable diode laser absorption spectroscopy, which takes a tunable diode laser and tunes the wavelength over a known range to measure absorption frequency by inspecting the light after a sample. This technique was used for the QCL in this work and is discussed in detail in Chapter 3. Another laser spectroscopy technique is Raman spectroscopy, which inspects scattered light from a sample as an alternative to the absorbed light. When light interacts with matter many interactions can happen and one of these is scattering, where a photon of wavelength ω_1 scatters from a surface it will have a new wavelength ω_2 which now carries information from the matter and the interaction. This scatter is the basic principle of Raman spectroscopy [94]. Raman spectroscopy is a well-developed method of sensing

vibrational and rovibrational spectra of solid or liquid samples. Raman spectroscopy has the benefit of detecting homogeneous species such as H_2 or O_2 which are typically invisible to IR radiation, making it attractive for gas spectroscopy. However, due to the low scattering Raman cross-section, the results are low-intensity spectra which require signal enhancement techniques and this results in Raman gas spectroscopy being uncommon [95].

1.5.2 THz Gas Spectroscopy Instrumentation

With the advances in THz sources and detectors discussed previously in this chapter, THz spectroscopy has become a more mature and realised technology. In the field of gas spectroscopy, THz lab-based spectrometers using a THz QCL in direct absorption or self-mixing have become increasingly reported in literature. High-resolution gas spectroscopy has been realised in multiple ways, one method is mixing the QCL emission with a gas laser such as a CO_2 laser. This method of mixing takes advantage of the narrow intrinsic linewidth of a QCL and the stability of gas laser emission. A high-resolution THz gas spectrometer was reported by H.W. Hübers, et al, in 2006 [96] where a QCL was stabilised using a gas laser and examined a MeOH line at 2.519112 THz, with an experimental accuracy limited by the gas laser stability of 1 MHz. High-resolution THz spectroscopy using a QCL has also been reported using frequency and phase stabilisation techniques. An example of a phase-locked system was reported by S. Bartalini, et al, in 2014 where a frequency comb stabilised 2.4 THz QCL was stabilised to a frequency uncertainty on the order of parts per 10^{-11} , giving a measured MeOH line error on the order of 10^{-9} . As well as detecting MeOH spectra, a lab-based THz spectrometer with a 4.7 THz QCL source has been reported by J. R. Wubs, et al, in 2023 [97] where atomic oxygen was detected in a plasma reactor at a detection limit of $2 \times 10^{13} \text{cm}^{-3}$.

Direct absorption spectrometers use a separate source and detector, but by directing radiation back into the facet of a QCL, the laser voltage can be used as a detector signal. The radiation coupling into a QCL facet causes interference with the modes within the laser cavity which is proportional to the amplitude of radiation coupling into the cavity, this mode of operation is called self-mixing. Self-mixing can be used in many applications such as interferometry, imaging or spectroscopy, in this work self-mixing will refer to gas sensing. As well as reducing the complexity of a system by using a QCL as a source and detector, self-mixing also doubles the path length through a sample which is useful in gas samples by effectively doubling the amount of material that absorbs radiation. Self-mixing THz gas spectrometers have been reported by H.W. Hübers, et al, in 2016 [98] with a frequency resolution of 10^6 and with a SNR 3.1 less than previous data obtained by liquid helium bolometer.

TDS is a popular method of sensing in the THz range and has the benefits discussed in Subsection 1.2.5. Photoconductive antennas provide a broadband THz source which would allow a large frequency characterisation of a gas sample at room temperature. THz spectroscopy benefits from the advantage of coherent detection, but gas spectra are limited by the resolution as the frequency

resolution will be limited by the temporal range of the scan which is typically 1 - 10 GHz in TDS systems. Many gas transitions can fit inside of a 1 GHz step, so the frequency resolution of a TDS system is undesirable for gas spectroscopy. A lack of sub-MHz resolution THz spectrometers means this method is not suitable for line shape measurements and high-resolution gas spectroscopy. When the time domain pulse propagates through a sample and is analysed, a series of uniformly spaced echoes will be present. These echoes can be used as a unique molecular identifier and the FFT of this time domain signal will have oscillations, the gaps between these oscillations relate to the absorption coefficient of a sample [99].

Although the rotational transitions are narrower than the spectral resolution of a TDS system, it is still suitable for distinguishing between gasses and could be used in air quality monitoring without the need for cryogenic components found in QCL spectrometers [100].

1.5.3 Spectroscopy Catalogues

When spectral lines are discovered through analytical or computational techniques, they are catalogued. Cataloguing is done through publications in scientific journals and databases which collect discovered spectral lines and standardise the format. The standardised formats are files which allow the scientific community to access and examine the spectrum of a molecule programmatically. An example of a spectral database is High-Resolution Transmission Molecular Absorption Database (HITRAN) which aims to have a consistent set of parameters that document both experimental and calculated parameters of the absorption spectra of molecules in the gas phase. The spectral information within HITRAN is part of a long-running project started by the Air Force Cambridge Research Laboratories in 1960 to document and maintain the spectral information in an accessible database and provide code to simulate molecular transitions [101].

Another molecular database is the NASA Jet Propulsion Laboratory (JPL) Submillimeter, Millimeter and Microwave Spectral Line Catalog. The JPL catalogue was used throughout this work and any mention of the JPL in this work is in reference to the spectral database. The catalogue spans submillimeter and millimetre spectral lines up to 10 THz and is intended to be used as an aid in the identification of spectral lines observed within Earth's atmosphere or the interstellar medium [102]. The JPL catalogue is managed by NASA and was first reported in 1985 [103]. As well as providing spectral line data the code used to simulate the molecular transitions is available from JPL [104]. Throughout this work, a Matlab program written by Dr Alexander Valavanis is used to access the JPL and plot spectral lines with the option to change pressure, temperature and frequency step.

The Matlab script first takes user inputs for pressure, temperature, frequency of interest, frequency step and species identifier. The Matlab script takes the species identifier and reads the JPL entry, takes the frequency and converts it from MHz to GHz.

The intensity is stored in units of $\frac{nm^2}{MHz}$ at 300 K and is converted it to a common IR unit $\frac{cm^{-1}}{molecule/cm^{-2}}$ at a user-defined temperature. The intensity is stored under the identifying tag LGINT which is the base 10 logarithm of the intensity in units. The peak then has the Beer-Lambert law applied, a Lorentzian profile applied for pressure broadening and a Gaussian profile applied for Doppler broadening. This broadened profile is applied to the centre frequency, the resulting spectrum is provided in both absorption and transmission [105].

1.5.4 Aims and Objectives

The goal of this project was to develop THz gas spectroscopy instrument with a sensitivity high enough to detect radicals such as atomic [O] and [OH]. Previous literature shows lab-based [O] observation at 4.74 THz in a plasma generator with a density of $9.6 \times 10^{14} \text{ cm}^3$ with an error on the concentration calculation of 30% [97]. The main goal of this project was broken up into work packages which relate to a thesis chapter where Chapter 2 covers the work package of THz sources and detectors, Chapter 3 is gas studies taken during the project, Chapter 4 shows work on developing a multi-pass gas cell and Chapter 5 presents a power stabilised THz QCL. Figure 1.21 shows a diagram of the instrument developed in the project and the different controllers and signal paths. The objectives of this work are summarised as follows:

1. Characterise a THz QCL which has sufficient tuning range to target MeOH and D₂O, these provide a means to calibrate system sensitivity and tuning.
2. Stabilise the source and detector to remove influences from ambient temperature and cryostat temperature.
3. Improve the sensitivity of the system using multi-pass optics.
4. Improve the speed of the system enabling the detection of fast photochemistry.

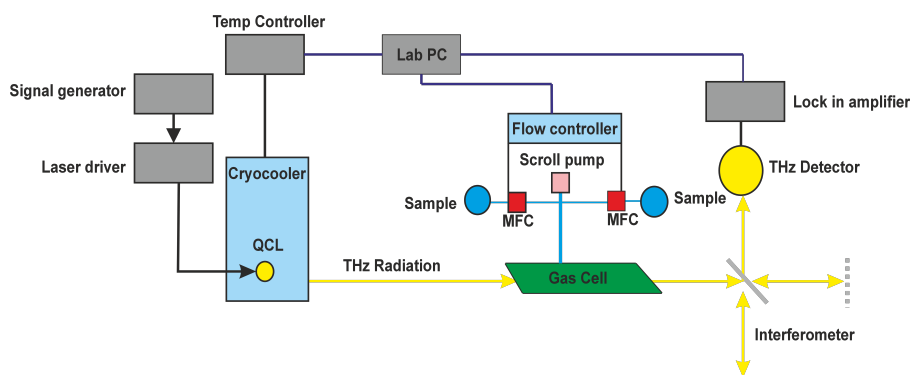


Figure 1.21: Diagram of the spectrometer.

Figure 1.21 shows a block diagram of the system developed in this work. The user interface and LabView programs are run on a PC which uses GPIB or USB to communicate with lab equipment. The temperature controller reads the internal cryostat temperature and can adjust an internal heater to increase the operational temperature of the QCL. The PC also controls a lock-in amplifier, the operation of a lock-in amplifier is discussed in Chapter 2. The lock-in amplifier reads the voltage signal from a THz detector and processes the signal. The third PC connection in this diagram goes to a flow controller which controls the flow of samples into the gas cell. The flow controller reads from two pressure gauges and controls the sample flow through an Mass Flow Controller (MFC). A signal generator supplies modulation to the QCL through a current driver, the current driver is connected by BNC to the signal generator. Using a ramp waveform can sweep the full QCL current range and tune across spectral lines.

The yellow arrows in 1.21 show the optical path, the THz radiation propagates through a gas cell and into the interferometer. Throughout this work, direct absorption measurements were taken, so the interferometer was parked. Future work will include a calibration method to measure both QCL frequency and correct for interferometer frequency errors in the same routine.

1.6 Thesis layout

The research field of THz QCLs has been investigated and improved upon over the years since their design, they are now at the point where lab-based systems are being realised and missions such as SOFIA have successfully targeted atomic oxygen using a QCL [2]. As discussed in Section 1.5 many molecules of interest and radicals have spectral fingerprints in the THz region.

The work in this thesis shows the development and improvement of an existing THz gas spectrometer and outputs delivered from the system over years of research. Chapter 1 introduced the motivation behind this project and why THz is of interest to atmospheric chemistry, as well as briefly reviewed popular gas spectroscopy methods. Laser theory is shown using a simple 3-energy

model and the principle of a QCL is explained, reviewing different waveguide active region designs. A review of THz detection methods has been discussed and a block diagram of the entire THz gas spectroscopy instrument is presented alongside the aims and objectives of this project.

Chapter 2 shows the data from characterising the QCL used in this project including beam profiles, spectral data and Light-Current (LI) characteristics. A section of this chapter will describe how the frequency of the laser was calibrated against the spectral data of MeOH and D₂O. The cryostat used to cool and maintain the QCL temperature is also discussed in this chapter.

Chapter 2 also looks at THz detection, starting with a review of THz modulation techniques and results from an investigation into power drifts on thermal THz detectors. A brief description of the operating principle of THz detection using FETs and results from characterising the FET detectors are presented.

Results from gas spectroscopy experiments using a single pass gas cell are presented in Chapter 3, the experimental system is described along with diagrams of the optical path and gas manifold. The species being examined are D₂O, MeOH and mixtures of the two molecules. These molecules were used to characterize the instrument as they are visible in the THz spectrum and are safe to vent into the atmosphere in small quantities.

To improve the sensitivity of the system, a multi-pass gas cell has been designed and fabricated which is a Herriott cell design. Chapter 4 contains a literature review on the Beer-Lambert law and why increasing optical path length is advantageous. Two multi-pass cell designs are reviewed which are the White cell and Herriott cell. Cavity-enhanced techniques are briefly reviewed as a suggestion for further work in multi-pass gas sensing. The principles of a Herriott cell are described in detail with the design for the entry optics into the multi-pass cell. Ray tracing results from the Herriott cell are present with Computer Aided Design (CAD) models of the purge boxes and mirrors. Photographs of the Herriott pattern on the mirrors using a visible laser are presented at the end of Chapter 4.

The last experimental chapter is Chapter 5 which presents the work done to power stabilise a QCL using a Photonic Integrated Circuit (PIC). A literature review describes the motivation behind laser stabilisation, the difficulties found when using unstabilised lasers and control theory. The laser with an integrated attenuator was designed and fabricated before the beginning of this project, Chapter 5 will show the results of using this device inside a control loop to achieve a power locked QCL.

The final chapter of this thesis is the Conclusion 6. The conclusion discusses each chapter and how the results from this work aligned with the project aims. Finally, a section discussing future work and where it fits within the original goals set out at the beginning of this project.

Chapter 2

Terahertz Instrumentation

The field of spectroscopy relies on knowing the characteristics of the electromagnetic radiation. If the application requires coherent detection, the radiation source must be characterised to a higher accuracy to obtain both phase and intensity. Different applications need various levels of precision known about a light source and in spectroscopy, a spectrum should be confidently identified by intensity and frequency. To obtain high confidence levels in a spectrum produced by a THz QCL, the source and the cooling equipment and detector should be characterised. This chapter will cover the 3.4 THz QCL used in this project and unless stated otherwise, this QCL was used as a THz source for experimental data.

In Chapter 1, the literature review described different QCL designs, the laser used in this work is a hybrid active region with a surface plasmon waveguide. Although the surface plasmon design gives a poorer optical power and operating temperature when compared to double metal, the improved beam quality seen from these waveguides is desirable for this project with the long optical path lengths in gas sensing.

2.1 Closed-cycle Cryocooler

THz QCLs are cryogenic devices, although devices operating with a Peltier cooler have been reported operating in pulsed operation at insufficient powers for most applications [106]. A QCL is mounted on a cryostat's cold finger, drawing the heat away from the active region. The cryostats used in this work are helium cryostats which can be either a continuous flow or closed cycle design. A cryostat must be under vacuum to thermally insulate the cold finger from environmental temperature and this is done using a turbomolecular pump and reducing the pressure to a magnitude of 10^{-6} Torr. Temperature probes are fixed inside a cryostat to monitor temperature and a heater can be biased to raise the temperature. An external control system monitors the cryostat temperature and can adjust the heater to maintain a user-defined temperature setting.

The QCL used for gas spectroscopy work was mounted inside of a closed cycle cryocooler. The THz emission is directed through a 3 mm thick HDPE window fixed to a port of the cryocooler and the other viewports on the cryocooler are quartz windows.

Helium flow cryostats flow liquid helium onto a cold finger where a device is mounted. A helium dewar is connected to the cold finger using a transfer tube, and the dewar pressure increases as helium boils. Liquid helium flows from the dewar into the cold finger when the dewar pressure is high enough to force a flow through into the cryostat and freeze the inside of the transfer tube. When the helium reaches the cold finger it boils and is vented into the atmosphere or a helium recovery system. Changing the internal pressure of the dewar can increase the heat lift by flowing larger volumes of helium but at the cost of consuming more liquid helium. A Janis ST-100 helium flow cryostat was used for work in Chapters 2 and 4, the helium flow for this cryostat is rated at 0.6 litres per hour at a 4 K base temperature.

A closed-cycle cryocooler uses a compressor and closed loop of high-pressure helium and a heat exchange to cool the gas. The compressor pumps high-pressure helium onto the cold finger, expanding and lowering the cold finger temperature before returning to the compressor. An external chiller loop cools the compressor, removing the heat in a heat exchange as the helium is recompressed. The operating principle of a closed-cycle cooler follows the ideal gas law 2.1 where p is pressure, V is the volume, n is the number of moles, R is the universal gas constant and T is temperature.

$$pV = nRT \quad (2.1)$$

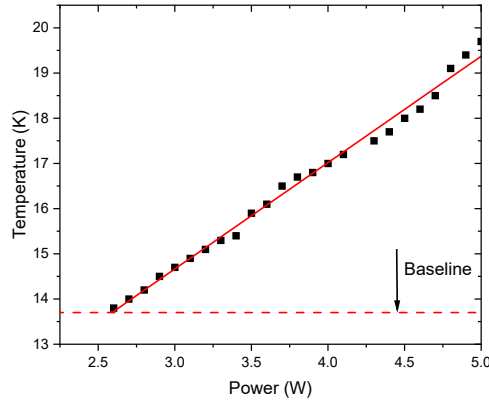


Figure 2.1: Illustration of the bias tee QCL modulation experiment.

The Cryocooler used in this work is a custom cryocooler manufactured by Cold Edge with a specified heat lift of 7 W of cooling at the sample and a base temperature of 6.5 K. Figure 2.1 shows the cryocooler temperature when power is applied to a 10 Ohm power resistor, the cryostat maintains base temperature

until approximately 2.5 W of electrical power is applied to the resistor. A linear fit has been applied to the data with a gradient of 2.35 K/W now when selecting a QCL, the baseline temperature at any bias can be estimated from the power consumption. The temperature performance appears to be less than the quoted values, but this is due to an additional cold finger which mounts the QCL adding thermal resistance to the cryocooler cold finger.

Without a helium recovery system, a helium-flow cryostat has high operating costs due to the price of liquid helium. The heat lift is related to the helium dewar pressure, where a lower pressure is likely to cause a temperature drift in the cold finger. Increasing the helium pressure and setting a heater can maintain a constant temperature as when the helium pressure drops, the heater bias is reduced. An alternative to increasing dewar pressure is to obtain the differential pressure by using a pump on the exhaust of a cryostat, drawing a constant stream of helium onto the cold finger. For example, the heater output can be set to 50%, where a drop in dewar pressure is compensated by reducing the heater output.

The Cold Edge cryocooler has a constant heat lift and a heater to raise the temperature of the cryostat, but the heat lift is lower than a continuous helium flow cryostat. A closed-cycle cryocooler allows longer running time at lower costs than venting helium into the atmosphere and the nature of the system allows it to be run over days without supervision, unlike the Janis cryostat used in previous work which requires supervision to operate. Due to the continuous heat draw provided by a cryocooler, the temperature is more stable when compared to a liquid helium flow which can change temperature due to helium dewar pressure. A cryocooler also has disadvantages when compared to the helium flow cryostat, a high cost is a disadvantage due to the complexity of the system. Additionally, a cryocooler can introduce vibrations due to the large compressor and motor within the cryostat, a cryocooler requires additional vibration compensation or vibrations can disturb an optical system.

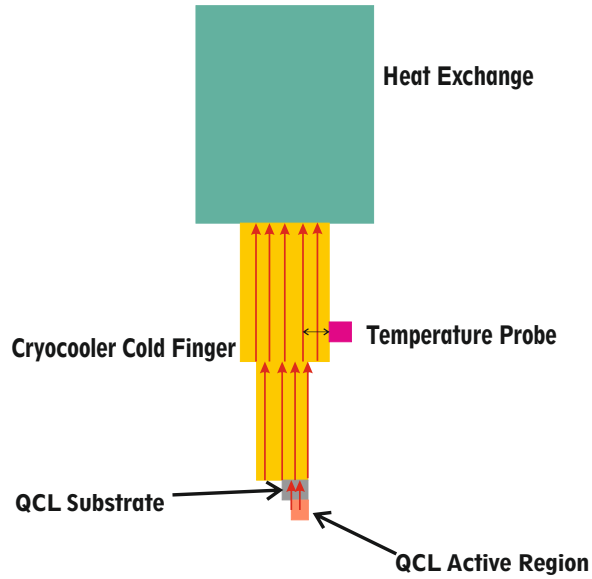


Figure 2.2: Illustration of the cryocooler.

Figure 2.2 is an illustration of the cryocooler cold finger. The heat exchange draws the heat generated from the QCL under bias. The yellow is oxygen-free copper which is fitted to the heat exchange. The QCL is mounted on the copper cold finger using bolts and thermal paste for improved thermal contact and the red arrows indicate the path heat takes to leave the cold finger. In the thermal circuit from temperature probe to QCL, there are many instances where the heat within the active region will be uncertain. The total thermal resistance will take the form $R_{Total} = R_{QCL} + R_{CF} + R_P$ where R_{QCL} contains the thermal resistance from the active region, through the substrate to the thermal paste. The cold finger thermal resistance R_{CF} is the total resistance from the QCL contact including interfaces through the length of copper to the temperature probe contact and R_P is the thermal resistance from probe contact to the temperature transducer. From these thermal resistances, it can be seen that what is reported on the cold finger is often not the temperature within the active region and using these values alone will cause uncertainties in the THz emission. The thermal resistance of a THz QCL active region has been experimentally demonstrated by M. Vitiello, et al, to be in the range of 8 to 12 K/W depending on the laser designs [107] [108].

2.2 Quantum Cascade Laser Optical Characteristics

The Light-Current (LI) characteristic of the 3.4 THz QCL was measured using an array type FET detector, the operation of these detectors is discussed in the second half of this chapter in Section 2.4. The QCL was used in CW operation, where the peak power of this laser was measured by a calibrated Ophir pyroelectric power meter to be 7.6 mW. THz radiation was sampled at 1 mA intervals in a current sweep from 350 mA to 1 A. A signal generator supplied the ramp for the QCL current source which has a conversion of 1 V = 200 mA and a 149.5 kHz TTL signal was supplied to the DAQ which was used to poll the detector to synchronise the sampling at 1 mA per sample. The LI experiments are run over 60 seconds before the data is averaged and saved using National Instruments LabView running on a PC. The result from a gas study at one cryostat temperature is 13,800 current sweeps being averaged. This sampling frequency was decided through the relationship $149.5 \times 10^3 = 230 \times 650$ where the requirement was to have 1 mA steps and have a sampling frequency less than 200 kHz due to limits in readout electronics.

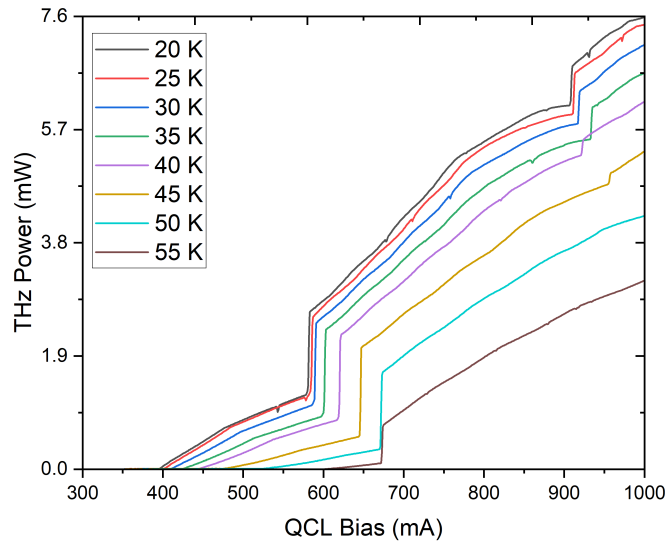


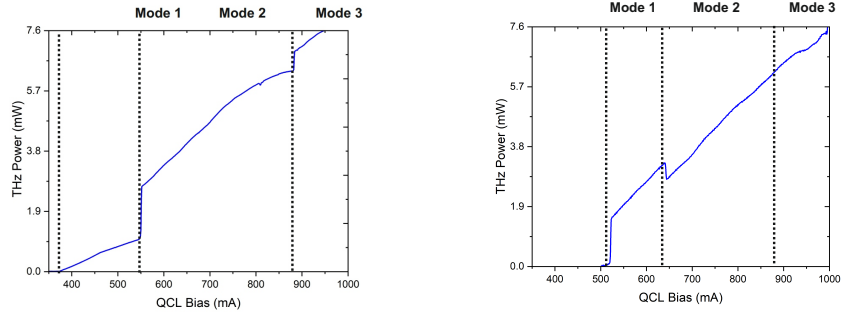
Figure 2.3: LI characteristics of the QCL.

Figure 2.3 is a plot of the LI characteristics of the QCL measured at a range of temperatures using an array TeraFET. The Y-axis on Figure 2.3 was found by scaling the TeraFET data by the peak power to estimate the THz emission power compared to the QCL bias. Care must be taken when observing this axis due to the difference in the aperture sizes of the TeraFET and Ophir power meter. The Ophir meter is a large aperture detector that will collect all of the radiation, unlike the TeraFET detector, which is smaller than the THz beam. This axis assumes the TeraFET collects all of the radiation.

The QCL threshold depends on the operating temperature, at lower temperatures lasing begins at 396 mA. The value of QCL current threshold increases with temperature to 602 mA at 50 K and at temperatures higher than 55 K the optical power drops significantly. This gives a threshold shift of 5.86 mA per 1 K increase in QCL temperature. The drop in optical power above 55 K resulted in the QCL not being operated above this temperature.

There are three optical modes of this laser which can be seen from the light characteristic, these are dominant a frequency which is supported in the cavity and only one frequency can emitted at a time, resulting in single mode emission. The weakest optical power mode can only be observed at temperatures below 30 K and the maximum CW operating temperature is 55 K. When operating the QCL with a current sweep or at the peak of 1 A, the minimum temperature of the cryostat was 21 K and as the cryocooler has been operating throughout the week, the base temperature will increase.

In Figure 2.3 results with temperatures above 40 K appear to have negative optical power, this is due to averaging. The detector amplitude is offset by a small negative voltage when there is no incident radiation and this value gives an apparent negative value in Figure 2.3. This negative offset is fixed by biasing the laser before the threshold and checking the offset value, this value is then corrected in post-processing to obtain the true detector value. Small dips in detected power are visible on the plot, this is due to D₂O contamination in the gas cell as these LI scans were taken as a set of blanks between a D₂O study.



(a) Normalised LI characteristic of the QCL at 35 K using an array TeraFET detector.

(b) Normalised LI characteristic of the QCL at 35 K using single patch TeraFET detector.

Figure 2.4: LI data of the QCL operating at a cryostat temperature of 35 K.

Figure 2.4a shows a single LI sweep which has been normalised and corrected for detector offset. Changes in the QCL lasing mode can be seen which supports three lasing modes: Mode 1 has the lowest optical power and spans 400 to 580 mA, Mode 2 is the widest mode which spans 585 mA to 910 mA and Mode 3 is the mode with the highest optical power and spans 915 mA to 1 A. The peak continuous wave THz power was measured to be 7.6 mW by an Ophir Vega calibrated power meter. The Ophir Vega uses a pyroelectric sensor to detect continuous wave THz radiation.

When first characterising the LI relationship of this QCL a single patch antenna TeraFET was used with a $64 \times 64 \mu\text{m}$ antenna. The single patch device has identical FET and patch antenna designs as the detector found in the array device used to sample the LI characteristics shown in Figures 2.4a and 2.3. The first QCL LI characteristic of this QCL using a single patch TeraFET yields a different LI characteristic seen in Figure 2.4b. At 650 mA in Figure 2.4b the signal drops, this can be seen in other LI characteristics and has to be accounted for when analysing gas spectra like any mode hop. There are many reasons this could be observed with the single patch device. One hypothesis for the drop in optical power was a mode hop that tuned to atmospheric absorption, but there are no water absorptions in this frequency range. Aligning the detector to such accuracy will result in standing waves throughout the optics and an enhancement in the signal could cause unexpected changes in amplitude as the THz frequency changes. The possibility of this drop in power coming from a standing wave in the system is also unlikely as the gas cell windows are orientated at the Brewster angle, minimising back reflections.

Previous work done by Eleanor Nuttall [87] using a multi-mode THz QCL showed that the lasing modes were spatially separated. If there is a spatial difference in modes for the 3.4 THz QCL used in this work then the $64 \times 64 \mu\text{m}$ area of the patch antenna could become misaligned as the QCL bias changes. When using an array detector such as in Figure 2.4a with an effective detector

size of 1×1 mm, the mode increased in power rather than dropping, confirming the modes are spatially separated. This also shows the care which must be taken when calibrating detectors with different apertures.

2.2.1 Beam Profiles

Beam profiles are a 2D image of the beam intensity propagating along the optical axis. A THz camera can take a beam profile, these use a large detector area of pyroelectric pixels which are sensitive to THz radiation. An alternate beam profiling method is to scan a small detector along the 2D plane and periodically sample to build a 2D image of the laser intensity. The TeraFET detectors were mounted on an automated 3D stage.

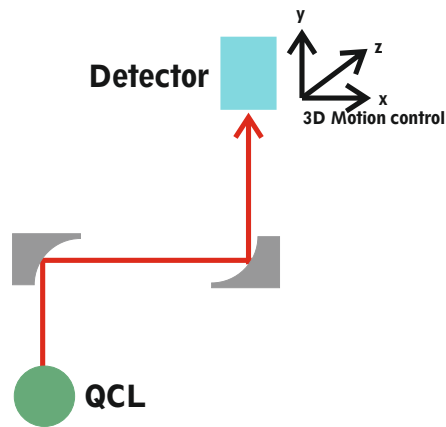


Figure 2.5: Schematic of the beam profiling system.

Figure 2.5 shows a schematic of the beam profiler used to take the results in this section. Using beam profiles to find the 3D coordinates, where X and Y are the detector position on a 2D plane and Z is the optical axis. The focus was chosen when integrating a single patch TeraFET into the system due to the small detector size. When the beam profile is obtained, no additional alignment is involved when switching TeraFET detectors due to them being mounted in identical packaging.

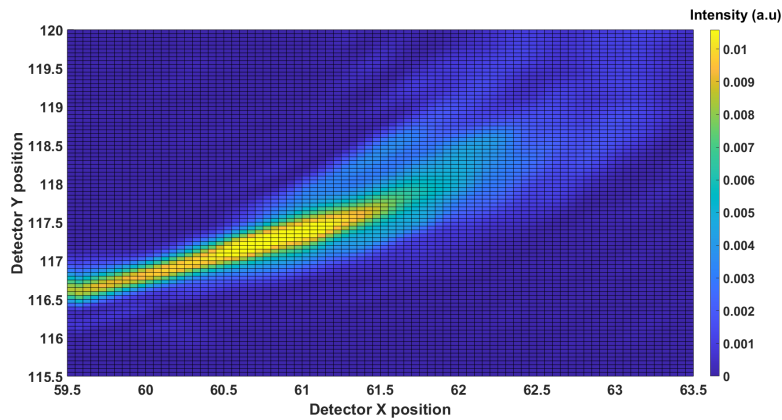


Figure 2.6: Two-dimensional view of the beam profile at a poor focus. The X and Y-axes are stage positions.

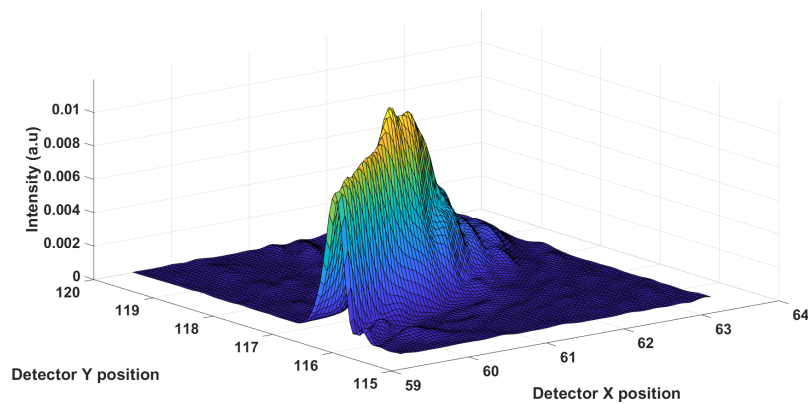


Figure 2.7: Side view of the beam profile at focus. The uneven beam pattern can be seen here.

Figures 2.6 2.7 show the non-gaussian profile of the QCL with a poor focus, the X and Y-axes shown are the stage position in millimetres and the Z-axis is the detector signal in millivolts. Various beam profiles were taken at intervals along the optical axis to inspect the beam and identify the peaks in intensity. Typically the alignment of a single patch antenna is difficult due to the small size where a side lobe of the laser could be targeted rather than the main peak. When alignment was lost in the system, an automated beam profile LabVIEW program written by Dr Michael Horbury scans the focus where the 3D coordinate can be identified by visually inspecting the results plotted in Matlab. Using controller software for the automated stage, the coordinates found through overnight beam

profiling can be manually entered into the relative detector position to give the optimal performance of the single patch device.

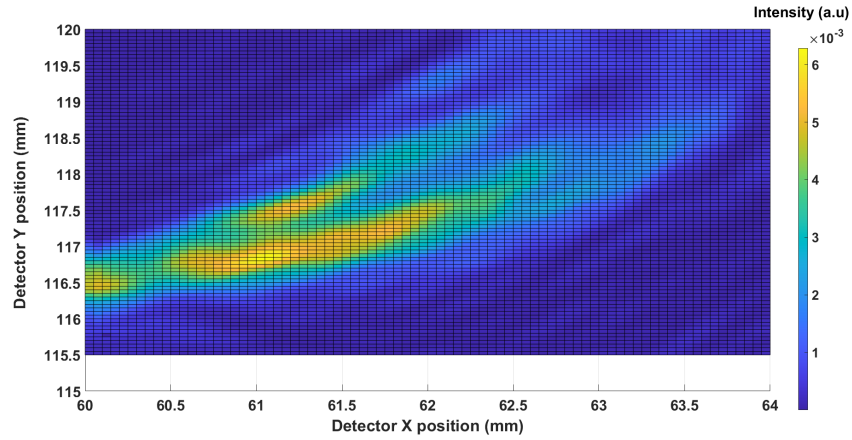


Figure 2.8: 2D view of the beam profile 0.3 mm before focus.

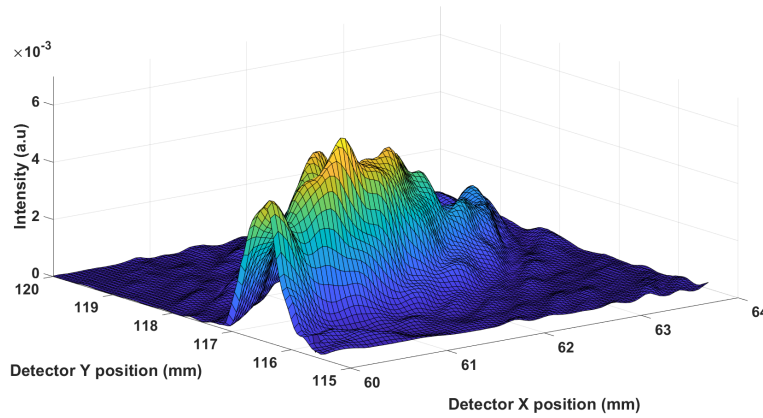


Figure 2.9: Side view of the beam profile before focus.

Figures 2.8 2.9 are beam profiles taken 0.3 mm along the Z-axis before the poor focus. Here the importance of aligning the single patch devices to the QCL can be seen, due to the non-gaussian shape and multiple lobes a large detector area would be required unless the focus was improved.

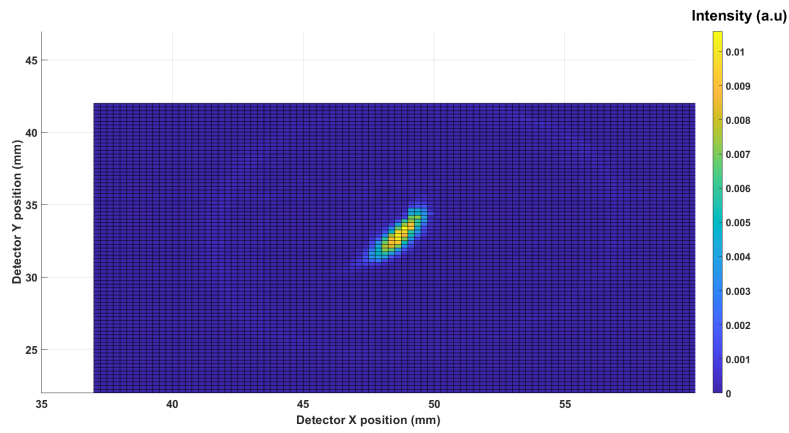


Figure 2.10: 2D view of the beam profile at a detector position of 106 mm.

By realigning the system with a visible laser, the optimised alignment yielded a higher-quality beam pattern where the multiple lobes were reduced. Running a beam profile from detector position 90 mm to 130 mm along the Z-axis in 2 mm steps, the focus appears to be at detector position 105 mm. Figure 2.10 shows the beam at a tighter focus sampled with an array TeraFET and in this figure, there is a faint ripple around the focus which is a result of the OAP mirrors in this system having an alignment hole in the centre.

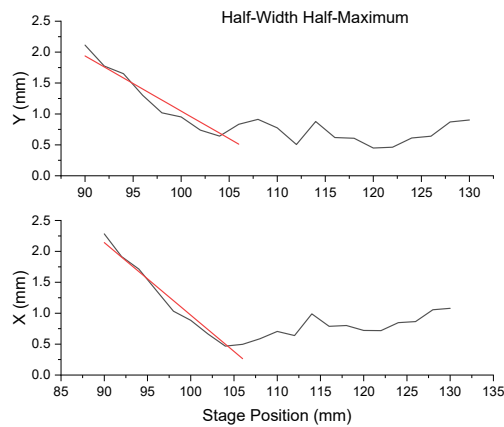


Figure 2.11: Full Width Half Maximum (FWHM) plot of the detector passing through focus.

The data in Figure 2.11 was obtained by using a Matlab script written by Dr Aleksandar Demic, which fits a Gaussian surface to the beam profile data and finds the FWHM using an elliptical fitting method. The FWHM on X and Y directions are plotted and compared to the detector displacement which ranges from 90 mm to 130 mm, travelling away from a focusing parabolic mirror. Because the data becomes difficult to use after 105 mm, A linear fit was applied to Figure 2.11 to obtain the beam waist at the focus. The waist in both the X-axis and Y-axis are $w_{0x} = 265 \mu\text{m}$ and $w_{0y} = 511.5 \mu\text{m}$.

The M^2 value is a unitless value which describes Gaussian beam quality, an ideal diffraction-limited beam has $M^2 = 1$ and the value increases as the beam becomes less ideal, the value increases. M^2 is found by comparing the Beam Parameter Product (BPP) which is the divergent half angle θ multiplied by the beam waist ω_0 to the BPP of a diffraction-limited Gaussian beam of the same wavelength ($\frac{\lambda}{\pi}$) giving the Equation 2.2.

$$M^2 = \frac{BPP}{\left(\frac{\lambda}{\pi}\right)} \quad (2.2)$$

The beam half divergences are $\theta_x = 7.63^\circ$ and $\theta_y = 6.91^\circ$. To find the M^2 value, the angles were converted to radians and the values were $M_x^2 = 1.247$ and $M_y^2 = 2.2$.

2.3 FTIR Results

The spectral data of the QCL was found in multiple steps, the first step was to use FTIR to find the frequency of the laser scaled by an unknown frequency error from the spectrometer. For the characterisation, a helium-cooled bolometer was used for detection. When using the bolometer Mode 1 of the QCL was below the noise floor, so the FTIR analysis aimed to examine the QCL biased from 500 mA to 1000 mA as Mode 1 was too low power to analyse. The FTIR data can be calibrated against a catalogued species to find the laser spectrum without experimental error. The FTIR experiment was done using an interferometer with 200 mm of stage movement giving an approximate resolution in wavenumber as $25 \times 10^{-3} \text{ cm}^{-1}$ and a frequency resolution of 750 MHz.

$$\Delta v = \frac{1}{20 \text{ cm} \times 2} = 25 \times 10^{-3} \text{ cm}^{-1} \quad (2.3)$$

To characterise the QCL tuning characteristics, the FTIR measurements were taken at a current step of 10 mA spanning 500 mA to 1 A and temperatures spanning 31 K to 55 K. At each current step, there was a delay before running the FTIR experiment to let the laser stabilise. The scan was saved once the experiment was complete and the current was increased. When the full current sweep was finished, the QCL bias was lowered to 500 mA, the cryostat temperature increased and a wait allowed the temperature to settle before continuing the next set of scans. Multiple scans were averaged to overcome noise and potential drift between experiments.

The temperature steps were: 31 K, 35 K, 40 K, 45 K, 48 K, 50 K and 55 K. After all the scans had finished, there were 350 files which needed to be examined and for this analysis, Matlab was used. The Matlab script processed the data by fitting a Gaussian profile to every current step at each temperature and then running a peak finder, the peak locations were saved and plotted in a scatter to show the mode positions. When troubleshooting the code, the width and prominence of the peaks were also extracted but this slowed the program and this information is not needed for the frequency calibration.

Figures 2.12, 2.13 and 2.14 show the three lasing modes separated to figures at a QCL temperature of 31 K. Later in this section, all of the FTIR data is expressed as heatmap with frequency on the X axis and bias current on the Y axis.

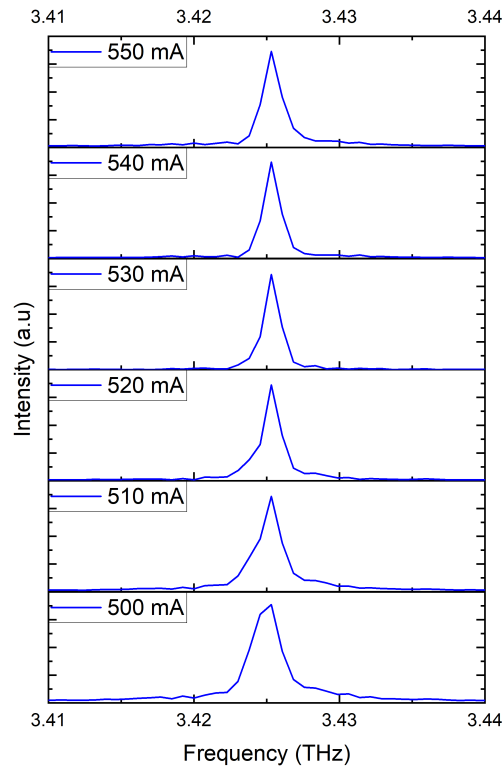


Figure 2.12: Spectral data of Mode 1 at a QCL temperature of 31 K.

Mode 1 is the lowest current and shown in Figure 2.12, this spectrum appears to be a higher frequency than Mode 2 in 2.13. Using gas calibration in Section 3.3 the data from Mode 1 was proved to be inaccurate, a possible cause of this inaccuracy is misalignment in the interferometer.

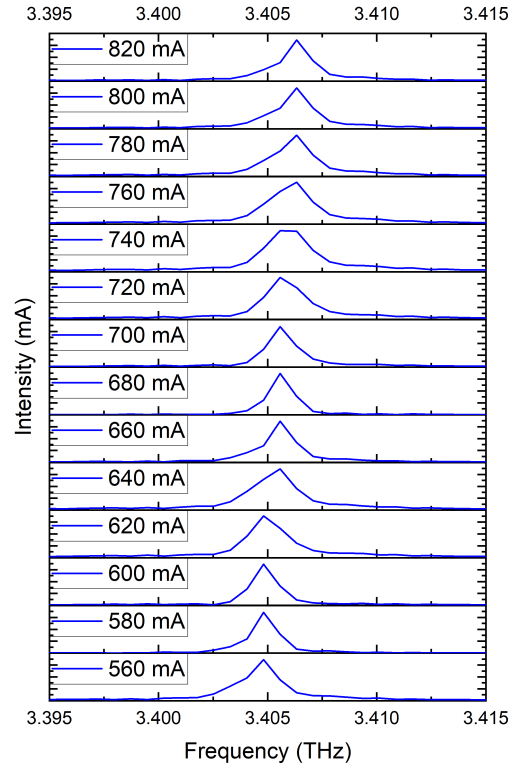


Figure 2.13: Spectral data of Mode 2 at a QCL temperature of 31 K.

Figure 2.13 shows the emission frequency when the QCL is emitting Mode 2, the QCL current was stepped in 10 mA steps during the FTIR experiment. To represent Mode 2 in one figure, the data is plotted in 20 mA steps.

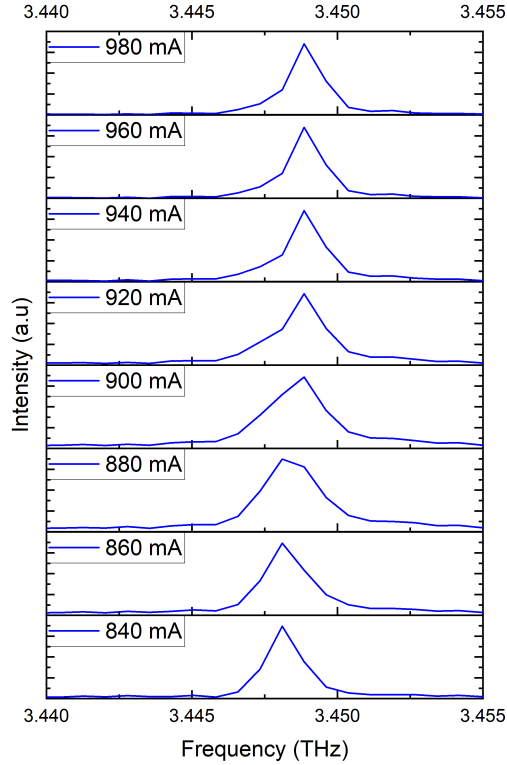


Figure 2.14: Spectral data of Mode 3 at a QCL temperature of 31 K.

Mode 3 is shown in Figure 2.14 is the highest optical power and highest THz frequency emitted by the QCL. This mode was plotted in 20 mA steps to fit the data into one figure.

The modes of this single-mode laser can be seen at 3.425 THz, 3.406 THz and 3.449 THz. The QCL was fabricated by Dr Iman Kundu and designed to emit at 3.4 THz with a 2 GHz tuning range. The QCL was fabricated from wafer number L1180 which was grown by Dr Lianhe Li at the University of Leeds. Operating at a cryostat temperature above 45 K reduces the emission to 1 mode at 3.4 THz. This spectral data contains a frequency error due to $\cos(\theta)$ error in the Michelson interferometer but will act as a guide to finding the true emission frequency. The amplitudes in this data show the low intensity of Mode 1 and full ranges of Mode 2 and Mode 3.

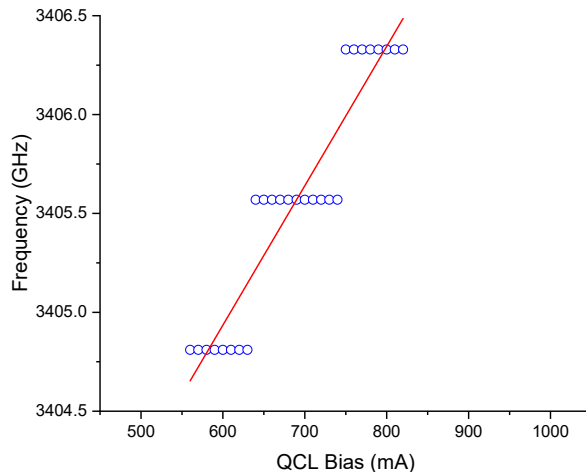


Figure 2.15: Scatter of the Mode 2 FFT peaks compared to the QCL bias current (blue). A polynomial fit of the points (red).

Figure 2.15 shows the peak frequencies of Mode 2 at a QCL temperature of 31 K. The QCL bias was stepped in 10 mA increments during the FTIR measurement. The red line shows the polynomial fit of this mode. There appears to be a jump in THz frequency as the bias is shifted, but this effect is due to the frequency resolution of the FTIR experiment which is limited by the stage travel. This quantisation limits the accuracy of a frequency axis obtained in this method. The steps appear to be 750 MHz which confirms the previous resolution calculation. When polynomials are fitted for frequency axis calibration, each mode is separated and fitted as in Figure 2.15.

2.3.1 Frequency Calibration

To calibrate the system the FTIR results need to be related to the QCL bias, where every 10 mA current step corresponds to the laser frequency and this was done by fitting polynomials to the peak values of all FTIR scans and scaling by an unknown error. Any entry saying No gradient is a frequency mode where the tuning is below the 750 MHz resolution of the experiment.

Laser mode	Term 2	Term 1	Term zero
31 K Mode 1	No gradient	No gradient	No gradient
31 K Mode 2	3.8×10^{-19}	7.1×10^{-6}	3.4
31 K Mode 3	-5.4×10^{-8}	1.0×10^{-4}	3.4
35 K Mode 1	5.4×10^{-8}	-0.55×10^{-3}	3.6
35 K Mode 2	-2.7×10^{-8}	4.3×10^{-5}	3.4
35 K Mode 3	-4.7×10^{-8}	8.4×10^{-5}	3.4
40 K Mode 1	-1.6×10^{-8}	2.6×10^{-5}	3.4
40 K Mode 2	6.6×10^{-8}	-1.2×10^{-4}	3.5
45 K Mode 1	-1.2×10^{-8}	2.1×10^{-5}	3.4
45 K Mode 2	No gradient	No gradient	No gradient
48 K	-5.3×10^{-9}	1.2×10^{-5}	3.4
50 K	-5.5×10^{-10}	3.8×10^{-5}	3.4
55 K	2.7×10^{-8}	-3.9×10^{-5}	3.4

Table 2.1: Table of the polynomial coefficients for each temperature step.

Table 2.1 shows the terms for the laser operating at various temperatures, this analysis was done for every laser mode. A table of the threshold shift of the modes compared to QCL temperatures are shown in Table 2.2.

Laser mode	I_{min} (mA)	I_{max} (mA)
31 K Mode 1	500	550
31 K Mode 2	560	820
31 K Mode 3	830	1000
35 K Mode 1	500	550
35 K Mode 2	560	840
35 K Mode 3	850	1000
40 K Mode 1	540	1000
40 K Mode 2	850	1000
45 K Mode 1	550	920
45 K Mode 2	930	1000
48 K	580	1000
50 K	550	1000
55 K	610	1000

Table 2.2: Table of the threshold current for each lasing mode.

Table 2.3 shows the standard error of the calculated coefficients. To use these values, the current value (I) is inserted into a polynomial using the above coefficients. For example in Equation 2.4 where the 50 K coefficients are used. The polynomials were calculated using Matlab's polyfit function which uses ordinary least squares regression. The standard error in the polynomial coefficients in Table 2.3 was computed using a covariance matrix method.

Laser mode	Term 2	Term 1	Term zero
31 K Mode 1	5.9×10^{-19}	6.2×10^{-16}	1.6×10^{-13}
31 K Mode 2	7.6×10^{-9}	1×10^{-5}	3.6×10^{-3}
31 K Mode 3	2.1×10^{-8}	3.8×10^{-5}	17×10^{-3}
35 K Mode 1	3.4×10^{-7}	3.6×10^{-4}	0.1
35 K Mode 2	5.7×10^{-9}	8×10^{-6}	2.8×10^{-3}
35 K Mode 3	1×10^{-19}	1.8×10^{-16}	8.3×10^{-14}
40 K Mode 1	5.5×10^{-9}	8×10^{-6}	2.9×10^{-3}
40 K Mode 2	3.7×10^{-8}	1×10^{-4}	50×10^{-3}
45 K	8.9×10^{-8}	1.4×10^{-4}	52×10^{-3}
48 K	2.6×10^{-9}	4.1×10^{-6}	1.6×10^{-3}
50 K	2.9×10^{-9}	4.6×10^{-6}	1.8×10^{-3}
55 K	7.3×10^{-9}	1.2×10^{-5}	4.6×10^{-3}

Table 2.3: Table of the standard error of each polynomial coefficient.

$$f = -5.5 \times 10^{-10}I^2 + 3.8 \times 10^{-5}I + 3.4 + \cos(\theta) \quad (2.4)$$

Applying these polynomials to the current sweep in the LI characteristic converts the axis from current to frequency. It should be remembered that there will be an error in the frequency axis if the polynomials alone were used, due to misalignment in the interferometer and uncertainty in the QCL active region temperature.

To find the correct frequency, a calibration gas was used where the frequency of spectral features could be compared to simulations in the JPL catalogue and the frequency offset due to misalignment can be found. Various Volatile Organic Compound (VOC)s were measured at the full range of QCL operational temperatures and frequencies. Propan-2-ol ($(\text{CH}_3)_2\text{CHOH}$), Acetone ($(\text{CH}_3)_2\text{CO}$), Ethanol (EtOH, $\text{C}_2\text{H}_5\text{OH}$) and Methanol (MeOH, CH_3OH) were first examined as they were available in the lab and are safe to examine in small quantities.

Propan-2-ol, Acetone and Ethanol have no spectral features in the QCL range but methanol does. Figure 2.16 shows the change in the detector signal when using the converted frequency axis and the QCL bias is shown at the top axis, data taken from a LI sweep at 50 K spanning 700 mA to 1 A as the QCL bias was stepped in 1 mA increments. For this experiment a TeraFET detector was used where the QCL current is swept at 230 Hz while the detector is sampled at 149.5 kHz, yielding a 1 mA sample rate of the laser. This experimental data is averaged over a minute, giving 13,800 samples in one LI sweep. In this experiment, Methanol was sampled at a 1 Torr inside the gas cell to give the absorptions seen in Figure 2.16. At a cryostat temperature of 50 K, there are observable Methanol features. In particular, there is a doublet at a QCL temperature of 50 K, a unique spectral feature that can be used to find the frequency compared to transmission simulation data.

The method behind obtaining absorption spectra such as the ones found in Figures 2.17a 2.17b will be discussed in detail in Chapter 3 Section 3.1.1.

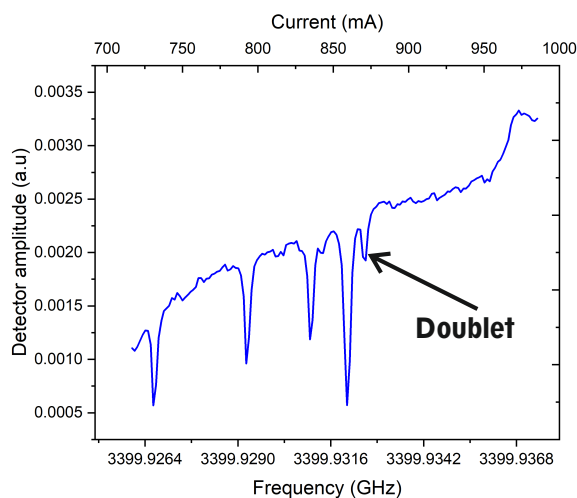
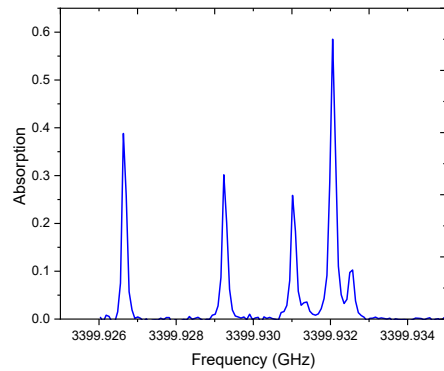
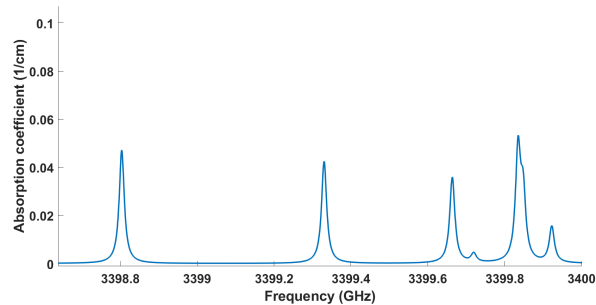


Figure 2.16: The LI characteristic of the laser with a methanol sample introduced into the gas cell at a QCL temperature of 50 K.

The experimental absorption was taken using the Beer-Lambert absorption law from the data shown in Figure 2.16. Comparing the absorption spectrum of the experimental data in Figure 2.17a to the JPL simulation results in Figure 2.17b the frequency offset can be found. The doublet is unique and used to find the spectral range of the QCL. Using the calculated frequency as guidance, the 3.34 THz region in the JPL catalogue was manually searched until the doublet was found.



(a) QCL temperature of 50 K with methanol inside the gas cell.



(b) JPL absorption spectrum of MeOH.

Figure 2.17: Comparison of the frequency of an observed spectrum vs the JPL.

The JPL results for MeOH at a pressure of 1 Torr were plotted in Matlab to inspect spectral features of methanol in a similar frequency range of the FTIR data, spanning 3398 to 4000 GHz. The peaks in the experimental data are located at (from left to right): 3399.927, 3399.929, 3399.93 and 3399.84 GHz. Whereas the JPL simulated data locates the peaks at: 3398.80, 3399.33, 3399.66 and 3399.84 GHz there is a frequency offset which ranged linearly from 0.092 GHz at the higher frequency to 1.127 GHz at the lower frequencies.

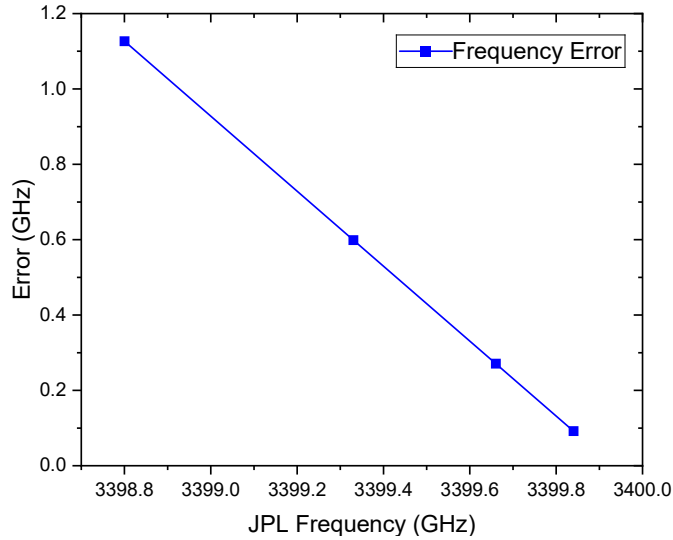


Figure 2.18: The error of the peak positions compared to the catalogues JPL peak positions.

Figure 2.18 shows the difference between the measured peak positions constructed using the FTIR polynomials compared to the JPL catalogue. The error is linear and decreases as the frequency increases, this is inverse to θ error which would cause the frequency error to increase with frequency. The cause of this error is likely due to the optical encoder in the linear stage requiring calibration and reporting incorrect distance measurements.

The FTIR data for every current and temperature range used in the frequency polynomials is shown below. The tuning range of the QCL can be better observed in the heat maps below. Every experiment used a 10 mA current step and the temperature ranges are: Figure 2.19 shows 31 K, Figure 2.20 shows 35 K, Figure 2.21 shows 40 K, Figure 2.22 shows 45 K, Figure 2.23 shows 48 K, Figure 2.24 shows 50 K, Figure 2.25 shows 55 K. The heatmap showing the lasing mode at 50 K with FTIR frequency axis is shown in 2.24 which shows the full tuning range of Figure 2.17a compared to QCL bias.

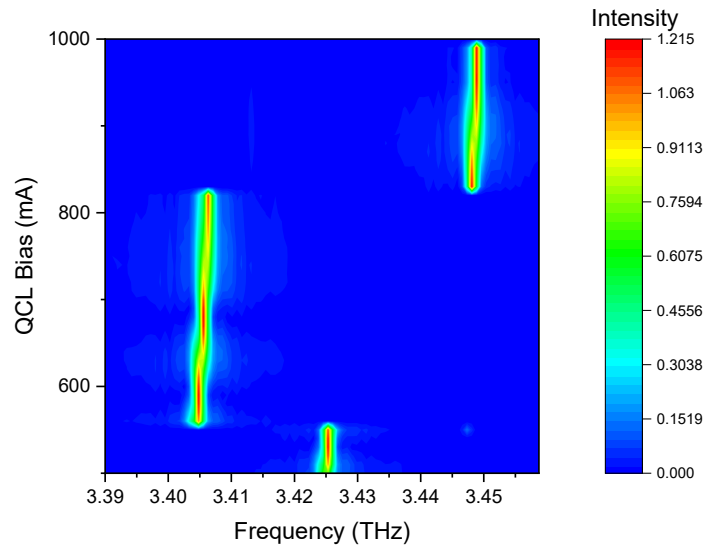


Figure 2.19: Heatmap of the QCL spectrum at a temperature of 31 K. Where the current is on the Y-axis in milliamps and frequency in THz on the X-axis.

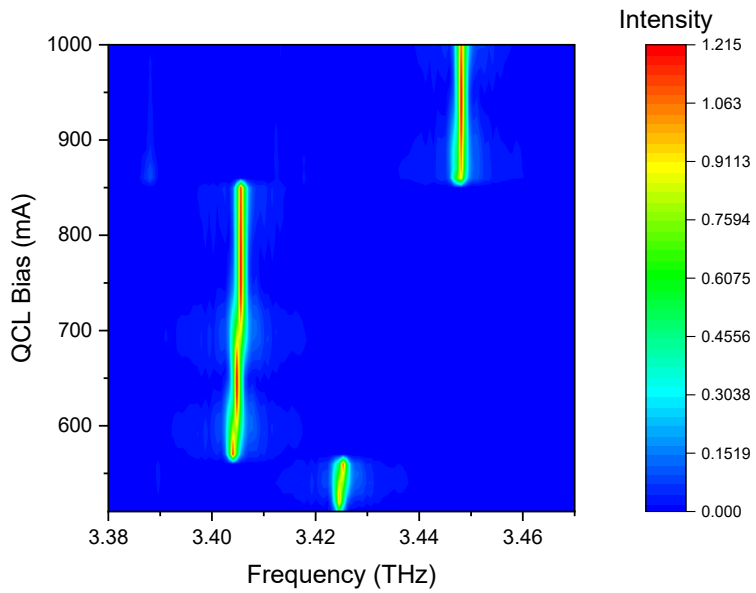


Figure 2.20: Heatmap of the QCL spectrum at a temperature of 35 K. Where the current is on the Y-axis in milliamps and frequency in THz on the X-axis.

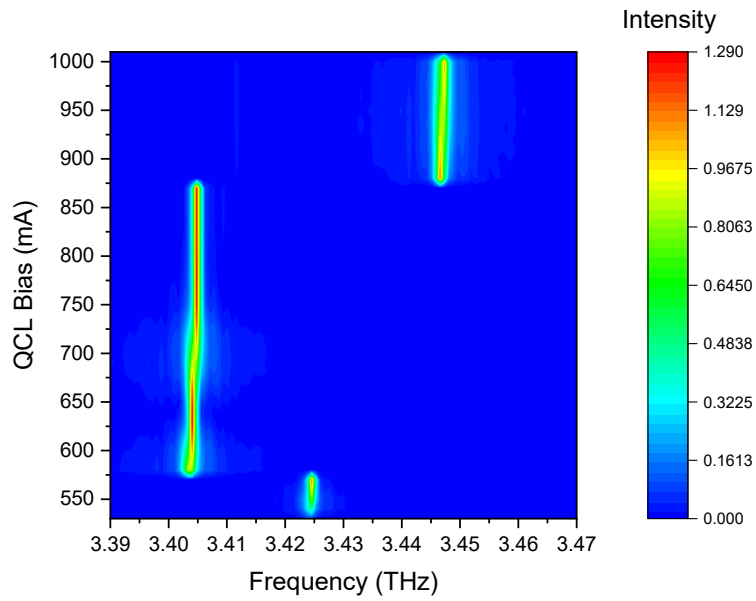


Figure 2.21: Heatmap of the QCL spectrum at a temperature of 40 K. Where the current is on the Y-axis in milliamps and frequency in THz on the X-axis.

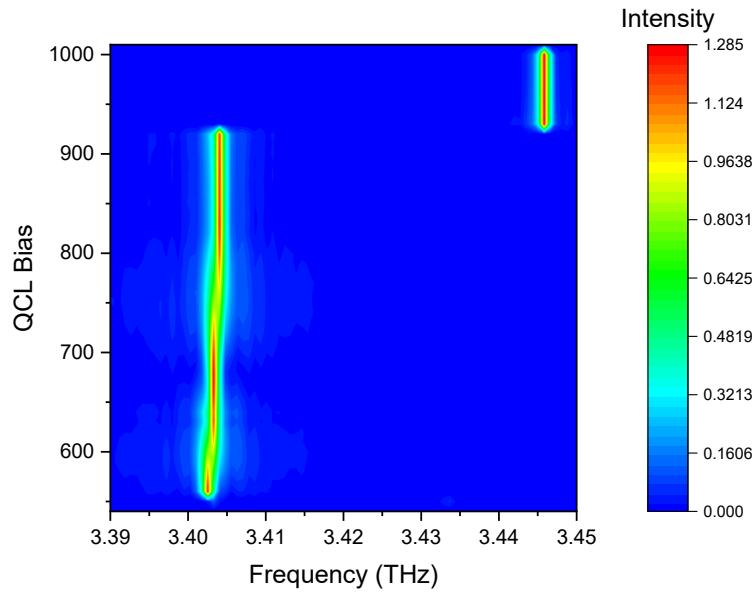


Figure 2.22: Heatmap of the QCL spectrum at a temperature of 45 K. Where the current is on the Y-axis in milliamps and frequency in THz on the X-axis.

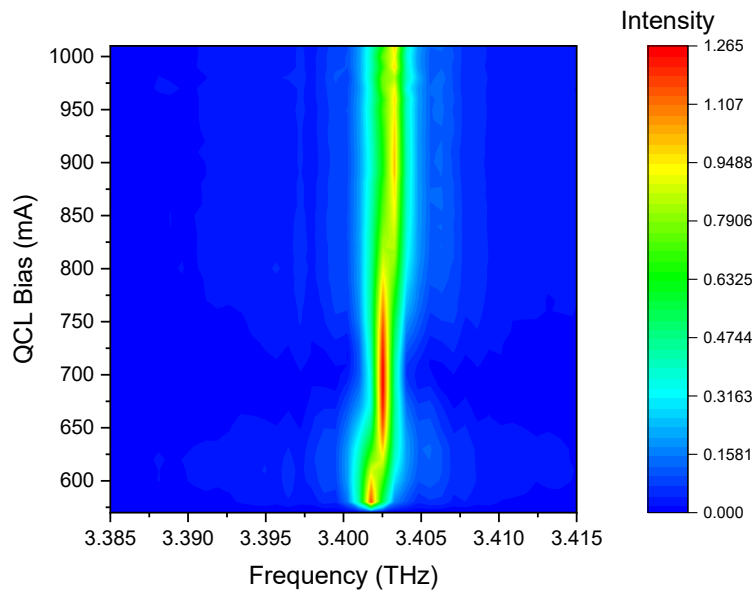


Figure 2.23: Heatmap of the QCL spectrum at a temperature of 48 K. Where the current is on the Y-axis in milliamps and frequency in THz on the X-axis.

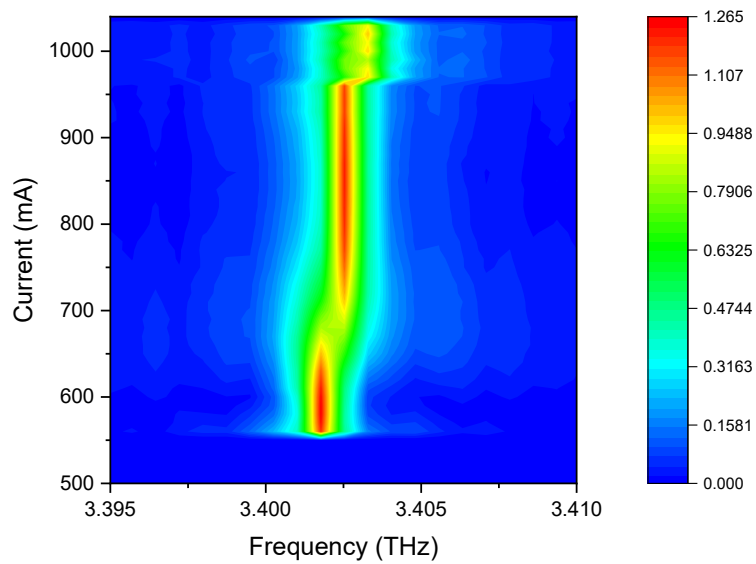


Figure 2.24: Heatmap of the QCL spectrum at a temperature of 50 K. Where the current is on the Y-axis in milliamps and frequency in THz on the X-axis.

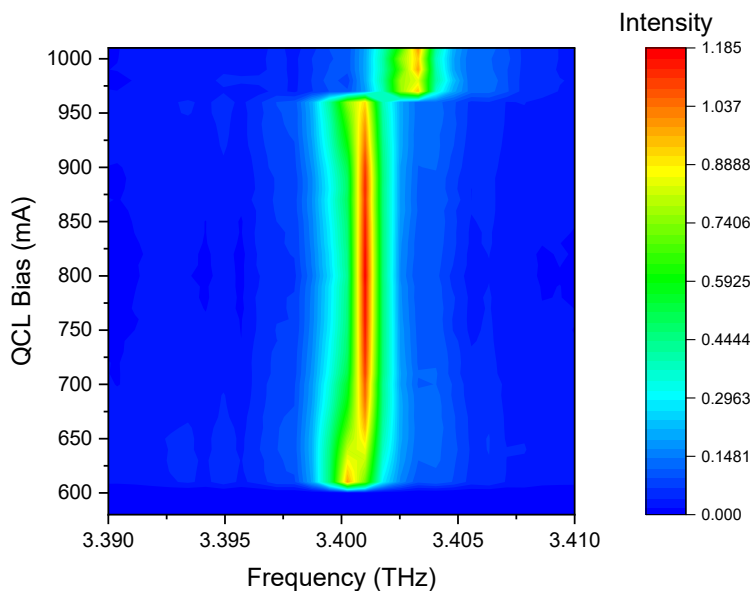


Figure 2.25: Heatmap of the QCL spectrum at a temperature of 55 K. Where the current is on the Y-axis in milliamps and frequency in THz on the X-axis.

In Chapter 3, using the JPL gas simulation results, to construct an accurate frequency axis is shown. The calibration gas method is accurate but requires catalogued lines to be visible in the THz spectrum under study. The FTIR method of calibration would need to be run daily for an experiment for frequency calibration of the system because the internal temperature of the QCL could shift over the space of a day. There should be no uncertainties in the frequency axis if an unknown species is being sampled. Due to the nature of this work, the system was rebuilt multiple times with new optical elements and detectors which were two bolometers and three array TeraFET devices. Realignment of the interferometer makes any previously obtained FTIR data inaccurate, as the frequency is related to the OPD in the arms of the interferometer.

To reduce the time needed for frequency calibration, the FTIR experiments were replaced by gas calibration in this work. Gas calibration is an effective method if there are documented peaks of the species under study in a spectroscopy catalogue. If unstudied gases are going to be examined, the calibration errors in the FTIR spectrometer would need to be fixed, a simple solution for this is a colinear alignment laser. Once the MeOH peaks were found the FTIR data was not used for building a frequency axis.

2.4 Fast THz Detection

Section 1.4 reviews different THz detectors, this section will focus on THz detection using the TeraFET. The first detector in this project was a helium-cooled bolometer. The bolometers have a maximum modulation frequency of approximately 1 kHz, if the detector were to be sampled faster than 1 milliseconds a faster detector would be needed.

TeraFET detectors are existing devices where the technology has been improved upon by collaborators at Goethe University Frankfurt and the particular devices used in this work were designed by Jakob Holstein. This Section will first discuss two modulation techniques used in this work and present results from an investigation into detector noise using thermal detectors. Techniques such as injection locking [109], acoustic phonon modulation [110] and external modulation [111] are high-speed modulation techniques which can exceed the speeds seen in direct modulation, but these methods are outside of the scope of this work. External modulators can be used to modulate THz emission and are discussed in Chapter 5. The operating principle of TeraFETs will be discussed before showing the characterisation work undertaken in Leeds using a QCL.

2.4.1 Modulation Techniques

Fast modulation is important in emitters as it allows technology such as communications, active mode locking, and rapid sampling in spectroscopy. Modulation techniques are required for detection as noisy signals are inherent in THz technology due to thermal fluctuations, atmospheric absorptions and detector noise. Signal processing is commonly used to extract the THz signal, popular methods include using a DAQ and programmatically processing the signal or using a lock-in amplifier. Lock-in amplifiers operate by demodulating a signal and extracting phase and amplitude information from a signal compared to a reference. When using lock-in detection or a detector with no DC response, modulation is required to acquire the THz signal.

A popular amplitude modulation method is an optical chopper, an optical chopper is a disk with holes cut to form blades. When an optical chopper is placed in the optical path, it periodically blocks the beam which modulates the signal. The maximum frequency of an optical chopper is limited by the driving electronics and blade materials, commercial choppers can reach modulation frequencies up to 100 kHz. Choppers can introduce thermal noise when chopping a signal, or from environmental noise reflected by the blades.

Another modulation technique is direct modulation where the QCL bias is modulated with an electronic signal such as a sine wave from a signal generator and the result can be measured on the THz signal amplitude, this modulation technique also modulated the emission frequency. It becomes apparent that when directly modulating the bias, issues RF engineers encounter with transmission line impedance and power matching requirements will limit the frequency. The non-ohmic nature of a QCL brings a unique set of challenges for modulation, where a change in temperature and driving current changes the

loading on the current source. As well as the challenges in impedance matching the QCL, the upper state laser transition time may affect the modulation frequency, models have shown the modulation frequency to be in the order of 100 GHz [112] [113]. Additionally, when modulating the bias, the laser emission is chirped due to the fast signal which can be undesirable. Direct modulation techniques and microwave transmission line matching, a QCL has been reported by W. Maineult, et al, in 2010 to be modulated at speeds up to 22.5 GHz [114].

2.4.2 Thermal Detector Noise

Self-mixing is a method of using a QCL as a source and detector. THz radiation is focused back into the QCL and detected through changes in the bias voltage. Previous work done by the group on the self-mixing gas spectroscopy results [115] and self-mixing instrumentation [116] have been reported in literature. Previous results from the gas spectroscopy measurements during self-mixing experiments were consistent between scans, but when moving to bolometers a drift in the detector signal was observed. Additionally, when moving from self-mixing to bolometer detection, the QCL cooling method was changed after self-mixing from a helium-flow cryostat to a closed-cycle cryocooler.

The investigation began with the temperature stability and power stability of the QCL, as drifts in temperature or driving current would result in the changing peaks in the spectrum and the change to a cryocooler was suspected to be the issue. These tests were done by driving the QCL in a self-mixing configuration and reading the QCL voltage and temperature using a LabView program.

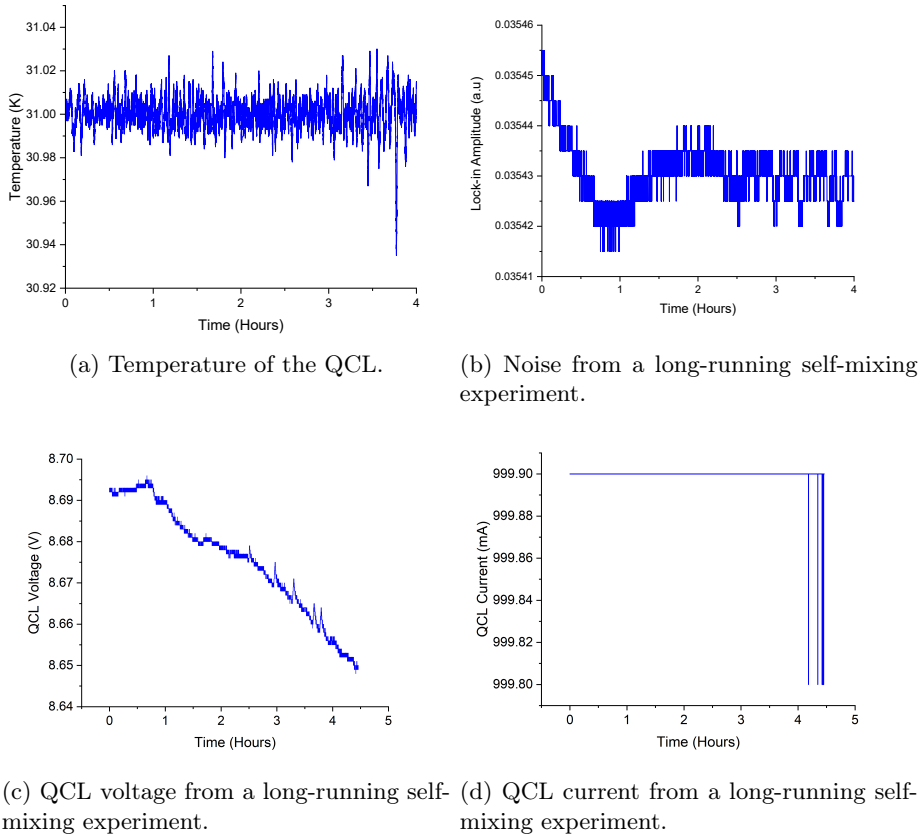
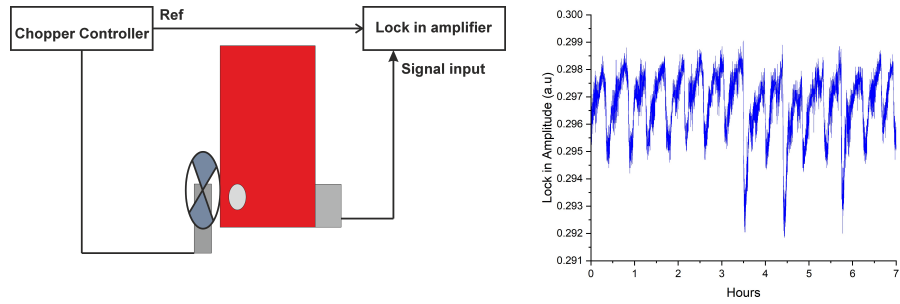


Figure 2.26: Self-mixing noise experimental data.

Figure 2.26 shows the QCL SM noise investigation. Figure 2.26a shows the cryostat temperature and Figure 2.26b shows the signal measured by the lock-in amplifier. Figures 2.26c and 2.26d show the voltage and current supplied to the QCL. The QCL was biased in CW at the peak emission of 1 A at a temperature of 31 K, the current was recorded and maintained at a constant 1 A throughout the test. The QCL had no temperature drifts which would be associated with a THz power drift and the detected signal had a detected signal drift of less than 0.1%. This self-mixing test proved the change in detector signal was not a drift in incident THz power on the detector, but rather a detector issue.

Characterising the detector noise was done using a modulated thermal signal. The easiest experimental setup for this is shown in Figure 2.27a where a chopper was placed by the bolometer window and run overnight. The experimental setup was simple to remove any additional sources of power drift, the chopper was running at 167 Hz and the chopper reference connected to a lock-in

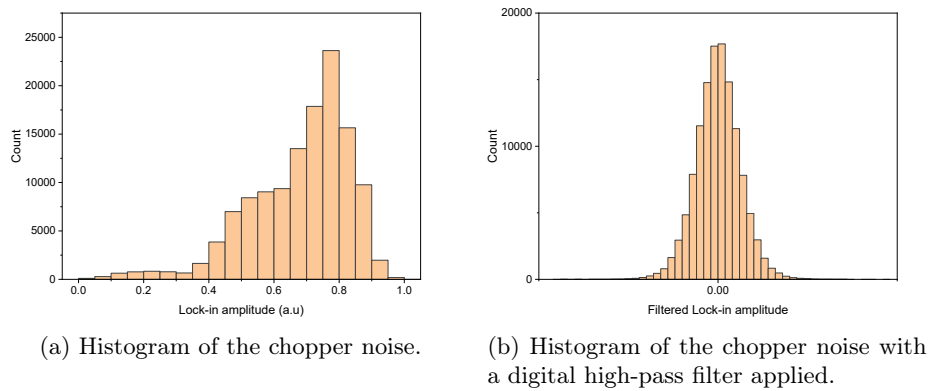
amplifier. The lock-in amplifier is locked to the thermal signal of the chopper blades running overnight.



(a) Illustration of the overnight chopper and (b) Signal recovered from the thermal bolometer experiment.

Figure 2.27: Overnight thermal noise experiment.

From Figure 2.27b, it can be seen that a periodic signal of approximately 30 minutes is on the output of the bolometer with a lock-in signal in the order of 10^{-6} arbitrary units. The modulation depth of this signal is 1.5% on the regular peaks but larger drops in signal appear around the 3.5 hour point and have a modulation depth of 2.2%.



(a) Histogram of the chopper noise. (b) Histogram of the chopper noise with a digital high-pass filter applied.

Figure 2.28: Histograms of the chopper thermal drift experiments.

A Gaussian noise distribution is expected in the thermal signal so the source is black-body radiation. To test this a histogram of the data in Figure 2.28a was taken where the Y-axis is the count of a specific amplitude value. The result can be seen in Figure 2.28b, the effect of the low-frequency noise can be seen here. A 10 Hz digital high-pass filter was applied to remove the noise and the expected Gaussian shape of a thermal noise signal remains. If the source of the detector noise was not found digital high-pass filtering can offer a solution to the signal drifts at the cost of removing low-frequency data.

Knowing the results were on the detector, the environment was checked for a large electrical load that activates approximately twice an hour which could cause interference. The problem was found to be the bolometer detecting the change in room temperature caused by air conditioning, but due to the thermal output of the cryocooler, it would be unsafe to turn the air conditioning off. A temporary solution was constructing a thermal shield for the focusing optic into the bolometer. A permanent solution was moving away from thermal detectors using an electronic THz detector.

2.5 TeraFET Detectors

All gas spectra presented in this work were using a TeraFET detector which was designed by Jakob Holstein and fabricated by Taiwan Semiconductor Manufacturing Company (TSMC) using a commercial 65-nm Complementary Metal-Oxide Semiconductor (CMOS) process. Using these detectors removed the room temperature drift seen using a bolometer, which is an electronic detector.

The channel of a FET can act as a resonator for plasma waves and depending on the gate and dimensions, the resonant frequency of this plasma wave can be tuned. To engineer a THz plasma wave resonance, the gate length must be sub-micron in length. The work of Dyakonov and Shur in 1993 used a model which showed electrons behaving analogous to waves in shallow water and proposed short field effect transistors to generate THz at the plasma wave frequency [117]. Although THz generation is possible with a FET the power is in the order of nanowatt range, the next development in 1996 from Dyakonov and Shur demonstrated that a FET biased from gate to source will generate a drain to source voltage when subject to electromagnetic radiation [118]. Figure 2.29 shows a simple diagram of a TeraFET detector with incident THz radiation.

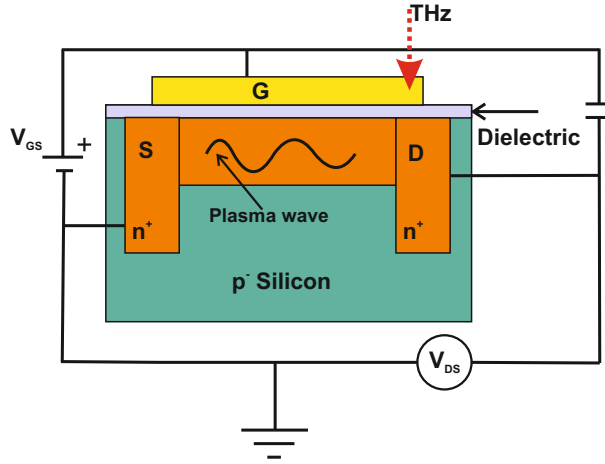
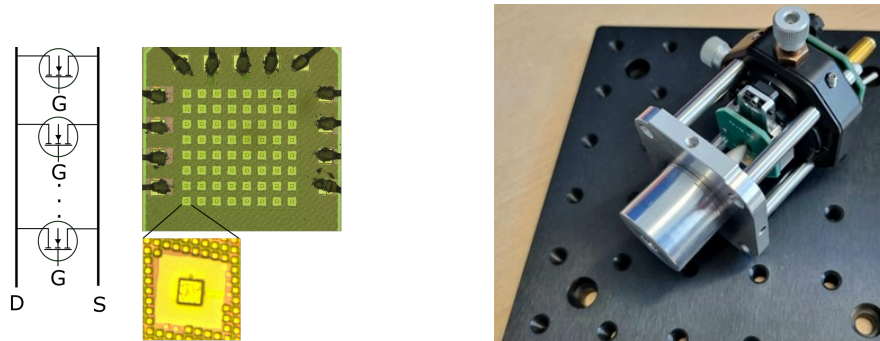


Figure 2.29: Illustration of the TeraFET THz detection process. The detector signal is the Drain-Source signal and the FET must be operated above the threshold.

The signal output is a rectification of the THz radiation which is proportional to the intensity, this voltage is described as self-mixing of the signal within the FET channel. The TeraFET devices used in this work have channel dimensions of 60 nm width and 1 μm length. To observe the plasmonic waves, there must be asymmetry within the channel managed by pinning one side to AC ground, which can be seen in the Drain of Figure 2.29. The FET must be biased over the threshold for rectification to occur ($V_{GS} > V_{th}$). All TeraFETs in this project have the drain coupled to AC ground and the detected signal is V_{DS} . If the channel conditions are symmetric, there would be no measurable rectification on either Source or Drain as the sum of plasma waves would equal zero [119]. The channel of a FET is sub-micron in size compared to the micron wavelengths of THz radiation, so the light must be coupled in through an antenna or grating which defines the effective detector area [120]. It should be noted that FET detectors using other gate materials such as graphene have been demonstrated, but are less mature as an instrument than the FET devices which take advantage of the well-developed CMOS technology [121].

Thermal detectors are limited by the detection method to a range of kilohertz. TeraFETs have a modulation bandwidth limited by readout electronics which act as a shunt resistance to the FET channel resistance, a lower channel impedance lowers the overall system RC time constant. In the array devices used throughout this project, the channel resistance was 300 Ω . Figure 2.30a shows a diagram of the parallel FET arrays in a TeraFET and a microscope image of an array TeraFET detector provided by Jakob Holstein. Figure 2.30b shows a photograph of an array TeraFET with coupling optics fixed to the front.



(a) (Left) A diagram of the FET devices in an array configuration. (Right) A microscope image of the array detector, each square shape is a patch antenna coupled to the FET. Figure provided by Jakob Holstein.

(b) A TeraFET sitting on a small optical breadboard.

Figure 2.30: Images of an array TeraFET detector.

There are two merits of performance for a detector: responsivity and Noise Equivalent Power (NEP). The detector voltage per incident power defines the responsivity of a detector, in a TeraFET this characteristic is dependent on the antenna-detector coupling which is related to the parasitic elements between the Gate and Drain under certain gate voltages. NEP is the thermal spectral noise density related by the responsivity. Typically in a detector, this noise is dominated by thermal noise in the detection element [122].

The single-patch device is an early design which consists of one FET coupled to a $15 \times 15 \mu\text{m}$ patch antenna, the small detector size results in a fraction of the beam being collected and a small detector area is advantageous in applications such as imaging as the detector can be scanned in two dimensions to obtain high-resolution images. In spectroscopy as much of the radiation should be collected, the effective detector area can be achieved through an array of FETs connected in parallel. This project used an 8×8 array of parallel single patch TeraFET detectors with a $75 \times 75 \mu\text{m}$ pitch between antennas, giving an effective detector area of $1 \times 1 \text{ mm}$ compared to one patch antenna [123]. Having FETs in parallel reduces the channel resistance which has three effects on a device:

1. Reducing Johnson-Nyquist noise. Voltage noise in the channel is the dominant noise contribution. The array devices reduce NEP by \sqrt{N} (N = number of parallel FETs).
2. Enables higher modulation bandwidth. Reducing the resistance reduces the shunt effect experienced by readout electronics capable of high modulation frequencies.
3. Reduced responsivity. A factor of N overall reduces the responsivity of the TeraFET. This reduction leads to an overall poorer NEP value from array detectors.

2.5.1 Gate Voltage Sweep

When characterising the performance of a TeraFET, a Gate voltage sweep is important to investigate the response as it shows the responsivity (R_V) and NEP. The Gate sweep has incident THz radiation on the antenna and the Gate bias is swept, the bias is then plotted against V_{ds} which is the detector reading. R_V is given by 2.5 which is the detector voltage (V_{det}) per incident optical power (P_{RF}).

$$R_v = \frac{V_{det}}{P_{RF}} \quad (2.5)$$

The noise contribution of the FET is dominated by the thermal noise voltage V_n of the channel resistance R_{ds} given by:

$$V_n = \sqrt{4k_B T R_{ds} \Delta f} \quad (2.6)$$

$$\Delta f = \frac{1}{4T_c} \quad (2.7)$$

Where k_B is Boltzmann's constant, T is the temperature and Δf is the detector's noise bandwidth. In this work, the noise bandwidth is given in Equation 2.7 where T_c is set by the lock-in amplifier's time constant and filter roll-off. The experimental time constant used throughout this work is 5 ms, but it is typical for NEP calculations to use a bandwidth of 1 Hz. The NEP is defined in 2.8.

$$NEP = \frac{\sqrt{4k_B T R_{ds}}}{R_v} = \frac{P_{RF}}{SNR_{linear} \times \Delta f} \quad (2.8)$$

When operating the TeraFET, the Gate voltage should be set to an operating point where the NEP is at a minimum and the responsivity is at a maximum but due to the nature of the devices this is not possible so the Gate voltage is set to a minimum NEP. The gate sweep experiment is taken using a Matlab script written by Jakob Holstein which steps the gate voltage of a TeraFET detector, records 1000 lock-in readings and takes the average. The experimental bandwidth is set by the lock-in amplifier time constant and amplifier bandwidth which are manually set. The time constant is set close to the Nyquist frequency

of the modulation frequency. It must be noted that the NEP measurement is reliant on an accurate power measurement, so a power measurement must be taken for each experiment to ensure the QCL power is known.

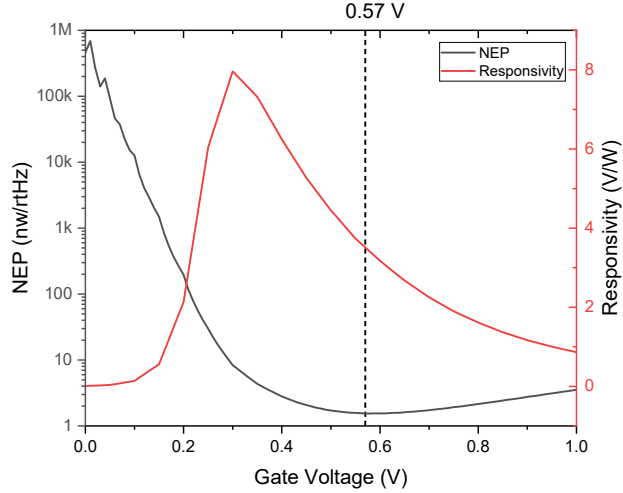


Figure 2.31: Results from the Gate sweep experiment using an array TeraFET.

Figure 2.31 shows the experimental data of the Gate Sweep of an array TeraFET where the minimum NEP of $1.55 \frac{nW}{\sqrt{Hz}}$ is at the Gate voltage 0.57 V. The NEP was anticipated by the collaborators to be below the value of $1.55 \frac{nW}{\sqrt{Hz}}$. The responsivity at this ideal operating point is 3.7 V/W. The expected NEP is higher than expected during these experiments, simulations undertaken in Frankfurt expect the NEP to be sub $1 nW\sqrt{Hz}$. The higher NEP is attributed to the amplifier noise in the readout electronics, a full noise investigation on array TeraFET noise has been reported by Jakob Holstein [123]. The gate voltage characteristic is identical between every TeraFET antenna design and for this reason, the noise characteristics shown in Figure 2.31 represent all TeraFETs used in this work.

2.5.2 Modulation Results

Two TeraFETs have been used for gas spectroscopy: the 200 kHz Array was an array device with a predicted 200 kHz -3dB point and the 20 MHz Array was an array device which was designed to have a 20 MHz -3dB point. A modulated QCL signal was used to verify the frequency response of these devices. The QCL was directly modulated using the modulation input of a Wavelength Electronics QCL 1000 laser driver driven by a Keysight 33600A function generator to a maximum frequency of 3 MHz. At frequencies past the modulation limit of the QCL 1000, a bias tee was used to power the QCL. Figure 2.32 shows the configuration when using the bias tee.

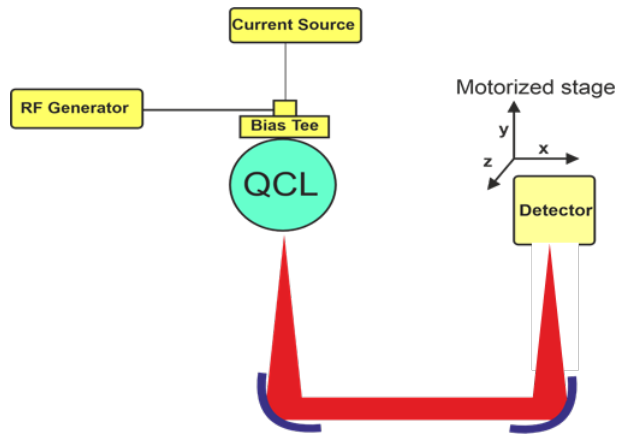


Figure 2.32: Illustration of the bias tee QCL modulation experiment.

The detection bandwidth was characterised using a 200 mA QCL current modulation on top of the QCL bias at 700 mA. The QCL was biased in Mode 2 because it is the optical mode with the largest tuning range, ensuring there are no contributions to the result by mode hops. The TeraFETs have relatively flat responses until the 3 dB cut-off. All of the TeraFET devices characterised are identical FETs using identical patch antennas, the readout electronics have improved through generations to improve modulation bandwidth. Due to the large signal voltage from a bolometer which ranges from 0 - 5 V, the results from these experiments have been normalised as the signal output from a TeraFET is in the order of millivolts.

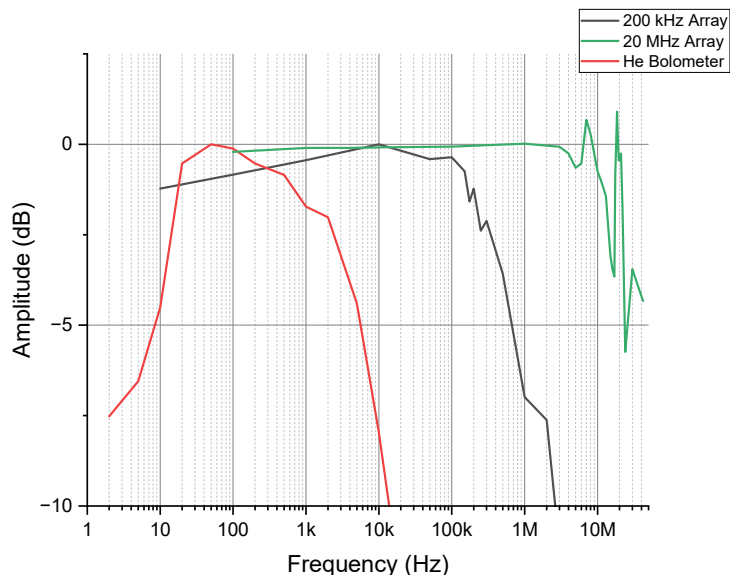


Figure 2.33: The comparison of the normalised amplitude of a bolometer, 200 kHz Array and the 20 MHz Array.

The results in Figure 2.33 show the improvement in modulation frequency of an order of magnitude between detectors. The bolometer has a cut-off frequency of approximately 1 kHz, the cut-off frequency of the 200 kHz Array is 150 kHz and the cut-off frequency of The 20 MHz TeraFET is 15 MHz. The reduced modulation bandwidth in detectors is due to a miscalculation in the readout electronics, reducing the bandwidth by a factor of 0.25.

When running gas spectroscopy measurements the QCL current is swept from 300 mA to 1 A in 1 mA steps. When using a bolometer or pyroelectric detector, the modulation frequency is 167 Hz giving a current sweep every 4.19 seconds. Sweeping the QCL bias the full 650 mA range and sampling the 200 kHz Array at 200 kHz would yield a full current sweep every 3.25 milliseconds with a 1 mA step in bias and the 20 MHz device at 20 MHz would give a QCL sweep every 32.5 microseconds.

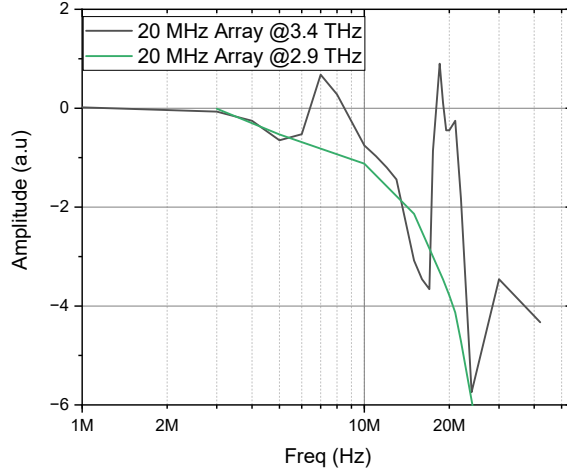


Figure 2.34: A comparison of the normalised amplitude of the 20 MHz Array using a 3.4 THz QCL and a 2.9 THz QCL.

A resonance appears in the plot of 20 MHz Array which occurs at approximately 20 MHz and has been present through repeated modulation tests. The 20 MHz Array was then mounted in a different optical system using a 2.9 THz QCL with a single metal waveguide which Dr Mohammed Salih fabricated. The QCL wafer was grown by L. H. Li with the wafer number L1599, a hybrid active region design. This QCL has a modulation bandwidth of 100 MHz and was used to test the modulation frequency response of the 20 MHz Array and this showed no resonance, showing the -3dB frequency cutoff of the 20 MHz Array to be 15 MHz and confirming the resonance is a result of the 3.4 THz QCL. This can be seen clearly when comparing the frequency response of the 20 MHz Array in Figure 2.34 where the enhancement dominates the roll-off and is non-existent when using the 2.9 THz device. This experiment used the same experimental setup as shown in Figure 2.32 and identical experimental parameters.

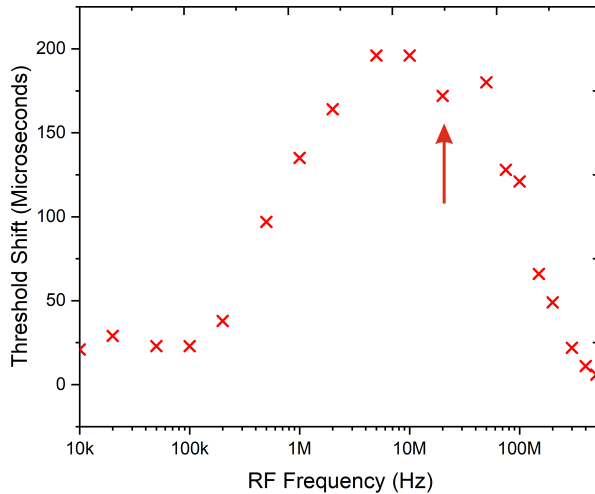


Figure 2.35: Modulation bandwidth of the 3.4 THz QCL. The red arrow indicates a possible resonance at 20 MHz.

An alternative measurement scheme was used to confirm the roll-off frequency observed by the 20 MHz Array in Figure 2.33 had no contribution by the QCL modulation bandwidth. In Figure 2.35 which shows the modulation bandwidth of the QCL, a short dip is seen at 20 MHz indicated in the figure by a red arrow. The frequency steps were coarse in this investigation, but this dip indicates a possible resonant feature within the laser. The laser driver was set to slightly below the threshold current at 300 mA and a slow 230 Hz ramp was applied to the driver so the QCL was periodically biased. The RF input of a bias-T was connected to a Keysight 33600A waveform generator with a 1 V sine wave and the DC port was connected to the laser driver. A high-frequency signal shifted the laser threshold time which can be seen in Figure 2.35, at frequencies below 300 kHz the high-pass filter of the bias-T removes the RF signal. This confirms that the QCL modulation bandwidth has a 3 dB cut-off of 200 MHz and shows how a TeraFET can be used in an indirect means of detecting fast QCL modulation through a change in time-averaged emission power. The point at 20 MHz suggests the resonance seen in Figure 2.33 is a contribution by the QCL output power and not a detector issue. This measurement was taken in coarse steps and will need repeating in a finer modulation frequency step to confirm the presence of resonance at 20 MHz.

Work is ongoing to identify the cause of the resonance seen in Figure 2.33, possible causes are enhancement effects in the radiation due to voltage coupling into the QCL or quantum effects in the QCL such as Gunn oscillations in the active region caused by a bistable state in the operating region.

2.5.3 Rapid Scan FTIR

The 20 MHz Array performed rapid-scan spectroscopy of a QCL using a commercial Bruker IFS/66 FTIR. The Bruker IFS/66 uses a colinear Helium-Neon (HeNe) laser with incoming radiation to correct the alignment errors in an interferometer. The TeraFET was used as an external detector, with a QCL being an external source to the spectrometer. Typically the internal detector is used for this FTIR spectrometer or a bolometer can be oriented to an external port where the Bruker focuses a beam out of an HDPE window. A second port Port B is an alternative to the bolometer where the radiation is collimated when exiting the spectrometer. Figure 2.36 shows the optical configurations available for the Bruker FTIR. An OAP was fixed outside Port B and focused the beam into the 20 MHz Array for rapid scan FTIR. The rapid-scan settings were programmed in OPUS, which is computer software used to run routines for the Bruker IFS/66 and collect data. In rapid-scan mode, OPUS will not display data in the GUI. Instead, a buffer in the Bruker FTIR stores the data as the interferometer is rapidly scanned. This limiting factor sets the number of scans per experiment in this mode of operation.

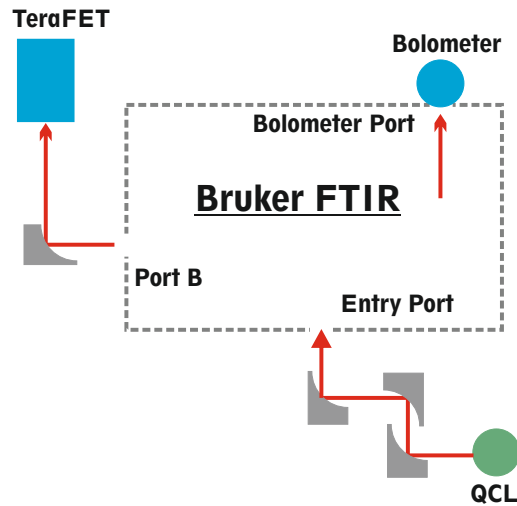
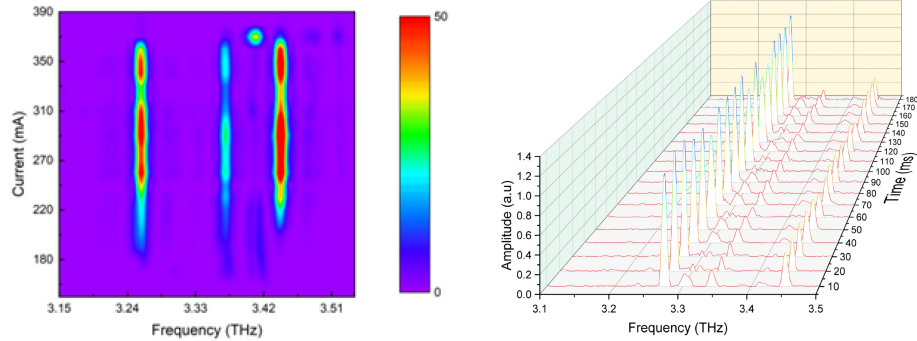


Figure 2.36: Diagram of the optical ports available for the Bruker FTIR. The optical path can either exit through the bolometer port or port B.

The laser is a multi-mode 3.4 THz waveguide block integrated QCL, a full characterisation and description of the waveguide can be found in work by Eleanor Nuttall [87]. The QCL was biased at 310 mA at a temperature of 10 K using a Janis helium flow cryostat. After rapid scans of continuous wave emission, the rapid-scan routine was set up to scan 100 samples a second when a high TTL trigger was sent to the Bruker FTIR. The trigger also went to a signal generator which swept the QCL bias from 0 to 350 mA over a second. This experiment intended to observe any thermal fluctuations in the optical modes

as the laser bias was slowly swept but the trigger port into the Bruker IFS/66 was faulty and stopped the rapid-scan experiment from triggering correctly.

Examining the data, a change in intensity can be observed compared to the usual typical time-averaged FTIR results. This technique could be used to study the thermal effects in QCL lasing dynamics when a device is switched on.



(a) FTIR data taken by Eleanor Nuttall showing the QCL emission at different bias currents.

(b) Rapid-scan FTIR taken of the QCL using a TeraFET as a fast detector at a fixed 310 mA QCL bias.

Figure 2.37: FTIR spectra taken from a 3.4 THz multi-mode QCL.

Figure 2.37a shows a previous time-averaged bolometer measurement of the multi-mode device taken from [87]. Figure 2.37b is the results from the rapid scan experiment using a TeraFET detector with a 0.55 gate voltage, where the scan time interval is 10 milliseconds. This experiment shows the capability of using time-resolved FTIR measurements to examine a time domain signal. Fluctuations in the THz amplitude show the effects of the radiation passing through an unpurged atmosphere. The frequency appears to be different between the averaged and time-resolved measurements, this difference in power is due to the alignment of the QCL into the system which can shift the measured frequency and water absorptions in the optical paths entering and exiting the Bruker.

Although the frequency has shifted due to the misalignment, the mode spacing is maintained. Figure 2.37a shows weak modes lasing with an approximately 23 GHz spacing and Figure 2.37b has a spacing of approximately 25 GHz. The lack of averages in the rapid scan technique has failed to detect the weak lasing modes, but the spacing can be seen clearly at the 3.3 THz point of Figure 2.37b. The TeraFET used an external detector port which does not have purging and is different to the port previously used in the bolometer experiments.

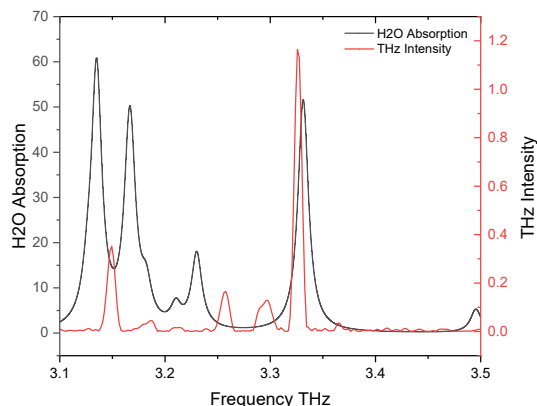


Figure 2.38: H₂O absorption compared to the FTIR characterisation of the multi-mode QCL.

Figure 2.38 shows the effects water absorption has on the QCL spectrum, by overlaying a single FTIR scan with simulated H₂O absorption from JPL at atmospheric pressure.

2.6 Summary

In this chapter, THz QCLs were introduced and the two methods used in this work to cool the laser which are a helium flow cryostat or closed-cycle cryocooler. The specifications of the Janis ST-100 helium flow cryostat and Cold Edge cryocooler were compared along with the advantages and disadvantages of each cooling method. Characterisation of the closed-cycle cryocooler uses an Ohmic load and laser driver to give a simple heat load relationship of the cold finger.

The LI relationship of the QCL is an important characteristic when using these lasers as a source. By examining the shape, users can see the threshold current, peak current and any mode hops that result in a change in intensity. This characteristic was taken over a range of temperatures, allowing the emission properties to be known across the full operating temperature range, as well as the maximum operating temperature of the QCL. When using a single patch antenna detector, the LI characteristic looked different, where Mode 2 dropped in intensity. The reason for this change in intensity is a spatial shift in THz intensity as a new mode is emitted from the QCL. The automated beam profile system was an effective method to overcome difficulties in aligning the single patch device's small surface area to the main lobe of the THz emission. The non-Gaussian beam profile is to be expected in a THz QCL due to the device being free-space coupled into the detector by a pair of OAP mirrors.

FTIR is a reliable method of obtaining a laser's frequency quickly and to a high degree of accuracy. The accuracy of a Michelson interferometer relies upon

knowing the distance a stage has travelled to reduce frequency error caused when scanning the stage. The FTIR data taken in this work spanned over multiple days due to the number of scans to average and the current 10 mA steps. Because of the long experimental time, the frequency error in measurements will also include QCL temperature drifts over time. The first step in data analysis was to identify the peaks of the laser at a range of 10 mA current steps spanning temperatures from 20 K to 50 K and fit polynomials to describe their relationship to driving current. The relationship to driving current gave a value which could translate the current axis on LI experiments to a frequency axis.

Using NASA’s JPL catalogue to compare methanol spectra in similar frequency ranges allowed the correct frequency range of the QCL to be found. The visibility of methanol using this QCL shows that this laser can be used with methanol samples as a calibration system to characterise the spectrometer sensitivity and resolution. Later in the system development, this QCL can be swapped for different devices to target specific gas species and repeating these characterisation steps will be necessary to understand the behaviour of a new QCL.

Two QCL modulation techniques have been presented and lock-in amplification has been discussed, as well as the applications which benefit from modulated electromagnetic radiation. An investigation into thermal detector noise was shown and compared to electronic signal drift from self-mixing experiments. The noise investigation showed a methodical fault-finding technique for unexpected noise within the system and came to the appropriate conclusion being the ambient temperature fluctuations. Locking to the thermal noise from a chopper blade worked as an alternative to leaving a QCL running overnight, this method works due to THz emitted as part of black body radiation.

A solution to the detector drift problem was found in the TeraFET detectors. Experimental data from TeraFET characterisation which were taken with Jakob Holstein and Harry Godden have been presented. Additional experimental data which was taken with assistance from Sanchit Kondawar using rapid scan FTIR has also been presented in this chapter. The fast THz detection was presented as a poster at Infrared Millimeter Wave and Terahertz (IRMMW-THz) and Infrared Terahertz Quantum Workshop (ITQW) in 2023 [124]. The noise characterisation of array TeraFETs contributed to a presentation at IRMMW-THz 2023 presented by Jakob Holstein [125].

The characterisation of array TeraFET devices shows an order of magnitude improvement with each device’s modulation frequency. The gate-sweep characterisation results confirm the FET designs are working as intended and the reduced noise performance does not dominate the improvement made through a larger effective detector side. The expected NEP is higher than expected during these experiments, simulations undertaken in Frankfurt expect the NEP to be sub $1 \frac{nW}{\sqrt{Hz}}$. The higher NEP has been attributed to the amplifier noise in the readout electronics through a thermal investigation undertaken by Jakob Holstein.

Future work would begin with further improving the readout electronics

integrated into the TeraFET detectors and increasing effective detector area without adding a shunt load onto the FET. This work is being undertaken in Frankfurt by the design of integrated optics and smaller array-type devices. The Gate voltage investigation could be repeated using low noise electronics to obtain a truer NEP value and this could be done with a low noise power supply. An alternate method is to measure the noise contributions of the power supply and cabling and remove them from the result. The rapid-scan FTIR demonstrated the capability of faster readout electronics, this experimental work can be moved to a home build FTIR which has a greater resolution than the commercial Bruker device. The change to an alternate FTIR, can allow rapid scan and step scan measurements to investigate the switching dynamics of a THz QCL. As well as rapid FTIR techniques, higher bandwidth readout electronics allow the use of high-speed lock-in amplifiers such as the Zurich Instruments MLFI to improve the acquisition speed of gas spectra in the time domain.

Continuing to use this THz QCL, a precise frequency calibration method should be developed as the frequency is already known. This can be realised by characterising the FTIR error and running a FTIR for each gas measurement where the resulting spectrum would have gaps corresponding to the sample absorption features. An alternative to FTIR is to use a calibration gas, this would involve a second detector and small gas cell where known absorptions act as a calibration to the frequency drift of an experiment. Including a colinear stable laser of a known wavelength can be used to accurately track the movement of the mirror and correct for the $\cos(\theta)$ as seen in commercial FTIR spectrometers such as the Bruker IFS/66 used for rapid scan. The calibration gas method is a simple way to obtain the frequency accuracy required for gas spectroscopy but limits the THz source to devices which have known absorptions to the gas sample under test. The FTIR frequency calibration method requires more analytical work and an effective monitor of QCL temperature. Still, it can be used without the restriction of needing a THz active calibration gas and a second detector.

The development of higher temperature THz QCLs brings new possibilities to future systems. A higher operating temperature reduces the size and power consumption and size of the QCL cooler. A smaller cryocooler can be flown on a balloon mission or taken in the field with a small power supply. An example of in-field detection would be monitoring the ammonia output from farms or air quality measurements in industrial environments. Using future high-temperature designs would allow a smaller cryocooler to be used and developed into a portable system.

Chapter 3

Single Pass Gas Spectroscopy

In 1900 Max Planck showed that energy in matter occupies quantised energy states and transitions between them rather than occupying a continuum of energy levels. This energy contained by a molecule can come in four forms: rotational, vibrational, electronic and translation energy where the matter is rotating about its centre of mass or vibrational energy where the molecule atoms are periodically displaced through vibrating bonds. Identifying these quantised states is the basis for molecular spectroscopy.

3.1 Molecular Absorptions

Using the two energy level model shown in Figure 1.14 where ΔE separates the two energy levels E_2 and E_1 , then absorbed radiation can take the form:

$$E_2 - E_1 = \Delta E = h\nu \quad (3.1)$$

Where the frequency is ν and h is Plank's constant, incident radiation with energy ΔE excites the molecule into the higher energy state. A detector measuring the incident radiation would see a reduced amplitude. In this simple model, these energy levels can be considered vibrational or rotational states in the molecule. Spectral features are not only limited to vibrational and rotational spectra; electronic transitions are another type of transition, but most are outside this work's scope. If the incoming radiation used a broad range of frequencies, it would be observed that only the frequency corresponding to a wavelength ν has been absorbed, which is called an absorption spectrum [126].

This example can be brought further where the quantised states of rotational spectral features in a diatomic molecule can be modelled as a simple rigid rotor, where two masses m_1 and m_2 are separated by a length R . If the length R is fixed, then the entire rotation will be about the centre of mass and the system can be thought of as one rotating molecule instead of two individual rotating masses. Using the rigid rotor approximation the energy levels can be written as Equation 3.2.

$$\bar{\nu}_J = \frac{E(J)}{hc} = 2B(J + 1) \quad (3.2)$$

Where J is the quantum number for the rotational momentum and B is the rotational constant. wavenumber $\bar{\nu}_J$ can be given by dividing the energy by h and c . The rotational constant B in wavenumber is defined as Equation 3.3 where I is the moment of inertia and μ is the reduced mass given in Equation 3.4.

$$B = \frac{h}{8\pi^2 I c} \quad (3.3)$$

$$I = \frac{m_1 m_2}{m_1 + m_2} r_0^2 = \mu r_0^2 \quad (3.4)$$

When a molecule is irradiated and transitions between rotational states with the selection rule $\Delta J = \pm 1$, the energy difference from J to $J + 1$ is given in Equation 3.5.

$$\Delta E(J + 1) - \Delta E(J) = 2B(J + 2) - 2B(J + 1) \simeq 2B \quad (3.5)$$

This can be useful for assigning quantum numbers to a transition because, in a rotational spectrum, the line spacing is related to twice the rotational constant.

In an elastic bond, the intrinsic frequency of oscillations in wavenumber can be given as:

$$\bar{\omega}_{osc} = \frac{1}{2\pi} \sqrt{\frac{k}{\mu}} \quad (3.6)$$

Where k is the force constant and μ is reduced mass from Equation 3.4. The vibrational energy is quantised like other molecular energies and can be imagined as simple oscillators with an energy $E(v)$ or wavenumber ϵ_v which are shown in 3.7.

$$\epsilon_v = \frac{E(v)}{hc} = (v + \frac{1}{2})\bar{\omega}_{osc} \quad (3.7)$$

Applying the selection rule for vibrational states $\Delta v = \pm 1$ the transitional wavenumber $\epsilon_{v+1} = \bar{\omega}_{osc}$. This approximation works when the vibrational states are at a low energy state, due to other factors such as harmonic potentials, these can be taken into account by expressing the energy as a series of increasingly higher-order correction terms. The internal energy of a molecule can then be expressed as the sum of its vibrational and rotational energies if electronic transitions are neglected.

A combination of vibrational and rotational features is a rovibrational spectrum and is seen in practice where closely spaced rotational states occupy a vibrational energy level. When examining molecules additional terms must be added to the approximations such as an anharmonicity constant to consider the

molecule not behaving as a harmonic oscillator in vibrational states and centrifugal distortion to account for non-rigid rotors in rotational states [86] [127] [128] [126]. All spectral features measured in this work are a combination of vibrational and rotational transitions.

Atomic oxygen has a unique spectral line in the THz region as it's a fine structure electronic transition. An electron possesses a magnetic moment through its spin and if it is bound within a molecule, another magnetic moment from the orbit. The interaction between the two magnetic moments is called spin-orbit coupling, where the strength of the coupling and its effect on energy levels depends on the orientation of the spin and orbital directions. The atomic oxygen transition in the THz region is at 2.06 and 4.74 THz where the spin-orbit dipole couples to the wavelength causing a transition [129].

Ideal gas spectral features are sharp and Lorentzian, but experience broadening factors which are Gaussian in shape, resulting in experimental gas lines having a Voigt profile. Doppler broadening occurs within a gas due to the random nature of the molecules as they move within the gas, the direction of the molecules can be moving towards the light source or away, giving gas features a finite width [130]. Doppler broadening is expressed as Equation 3.8 where the linewidth broadening is $\Delta\nu$, the mass of the atom is m and the average optical frequency is ν_0 .

$$\Delta\nu_D = \frac{2\nu_0}{c} \sqrt{2 \ln 2 \times \frac{k_B T}{m}} \quad (3.8)$$

An experimental factor attributed to the broadening of a spectral line is pressure (or collision) broadening where a higher pressure results in wider absorption peaks. The broadening is due to the number of collisions of the gas molecules increasing with pressure. When examining spectra with closely spaced absorptions such as rotational transitions, the pressure of a sample can blur the lines and obfuscate fine transitions.

Information about a specific molecule can be found through the amplitude and location of an absorption feature in the spectrum. The absorption frequency can be decoded by analytical techniques to tell us the atomic number of the transition.

3.1.1 Beer-Lambert Law

The Beer-Lambert law is used in absorption spectroscopy and helps describe the strength of absorbance.

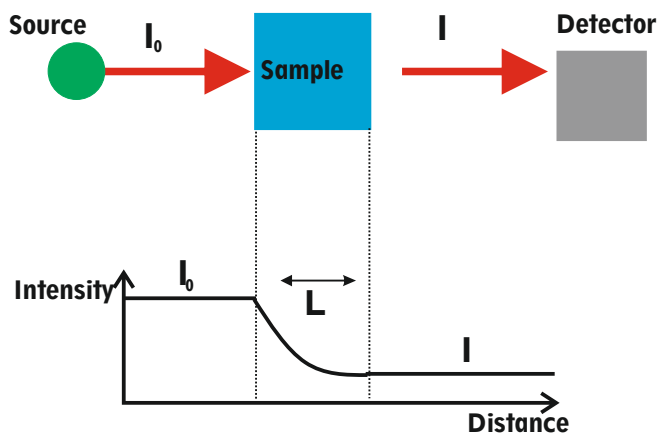


Figure 3.1: (Top) An illustration of a simple direct absorption measurement. (Bottom) The light intensity compared to distance as it passes through the sample.

$$A(\lambda) = \epsilon l C = \log\left(\frac{I_0(\lambda)}{I(\lambda)}\right) \quad (3.9)$$

As radiation penetrates a sample it is absorbed at different rates depending on the wavelength of the radiation or the material properties, this can be expressed in a unitless value called Absorbance (A). A simple diagram of absorbance is shown in Figure 3.1. Absorbance depends on multiple factors, one value is the optical path length at which the radiation passes through the sample where more distance through a sample results in stronger absorption. The molecular absorption coefficient (ϵ) is a material property which describes the amount of light a sample absorbs depending on the wavelength. The incident light on the detector, that is the light from the source with no sample (I_0) and the light on the detector with a sample in the optical path (I). The optical path length through the sample is (l) and the sample concentration (C).

$$T(\%) = 100 \times \frac{I(\lambda)}{I_0(\lambda)} \quad (3.10)$$

As well as Absorbance, the data can be described as Transmittance by referencing the sample ratio. The Transmittance is commonly expressed as a percentage $T(\%)$, this is shown in Equation 3.10.

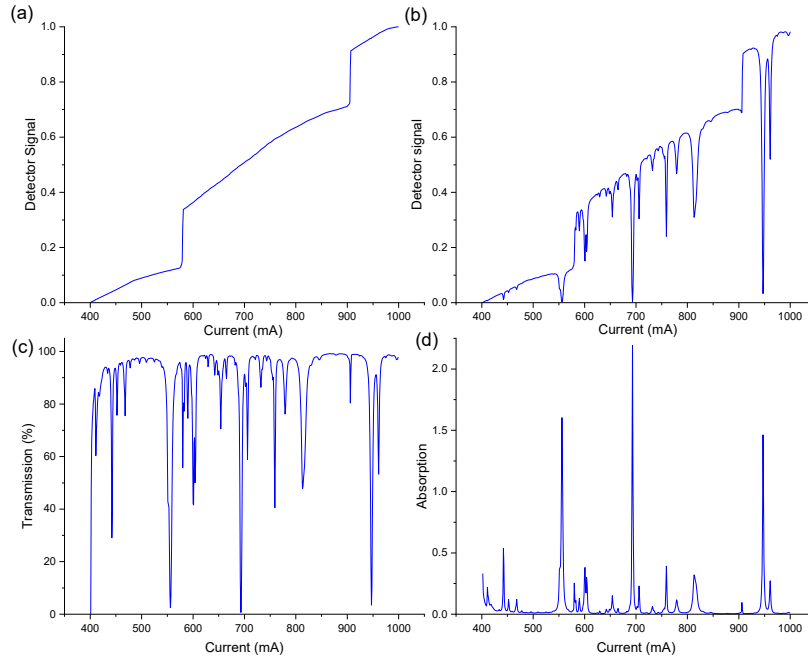


Figure 3.2: (a) Current sweep of the QCL with a vacuum blank gas cell. (b) Current sweep of the QCL with MeOH in the gas cell. (c) Transmission as a percentage through the sample. (d) The absorbance of the sample.

Figure 3.2 shows the steps to obtaining an absorption spectrum using a QCL current sweep with 1 mA steps, a gas cell and a TeraFET detector. During each experiment, the QCL current is swept over a minute and averaged in software before giving users the averaged output. In Figure 3.2 the three QCL modes have not been separated. If the spectrum is converted from bias current to frequency, the three lasing modes would be separated on the LI before transforming the axis. Each experiment is taken with one vacuum blank and one sample at one temperature step, resulting in two data sets for each QCL operating temperature. The bias is a current ramp which sweeps the full LI characteristic and emission frequency of the QCL which can be seen in Figure 3.2 (a). In (a) there is no sample in the gas cell giving I_0 in the Beer-Lambert law. When a sample is introduced to the gas cell there are now absorption features in the LI characteristic due to the transitions of the sample, this can be seen in (b) which gives I . When applying the Beer-Lambert transmission law stated in 3.10, the transmission spectrum as a function of QCL bias is given which is shown in (c). Transforming this from transmission to absorbance can then be done using the Beer-Lambert absorption law given in 3.9 where a baseline and peak detection is run to improve the noise floor. Each current step in a LI can be transformed into a THz frequency through calibration which was discussed in Chapter 2 using the table of polynomials in Section 2.3. Due to the QCL having mode hops

in the emission frequency, each mode is manually separated before analysis and treated individually resulting in three spectra from an experiment using this laser. For Mode 1 the tuning range across the operating temperature of 19.2 K to 55 K is 3337 to 3340 GHz, for Mode 2 the full frequency range is 3398 to 3404 GHz and for Mode 3 the tuning range is 3443 to 3444 GHz.

3.2 Experimental Setup

The gas phase measurements taken were in direct absorption configuration throughout this work. It is possible to use FTIR measurements where the collimated radiation passes through a gas cell before entering an interferometer and the resulting laser spectrum will have dark spots where there is an absorption. This method of gas spectroscopy acquires the laser frequency and absorption frequencies at the same time. Due to the frequency error described in Chapter 2, the FTIR method was not used because the error has not been characterised. The emission frequency of a QCL is related to the drive current, but it is not set directly through the bias. The frequency axis must therefore be determined through a separate calibration method such as the methods described in Sections 3.3 and 2.3.

Two gas cells were used in this work, a 35 cm in length metal gas cell and a 95 cm glass cell. Results will be presented from multiple gas manifold designs as the components were changed to achieve lower gas cell pressures. A Leybold Scrollvac SC 5 which has an ultimate pressure of 0.037 Torr was used to pump down the gas manifold and gas cell. A waveform generator supplied the QCL current source with a 3.25 V 230 Hz ramp signal which modulated the QCL bias from 350 to 1000 mA. The detector used in this section was the array TeraFET with a 200 kHz modulation bandwidth. The detector signal was synchronised by a 149.5 kHz TTL signal from the waveform generator, sampling the detector in 1 mA increments of the QCL bias.

3.2.1 Gas Manifold

The gas manifold is a system comprised of standard vacuum components using ISO-KF 16 and Swagelok fittings. Two pressure gauges are connected in the manifold, one ranges from 1000 to 10 Torr and the second from 10 to 10^{-6} Torr. One pressure gauge is connected to the gas manifold and another is directly connected to the gas cell. Between the gas cell and manifold, a quarter-turn Swagelok valve seals the cell and allows the manifold to be purged while experiments are running. These pressure gauges connect to an MKS 946 vacuum system controller which can adjust a Mass Flow Controller (MFC) which are programmable valves which can control the flow of samples into the manifold. The controller can set the flow rate and gas samples are added to the system using test tubes holding a liquid sample. This vapour analysis method limits the system's time-resolved speed to diffusion from the gas manifold to the gas cell. An image of the gas manifold can be seen below in Figure 3.3.

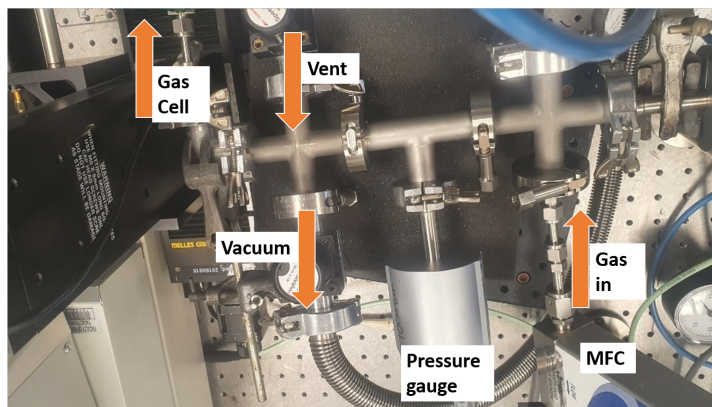


Figure 3.3: Photo of the gas manifold with two MFCs. The second MFC is off-camera perpendicular to the gas in MFC.

There are no water absorptions in the THz spectrum emitted from this QCL which spans 3336 to 3340 GHz in Mode 1, 3398 to 3404.5 GHz in Mode 2 and 3443.5 to 3444.8 GHz in Mode 3. Due to the lack of water absorption the gas manifold was vented into the atmosphere during vacuum purging. The gas cell would be pumped and vented between samples to remove the remaining atmosphere before beginning an experiment.

When undertaking time-resolved measurements and observing the diffusion of a sample into the gas cell, a trigger is needed to indicate the valve opening point. A +5 V signal was wired from the DAQ to a switch fixed to the handle of a Swagelok quarter turn valve. A break in 5 V in signal resulting from the quarter turn valve can be used to indicate when a sample begins flowing into the gas cell.

Figure 3.4 shows the gas manifold used for time-resolved measurements. Initially the sample and MFC were connected directly to the gas cell and this design worked for static gas measurements of one sample. The samples used were liquid MeOH or D₂O where the vapour diffused into the gas cell. A vapour chamber was added to reduce the time it takes for a vapour sample to fill the gas cell. The gas cell used in this experimental configuration has a volume of $2.78 \times 10^{-3} \text{ m}^3$. The vapour chamber was a metallic KF25 pipe with a $8.1 \times 10^{-5} \text{ m}^3$ volume, this cell was filled to a value set by using the MFC and 10 Torr pressure gauge. Using the gas law 3.11 the correct gas pressure could be set to the larger gas cell as the volume for both cells and pressure inside the vapour cell is known. When looking at gas mixtures the large gas cell would first be filled with a sample and closed off, then the gas manifold purged and filled with the second gas. This approximation uses the volume V_1 as the total volume of the gas and vapour cells, pressure P_1 is the desired total pressure after the valve is opened and volume V_2 is the volume of the vapour cell.

$$P_1 V_1 = P_2 V_2 \quad (3.11)$$

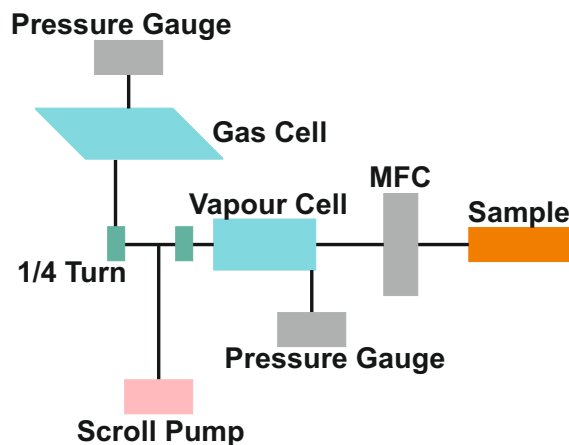


Figure 3.4: Diagram of the time-resolved gas manifold.

The experimental process for time-resolved measurements of a single gas is shown below.

1. With the system at atmospheric pressure close the chamber, open the gas cell valve and begin pumping down.
2. Attach a sample and set the MFC to open.
3. Close the gas cell and open the sample chamber to purge the atmosphere from the test tube. The atmosphere has been removed once the pressure gauge inside the chamber has stabilised.
4. With the atmosphere removed, close the MFC and pump the chamber.
5. Run a test scan to ensure there is no contamination in the gas cell. If there are no contaminants, close the gas cell valve and close the scroll pump.
6. Flow the sample into the chamber at the appropriate pressure and run the experiment.
7. With the experiment running open the gas cell valve and allow time for the pressure gauges to stabilise.

3.2.2 Single Pass Cell

Throughout this project, two gas cells were used, a glass gas cell 95 cm in length with a $2.78 \times 10^{-3} \text{ m}^3$ volume. Figure 3.5 shows the glass gas cell with Brewster angle transparent Polymethyl Pentene (TPX) windows. The second is a metal gas cell 35 cm in length and $8.1 \times 10^{-5} \text{ m}^3$ volume, this gas cell is made from ISO-KF standard parts and uses two flat quartz windows and is shown in

Figure 3.6. When using a gas cell with flat windows, standing waves between the gas cell windows and the cryostat window will be present.

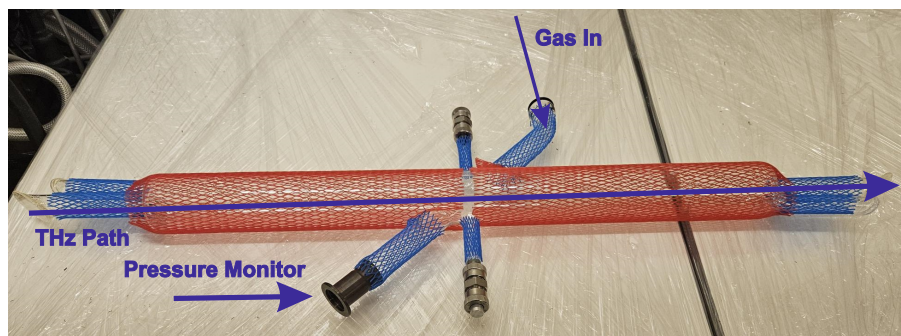


Figure 3.5: A picture of the glass gas cell used in this work.

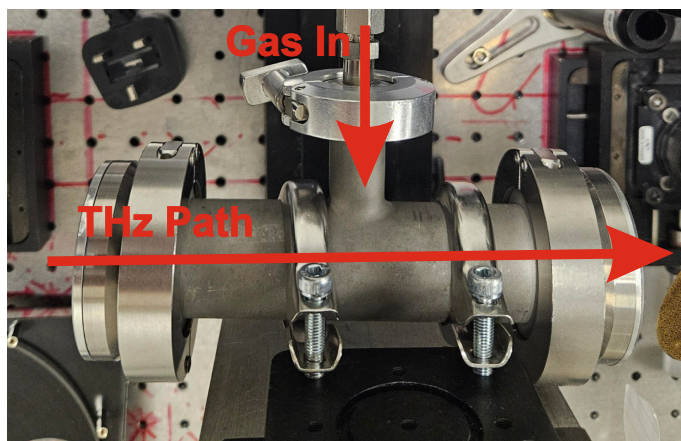


Figure 3.6: A picture of the metal gas cell used in this work.

3.3 Static Measurements

Well-studied species in the THz gap were used for calibration and system characterisation. The gas manifold and scroll pump vent into the atmosphere so the calibration gas must be safe to vent in small concentrations and stable. D_2O (Sigma-Aldrich, 99.9% D) and MeOH (Sigma-Aldrich, 99.8% anhydrous) were used to calibrate the system as they are documented in the JPL molecular spectroscopy catalogue, safe to vent in small quantities and can be mixed to observe H/D exchanges. After characterising the laser frequency, these gases were examined in detail to find the minimum observable concentration inside the gas cell.

When analysing gas spectra, both transmission and absorption spectra were used and these were fitted to remove continuum noise between peaks. When the absorption spectra have been taken, the peaks are fitted using OriginLab's peak analyser package which first removes the noise floor and identifies a peak using local maxima. Once the noise floor has been removed and peaks identified, Voigt profiles fit the spectral features to give a cleaner plot where subtle shifts in frequency calibration or small absorptions can be identified. Figure 3.7 is a data acquisition process block diagram.

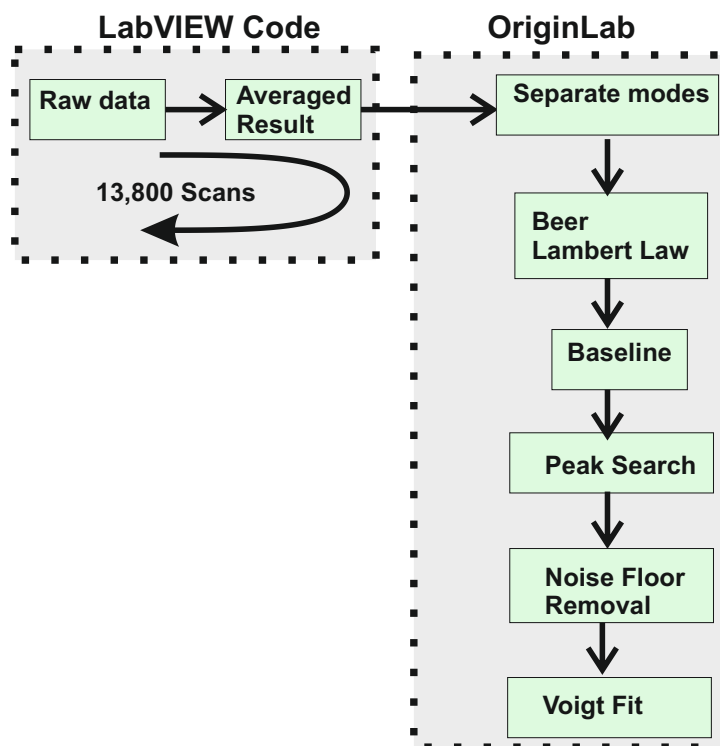


Figure 3.7: A flow diagram of the data acquisition and data processing.

3.3.1 Metal Gas Cell Methanol and D₂O Study

The uncertainties in QCL emission frequency, when compared to the bias current, caused issues between the cooldown cycles of the cryocooler. This issue can be seen below in Figure 3.8 which shows two MeOH spectra taken on different weeks biasing the QCL from 350 mA to 1 A, with a 1 mA current step and using the 200 kHz TeraFET with a 0.5 V gate potential. The top spectrum in Figure 3.8 (a) was taken at a sample pressure of 0.5 Torr and (b) was at 1 Torr.

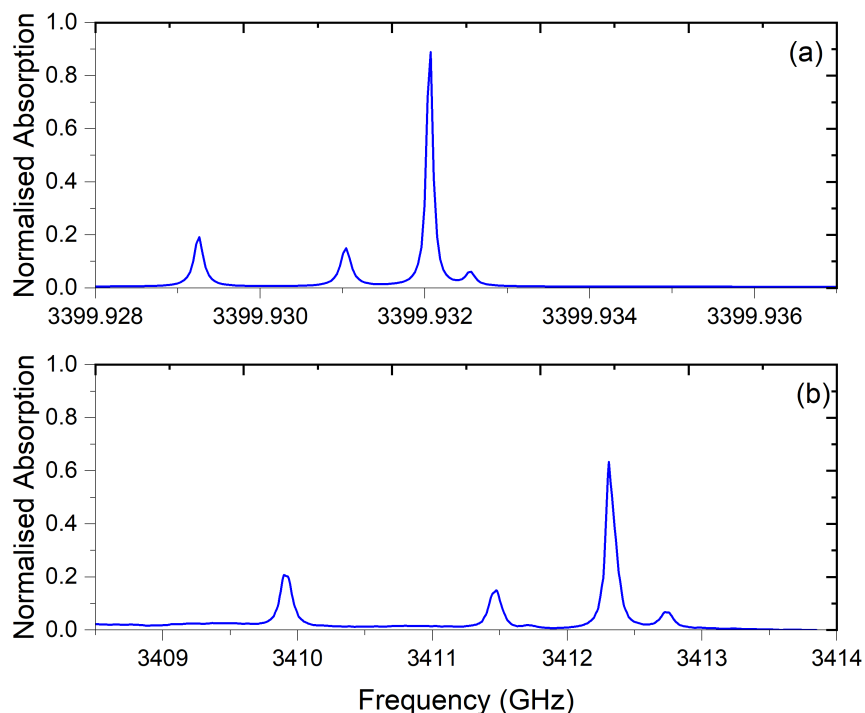


Figure 3.8: Two MeOH experiments taken during different cooldown cycles using the same QCL bias to frequency calibration. (a) MeOH at a gas cell pressure of 0.5 Torr. (b) MeOH sample at a gas cell pressure of 1 Torr. The spectral features are approximately 10 GHz offset.

The experimental data was taken by using the previously shown steps in Figures 3.2 and 3.7. The frequency axis was constructed by applying the 50 K polynomial from Section 2.3, transforming a QCL bias axis to frequency. Ignoring the broadening from gas cell pressure, both experiments used the same QCL temperature of 50 K and the same detector but the frequencies do not agree due to a drift in the frequency calibration. For ease of comparison, the absorption has been normalised. This example shows the difficulties introduced when developing a THz QCL system as this apparent 10 GHz shift in frequency is a result of changes of alignment and ambiguous active region temperatures.

Pairing D₂O with MeOH spectra, the calibration gas technique of frequency calibration can be used to identify the lasing frequency. Shown in Figures 3.9a and 3.9b is the spectral data taken from the JPL catalogue of D₂O and MeOH in the QCL frequency range the low population of D₂O absorptions can be used as an additional marker to calibrate the frequency.

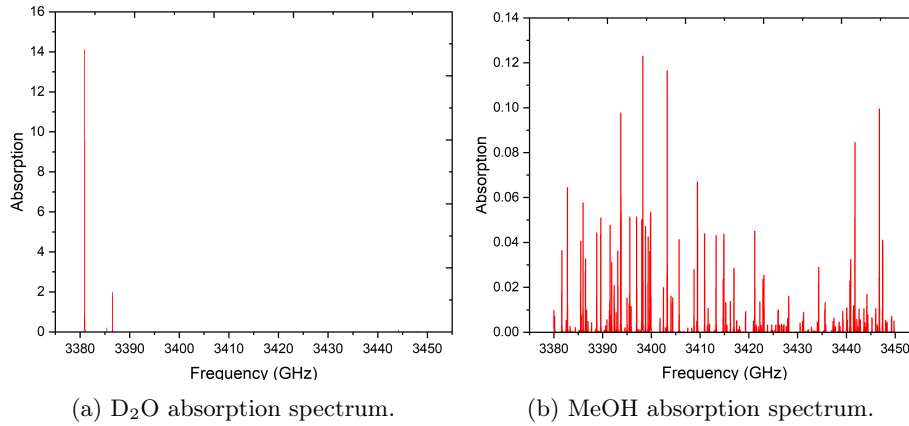


Figure 3.9: Simulated data from the JPL catalogue ranging 3380 GHz to 3450 GHz.

The MeOH spectrum in this frequency range is crowded with features so it would be difficult and time-consuming to find the absorption features by pattern alone. Using the frequency polynomials found in Section 2.3 helps reduce the spectrum that needs searching to find the frequency. D₂O has a relatively sparsely populated spectrum compared to MeOH in this region and when searching for calibration gases, the spectrum has visible D₂O and MeOH peaks making calibration easier. The spectra in this experiment were taken with the 200 kHz bandwidth array TeraFET at a current sweep spanning 350 mA to 1 A. The TeraFET was sampled every 1 mA step in the QCL bias and averaged 13,800 times. The QCL operating temperature was 50 K. The gas cell pressure for this study was 0.5 Torr.

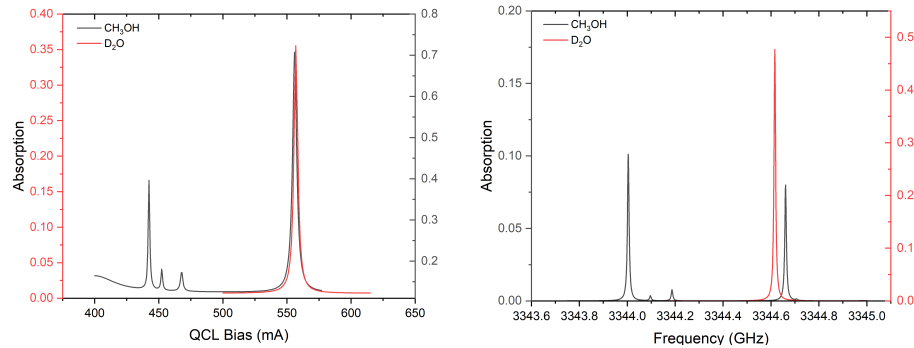


Figure 3.10: Mode 1 experimental data and JPL data showing the same peaks.

There are no polynomials for Mode 1 as it was not visible during the FTIR measurements due to the noise floor being above the low THz power. Looking at the experimental data in Figure 3.10a an overlap with a weak D₂O absorption is present at the 560 mA bias, a unique feature in this spectral range due to the low number of D₂O absorptions. Checking the JPL catalogue for a crossover in Figure 3.10b a low amplitude D₂O feature and MeOH peak with the distinct pattern seen at 450 mA, the frequency of these visible lines was found at the range 3343.8 GHz to 3345 GHz. There is a variation in frequency where the D₂O and MeOH peaks do not overlap, a result of frequency error between measurements. The MeOH and D₂O experiments were taken over a week giving a different cryocooler base temperature between experiments.

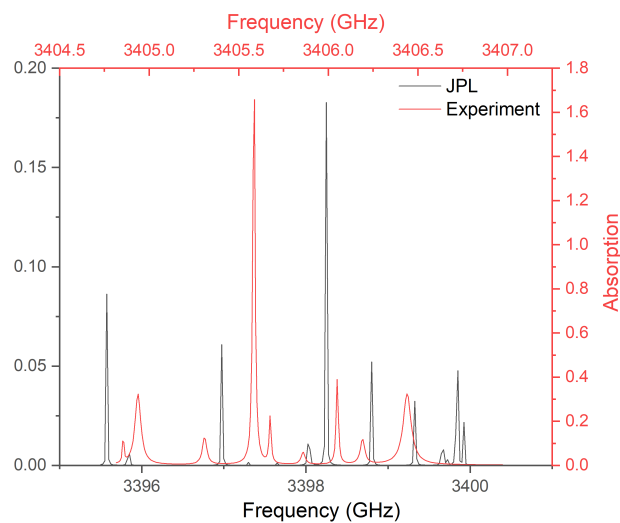


Figure 3.11: Experimental data showing MeOH absorptions in Mode 2 compared to simulated data in the JPL catalogue.

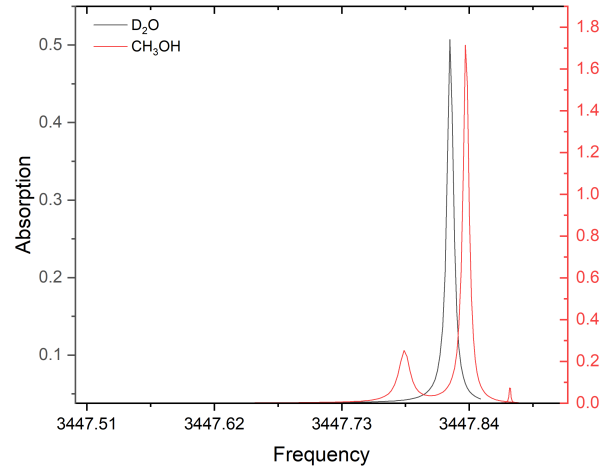


Figure 3.12: Experimental data showing MeOH absorption and D₂O overlap in Mode 3.

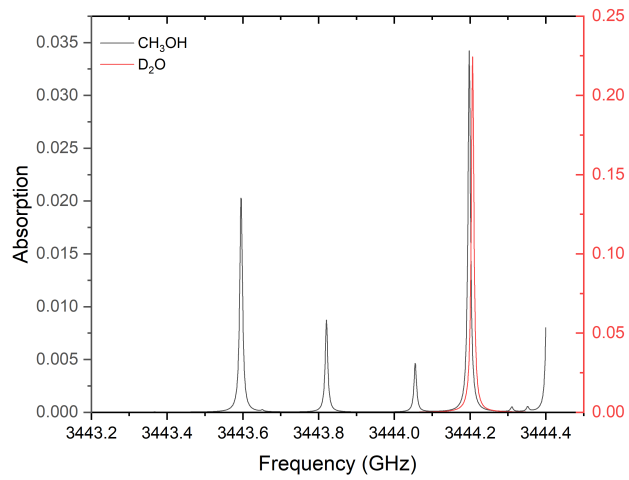


Figure 3.13: MeOH and D₂O absorptions in Mode 3 taken from the JPL catalogue.

Mode 2 is shown in Figure 3.11 where the frequency axis for the JPL catalogue is shown on the bottom X-axis and the experimental frequency axis on the top. The spectrum of the QCL emission in Mode 3 is shown in Figures 3.12 and 3.13. Figure 3.12 shows the experimental data of the unique spectral feature which is the D₂O overlap with MeOH in this region. The same spectral feature can be seen in the JPL catalogue and is shown in Figure 3.13.

Due to the high noise floor in the FTIR data, there was no polynomial for Mode 1, resulting in a missing frequency axis for this comparison. The frequency range shown in the JPL was found manually by using the unique overlap of D₂O in this frequency range and manually searching the JPL data.

The experimental data in Mode 2 was offset from the JPL catalogue by approximately 3.64 GHz. The tuning range appears to be smaller than the simulated data giving a tuning range of 40 GHz and the experimental data has a range of 30 GHz based on FTIR calibration. The frequency axes were constructed using the FTIR polynomials and comparing the features to the JPL catalogue there are no D₂O transitions in Mode 2 so only the MeOH data could be used for calibration.

With an observable D₂O absorption in Mode 3, frequency calibration of the highest current mode was found by using overlapping spectral features at 3.442 THz. The JPL catalogue data in Figure 3.13 shows the unique spectral fingerprint used to identify the tuning of the final mode which is smaller than the previous two. The experimental data shows a tuning range of approximately 300 MHz whereas the JPL data shows a broader spectrum, spanning approximately 4 GHz from 3440 GHz to 3444.4 GHz. Additionally, there appears to be an offset of approximately 4 GHz between the FTIR frequency calibration and the catalogued data in the JPL.

The spectral features in the MeOH study appear broad, where smaller features such as a closely spaced doublet are blurred into single absorption lines. The features in the Mode 2 experimental data appearing to be broader in this study were discovered to be from an offset in the pressure gauges. The experimental pressure reading was 0.5 Torr but the gas cell pressure was higher and can be seen when comparing experimental line thickness to simulated data in the JPL catalogue. To obtain spectra without broadened features, the metal gas cell was replaced by a 95 cm glass gas cell, the seals in the gas manifold were replaced and the pressure gauges were zeroed to fix any pressure inaccuracies.

3.3.2 Glass Gas Cell Methanol and D₂O Study

A MeOH study was taken in a single day for frequency calibration before examining MeOD (CH₃OD). The following experiments and the data analysis taken with Dr Michael Horbury were done after the improvements to the gas manifold. The experiment was conducted at the start of a cooldown cycle to give the best temperature performance for the QCL and the gas cell was at a pressure of 0.5 Torr for all tests.

When the QCL bias is swept from 350 mA to 1 A, the cryocooler base temperature is 19.2 K with a full laser range of 19.2 to 55 K. The absorption

features were assigned peaks using Originlab peak fitting and these are compared to the data in the JPL catalogue in similar regions to the frequencies found in Figure 3.11. A table of peak positions at different temperatures is built and compared to the JPL catalogue peak positions. A linear fit changes the peak position shift in QCL current to the JPL catalogue peak frequencies. Table 3.1 shows the coefficients used for each linear fit and the standard errors. The values are in GHz and the peak positions are used for this conversion, not the QCL current value. This linear fit is how the frequency axis was constructed. These results were used as frequency calibration for a MeOD study and contributed to a publication in progress which reports MeOH and the first MeOD spectra at 3.4 THz using an array TeraFET detector.

	Slope	Intercept
Mode 1 Coefficient	0.0106	3326.4511
Mode 1 Error	4.02×10^{-4}	0.09152
Mode 2 Coefficient	0.00715	3398.05
Mode 2 Error	1.09×10^{-4}	0.049
Mode 3 Coefficient	0.0044	3442.0032
Mode 3 Error	9.5×10^{-4}	0.00441

Table 3.1: Table of the coefficients for each linear fit.

The MeOH study shown in Figures 3.14, 3.15 and 3.16 was taken over the space of one day at a gas cell pressure of 0.5 Torr. The QCL bias was ramped from 350 mA to 1 A with a 230 Hz ramp signal and the TeraFET was sampled at 149.5 kHz giving a 1 mA sample rate on the detector. The scan ran for 1 minute giving a total of 13,800 averages. After an experiment was complete, the QCL temperature was stepped and the study was repeated to give the full QCL tuning range. The detector used in this was the 200 kHz modulation bandwidth TeraFET detector.

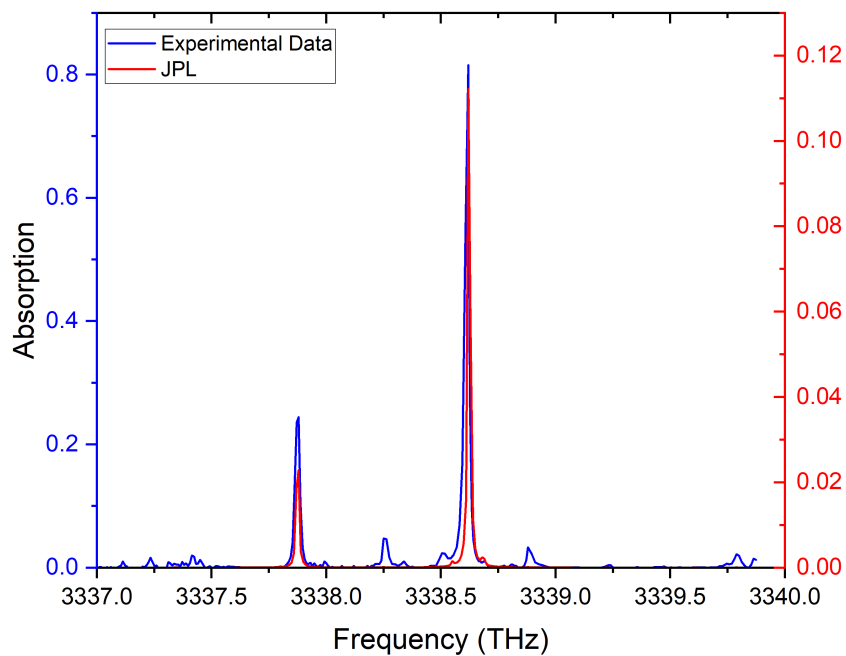


Figure 3.14: Methanol spectra taken at a 0.5 Torr, QCL Mode 1.

Figure 3.14 shows Mode 1 with a temperature sweep from 19.2 K to 50 K. This data now has sharper spectral features when compared to the study in Subsection 3.3.1, this is due to the improved performance between the two gas cells.

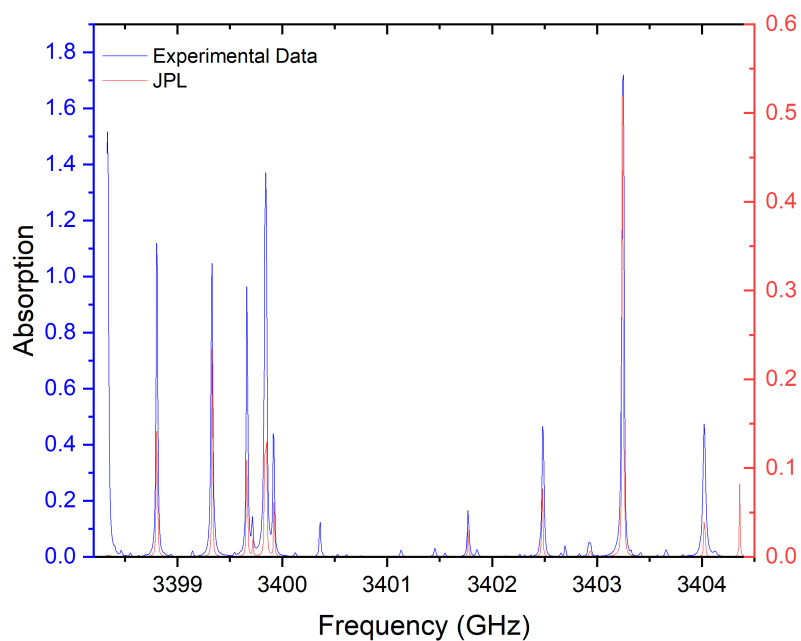


Figure 3.15: Methanol spectra taken at a 0.5 Torr, QCL Mode 2.

In Figure 3.15 there is a simulated absorption which is missing at the higher frequency of 3404.36 GHz and the lower frequency of 3398.25 GHz an experimental absorption line is missing from the simulated data. The missing peaks at the ends of the spectra are due to a scaling error in the frequency axis conversion at the beginning and ends of the QCL mode.

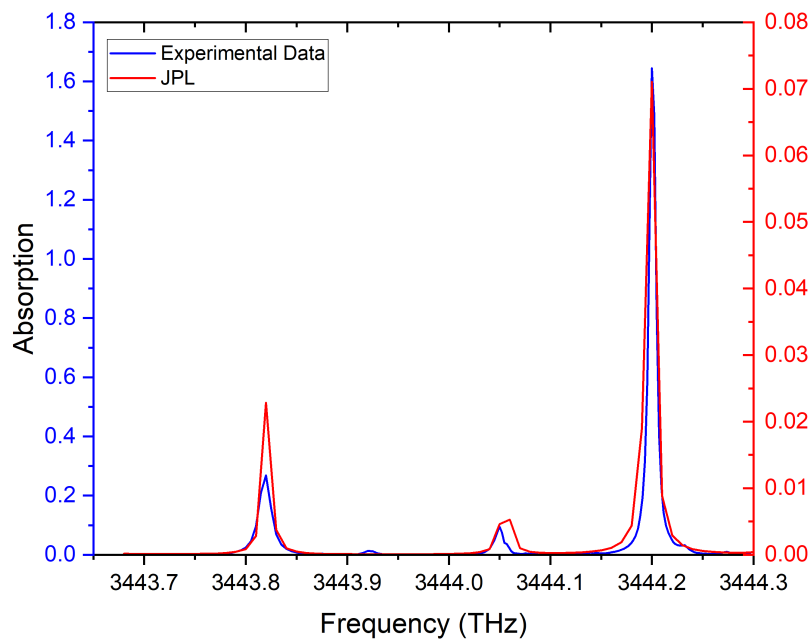


Figure 3.16: Methanol spectra taken at a 0.5 Torr, QCL Mode 3.

With a full temperature sweep spanning 19.5 K to 50 K, and a sample pressure of 0.5 Torr, the tuning range for all modes was identified using MeOH as a calibration gas giving Mode 1, Figure 3.14 a range of 2.98 GHz. Mode 2 is Figure 3.15 a range of 6.11 GHz and Mode 3, Figure 3.16 a tuning range of 620 MHz. The absorption amplitudes do not match in Figure 3.16 but the frequency of the absorptions has successfully been adjusted to find the full laser spectrum without the GHz errors seen in the FTIR data. The inaccuracies in amplitude are due to the JPL catalogue having large uncertainty in amplitude calculations. There are features which appear in the experimental data that are not present in the JPL catalogue, this suggests that the system has reached a point where the sensitivity can now detect features which are uncatalogued.

JPL Line Index	Experimental Frequency	Experimental Absorption	JPL Catalogue Frequency	JPL Absorption
49230	3337.871	-24.3	3337.875	-2.89
49234	3338.254	-6.20	3338.255	-7.62
49238	3338.505	-4.20	3338.499	-5.89
49239			3338.553	-4.51
49241	3338.615	-58.2	3338.617	-6.01
49242			3338.624	-2.31
49248	3338.880	-2.83	3338.875	-5.63
49254	3339.790	-4.27	3339.787	-6.01

Table 3.2: Table of Mode 1 MeOH absorptions compared to the JPL catalogue.

JPL Line Index	Experimental Frequency	Experimental Absorption	JPL Catalogue Frequency	JPL Absorption
50520	3443.8192	-29.2	3443.8208	-3.25
—	3443.9210	-1.09	—	—
50521	3444.0499	-8.31	3444.0553	-3.52
50524	3444.2005	-60.3	3444.1978	-2.65
—	3444.2325	-1.16	—	—

Table 3.3: Table of Mode 3 MeOH absorptions compared to the JPL catalogue.

In Mode 1 Figure 3.14, two absorption features appear in the experimental values at 3338.25 GHz and 3338.88 GHz which are not visible in the JPL data for Figure 3.14. These absorptions are catalogued but with a significantly smaller amplitude, this can be seen in Table 3.2 by comparing the JPL index lines 49234 and 49248 where the values in the JPL catalogue are smaller than experimental values.

Mode 3 has the highest optical intensity and the fewest absorptions in the QCL emission. There are two uncatalogued lines in this mode which are seen in Table 3.3. Any blank entries for the JPL catalogue data indicate an uncatalogued spectral line.

JPL Line Index	Experimental Frequency	Experimental Absorption	JPL Catalogue Frequency	JPL Absorption
49970	3398.80	-10.9	3398.803	-2.21
—	3399.143	-0.20	—	—
49974	3399.330	-12.3	3399.330	-2.25
49980	3399.660	-8.81	3399.664	-2.33
49981	3399.713	-2.92	3399.719	-3.31
49982	3399.840	-15.7	3399.834	-2.22
49983			3399.847	-2.45
49984	3399.914	-5.21	3399.922	-2.70
49985	3400.123	-0.16	3400.220±0.04	-7.68
49988	3400.360	-1.72	3400.360	-4.86
49989	3400.522	-0.10	3400.577±0.01	-7.80
49990	3400.611	-0.10		
49999	3401.135	-0.40	3401.060±0.20	-8.78
50002	3401.453	-0.53	3401.402±0.06	-6.78
50003	3401.548	-0.19	3401.586	-5.17
50007	3401.856	-0.46	3401.868	-6.91
50008			3401.868	-6.91
—	3402.261	-0.09	—	—
50017	3402.480	-7.23	3402.477	-2.58
50019	3402.659	-0.14	3402.679	-7.77
	3402.694	-0.45		
50020	3402.831	-0.28	3402.833	-11.0
50021			3402.833	-11.0
50023	3402.925	-1.45	3402.927	-3.68
50024			3402.943	-3.70
50029	3403.250	-16.5	3403.242	-1.85
50030			3403.255	-2.66
50031			3403.255	-2.66
50033	3403.414	-0.28	3403.418	-5.17
—	3403.658	-0.42	—	—
50039	3404.020	-10.2	3404.024	-2.67
—	3404.125	-0.53	—	—

Table 3.4: Table of Mode 2 MeOH absorptions compared to the JPL catalogue.

Mode 2 is a crowded spectral range with one peak at 3400.36 which appears to have a large disagreement between experimental 124.7×10^{-3} and simulated 0.783×10^{-3} amplitudes. Any additional peaks here are not due to large amplitude disagreements between experimental and simulated data but are uncatalogued. The absorption features for Mode 2 are shown in Table 3.4.

A possible cause of these observed features is isotopes of common species such as ^{13}C which makes up 1.1% of the natural carbon found on Earth and has an additional neutron, altering the atomic mass of the carbon atom. The

altered atomic mass of ^{13}C could result in an absorption feature appearing in the spectrum. The equations given in Section 3.1 show how the altered mass can change the spectrum of a molecule by adjusting the transitional energy.

The D_2O study was taken with the same operating conditions as the MeOH study with a full temperature and QCL bias sweep at a gas cell pressure of 0.5 Torr. The 200 kHz modulation bandwidth TeraFET was used as a detector with a gate voltage of 0.55 V. The spectra from this set of measurements were taken with a current sweep ranging from 350 mA to 1 A in a 1 mA sampling step. The 200 kHz modulation bandwidth array TeraFET was used and sampled at 149.5 kHz with a 230 Hz current ramp driving the QCL. Each QCL temperature step was sampled over 1 minute giving 13,800 samples to be averaged.

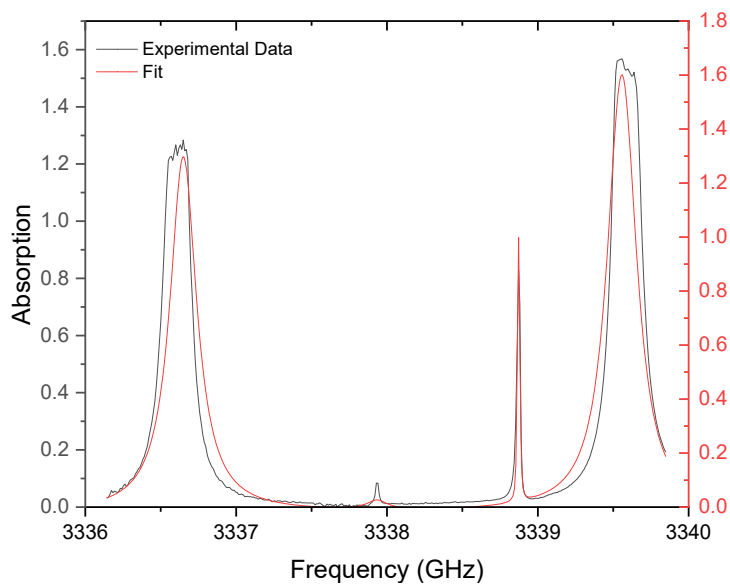


Figure 3.17: D_2O spectra taken at a 0.5 Torr using QCL Mode 1.

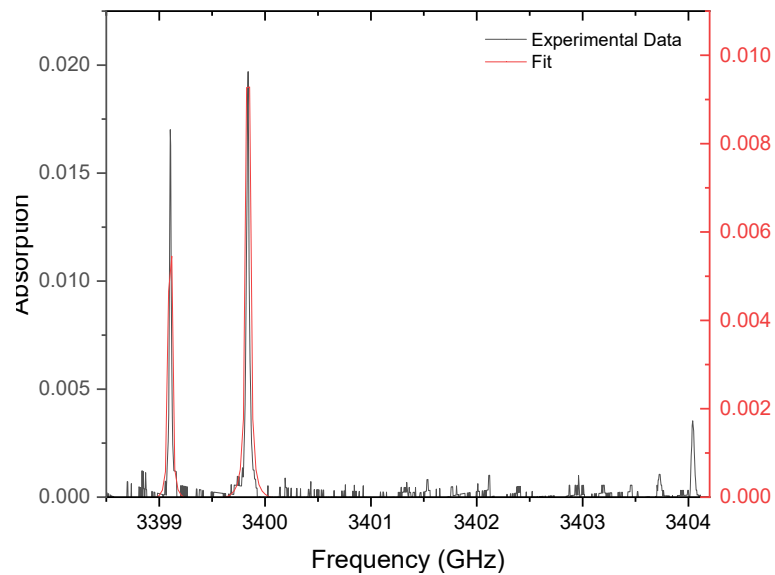


Figure 3.18: D₂O spectra taken at a 0.5 Torr using QCL Mode 2.

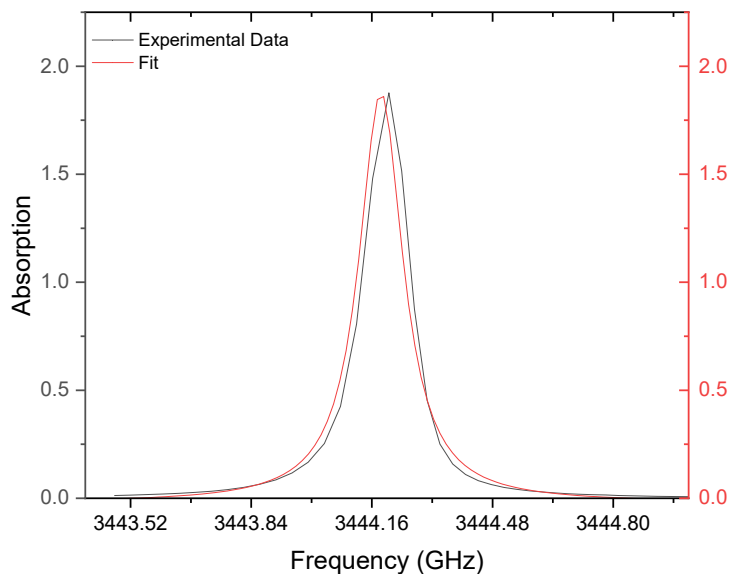


Figure 3.19: D₂O spectra taken at a 0.5 Torr using QCL Mode 3.

Figure 3.17 shows the QCL spectrum spanning Mode 1. This is the lowest emission frequency span from the laser. Mode 1 is the weakest optical mode and does not accurately represent the absorption at this frequency due to a flat top in the absorption feature. This flat top is caused by saturation of the signal due to the weak optical signal and strong deuterium absorption at the frequency.

Figure 3.18 has data from Mode 2 showing two low-amplitude absorptions which are catalogued in the JPL database at 3399.1 GHz and 3399.84 GHz, these peaks are orders of magnitude smaller than the other spectral features in this region. Figure 3.19 shows data from Mode 3 and the higher optical power have a strong absorption at 3411.2 GHz

This method of calibration is a reliable way of obtaining the lasing characteristics without the post-processing involved in obtaining the FTIR polynomials seen in Chapter 2. This method only applies to a QCL which can observe a catalogued species for calibration and is time-consuming compared to running an FTIR experiment for simultaneous frequency calibration and sampling. This calibration method is accurate but requires multiple scans at various temperatures to construct a frequency axis with low error. The error between FTIR and gas calibration can be seen through the tables in Section 3.2.2 and Section 2.3. Later in this work, results are presented with a QCL bias X-axis as it was impractical and unnecessary to do a full frequency calibration for system characterisation.

3.3.3 Detection Limit

After identifying the spectrum of the THz QCL emission through the JPL catalogue, the calibration gases were examined at lower pressures until peaks were not visible or the ultimate pressure of the scroll pump limited the experiment. This measurement shows the minimum observable concentration of D₂O and MeOH.

MeOH peaks were observable until a gas cell pressure of 0.05 Torr and using D₂O a peak was visible down to 0.04 Torr. The sensitivity of the D₂O experiment is limited by the scroll pump at an ultimate pressure of 0.037 Torr. By arranging the ideal gas law to find the number of molecules, Equation 3.12 can be used to find the number of particles observed per m³ by converting pressure to pascal.

$$\frac{N}{V} = \frac{P}{kT} \quad (3.12)$$

Knowing the gas cell volume of $2.78 \times 10^{-3} \text{ m}^3$ and the room temperature of 25 °C, the observable concentrations of D₂O and MeOH can be calculated using the minimum pressures and Equation 3.12. The minimum observable concentration for MeOH at a pressure of 6.67 Pa (0.05 Torr) is 1.62×10^{15} particles per cm³ and D₂O at P = 5.33 Pa (0.04 Torr) has a minimum observable concentration of 1.3×10^{15} particles per cm³. Because the D₂O measurement was limited by the ultimate pressure of the scroll pump, the test would need

repeating with a lower pressure pump to find the lowest detection limit. Figure 3.20 shows an absorption peak as the sample pressure is reduced. The linear fit in Figure 3.20b had 1 Torr removed as they do not fit the linear relationship of concentration and absorption and are likely experimental errors. The outlier data point at 1 Torr is shown as a hollow point in Figure 3.20b. This method depends on the detector noise and integration time of a measurement when the lower pressures are present, this could be improved through longer experimentation time.

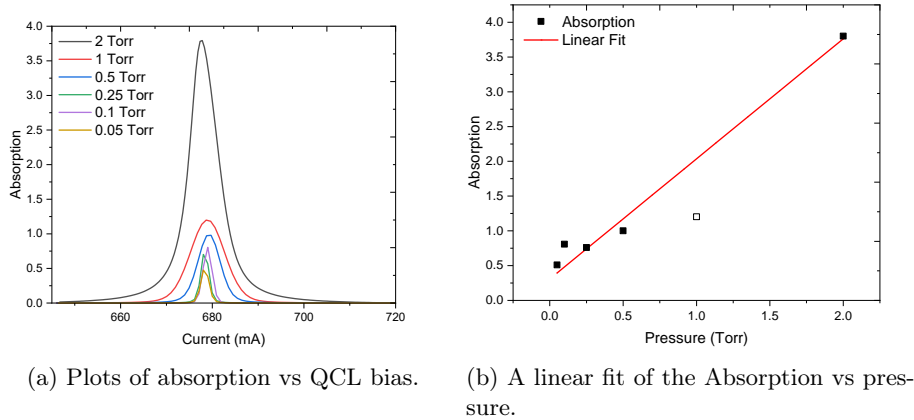


Figure 3.20: Experimental data of one D_2O peak as the gas cell pressure is reduced.

The minimum absorption $A_{min} = 0.51$ can be used to calculate the minimum concentration of different species with entries in the JPL catalogue under ideal conditions from the JPL simulation. An interesting species which is visible in the frequency range of the QCL is formaldehyde (CH_2O), an air pollutant that has an absorption at 3399 GHz which is in the spectrum of the QCL and has a JPL catalogue absorption of 1.75×10^{-5} . Comparing this with MeOH, a minimum concentration of CH_2O can be found using the results from simulated data. With an identical path length and pressure, the absorption coefficient and concentration for two species can be related by $\epsilon_1 c_1 = \epsilon_2 c_2$ then to see an absorbance of 0.51 needs to be realised using the CH_2O absorption coefficient. The absorption coefficient was taken from a JPL catalogue simulation at the same spectrum as the QCL where one low-intensity transition was located with $A = 6.78 \times 10^{-5}$ and $\epsilon_2 = 4.6 \times 10^{-22}$. This can be compared with the minimum concentration of MeOH and then put into the ideal gas law to find the pressure to obtain an absorption of 0.51.

$$c_2 = \frac{\epsilon_1 c_1}{\epsilon_2} \quad (3.13)$$

$$P = \frac{NkT}{V} \quad (3.14)$$

From Equations 3.13 and 3.14, the pressure required to do this would be 14.7×10^3 Torr. This result shows that it would not be possible to sample this feature using the glass gas cell as the windows are held one by vacuum pressure. A solution would be to increase the optical path length with a multi-pass cell or change QCL to observe a stronger THz transition of CH₂O.

For an absorption feature to be reasonable, it must be three times larger than the SNR. Using previous characterisation work from Chapter 2, MeOH's minimum absorption and concentration can be calculated. From the gate voltage characteristic in Section 2.5, at a gate voltage of 0.55 V gives the responsivity $R = 3.7 \frac{V}{W}$ and $NEP = 1.17 \frac{nW}{\sqrt{Hz}}$. Using these values, a detector noise voltage V_{Noise} can be estimated which is shown in Equation 3.16, where the measurement bandwidth is set by the integration time of the lock-in amplifier ($\frac{1}{T_c}$) or the number of averages. For this example, the bandwidth is set by the experimental parameter of 13,800 averages.

$$BW = \frac{149.5 \times 10^3}{13800} = 10.8 \text{ Hz} \quad (3.15)$$

$$P_{Noise} = NEP \times \sqrt{Bandwidth} = 5.26 \times 10^{-9} \text{ W} \quad (3.16)$$

From the QCL characterisation it was shown that the optical power is 7.6 mW with a beam quality of $M_x^2 = 1.2$ $M_y^2 = 2.2$ and by dividing the peak power by the M_y^2 value, the Gaussian component of the THz emission is given at $P_0 = 3.45 \text{ mW}$ of THz power. The non-Gaussian component will be assumed to have not coupled into the gas cell and the TeraFET detector couples 100% of the incident radiation.

The absorption coefficient to MeOH in this spectrum has been found experimentally to be $\epsilon = 128.1 \times 10^{-18}$ particles/cm². Using this, the minimum concentration of MeOH detectable by the system can be calculated, using the values calculated above.

To find the absorption limit, the absorption limit can be assumed to be very small and using the Beer-Lambert law, it can be expressed as a first-order MacLaurin expression as shown in Equation 3.18 which is transformed from Equation 3.17.

$$\frac{P}{P_0} = e^{-\epsilon c L} \quad (3.17)$$

$$\Delta P = -AP_0 = -\epsilon c L P_0 \quad (3.18)$$

The expression for ΔP can be applied to find the minimum detectable concentration of MeOH. As the minimum detectable absorption should be a minimum of 3 times the noise power, the values can be combined into an expression for c_{min} which is given in Equation 3.19.

$$c_{min} = \frac{3 \times NEP \sqrt{BW}}{P_0 \epsilon L} \quad (3.19)$$

Where the minimum concentration for this MeOH absorption is found to be 3.76×10^8 particles/cm⁻³. This calculation does not take into account effects from pressure broadening and to achieve a measurement at such a low concentration a balance gas would need to be used. The main limit to achieving such a low limit is THz attenuation in the system and collecting all of the radiation. The detector will not be collecting 100% of the radiation and as a result, the detection limit is much higher in practise.

3.4 Mixture Measurements

Once frequency calibration had been completed, uncatalogued species were examined to document new spectral lines. Deuterated methanol (MeOD, CH₃OD) is an isotopologue of MeOH where a hydrogen atom is replaced by deuterium, this reaction was chosen because the system could observe a H/D exchange. Additionally, MeOH and D₂O were available in the lab, have already been studied using the system and are visible to the QCL in the system. When doing the study this way, several reversible reactions will occur and are discussed in detail by Faure et al [131], where there are several hydroxyl-deuterated isotopologues of MeOH and water including H₂O, D₂O, CH₃OH, CH₃OD and HDO.

Mixtures were first investigated by having one species inside the gas cell, purging the gas manifold and then introducing the second using the time-resolved gas manifold described in Section 3.2.1. Using the chamber to extract the vapour and then closing the MFC before mixing prevented contamination of samples. Because the reaction is reversible, MeOH and D₂O were sampled before the 1:1 mixture as these species are present in the results. The mixtures were allowed to reach equilibrium by giving a minimum mixing time of 30 seconds to diffuse. 30 seconds was an overestimation as later in Section 3.5 it is shown the approximate diffusion time for half the sample to flow into the gas cell is 6 seconds.

These experiments were taken at a QCL operating temperature of 19.2 K and used the 200 kHz array TeraFET detector. The QCL bias was swept at a rate of 230 Hz from 350 mA to 1 A and the TeraFET was sampled at 149.5 kHz. The experiment ran for 1 minute before the 13,800 samples were averaged to get the resulting spectra.

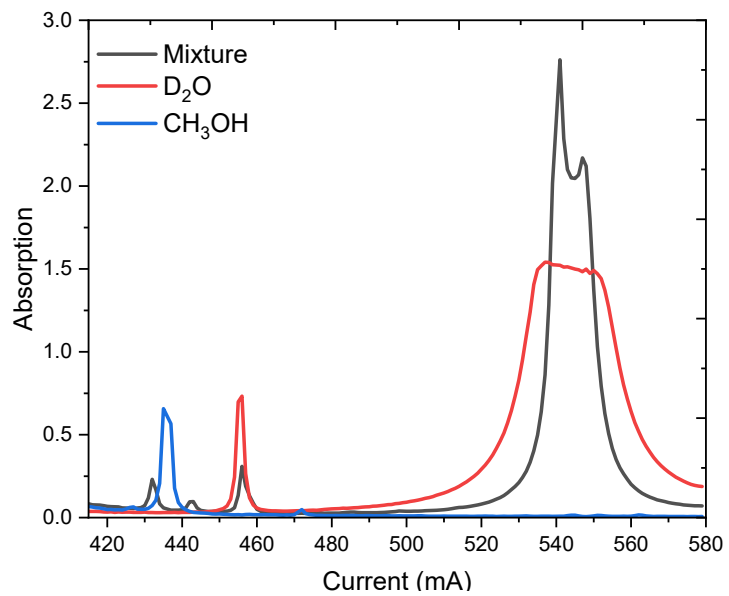


Figure 3.21: Results from Mode 1.

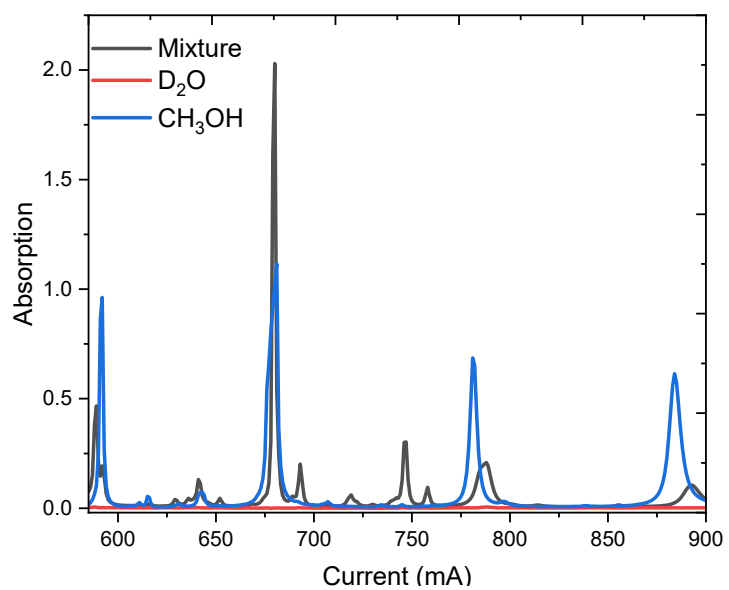


Figure 3.22: Results from Mode 2.

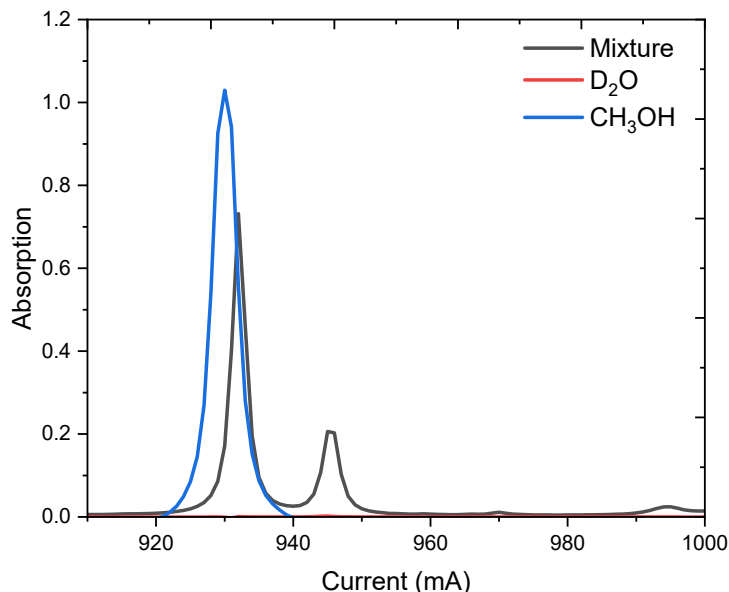


Figure 3.23: Results from Mode 3.

Figure 3.21 has data from Mode 1, where a strong D_2O absorption at 540 mA saturates the intensity, but in the mixture results a new feature appears suggesting a change in D_2O concentration. The lower current in Mode 1 observes a MeOH line which disappears and is replaced by two smaller absorption features in the mixture. Still, another D_2O absorption masks the spectrum around 455 mA. Figure 3.22 shows Mode 2, a busier area with multiple features appearing which can be attributed to the reaction taking place and with no D_2O features in this mode a new spectral fingerprint is observed between 700 mA to 775 mA. Mode2 is the lasing mode with the widest tuning range and it can be seen that additional peaks appear spanning the range of 675 mA to 800 mA.

Mode 3 is presented in Figure 3.23 and is the clearest evidence of the H/D exchange as a MeOH peak which was previously visible is replaced by two new absorption features. This mixture text shows the system can observe new spectral lines and reports on the first observation of MeOD in this spectral region. These experiments are further compared by a study using MeOD (Alfa Aesar, 99.5% D) with the same operating parameters discussed above.

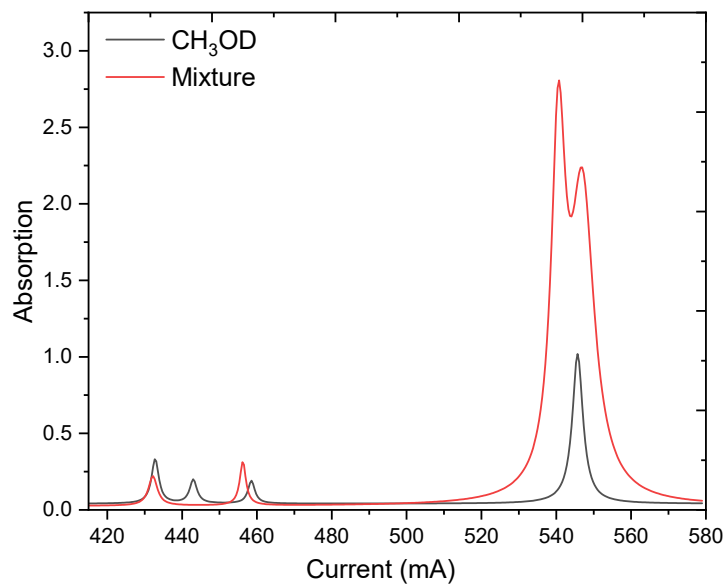


Figure 3.24: Mode 1 comparing MeOD to a 1:1 mixture of MeOH and D₂O.

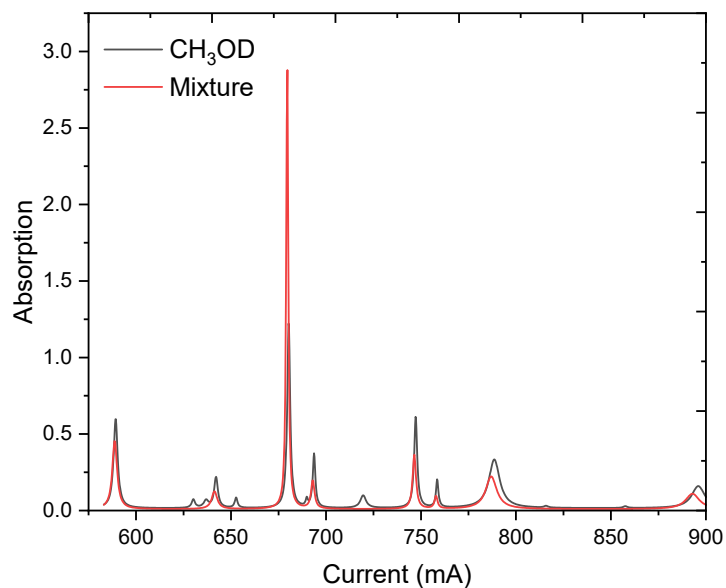


Figure 3.25: Mode 2 comparing MeOD to a 1:1 mixture of MeOH and D₂O.

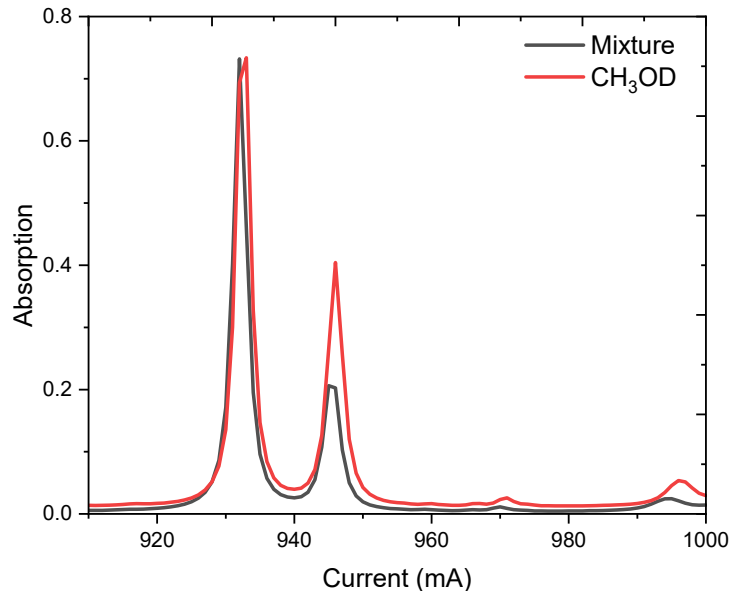


Figure 3.26: Mode 3 comparing MeOD to a 1:1 mixture of MeOH and D₂O.

Figures 3.24, 3.25 and 3.26 shows the first observation of MeOD in the 3.4 THz region. Mode 1 is shown in Figure 3.24, data from Mode 2 is in 3.25 and the data from Mode 3 is shown in 3.26.

The observed MeOD features in Figure 3.24 are present at a QCL bias of 433 mA, 443 mA, 560 mA and 546 mA. These values agree with the mixture in Mode 1 and show a H/D exchange in the mixture. A peak at the QCL bias of 445 mA is missing in the mix when compared to commercial MeOD. Figure 3.25 has a large number of features which all agree, absorption at a bias of 720 mA does not appear in the mixture but is present in the commercial MeOD this is likely due to the isotopologues in the mixture reacting. These measurements are of commercial MeOD and confirmed the mixture experiment had observed confirming the measurements in Figure 3.23 observed MeOD among other reagents in the H/D exchange. Figure 3.26 shows the unique spectral feature of the H/D exchange of MeOH where the peak splits. In MeOH, this is a large strong absorption peak seen in Figure 3.23 and the commercial sample agrees with the mix.

3.4.1 Food Safety Applications

The THz frequency emitted by this QCL can observe MeOH but EtOH is invisible to the emission. This frequency could be useful for the food industry, particularly brewing where there should be low concentrations of MeOH in an environment rich in EtOH. To test the possibility of a THz QCL being used

in this environment, cider was used as a sample in the gas cell to see if other species within the cider would obscure the MeOH spectrum. The cider sample was taken at a QCL temperature of 23.2 K and a 0.5 Torr gas cell pressure and the QCL temperature was not changed for this study. The array TeraFET with a 200 kHz modulation bandwidth was used at a sample rate of 149.5 kHz. The QCL bias was swept from 350 mA to 1 A with a 230 Hz frequency, each sample was taken over a minute and the resulting 13,800 bias sweeps were averaged. Only data from Mode 2 is used for analysis as it has the widest THz spectrum.

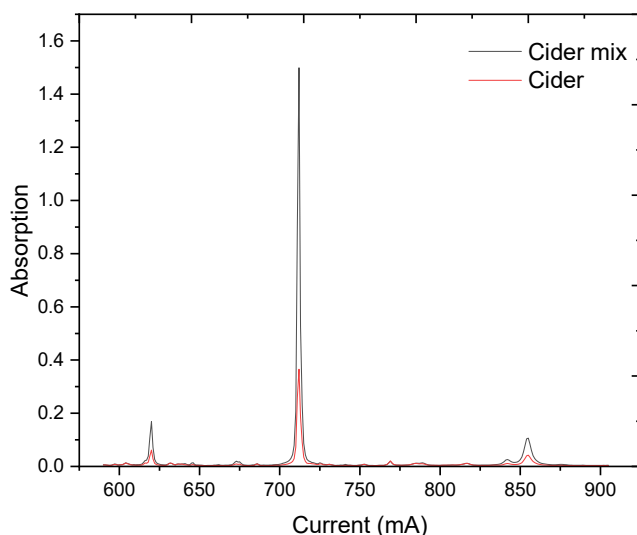


Figure 3.27: The QCL observing cider and a 90% cider, 10% MeOH mixture.

The results from the cider experiment are shown in Figure 3.27 and show no obscured lines in the cider sample. First, the cider was sampled with no additions to see if the MeOH lines were visible and then a mixture of 90% cider and 10% MeOH was tested. The MeOH was mixed with the cider to observe the intensity of the lines in Figure 3.27 increasing, confirming the peaks shown were MeOH. This mixture showed an increase in the intensity of the spectral features at 640, 710 and 860 mA, confirming these are MeOH features.

The absorbance of a mixture is the sum of all contributing species which can be written as $A = \epsilon_1 c_1 + \epsilon_2 c_2 + \epsilon_n c_n$. In this frequency, only MeOH is visible so to work out the concentration of MeOH inside the cider sample, the ratio between the absorbance of MeOH in the cider sample A_{cider} and cider mixture A_{mix} should be found. From the cider sample, the concentration of MeOH in an be related to the absorbance $A_{cider} = \epsilon_m x_m cl$, where x_m is a fraction of MeOH within the sample.

$$A_{mix} = (\epsilon_m 0.1 + 0.9x_m \epsilon_m) \quad (3.20)$$

Equation 3.20 shows the absorbance of the cider mixture and when examining the ratio of A_{cider} and A_{mix} the ratio (r) can be expressed as Equation 3.24.

$$r = \frac{A_{cider}}{A_{mix}} = \frac{x_m}{0.1 + 0.9x_m} \quad (3.21)$$

When solving the ratio for x_m , the relationship becomes:

$$x_m = \frac{0.1r}{1 - 0.9r} \quad (3.22)$$

The experimental absorptions are $A_{cider} = 0.366$ and $A_{mix} = 1.5$, giving $r = 0.244$. Using the ratio of absorbance the original percentage of MeOH is 3.1%, this percentage is an overestimation due to the volatility of MeOH being higher than the volatility of the other molecules in cider such as water. Knowing the species volatility within the cider sample allows a better representation of the MeOH concentration cider.

$$P_{\text{solution}} = X_{\text{solvent}} P_{\text{solvent}}^* \quad (3.23)$$

Equation 3.23 is Raoult's Law which relates the vapour pressure of a solvent to the pressure of the pure solvent scaled by the molar fraction present within a mix. Assuming the cider is made from three components H_2O , MeOH and EtOH, the ratio of molecules within the gas cell can be estimated. First by finding the vapour pressures of each component at $25^\circ C$ which are: $P_{H_2O}^*$ at 27.79 Torr, P_{EtOH}^* at 60 Torr and P_{MeOH}^* at 127 Torr.

The H_2O concentration is found using the over-estimated MeOH value 3.1% and EtOH concentration of 8% provided by the producer, leaving a concentration of H_2O 88.9% ($X_{H_2O} = 0.895$) in the cider. Using Raoult's Law 3.23 the solution pressures were found to be $P_{MeOH} = 3.937$ Torr and $P_{H_2O} = 22.21$ Torr.

$$R = \frac{P_{MeOH}}{P_{H_2O}} = \frac{3.937}{22.21} = 177 \times 10^{-3} \quad (3.24)$$

Multiplying the molar fraction by R , the corrected MeOH concentration is 0.55%, which is an overestimation due to the full composition of the cider not being known, this study assumed the cider to be a mixture of three parts. This does not fit the work undertaken by Y. Hang and E. Woodams in 2010 which found the MeOH content of hard cider to range from 0.037% to 0.091% [132]. Although a simple proof of concept experiment, this demonstrated the possibility of using a THz QCL in direct absorption measurements for food analysis if the full composition of the sample was known. A full characterisation of a brewing process and chemical analysis could be incorporated into a THz instrument for in-situ measurements instead of the commonly used method of periodically taking a sample to examine in a lab with methods such as gas chromatography.

3.5 Time-Resolved Measurements

Time-resolved experiments used the glass gas cell and the gas manifold shown in Figure 3.4. The first time-resolved measurements were taken using MeOH and D₂O mixtures, where one gas was held inside the gas cell and a second was added after the experiment began. The QCL bias was manually tuned using the laser driver to find a strong absorption feature by reading the time domain signal as the laser frequency is tuned. Once a strong feature was found, the laser bias was set and the temperature was allowed to stabilise at 19.2 K by setting the heater. After a peak was identified, the experiment began and the second species was introduced from the vapour cell into the gas cell. No change in the detector signal was observed due to any change in concentration hidden by the signal noise. The expectation was to see a change in detected concentration as the H/D exchange took place and concentrations began to shift. This experiment used a National Instruments DAQ board which polled the detector at a rate of 150 kHz and recorded the intensity, averaging was done in Originlab after the data was acquired.

As an alternative to observing an H/D exchange, the QCL was manually biased to observe a MeOH absorption before purging the gas cell from any sample. The vapour cell was then filled with 2.0058 Torr of MeOH to total 2 Torr during the experiment, this is assuming the total volume of the gas cell is now the sum of the vapour cell and gas cell volumes and there is no change in temperature. Once the experiment was running, the valve was opened and a change in detected THz radiation was detected which was MeOH diffusing into the empty gas cell.

$$[A] = [A]_0 e^{-kt} \quad (3.25)$$

$$\ln[A] = \ln[A_0] - kt \quad (3.26)$$

Equation 3.25 shows a first-order equation where $[A]$ is the concentration of the reactant, $[A]_0$ is the starting concentration of the reactant, t is the elapsed time and k is the rate constant. The vapour diffusion into the gas cell took on an exponential shape and can be assumed to be analogous to a reaction where the gas has diffused and instantly reacted within the gas cell. Flick's law describes diffusion from a high to low concentration, but for this experiment, it is assumed this is a first-order reaction.

The QCL was biased at 556 mA using the 200 kHz modulation bandwidth array TeraFET which used a V_{gs} of 0.55 V. This experiment is dependent on the frequency stability of the frequency stability of the QCL and the stability of the laser power supply. The QCL bias was set to the top of the peak and as the MeOH was released into the cell, the optical intensity was reduced.

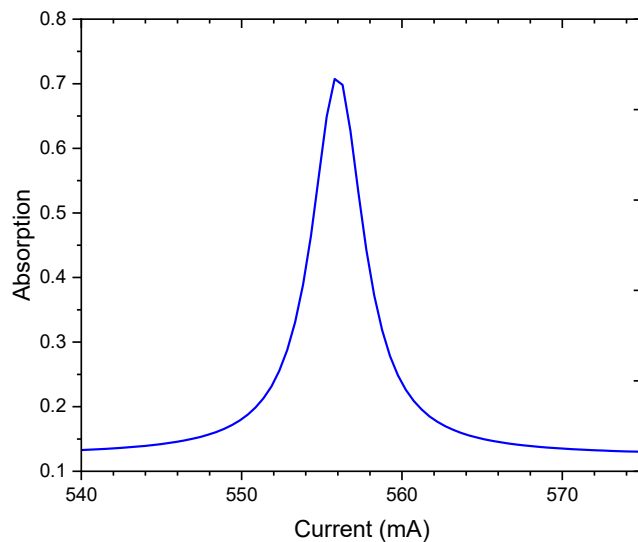
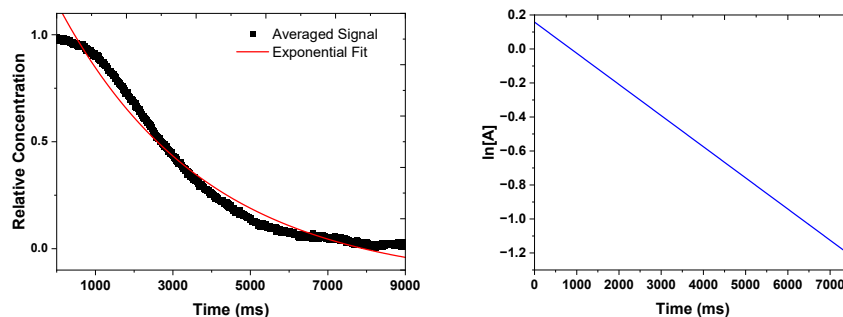


Figure 3.28: The MeOH peak observed by QCL.

Figure 3.28 shows the peak which was monitored as the MeOH was diffused into the gas cell. The rate can be extracted from the exponential term k from Equation 3.25 and by taking the natural logarithm as shown in 3.26 the equation takes the form of a linear line equation where the gradient is $-k$ which is shown in Figure 3.29b.



(a) Averaged signal compared to the exponential fit. (b) Linear fit showing $\ln[A]$ vs time.

Figure 3.29: Experimental data of the detector signal as MeOH is introduced into the gas cell.

Figure 3.29 shows results from the MeOH diffusion. Subplot 3.29a shows the relative change in THz signal. The signal is offset due to the negative voltage offset from the TeraFET detector, the signal starts high and lowers as the MeOH absorption saturates the detector. Before analysis, the signal baseline is removed from the negative detector offset. The valve was opened at 5 seconds, so the first data points were removed to aid in fitting an exponential. After removing the first 5000 samples, the signal was averaged and an exponential fitted giving Figure 3.29b.

To find the hypothetical rate of this process observed by the QCL signal the gradient from Figure 3.29b was found to be $-k$, resulting in a rate constant of $k = 2.26 \times 10^{-4} \text{s}^{-1}$.

$$t_{1/2} = \frac{\ln(2)}{k} \quad (3.27)$$

Equation 3.27 is used to find the half-life $t_{1/2}$ where the concentration is half of the volume of the gas cell which is 3067 milliseconds or approximately 3 seconds.

3.6 Conclusion

This chapter introduces the principle of molecular absorptions and relates them to the wavelength of incident radiation. Simple models are given of how the rotational or vibrational quantum numbers can relate to the momentum of particles. The Voigt shape of an absorption in a gas spectrum and the factors contributing to the finite width of a spectral feature are also presented. After discussing absorption features in a spectrum, the absorption strength and the process of obtaining the spectra are shown using the Beer-Lambert law. The Beer-Lambert law is important in this work and methods to further improve the optical path length are discussed in detail in Chapter 4 where the work on designing a multi-pass cell is presented. Four plots in Figure 3.2 showing how a QCL bias sweeps can be transformed into absorption or transmission spectra are given using MeOH data.

Before presenting data taken throughout this work the experimental setup is described and the bias conditions of the QCL are given alongside the sampling frequency of the detector. The modulation and sampling frequencies ensured the detector was operating within the modulation bandwidth and was sampling the THz radiation at 1 milliamp increments of the QCL bias. The gas manifold had two designs depending on the experiment when a static spectrum was taken of one species a MFC could be connected and the gas under test is allowed to flow into the gas cell. If gas mixtures or time-resolved measurements were to take place, a second design was made which incorporated a vapour cell which was a small cell $8.1 \times 10^{-5} \text{ m}^3$ in volume which held a sample separate from the gas cell. The chamber allowed the desired amount of vapour to be held before beginning an experiment. The two gas cells used in this work were shown and their specifications are given.

All spectroscopic data in this work was taken using an Array TeraFET detector. When running the QCL continuously for days, using a frequency axis constructed from FTIR experiments taken in the previous year using a different optical setup would not yield an accurate QCL bias to THz frequency conversion. Section 3.2.2 builds a frequency axis using MeOH and D₂O as calibration gases as an alternate means of constructing a frequency axis. Lines in the JPL catalogue are shown and compared to a frequency axis constructed from a polynomial from Chapter 2 and the difference is in the order of GHz. Once the cryocooler is switched on it is left operating for two weeks and the base temperature gradually increases. The method of temperature monitoring inside the cryocooler is a temperature probe monitoring the top of the cold finger. As time progresses between cooldown cycles, this temperature becomes uncertain due to the base temperature rising within the cryocooler over time. The effects of the temperature uncertainty are resolved through the calibration gases which build a frequency axis in Figure 3.16. Once the frequency axis has been found, a full MeOH study is shown spanning the full tuning range of the QCL. When observing the MeOH spectrum of the full tuning range compared to the JPL catalogue, peaks are observed which are not catalogued. A possibility for these peaks was discussed is the possibility of isotopes altering the atomic mass and an example of this is ¹³C which has an additional neutron. The low amplitude absorptions can be probed further using a long path length cell which may find additional low amplitude peaks, this will be discussed further in Chapter 4.

The sensitivity of the system using a glass gas cell with 2.78×10^{-3} m³ volume was shown using MeOH spectra by filling the gas cell with 2 Torr of sample and pumping the sample out until the peak was not visible above the noise floor. This test was done with D₂O but the absorption was visible in Mode 1 which is the lowest optical power and the amplitude of the absorption saturated the signal. The scroll pump limited the experiment as D₂O was still observable at the ultimate pressure of the scroll pump. A 1:1 mixture of D₂O and MeOH has been sampled at 0.5 Torr to examine an H/D exchange. Although the reaction has many products, they are reversible reactions which are constantly happening and a concentration of MeOD was observed. Still, some peaks could be attributed to residual D₂O or MeOH. Static MeOD was sampled to confirm that the new peaks observed in the mixture resulted from the H/D exchange reaction. Static MeOD data was an important part of the work as MeOD has no catalogued data in the 3.35 THz region. This data has contributed to two publications by Michael Horbury a IRMMW-THz 2023 presentation [133] and a publication currently being written on the gas spectroscopy results using a TeraFET array.

The improved modulation bandwidth of the TeraFET detectors has allowed time-resolved measurements using the 3.4 THz QCL. The first experiments used a 1:1 mix of MeOH and D₂O where the detector signal was sampled in an attempt to observe a H/D exchange by monitoring the change in amplitude of a MeOH absorption as the D₂O was introduced into the gas cell. The change in amplitude was below the noise floor and resulted in no observable concentration change in the MeOH. As an alternative, the gas cell was purged and then a

MeOH sample was let into the gas cell analogous to a first-order reaction where the rate is dependent on one species. This proof of concept was used to show the potential use of this system in time-resolved applications and the half-life of the MeOH diffusing into the gas cell was 3067 milliseconds. The noise floor of the measurement limited the measurement, to observe an H/D exchange the absorption feature should be targeted where there is a larger change in concentration. As well as finding an alternate absorption line, the experiment should be repeated in sets and averaged to reduce the measurement noise. Improvements in the data acquisition could improve the time resolution by moving away from an NI DAQ board to a Zurich Instruments MLFI lock-in amplifier which has a 5 MHz bandwidth allowing the time-resolved data to benefit from a noise reduction through lock-in amplification.

Future work can improve the gas manifold to allow mixing without the risk of cross-contamination samples. Storing liquid samples and extracting the vapour works for safe and stable species. Still, this method must be improved and safe venting methods must be in place before anything harmful or unstable to the atmosphere can be studied. A dry air or nitrogen purge must be included and a pump with a lower ultimate pressure is needed as D₂O sensitivity is stronger than the ultimate pressure of the scroll pump. The cider analysis could continue with potential collaborations with the School of Food Science and Nutrition to explore the potential of using the spectrometer to examine more relevant species in food safety as an alternative to detecting MeOH concentrations.

Time-resolved measurements are possible when studying a chemical reaction which isn't limited by diffusion. The experiment could be excited by light or heat while a sample is inside the gas cell. Atomic oxygen is a species of interest in the THz region and a means of generating this should be developed before the QCL is swapped for a laser which can emit at 4.7 THz. Increasing the sensitivity of the system to observe molecules in lower concentrations can be done with multi-pass optics, the work on a multi-pass gas cell is shown in Chapter 4.

Chapter 4

Multi-Pass Cell

The project aims to develop a THz gas spectrometer which is capable of observing molecules in low concentrations. Fast and sensitive THz detectors will be needed to observe fast reactions such as generating atomic oxygen using a UV source. The amplitude of observed spectral features can be increased by increasing the optical path length through a sample to reduce the requirement for sensitive detectors. The Beer-Lambert law discussed in Chapter 3 shows that the absorption of a species increases with optical path length through a sample. When performing trace gas analysis or examining species with low absorption cross sections, the amplitude of the absorption feature is low. To target a trace gas, the optical path length can be increased to increase the absorption amplitude and make the spectral feature easier to detect.

This chapter discusses the theoretical background of two multi-pass cells, the White and Herriott, other multi-pass cell designs exist such as the Pfund cell but will not be discussed in this work. The operating principles for White and Herriott cells are discussed and the reasoning for building a Herriott cell is justified in this chapter. Ray tracing is the method used to simulate the Herriott mirror and used to practise aligning the complex optical system before physical alignment. The ray tracing software used was Zemax which is a commercial package offered by Ansys and uses non-sequential or sequential ray tracing. The methods of non-sequential and sequential ray tracing are compared in this chapter and models for each are shown. The entry optics for the Herriott cell and collection optics are also ray-traced and presented in a section within this chapter. The purge box for the multi-pass gas cell operates under a vacuum to lessen the pressure broadening of samples. The fabrication was a complex process which was a custom order from the vacuum component company Kurt J. Lesker.

This chapter's final section shows the alignment results with an optical laser. The optical alignment shows the path a THz beam will take across the optical bench and from the entry optics, through the Herriott cell to the exit optics and detector. The final section of this chapter summarises future work for the multi-pass gas cell work.

4.1 White Cell Background

A White Cell is named after the creator J. White who published the work in 1942 describing a multi-pass cell using three concave mirrors. The White cell operates by having two mirrors oriented towards a larger mirror. The beam for a White cell enters from the side of the optics allowing light to enter from the side of the cell rather than from the optical axis of the gas cell [134].

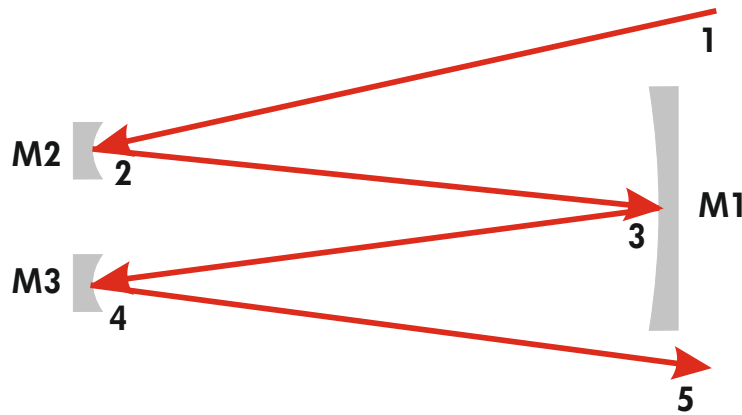


Figure 4.1: Diagram of a White cell. The beam enters at point 1, reflects off M2 and exits at point 5 after being reflected off M3.

The alignment of a White cell depends on the separation of mirrors and is only sensitive to angle adjustments on the horizontal plane in mirrors M2 and M3. The arrangement of a White cell limits the number of reflections inside the cell to multiples of 4. Figure 4.1 shows the arrangement of a White cell where a collimated beam is directed into the cell (1) and reflects off M2 (2). The reflected beam hits the larger M1 mirror (3) and is reflected to the second smaller mirror M3 (4) before being directed out of the White cell (5) where the beam converges as it exits. The White cell has been used in multi-pass THz gas sensing to detect greenhouse gasses at an optical path length of 20 m [135]. The White cell has the disadvantage of needing three mirrors of the same focal length and complex mirror mounts to reduce drift over the typical long-time alignment a multi-pass gas cell sees. The White Cell is sensitive to long-term drift where misalignment of an objective mirror in the system leads to a large displacement at the detector port of the White cell. If a system is sensitive to misalignment, such as a small detector or long optical path after the multi-pass cell, thermo-mechanical stabilisation in the White cell is needed to prevent losing the optical signal [136].

4.2 Herriott Cell Background

A Herriott cell is an optical cavity which can be used as an optical delay line which can introduce large optical delays without the need for a large distance between mirrors. The Herriott cell is also used in cavity lengthening for mode-locked lasers, or path length extension for gas spectroscopy. In this work, a Herriott cell was fabricated for long optical path length gas spectroscopy.

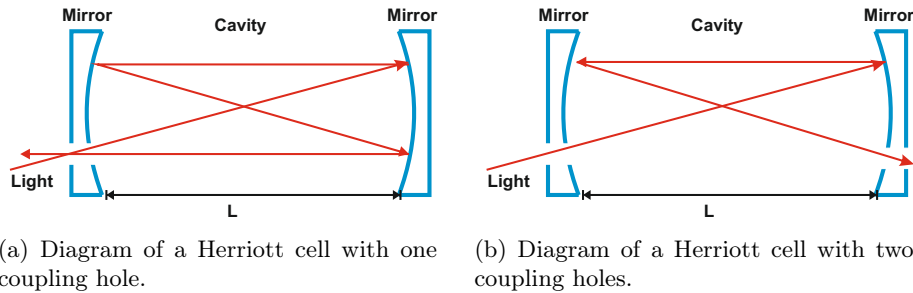


Figure 4.2: Two Herriott cell designs which maintain the optical axis.

Figure 4.2 shows two diagrams of the side view of a Herriott cell. The circular pattern of a Herriott cell allows radiation to be injected into the cavity along the optical axis and then collected from the same coupling hole. Alternate designs use two coupling holes on both mirrors, allowing the radiation to be injected into one mirror and collected from the opposite mirror, this allows the radiation to continue in the same direction along the optical axis.

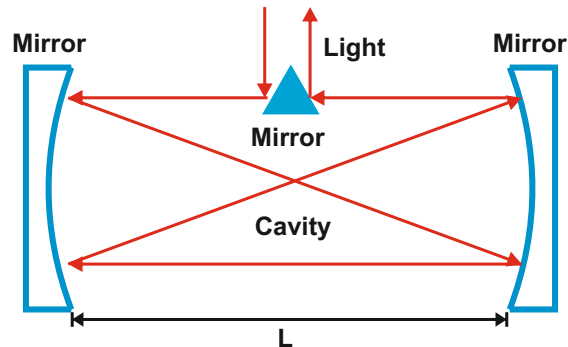


Figure 4.3: Drawing of a Herriott cell with an addition optic to couple radiation into the side.

Coupling into the Herriott cell is not restricted to the optical axis, alternate coupling schemes use optics to pick off the radiation within the cell and can direct the radiation out of the sides of the optical cavity. Figure 4.3 shows an

example of an alternate coupling design which uses a mirror to direct radiation 90 degrees from the Herriott cell axis.

4.2.1 Herriott Cell Theory

The first Herriott cell was reported by D. Herriott in 1964, reporting on spherical interferometry using two spherical mirrors of focal length (f) spaced at distances close to $d = 2f$. The two mirrors form an optical cavity where light is reflected and focused between consecutive passes in the cavity, conditioning the beam and allowing long optical path lengths within the cavity. This can be modelled as a series of equally spaced thin lenses at distance d where the centre of a lens represents a reflection off of a mirror and the light is repeatedly refocused [137].

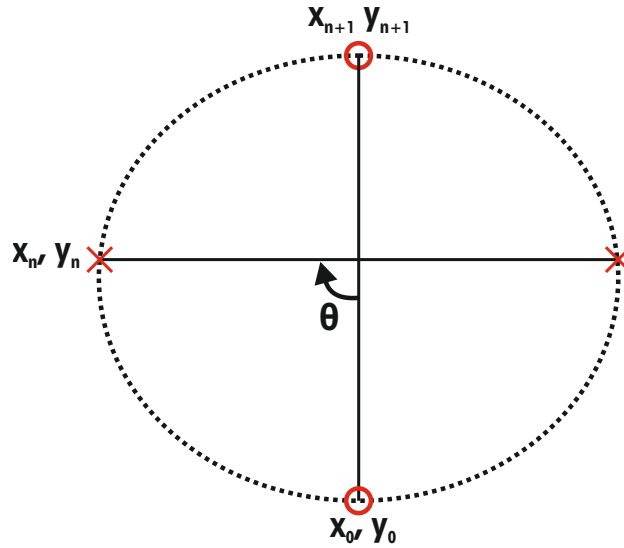


Figure 4.4: Drawing of four passes between the two mirrors on one plane. X represents spots on the far mirror and O represents spots on the near mirror.

The Herriott cell used in this work has one mirror with an off-axis hole where the THz can be injected and collected from the cavity, designs also exist where a separate entry and exit port are on both mirrors. When describing the Herriott mirrors, the front mirror is the optic with the coupling hole and the rear mirror is the opposite optic with no coupling hole. The entry port has the coordinates (x_0, y_0) and rays entering through this port have an initial position (x_0, y_0) and directions (x'_0, y'_0) . When the mirrors have identical focal lengths, the rays reflect in an elliptical pattern and exit the cavity after an even number of passes (N) with the coordinates (x_N, y_N) . Figure 4.4 shows a circular pattern on a vertical plane with 4 passes, each reflection rotates the rays 90 degrees along the vertical plane, odd numbers (X) indicate a reflection on the rear mirror and

even numbers (O) represent a reflection on the front mirror.

Astigmatic mirrors can be used to achieve cells with dense optical patterns but were not used in this work due to the added complexity and manufacturing requirements of designing such cells. The machining accuracy to fabricate astigmatic mirrors typically involves expensive diamond turning methods [138]. Herriott derived the following relationship for the coordinates of the n th reflection of rays in the Herriott cell as Equation 4.1 where a similar equation exists for the y coordinate.

$$x_n = x_0 \cdot \cos(n\theta) \sqrt{\frac{d}{4f-d}} (x_0 + 2fx'_0) \cdot \sin(\theta) \quad (4.1)$$

θ is the rotation rays make along the vertical plane between reflections, n is the n th reflection, d is the mirror separation and f is the focal length of the mirrors. The relationship between θ and mirror separation can be expressed as 4.2.

$$\cos(\theta) = 1 - \left(\frac{d}{2f}\right) \quad (4.2)$$

The closing condition is a condition when applied to the Herriott pattern results in rays making M circulations of the optical axis in N passes and the coordinates of the entrance being equal to the coordinates of the exit ($x_N = x_0$), ($y_N = y_0$). The pattern can be seen to repeat from 4.2, so to express the closing condition, constraints are set to d and θ so that $f \leq d \leq 2f$ and $\frac{\pi}{3} \leq \theta \leq \frac{\pi}{2}$ sets the mirror separation between the range of 1 to 2 focal lengths. The closure condition then gives $N = 2(2M + 1)$. θ from the closure conditions can now be expressed as Equation 4.3.

$$\theta = \frac{2M\pi}{N} = \frac{N-2}{2N} \cdot \pi \quad (4.3)$$

The distances of mirror separation which satisfy the closure condition are given in Equation 4.4 [137] [139].

$$d_n = 2f \cdot \left(1 - \frac{N-2}{2N} \cdot \pi\right) \quad (4.4)$$

Rays exiting the cell have an angle (x'_{N-1}, y'_{N-1}) which is not disturbed while changing the separation of the mirrors in the cell. The exit angle is translated from (x'_0, y'_0) and not from mirror separation as shown in Equation 4.5, which is derived from the thin lens approximation [140].

$$x'_{N-1} = \frac{x_0}{f} + x'_0 \quad (4.5)$$

To effectively use the mirror space the spot pattern needs to be circular, if the spherical mirrors are pointed directly at each other the pattern will be elliptical. Tilting the mirrors off-axis changes the shape of the ellipse on the mirrors, this tilt can also be used to correct manufacturing defects between the two mirrors as machining inaccuracies lead to non-circular patterns.

4.2.2 Optical Interference Fringes

Light injected into a multi-pass cell will reflect between the optics with a distance of L . The mirror surface roughness will result in a scattering of rays at each reflection and these scattered rays will now reflect between the mirrors and reach the detector with an optical path length ΔL . When the scattered rays and input rays interact or when the scattered rays are collected and focused on a detector with a delay of $L - \Delta L$, constructive and destructive interference appears analogous to an interferometer. These unintentional Fabry-Perot interference fringes limit the sensitivity of measurements and can be hard to filter in post-processing due to their periodic sinusoidal shape in the signal background. The interference fringes become a larger problem the shorter a multi-pass cell is and are present in cells 1m in length and below. The interference patterns tend to be too unstable to successfully eliminate and stable enough to persist through averaging [141].

A method to reduce the optical interference fringes is through frequency and amplitude modulation of a laser source. Modulating the bias of a laser can reduce the interference fringes, or in continuous wave operation applying jitter to a Herriott mirror targeting the width of an interference fringe can improve the SNR through lock-in amplification of the jitter [142]. Interference fringes are more prevalent in White cells but still present in the Herriott multi-pass cell. The spacing of beams has a large contribution to interference fringes, as when a reflection occurs, scattered light acts as a cone reflecting from the spot and interacts with neighbouring reflections. The largest contribution of interference fringes within the Herriott cell comes from the spots neighbouring the off-axis coupling hole, where scattered light exits and is collected by the coupling optics and focused on the detector.

The optical interference fringes can be reduced by selecting mirror separations which reduce the spot size of reflections on the mirror neighbouring the coupling hole. In particular, narrow interference fringes are found under the condition $N = 4M \pm 4$. The following derivation is taken from McManus which shows what combination of orbits and passes should be selected to narrow interference fringes within a Herriott cell [143].

Each reflection within the cell is represented by J and angular coordinate ψ , where J is the number of the reflection, during the input ($J = 0$) and the output ($J = N$) at ($\psi = 0$). With each reflection, the angular coordinate changes by θ described by Equation 4.2. The mirror separation is near the condition $d = R$ resulting in θ being close to $\frac{\pi}{2}$ and $\cos(\theta)$ having a small value. Under these conditions, θ is constrained to the exit condition where the number of orbits M related to the number of passes N is given in Equation 4.6.

$$N\theta_R = \pm 2\pi M \tag{4.6}$$

For combinations of M and N , the angular position ψ is given by a modular equation $\psi_J = (J\theta)_{mod 2\pi}$ which constrains the angle within one rotation of the vertical plane. An alternative angular variable is defined as $\phi = \theta_R - \frac{\pi}{2}$ and

remembering that the mirror separation has $\theta \approx \frac{\pi}{2}$ we get a small ϕ . Using the new angular variable the re-entrant condition is given as Equation 4.7.

$$\phi = 2\pi\left(\frac{M}{N} - \frac{1}{4}\right) = \sin^{-1}\left(\frac{d}{R} - 1\right) \approx \frac{d}{R} - 1 \quad (4.7)$$

Equation 4.7 shows that the angular variable is about equal to the mirror separation from confocal spacing normalised by R. The combination of re-entrant conditions which give a small ϕ can be expressed in a family of (N, M) values given in Equation 4.8 where K is a small even integer.

$$N = 4M \pm K \quad (4.8)$$

McManus found through experimental work that by setting $K = 4$ to the relationship 4.8, the neighbouring spots to the coupling hole will have minimal spot sizes.

4.2.3 Cavity Enhanced Techniques

Absorption spectroscopy is limited by fluctuations in the source (I_0) and when the sample has low absorption features as in trace gas analysis, extending the path length is a simple solution to reduce the limitation of fluctuations in I_0 and low absorption coefficients in an experiment. Another method to reduce the noise and overall sensitivity of a measurement is to remove the dependence on source stability in shot-to-shot measurements. Cavity Ring Down Spectroscopy (CRDS) is a spectroscopic method which uses cavity-enhanced techniques to not only increase the optical path length into the range of kilometres but also reduce the dependence on I_0 stability by measuring light decay rather than laser amplitude. The principle of CRDS builds upon the multi-pass cells Herriott cell and replaces the mirrors with highly reflective mirrors ($R \geq 99.99\%$) forming a resonant cavity [144]. Light is coupled into the cavity and tunes to the dominant optical mode, the light will then reflect with minimal mirror losses within the cavity. In the cavity the light decays per the Beer-Lambert law.

$$k = (1 - R)\frac{c}{L} \quad (4.9)$$

The first use of the ring-down method was a means to test the reflectivity of a mirror, by injecting a pulse into a cavity formed of two highly reflective mirrors the decay could be measured as in Equation 4.9 where R is the reflectivity, L is the mirror separation and c is the speed of light, the inverse of the exponential decay rate (k) is the ring-down time and τ is the average time a photon lasts inside the cavity. If a gaseous sample is placed within this cavity then the absorption contributes to the optical decay (k) and the absorption coefficient can be extracted by sampling the exponential decay of light. This measurement system detects the decay of light and not the incident radiation, removing the dependence on shot-to-shot variation found in laser absorption spectroscopy. A simple CRDS spectrometer is shown in Figure 4.5, the optical setup is very similar to a direct absorption gas spectrometer and would have minor alterations

to an existing system [145] [146]. The main limitation of a CRDS system is finding suitable materials for an optical cavity, with such a high requirement of reflectivity ($R \geq 99.99\%$) fabricating such a cavity at long wavelengths found in the THz region is a difficult task. A THz spectrometer using CRDS has been reported in literature using a multiplier circuit radiation source operating at 600 GHz and a corrugated waveguide between the photonic mirrors as the cavity and showed a limit of quantification of 3 parts per billion in mixed samples. This device probed a weak N_2O line which is catalogued to be centred on 622.579 GHz with a line intensity of $6.58 \times 10^{-27} \text{cm}^{-1}/(\text{molecule cm}^{-2})$. The experimental result measured a line intensity of $6.69 \times 10^{-27} \text{cm}^{-1}/(\text{molecule cm}^{-2})$. This system used a Schottky detector and used 10^5 averages to obtain the signal [147].

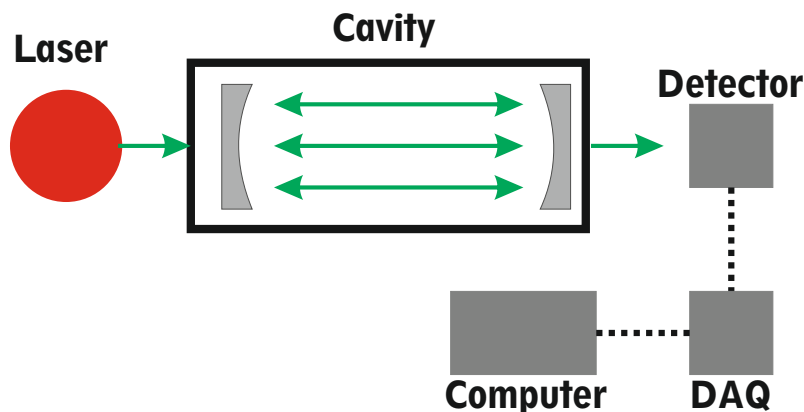


Figure 4.5: Drawing of a simple CRDS system.

4.3 Ray Tracing

Ray tracing is a mathematical method of describing light passing through an optical system such as a series of lenses and non-spherical optical components such as gratings or Fresnel lenses. Ray tracing is designed for computer simulation and tackles the trigonometric functions encountered in optic design by converting the functions into algebraic form. The ray tracing in this work was done on Zemax which can be used for sequential and non-sequential ray tracing.

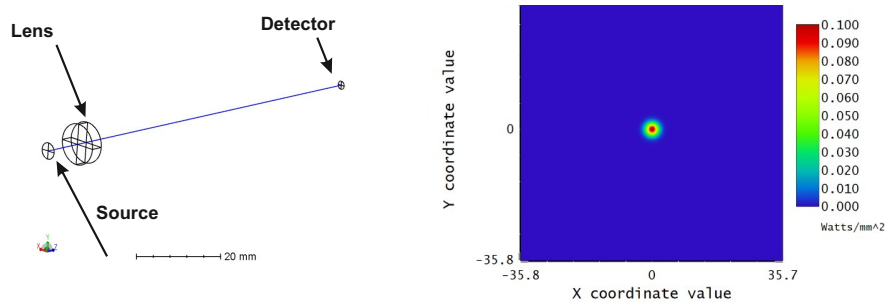
4.3.1 Sequential Ray Tracing

Ray tracing can be split into sequential or non-sequential ray tracing. Sequential ray tracing operates by defining a bundle of rays at a beginning point and image plane. Each interaction the bundle of rays make is defined in sequential order through the optical simulation. The ray tracing handles simulating optics by describing each ray as a set of 3D coordinates $\vec{X}_0, \vec{Y}_0, \vec{Z}_0$ with directional

cosines $\bar{k}, \bar{l}, \bar{m}$ to describe a location and direction of travel. Rays originate from a point \bar{P}_0 through a reference coordinate system $\bar{X}, \bar{Y}, \bar{Z}$ with an origin \bar{O} . Simulation parameters are set globally such as wavelength and units of measurement.

When a surface is defined inside the simulation, the material properties, thickness and geometry are defined. Depending on the properties of the surface, a function S is generated which describes the interaction. When an interaction occurs between surface and ray, the positional coordinates $\bar{X}_0, \bar{Y}_0, \bar{Z}_0$ and direction cosines $\bar{k}, \bar{l}, \bar{m}$ are transformed into the reference coordinate system $\bar{X}, \bar{Y}, \bar{Z}$ and the appropriate function is applied to the rays depending on the material properties and ray wavelength. After the interaction, the new directional cosines and 3D coordinates are converted back into the positional coordinates $\bar{X}_0, \bar{Y}_0, \bar{Z}_0$ and $\bar{k}, \bar{l}, \bar{m}$ before the rays continue to the next surface in the simulation [148].

Geometric ray tracing shows the path rays take through an optical system and can be used to model imaging and illumination systems, but this is not the full description of light in a system. As a wavefront travelling through a system, it can coherently interfere with itself, Physical Optics Propagation (POP) is a method available in the sequential mode which takes more computational power but accurately simulates this coherent interaction. POP enables modelling beyond geometric ray tracing such as single or multi-mode fibre coupling and laser simulations through complex materials including M^2 calculations. Another benefit of using POP is the file format ZBF which is a wavefront, a ZBF is saved at the beam launch and on each surface throughout the system. A ZBF file can be imported from existing data such as simulated or experimental data and propagated through a sequential model within Zemax. Figure 4.6a shows 3D wireframe of a simple simulation of rays (blue) being laser being launched from the left and passing through a lens before hitting a detector on the right. Figure 4.6b shows a heatmap from the detector in the POP simulation.



(a) 3D Layout of a lens simulation.

(b) Simulated laser power in POP.

Figure 4.6: An example of sequential ray tracing in Zemax. An optical laser is defined in POP launched through a lens (Left) and focused on a detector (Right).

4.3.2 Non-Sequential Ray Tracing

When discussing ray tracing in a sequential method as in Section 4.3.1, a problem arises when modelling unknown light interactions and multi-pass optics. If the Herriott cell was modelled in sequential mode, each reflection would need to be modelled as a series of OAP mirrors or a paraxial lens approximation. Modelling that involves illumination systems, splitting rays or scattered rays can be accomplished in Zemax using non-sequential mode. In non-sequential modelling, rays are launched from a source and left to propagate through a 3D model and interact with surfaces. Rays cannot be observed within a non-sequential surface unless they hit a detector surface, unlike POP where every interaction is stored in a ZBF file. An example of non-sequential ray tracing is shown in Figure 4.7 which is a screenshot of a Herriott cell simulation taken at the beginning of this project.

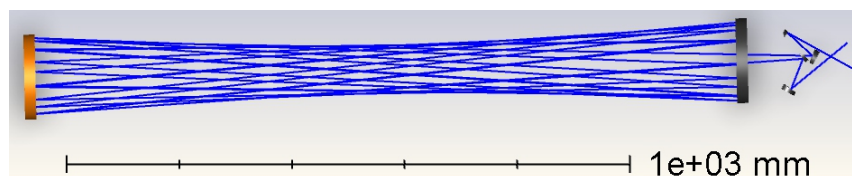
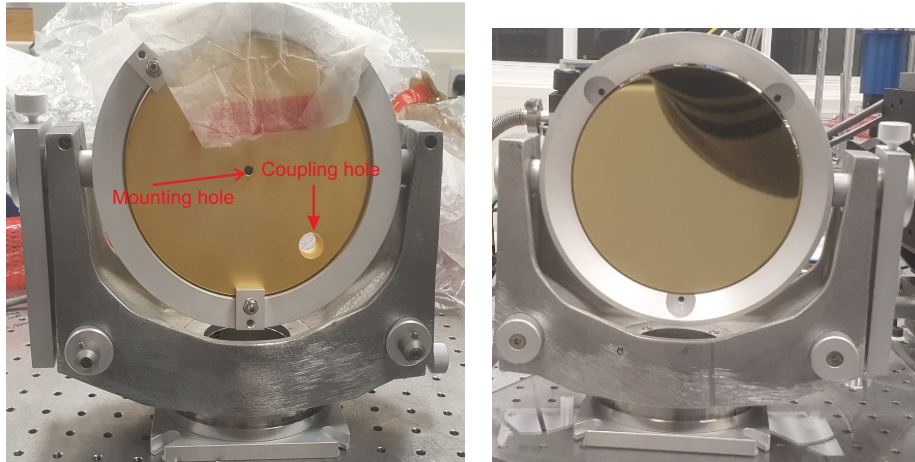


Figure 4.7: Non-sequential simulation of the Herriott mirrors.

Non-sequential modelling can be combined with sequential for mixed-mode where a 3D non-sequential space can be added as a component within a sequential system. The simulation begins as a sequential system where the rays are defined at the object and propagated through a system, the non-sequential space is defined as an entry and exit port for the sequential rays to couple into. Within the non-sequential system, the rays are converted into Non-Sequential Component (NSC) rays and propagated through the optics before being converted back to sequential rays upon passing through the exit port. When simulating the alignment of the Herriott cell, non-sequential ray tracing was used with CAD files from optics catalogues and custom files for the Herriott mirrors. Mixed-mode models were used to simulate a wavefront passing through the Herriott cell using POP. The radiation source for the mixed mode simulations was taken from experimental beam profiles which were converted into ZBF files using Python, the beam profile was then launched into the system as a collimated source.

4.4 Herriott Mirrors

The main optical component of the Herriott cell is the mirrors, in the THz region, protected gold mirrors are commonly used for reflection systems. The mirrors used in this work are gold mirrors which were provided by Rutherford Appleton Laboratory (RAL) which was previously used in work on multi-pass THz optics.



(a) Front Herriott mirror with coupling hole.

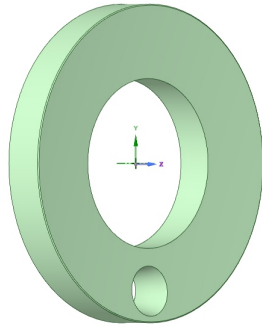
(b) Rear Herriott mirror.

Figure 4.8: Pictures of the Herriott mirrors loaned from RAL in mounts.

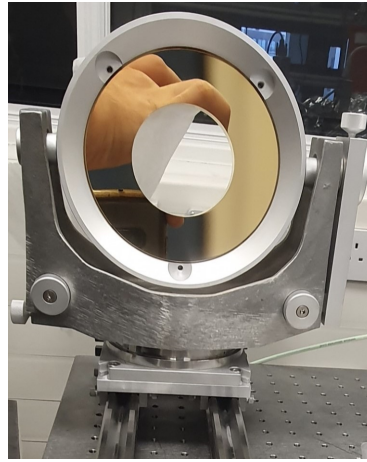
Figure 4.8 Shows the Herriott mirrors provided by Dr Neil Macleod of RAL, these have a 500 mm focal length and 150 mm diameter with a 60 mm off-axis conical coupling hole which is 12 mm to 16 mm in diameter. These mirrors were fabricated in 2009 by Laser Beam Products LTD and were aligned with a visible laser as a proof of concept for a Herriott cell using a THz QCL source. The focal length of 500 mm is chosen for convenience, giving the parabolic mirror's radius of curvature at 1 m and under the condition $\theta \approx \frac{\pi}{2}$, the distance to radius of curvature should be equal, giving a mirror separation of 1-metre. Aligning the mirrors with $d = R = 1$ m fulfils the condition of Equation 4.8 where $K = 4$.

Future improvements for the Herriott cell are to use a UV source to pump and THz to probe photolysis experiments. The pattern of the Herriott cell will not use the whole surface of the mirror unlike the dense patterns seen in astigmatic mirrors. The multi-pass mirrors are mounted in Newport SL-A 15ABHC gimbal mirror mounts which can be coarsely adjusted by hand and finely adjusted using an Allen key locking adjustment.

The circular pattern of a Herriott cell leaves the centre of the mirrors unused, so the mirrors were redesigned to resemble an annulus where an 80 mm radius cut is taken from the mirror centre. The coupling hole was also increased from 19.6 mm to 23.5 in diameter to accommodate larger beams to be coupled into the Herriott cell. The width of the new mirror surface is now 35 mm.



(a) CAD model of the front mirror.



(b) Picture of the rear Herriott mirror.

Figure 4.9: A CAD design and photo of the redesigned Herriott mirrors.

Figure 4.9a shows the CAD model of the front mirror compared to a picture of the mounted rear mirror. Figure 4.9b shows the rear Herriott mirror mounted to an optical table, the redesigned Herriott mirrors were fabricated by Laser Beam Products LTD in 2021. The Herriott mirrors were designed in SpaceClaim which is a CAD software package offered by Ansys, this software was chosen over the more popular CAD software Solidworks because licenses are available in the Schools of Engineering. A 3D model of the new mirror design along with the drawings from the mirrors fabricated in 2009 was sent for fabrication.

4.4.1 Entry Optics

The THz optical path runs the length of an optical table, with room for a 1-metre gas cell and long path interferometer utilising a 600-millimetre linear stage. To accommodate the multi-pass gas cell and entry optics, a new optical path running in parallel to the interferometer arm needs to be installed.

Figure 4.10 shows the optical path taken by THz radiation passing from the QCL through the Herriott cell by use of a sliding mirror which would enable users to quickly switch between operating modes. A sliding mirror will drift over time when it is repeatedly moved in and out of the beam path and increases the chance of misalignment due to knocking the optic. To correct any issues of mirror drift, irises are placed within the multi-pass arm of the system so users can align a colinear IR beam to a target.

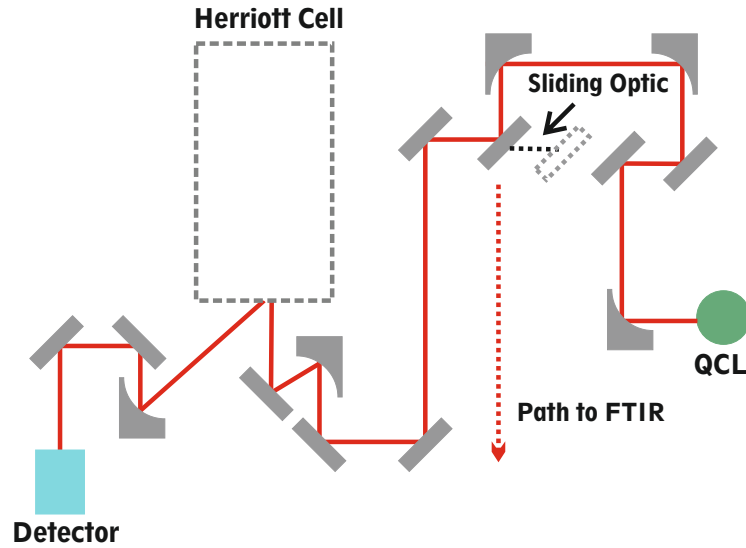


Figure 4.10: Optical layout of the proposed THz path for multi-pass spectroscopy.

Light coupled into the Herriott cell must be focused into the middle to match the focus of the spherical mirror. Large transmission losses in the THz region lead to mostly reflective optical systems, so to remove the transmission losses associated with THz lenses, a long focal length OAP was used to couple light in and collect THz from the cell. When light exits the coupling hole, it expands and should be collected immediately to reduce losses. The OAPs used in the coupling optics are commercial mirrors from Edmund Optics which have a 15-degree offset and an effective focal length of 646 mm. These mirrors were selected for convenience as they were available from the catalogue and had a focal length of over 500 mm. These mirrors give space to position the optics outside of the Herriott cell without the need for a custom-manufacture order.

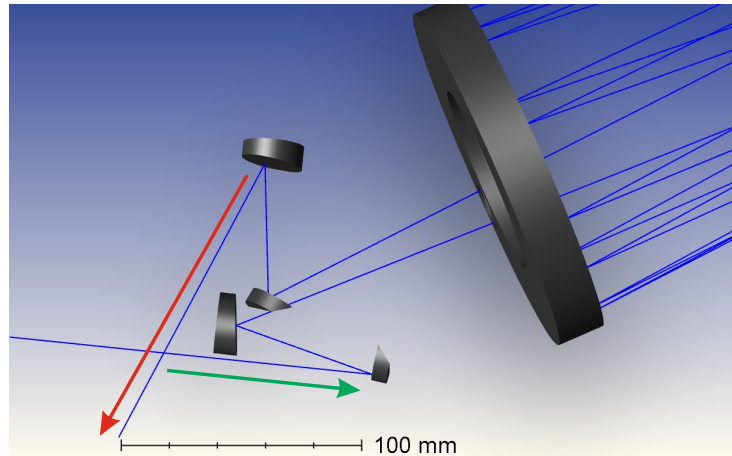


Figure 4.11: Zemax simulation of the first coupling optic design.

Figure 4.11 shows a non-sequential ray trace of the coupling optic design directing rays into the Herriott cell using CAD models of mirrors from the Edmund Optics catalogue. The red arrows show the direction of travel for rays exiting the cell on the left and the green arrows show the rays entering the cell on the right. This design used two D-shaped mirrors to direct a pilot beam through the multi-pass optics. This model showed that the OAP placed 146 mm away from the back of the front Herriott mirror can direct light through the coupling hole and to the rear mirror.

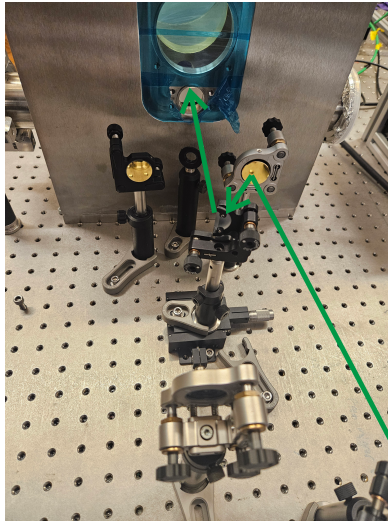
The optical design in Figure 4.11 was first used for simulations but this design proved to have two main issues: one was an increased sensitivity to alignment errors and the other was the overlapping beams. The first optical design was only used in geometric ray tracing and no simulations were run from the model.



Figure 4.12: Zemax simulation of the final optical design.

Figure 4.12 shows the final optical design which was used in the physical system and for the simulations used throughout this work. As a result of this simulation, the final design of the entry optics was changed from Figure 4.11 to the physical design in Figure 4.13, so that rays enter normal to the coupling hole of the front mirror. The orientation of the optics in Figure 4.12 gave a higher tolerance to drift than in the previous design shown.

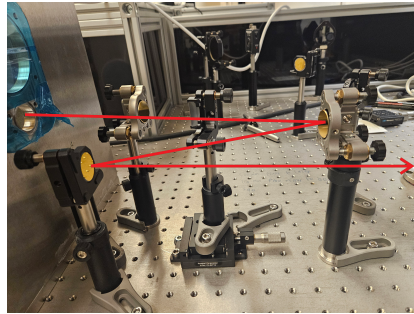
Figure 4.13 shows the final design, the entry optic has been rotated so the OAP faces the optical axis of the Herriott cell. Both entry and OAP mirrors are mounted in low drift mirror mounts to reduce the frequency of entry optic realignment. The collection optic was swapped from a D mirror seen in Figure 4.11 to have the larger mirror surface to collect the expanding rays. The entry optic was also changed from an OAP to a D mirror to reduce any stray light that might get coupled back into the cell. The collection optic is a 1-inch planar mirror rather than the D-shaped mirror seen in Figure 4.11, to ensure all of the expanding exit beam is collected. A HeNe laser was used to align the entry and collection optics before the Herriott mirrors. Blue film seen in Figure 4.13a has been fixed to the coupling holes to protect the O-ring grooves from dust. Figure 4.13b is a picture of the aiming mirrors before the Herriott cell, these mirrors were not included in the ray tracing simulations. Figure 4.13c shows the collection optics for the Herriott cell, these mirrors will focus the beam onto the detector after the light has passed through the gas cell.



(a) Entry optics for the Herriott cell.



(b) Aiming mirrors before the entry optics.



(c) The collection optics for Herriott cell.

Figure 4.13: Pictures of the optical path through the entry and exit optics.

4.4.2 Herriott Cell Simulation

A POP simulation includes the ability to define a beam file using experimental data and in Subsection 2.2.1 beam profiles were taken experimentally from the 3.4 THz QCL.

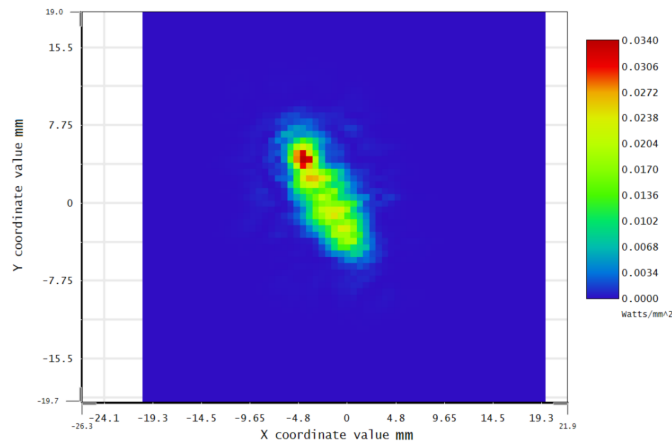
Converting a beam profile to a ZBF format is a multi-step process. After obtaining a beam profile, it is converted from a colourmap plot to a PNG file with 8-bit colour. The exported 8-bit colour PNG should be saved at a 1:1 aspect ratio and the graph and page sizes should be manually changed to represent the beam size accurately. In addition to this, the file dimensions (in pixels) must be a power of 2. This requirement is for the conversion which is done in Python

using the Python Zemax Dynamic Data Exchange (PYZDE) library which is under an MIT license. The PYZDE has many functions for handling Zemax data and the one used in this work is WriteBeamFile which is intended for use with cameras within an optical system. The function overlays a grid and takes each square as an intensity within the beam profile, then writes a ZBF file. This Python script converted the beam profile in Figure 2.10 and used it as a source in the POP ray trace.

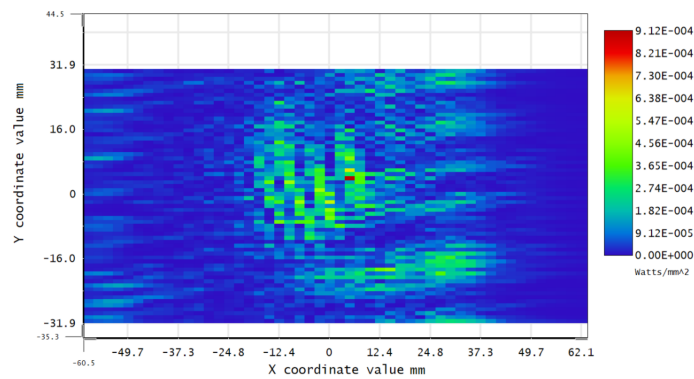
To take advantage of POP, a mixed-mode simulation was made where the beam profile is launched in sequential mode and propagated through the coupling optics before being directed into a non-sequential entry port. Inside the NSC space, the rays are reflected through the Herriott cell and directed through an exit port. The sequential space after exiting the Herriott cell focuses the rays onto a detector 646 mm along the optical axis from a collecting OAP. The optical path of the simulation can be seen in Figure 4.12 where the rays entering the simulation are indicated by a green arrow and the exiting rays are red. The rays exiting the simulation are in sequential mode and are left to reflect in an arbitrary direction from the OAP to a detector as they will not interact with any previous components.

This mixed-mode system will have some errors in representing the Herriott cell as POP cannot operate in non-sequential ray tracing, but this simulation method gives the best indication of what the QCL beam passing through the optics would look like.

The first optical simulations were done in non-sequential mode using CAD models taken from the Edmund Optics catalogue and the 3D model used for the fabrication of the Herriott mirrors. The model used can be seen in Figure 4.7 where there are 24 passes and 7 orbits within the gas cell.



(a) The rays launched.



(b) The rays on the detector.

Figure 4.14: The ZBF from the Herriott cell POP simulation.

The input rays were taken from experimental beam profiles and set to have a total peak power of 1 W for simplicity, the wavelength is $88 \mu\text{m}$ which is approximately 3.4 THz. For mirror surfaces the material selected is the material Mirror which is a reflective surface and the coating was set to be gold, this reflection mode assumes there is an infinite thickness gold coating on the mirror surface. The rays launched in Figure 4.14a is a 64×64 pixel image, giving an approximately 40×40 mm total wavefront in the ZBF file. After passing through the system, rays are focused on a detector which is shown in 4.14b.

The beam pattern appears to have failed to accurately trace as it is pixellated and distorted; this effect is due to improper sampling within the NSC part of the simulation. Although the geometric ray trace seems to have failed, Zemax can interpolate the data to better represent the beam pattern. Figure 4.15 shows the interpolated optical power out in this simulation, which was 44% of the input and can indicate what will be coming out of the physical Herriott cell.

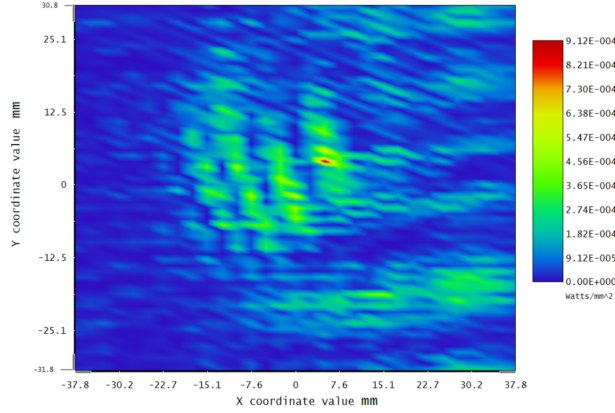


Figure 4.15: Interpolated ray trace of the Herriott cell.

The beam can be expected to have no central spot and have at most 44% of the input optical power. A detector with large collection optics will be required to collect as much of the light as possible, such as a bolometer with large sensitivity and large aperture or a TeraFET using a large coupling optic such as a Winston cone. This simulation shows the important role of a high beam quality and sensitive detector when using multi-pass optics, as the non-Gaussian shape of the QCL emission has heavily distorted the wavefront.

4.4.3 Performance Improvement

The minimum MeOH calculation used in Subsection 3.3.3 can be used with the simulated Herriott cell performance from Subsection 4.4.2 to give an estimated detector signal from the Herriott cell. For this analysis, the operating parameters in Subsection 3.3.3 are used to target the same MeOH peak spanning 650 to 700 mA. Using M^2 in the Y direction, the Gaussian component for the beam profile is $P = 3.45$ mW which is the optical power assumed to couple into the Herriott cell, this is further reduced as a simulated 56% of the coupled radiation is expected to be lost. The total power expected to couple into the detector becomes 1.518 mW. Using a gate voltage of 0.55 V, the responsivity is $R = 3.7$ V/W and the detector signal would be $V_{detector} = 5.62$ mV.

$$V_{Signal} = 3.7 \times 1.52 \times 10^{-3} = 5.62mV \quad (4.10)$$

The minimum concentration of particles inside the gas cell can be calculated if the optical path in the Herriott cell is 95 cm using the expression:

$$c_{min} = \frac{3 \times NEP\sqrt{BW}}{P_0 \epsilon L} \quad (4.11)$$

The Herriott cell has a c_{min} at 95 cm is 8.53×10^8 particles/cm³ which is larger than the minimum of the glass gas cell which is 3.76×10^8 particles/cm³. If the optical path length was increased to the alignment distance of 4 m, c_{min} for the Herriott cell is now 2.03×10^8 particles/cm³. Although the optical losses are lower in the glass gas cell, the improvement in optical path length compensates for this loss and yields a lower minimum concentration. When the Herriott cell is first operated, the optical path length will be 4 m to characterise the system experimentally, before further passes are used for MeOH calibration and low-concentration measurements.

4.5 Purge Box

A purge box is important in optical labs for many reasons, one is creating a laser enclosure to protect lab workers from stray light. In the THz band, water is a strong absorber, so a dry nitrogen or dry air purge is needed to remove these atmospheric absorption features. When using the Herriott cell, the system be mounted inside of a purge box to reduce atmospheric absorptions as the THz passes through coupling optics and the Herriott cell itself will be purged. Because the gasses under test will be below atmospheric pressure, the Herriott purge box must be capable of withstanding atmospheric pressure as it is pumped below 1 Torr.

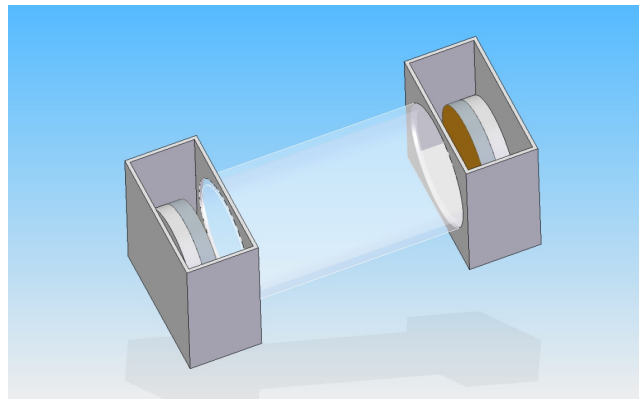


Figure 4.16: CAD drawing provided by Dr Neil Macleod from RAL.

The first design was from a concept supplied with the loaned mirrors from RAL which puts the mirrors inside the gas cell shown in Figure 4.16. As mentioned in Section 4.3, transmission losses in the THz region tend to be high and having the mirrors outside of a gas cell gives a high number of passes through THz windows resulting in high losses in a system where optical power is already expected to be low. This design assumes a static Herriott cell where the distance is set and unaltered. This can be improved upon with a removable centre section where adjusting the middle length will change the number of passes.

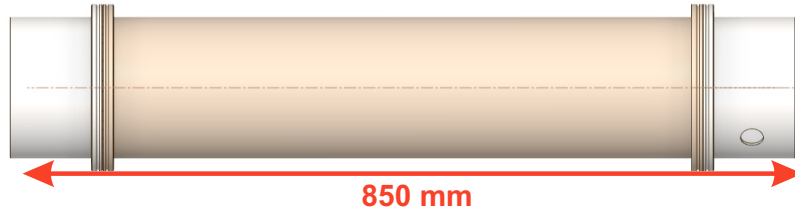
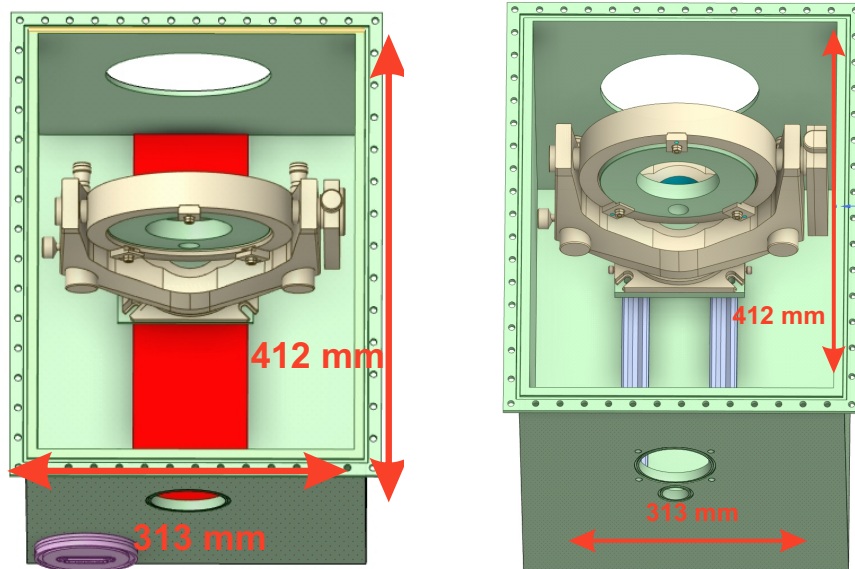


Figure 4.17: Middle of the multi-pass gas cell made from ISO-LF standard parts.

The centre of the multi-pass cell was the first part to be designed. The middle is designed to be interchangeable and consists of ISO-LF claw clamp fittings which can be welded to the purge boxes. The inner diameter is 160 mm which is 10 mm larger in diameter than the mirrors. A removable middle allows the centre to be changed in future work such as being altered in length, replacing the metal part with glass for using flash lamps, or including more advanced designs such as a T piece to inject a stream in the middle. The two half-nipples are 80 mm in length with a 690 mm full nipple connecting which is shown in Figure 4.17.

Figure 4.18a shows the first design of the purge box containing the rear mirror. The first design intended to have both mirrors on moving stages, one for coarse adjustment and then a Newport UTM vacuum-compatible stage for fine adjustments using an XPS motion controller. The vacuum-compatible stage would allow sub-mm resolution motion with the ability to keep the purge box under vacuum and remotely adjust the mirror. The XPS cable would need ISO-LF electrical feed-throughs to pass signals through the chamber walls. Both purge boxes have an 82 mm diameter cut for fitting UV windows with an O-ring groove 2.13 mm wide and 1.32 mm deep which fits 2.62 mm O-rings, this groove design was taken from the Parker O-ring guide [149].



(a) First design for the rear mirror purge box. Red represents the Newport stage.

(b) First design for the front mirror purge box.

Figure 4.18: The first CAD designs of the Herriott cell purge boxes.

The first design for the front purge box is shown in Figure 4.18b where the front mirror is mounted on a rail and carrier assembly for coarse adjustment. The dimensions for the purge boxes are shown in Figure 4.18, the height of both purge boxes is 368 mm. The gimbal mount is bolted using M6 bolts to an adapter plate raising the mirror's optical axis to match the rear mirror and connect both rail carriers. The carrier rail assembly is a Newport X26 four-sided rail which is vacuum-compatible, to ensure the carrier cannot slide off the rail the purge box has been sized slightly larger than the assembly. When using blind holes in a vacuum environment there should be a way for gas trapped by a bolt in a blind hole to vent and in the purge box design, there are no vents to

release the pressure so the rail feet must be fixed using vented bolts.

The only change made between the initial and final design of the middle section is a KF-25 bend has been added to the half-nipple to direct hoses and fittings away from the purge box. These half-nipples are 85 mm in length and fixed to the faces of the purge boxes. Figure 4.19 is a 3D model of the final half nipple design.

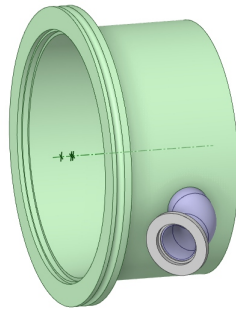
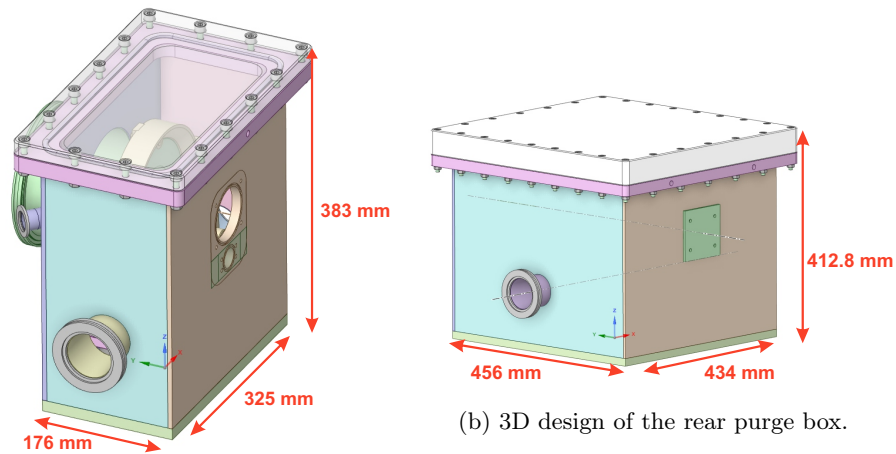


Figure 4.19: CAD model of the half nipple.



(a) 3D design of the front purge box.

(b) 3D design of the rear purge box.

Figure 4.20: The final CAD designs of the Herriott cell purge boxes.

Figure 4.20 shows the final design of the purge boxes by Kurt Lesker with the dimensions included in the figure. Figure 4.20a is the final CAD design for the front purge box containing a coupling port for the THz probe. The purge box is smaller than in Figure 4.18b as the mirror is static in this design, moving

the front mirror would reduce the input angle of THz radiation due to the possibility of the mirror being moved further away from the coupling port. The off-axis height for the THz beam is 173 mm and the optical axis for the mirrors and UV viewports is 233 mm. This optical height was set by the height of the mirrors inside of the purge box assembly, the optical axis for the Herriott cell should be above the height of the rest of the system as the beam is directed at an angle in both X and Y direction. The THz window will be 3 mm thick TPX, similar to the cryocooler window as it can withstand vacuum pressures and has low THz transmission losses. The lids for both purge boxes are thicker and were designed by Kurt Lesker during the manufacture. These lids are transparent acrylic, allowing visual inspection without removing the lids, which would be impossible if the lids were steel.

The rear mirror in the final design is the only mirror which can change the separation inside the Herriott cell. The UV port is blanked with a steel plate as this photolysis work will not occur during this project. The sides of the box have ISO-LF 63 claw clamp ports which are blanked, these blanked ports are designed to be an inlet for a purge and electrical feed-through should future designs need actuators.

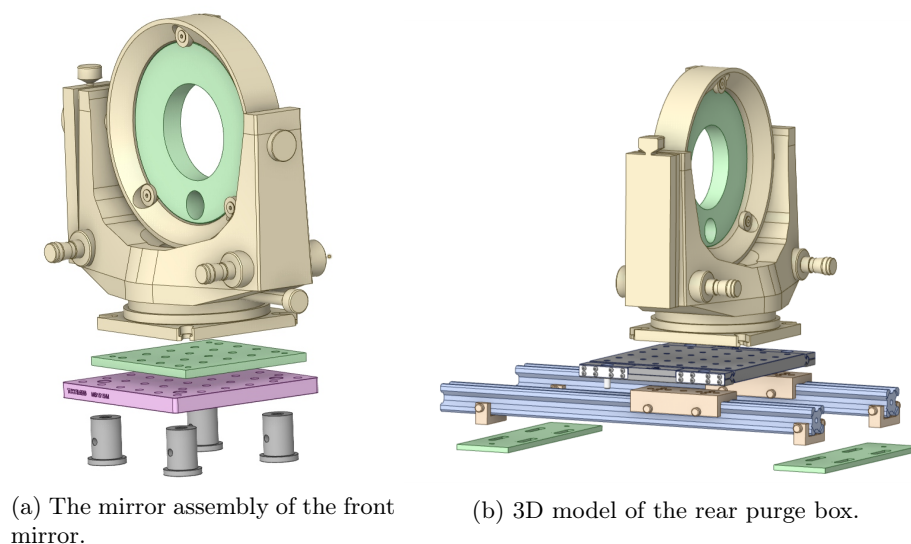


Figure 4.21: CAD models of the mirror assemblies.

The front mirror assembly is shown in Figure 4.21a mounted on an optical breadboard with four posts, these posts can be mounted by clamps or M6 grub screws into an optical table. The front purge box has four M6 blind holes for these posts to be fixed, the blind holes have no venting holes so vented M6 grub screws are used to prevent unwanted pressure build-up. The assembly has been designed to be built from the bottom up where users only have access from the

top due to the walls of the purge box.

The rear mirror combines coarse and fine adjustments to one carrier and rail system in the final design shown in Figure 4.21b. The carrier and rails are the Newport X26 rails and these are mounted on adapter plates which set the optical height to match the front mirror and fix the rail feet to the purge base of the purge box. Fine adjustment comes from the optical breadboard the mirror is mounted on, a Thorlabs TBB1515-M large-area translation stage. This translation stage has 60 mm of movement and is adjustable by a hex screw for fine adjustments, as well as having an Allen key lock.

The mirror assembly was designed to be mounted inside the purge box without access to the sides and is assembled in the following order:

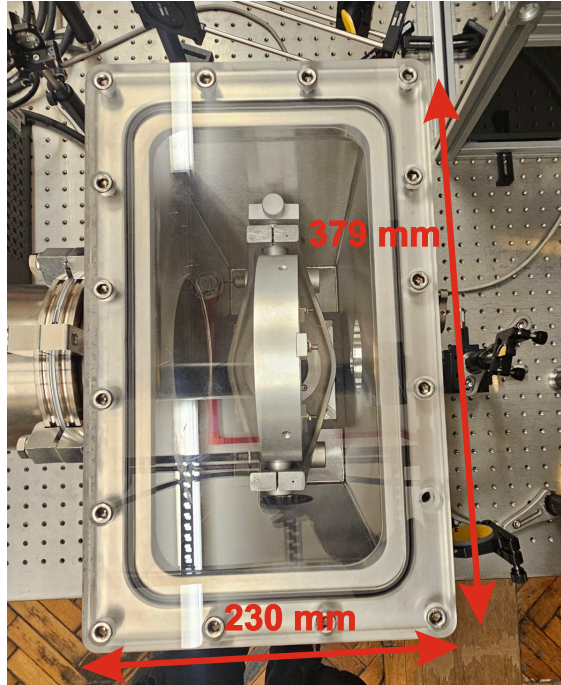
1. Screw the rail feet onto the adapter plate.
2. Keeping the orientation of the feet straight, slide the rails onto the feet and tighten the feet.
3. Slide the top carriers onto the opposite side of the rail to the feet.
4. Place the assembled rail and carriers into the purge box and fix them to the base of the purge box using vented M6 bolts.
5. Assemble the mirror and translation stage, then mount the stage to the rail carriers.

4.5.1 Purge Box Fabrication

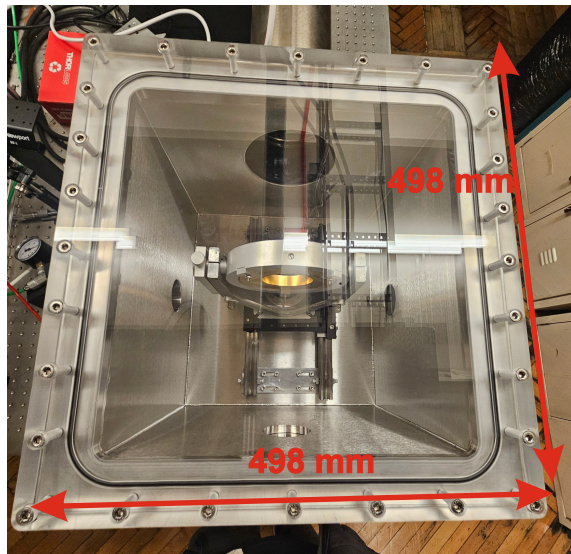
To house the mirrors under a vacuum, a steel purge box was designed to withstand the external pressure of a vacuum. The first CAD designs in Figures 4.18a and 4.18b were sent to Kurt Lesker as a concept to fabricate the Herriott cell and the designs were finalised and returned which are Figures 4.20b and 4.20a. The middle pipe is constructed with nickel-plated steel to reduce reactions occurring on the walls of the steel gas cell, as this area is where the higher concentrations of species will be present.

Figure 4.22a shows the front mirror mounted inside of the fabricated purge box. The coupling holes for THz radiation and larger UV hole are visible inside the purge box. This mirror is mounted on a small optical breadboard fixed to optical posts bolted to the floor. This box can be small as there is no need to move the front mirror.

The rear mirror mounted on a rail and carrier assembly is shown in Figure 4.22b which has been placed inside the larger purge box. The rear UV port is visible with a blue film protecting the O-ring groove. The rail has a travel distance of 300 mm which when fulfilling $K = \pm 4$ can provide patterns spanning from four passes to over 50. Fine adjustments to mirror separation are possible due to the Thorlabs translation stage to which the mirror mount is fixed.



(a) The fabricated front purge box with the mirror assembly.



(b) The fabricated rear purge box with the mirror assembly.

Figure 4.22: Pictures of the purge boxes with the mirror assembly mounted inside.

4.6 Optical Alignment

As this work uses lasers which emit radiation invisible to the eye such as IR or THz, the Herriott mirrors were aligned by a visible HeNe laser to observe the circular reflection pattern in the multi-pass cell. Before mounting the mirrors inside the purge box, they were aligned flat to the table by directing the beam back into the laser cavity over the optical table, giving a direct reflection over a 4 m path length.

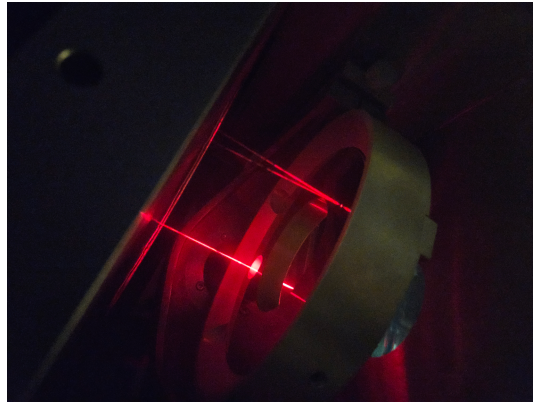


Figure 4.23: A picture of the front Herriott mirror aligned with four passes in the cell.

Figure 4.23 shows the Herriott cell aligned with four passes using visible light. The mirrors were separated at a distance of approximately 1 metre. The light here can be seen entering the coupling port of the cell through the purge box and front mirror. Dry ice in a water container was used to observe the optical path.

After aligning four passes ($N = 4$) to match the conditions set in Section 4.2.2 to give $K = -4$, the mirror separation was increased, keeping the distance within the limit $2f < d < 3f$.

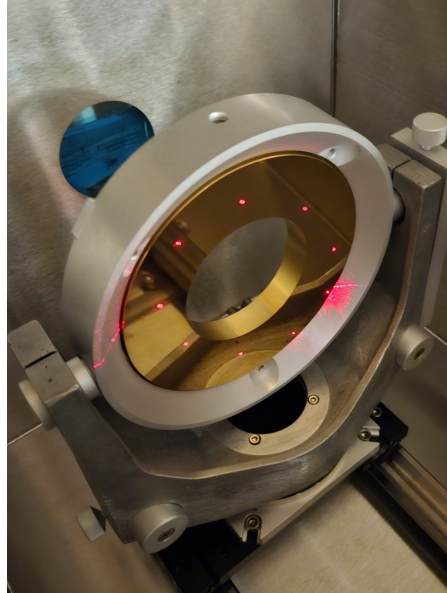
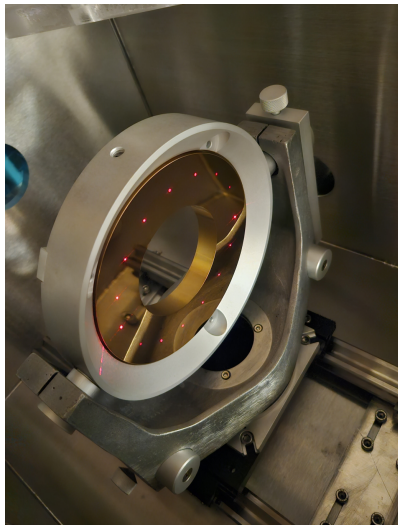
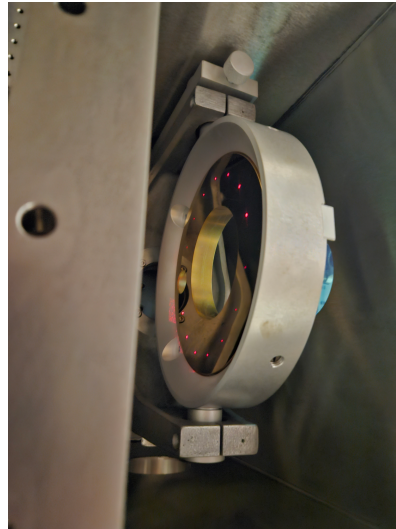


Figure 4.24: A picture of the Herriott cell aligned with the mirrors facing forward ($N = 18$) giving an elliptical pattern.

When aligning a Herriott mirror, the pattern will be elliptical and any manufacturing tolerances will further distort the ellipse. When the mirror spacing was increased from 1 m to an arbitrary distance to observe the pattern evolving, the elliptical pattern became apparent with more passes ($N = 18$) and is shown in Figure 4.24. In Figure 4.24, the beam appears to have a large spot size and a side lobe, this is due to a damaged shutter on the output of the HeNe laser.



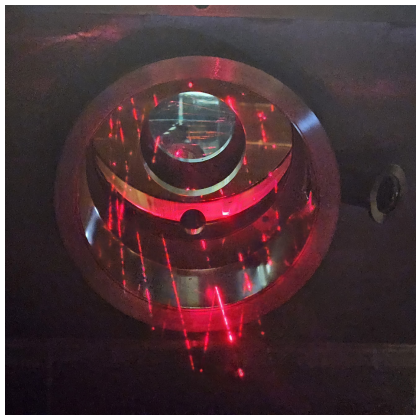
(a) The rear Herriott mirror with a circular spot pattern.



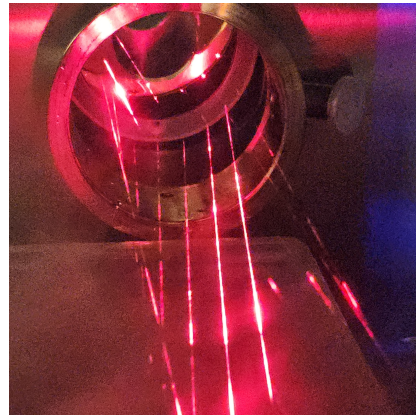
(b) The front Herriott mirror with a circular spot pattern.

Figure 4.25: Visible alignment after adjusting the off-axis tilt of the Herriott mirrors ($N = 30$).

The rear mirror was tilted off-axis by hand to make a circular spot pattern and moved further from the front mirror to create a dense pattern ($N = 30$) to see the pattern shape. Fine adjustments were made by Allen key adjustment to correct the spot pattern and lock the mirror in place, preventing further off-axis tilt. Figure 4.25 shows the mirrors with a circular Herriott pattern after adjusting the tilt.



(a) A side view of the Herriott pattern.



(b) A side view of the Herriott pattern.

Figure 4.26: A side view of the Herriott cell aligned with a HeNe laser.

The Herriott pattern is circular when examining the spots along the optical axis and looking at the length of a Herriott cell on the X or Y-axis, the pattern will have a hyperbolic shape with a minimum width in the centre. The full pattern was observed using a large shallow tray of water and dry ice. Figure 4.26 shows the centre pattern of the Herriott cell, unfortunately, due to the thin water vapour the full pattern was not visible in photographs. If this test were re-attempted a thin smoke or consistent source of mist would be needed to photograph the full pattern. An alternative photography technique such as long-exposure photographs could also capture the full pattern.

4.7 Summary

Chapter 4 discussed the motivation for multi-pass gas cells and reviewed the White and Herriott cells. The operating principle of the Herriott cell has been discussed in detail and the geometry of rays passing through the cell is shown. The Herriott cell was chosen for this work due to the ease of fabricating the mirrors, simple mirror mounts and previous work undertaken at RAL investigating multi-pass optics for the THz region. When applying boundary conditions to the Herriott cell, the number of passes can be changed while constraining the mirror separation within the distance of one focal length. These boundary conditions let the number of passes be adjusted without perturbing the entry or exit angle to the optics. This constraint is important as the angle of light coupled into the light is translated to the light exiting the cell and is not dependent on the mirror separation. The effect of optical interference inside the Herriott cell is discussed and ways to reduce it have been presented, with the popular method being the $K = \pm 4$ solution. The CRDS method is also reviewed and difficulties in manufacturing such systems are discussed and a successful THz CRDS spectrometer which successfully probed low-intensity spectra with amplitudes on the order of $10^{-27} \text{ cm}^{-1}/(\text{molecule cm}^{-2})$.

The Herriott mirrors were simulated using Zemax and in this chapter ray tracing was described. The simulation method used was a mixed-mode system of sequential and non-sequential ray tracing. Experimental beam profiles from Chapter 2 and defined in a ZBF file to be launched in POP simulation. The non-sequential simulation space contains the Herriott mirrors that contain unknown reflections and are CAD files with gold coatings. The rays are then directed to coupling optics and focused onto a detector plane. The design of the mirrors in CAD models and the mounted physical mirrors are shown and an optical layout is shown to aid in understanding the footprint of the multi-pass spectrometer. The different designs in the Herriott cell process are shown with reasoning for adjusting the layout and photos of final mounted coupling optics have also been shown in this chapter. The POP simulations have shown a process to take physical beams experimentally and propagate them through an optical system. This method requires further work to improve the sampling in beam profiles and to avoid propagating the non-Gaussian wavefronts, as this is causing a pixelation on the final result.

The concept design provided by Dr Neil Macleod from RAL was taken and developed into the final design seen in Section 4.5.1. The design went through two phases, the first had both mirrors on stages to change the separation which is shown in Figure 4.18. Using two stages to move the mirrors was decided against due to the complexity of the design process and moving the front mirror would change the angle coupling into the Herriott cell. The final design used one static mirror and one mixing mirror which is shown in Figure 4.21 The final design uses standard parts ordered from Thorlabs and Newport to assemble the mirrors and the rear mirror moves on a carrier and rail system. This design was sent to Kurt Lesker who fabricated the purge box with steel and a clear acrylic lid. After assembling the mirrors and purge boxes, a HeNe laser was used to align the mirrors and coupling optics. The visible alignment has been used to fix irises to the ideal optical path.

Future work on the multi-pass optics will need to finish the alignment with a colinear IR laser to the THz before attempting alignment with the QCL. The Herriott cell will be used for trace gas analysis and in particular used to probe chemical reactions and in particular UV photolysis will be examined. Future work with the Herriott cell will have to find a suitable path for UV and THz overlap within the cell which will help maximise sensitivity in photolysis experiments. The Herriott cell will first need to be aligned and have a QCL operating in pulsed mode to have the best chance of alignment. Tools to make the THz radiation visible such as a THz camera will also be needed to ensure the radiation is coupled efficiently into the detector.

Chapter 5

QCL Power Stabilisation

A free-running laser is suitable for many imaging, communications or spectroscopy applications. Small drifts in optical power are inherent in any laser source due to mechanical vibrations or minor temperature changes. This chapter will discuss different methods of source stabilisation, then show work using a Photonic Integrated Circuit (PIC) approach with a resonator coupled to a QCL ridge. Using the PIC approach, this chapter demonstrates a THz QCL which was power stabilised for 623 seconds. The typical integration time in Earth observations is 5 to 10 minutes, making this stabilisation technique adequate for Earth observation instrumentation.

5.1 QCL Stability

A range of stabilisation techniques can be used to control a laser's frequency, amplitude or phase. The reliability of an absorption spectrum or the repeatability of an experiment can be directly affected by power drifts inherent in the operation of a THz QCL. The group has previously misinterpreted drifts in the temperature of the cryostat or room as THz power drifts as they appear as intensity changes on the detector.

There are many contributing factors to the linewidth of a QCL, one common contribution to a laser's instability is noise from the power supply. Fluctuations in a laser driver's power source are directly transferred to the QCL bias so a low noise power source is needed to reduce this effect. In addition to environmental sources, gain medium fluctuations can contribute to broadening linewidth. Figure 1.16 in Section 1.3.4 showed how the laser emission is a series of optical modes amplified by the gain bandwidth. The frequency of this gain medium can be stark-shifted from changes in electric field within the QCL which translates into a broadening in linewidth as previously unsupported modes are now emitted as the gain bandwidth shifts [73]. Optical feedback into the facet of a QCL causes mixing between the internal modes and reflected light. The mixing results in a change in terminal voltage which is measurable and used in self-mixing,

but also causes fluctuations in optical power. The reflected light interferes with the electric field within the gain medium, shifting the QCL threshold gain and optical power [150].

Laser stabilisation's basic principle is maintaining the main optical mode in the cavity through changes in electrical bias, mechanical alterations to the cavity or temperature changes [151]. Inside the laser cavity, multiple modes interact, and adjusting the optical path length properties inside the cavity changes the interaction between lasing modes. The temperature in the active region of a device will be higher than what is recorded on a heat sink, this is due to the thermal resistances introduced from the substrate and physical contact with the cold finger [152]. For this reason, passive stabilisation of a THz QCL is used where there isn't a need for precise stabilisation and results in line-widths in tens to hundreds of kilohertz [153].

5.1.1 Proportional Integral Derivative Control

Feedback control has a long history dating back to the improvement of the first steam engine, by James Watt in 1769 and has been used in automation ever since. Negative feedback loops work on the principle of subtracting the output of a system by a set point, this results in an error. Using the error signal, a control system will adjust the process to correct the output [154] [155].

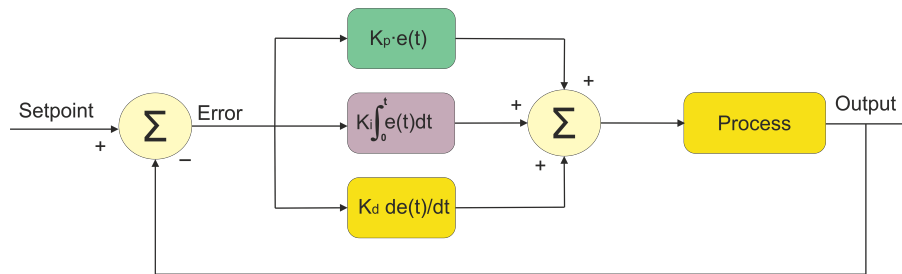


Figure 5.1: Block diagram of a parallel PID controller, a common PID configuration.

Figure 5.1 shows a typical closed-loop system, there is the Set-point Variable (SV) which is the reference value, the Process Variable (PV) which is the signal being controlled and the Error which is the difference between the two. PID controllers have three internal gains: Proportional gain K_p which is a constant multiplying PV by the error. This proportionally changes the PV, setting the gain too high will cause the system to overshoot the set point or oscillate. The Integral term K_i is used to correct a steady state error in the PV by examining the error value over time, Integral terms have a gentle correction compared to the proportional component. If the Process were to stall and leave a constant error, the integral correction would become large causing overshoots or oscillations. The Derivative term K_d can only be used if the error's rate of

change can be examined. If so, the derivative term can add a prediction to the controller by adjusting based on the rate of change. Care must be used when setting the derivative term as it is sensitive to noise and will cause oscillations in the system [156].

5.1.2 Power Locking

Drifts in laser power during a measurement can obscure weak absorption features in a spectrum, optical power modulation is important for other applications such as communications or sensing. Power locking a THz QCL through optical modulation is important for examining fine features in a spectrum such as those found in trace gas analysis. In heterodyne spectroscopy, a stable LO source should be used as noise in the LO can appear in the IF due to the signal mixing.

Power locking a THz QCL can be done both actively and passively, Passive power stabilisation is a method such as controlling the temperature of the cold finger. Stabilising the temperature is a common technique but the thermal resistances between the sensor, active region and heater result in different temperatures throughout the system compared to what is reported by a temperature sensor [152]. The temperature change in a cryostat due to a heater is limited by the thermal resistance of the cold finger, using external modulators can remove the limitation of the cold finger thermal conduction by using external optical stabilisation.

Direct modulation of a THz QCL has been demonstrated at a frequency of 13 GHz. Still, limitations quickly arise when modulating a QCL this way such as the parasitic impedance in the bonding wires or the cryostat wiring [112]. Although modulation through direct detection and adjusting the bias is attractive, it can lead to undesired effects on the frequency of the laser. An external modulator can be used if the THz power is sufficient. Most external modulators work on a similar principle, having a variable attenuator in the beam path and varying the attenuation to stabilise optical power. External modulators have existed for a long time at various wavelengths. As THz technology has evolved there has been a wide range of reported modulation techniques such as metamaterial modulators. For example, X. G. Peralta, et al, reported a modulator in 2010 which operates at 2.8 THz with a modulation depth of approximately 60% with a modelled modulation frequency in the order of MHz [157]. D. S. Jessop, et al, reported Graphene metamaterial modulators in 2016 with experimental modulation speeds up to 100 MHz and calculated frequencies up to 10 GHz [158]. 100% modulation depths with a 100 MHz modulation speed have been achieved by integrating graphene onto a QCL, or by creating reflective and electrically controllable cavities which have been demonstrated in 2017 by S. J. Kindness, et al [111]. S. Savo, et al, in 2014 reported on Liquid crystal metamaterial modulators which have exhibited modulation depths of 75% [159]. A. Dunn, et al, reported a liquid crystal absorption cell in 2020 which was used for THz modulation, by applying a voltage to a liquid crystal cell a modulation depth spanning 5% to 40% was reported with recovery speeds spanning seconds to 400 seconds for the 40% modulation depth [110] [160].

5.1.3 Frequency Stabilisation

For applications that need high stability, active stabilisation is used. Active stabilisation uses the value of a stable reference compared to the value of the detector, the difference in these values gives the controller an error which will be used to correct the laser output by changing the bias. This change in bias from a controller locks the laser frequency to the stable reference. Components such as phase-lock loops, frequency discriminators or a reference laser can be used to achieve line widths in the order of sub Hz. Many active stabilisation methods have been reported in literature such as stabilisation with an external source [161] [162] or Phase and frequency locking using a phase-lock [163] [164].

QCLs are ideal LO sources in heterodyne measurements due to their narrow line width and milliwatt optical powers. The intrinsic linewidth of a QCL is theoretically in the sub kilohertz range, but due to thermal effects and optical feedback, the linewidth of a free running QCL is typically in the range of MHz [165]. When resolving narrow features in astronomical observations and atmospheric spectroscopy, the LO needs to be either phase or frequency stabilised in the sub-MHz range (1 part in 10^6 for THz lasers), so Doppler motions can be observed with 1 km s^{-1} accuracy. This was a motivation for A. L. Betz, et al, when reporting the first THz QCL being stabilised in 2005 to an order of 10 kHz (1 part in 10^8) [163] [166].

Frequency discriminators such as molecular absorptions or the mixing of a frequency comb are commonly used for frequency stabilisation. Using these as a reference, the conditions inside the cavity of a THz QCL can be maintained by correcting the bias. A molecular absorption is an exact frequency reference that can be locked to through a control loop. Using a small gas cell filled with an active gas in the THz region such as methanol and a detector to monitor frequency drift in a QCL is a simple optical setup for frequency locking. To lock to a gas absorption first one must be identified in the laser's linewidth, once found the QCL is tuned to the rising or falling edge of the feature. An example of this is shown in Figure 5.2, where any drift in frequency will correspond to a drift in amplitude and result in an error signal in the control system.

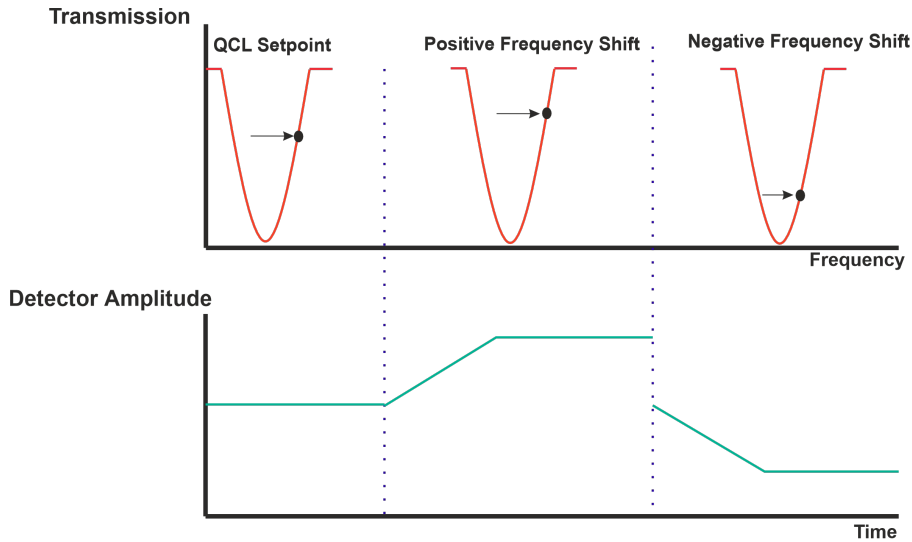


Figure 5.2: QCL emission (Black spot) on the side of a frequency feature. A change in the laser frequency results in a detected shift in amplitude, this shift creates an error signal inside the controller.

5.1.4 Phase Locking

Another method of controlling the frequency of a THz QCL is to lock both the frequency and phase in a Phase-Locked Loop (PLL). An example of this is A. V. Khudchenko, et al, who published a phase lock at 4.7 THz using a superlattice diode as a mixer [167]. The phase locking techniques have also been demonstrated at the lower band of QCL operation, for example, A. Danylov, et al used a 2.33 THz QCL with a Schottky diode mixer and frequency deviations in the sub Hz range [168].

The Phase locking method has three main components: the source, the mixer and the reference. Phase locking is difficult in the THz range due to the lack of available reference sources or mixers. Mixers are the key component in the PLL, as they generate the difference frequency between the QCL and reference [129]. It is widely accepted that the high harmonic of a very stable microwave synthesizer is an ideal frequency reference, but the SNR of the beat signal decreases with the higher harmonics. As well as a decreasing SNR, as we go into higher frequencies Schottky diode mixers can struggle to output a sufficient IF power for frequency or phase locking [168]. Schottky diodes have been demonstrated to detect THz frequencies up to 3 THz [169]. Figure 5.3 shows a simple block diagram of a phase-locking system which uses a microwave source and a mixer.

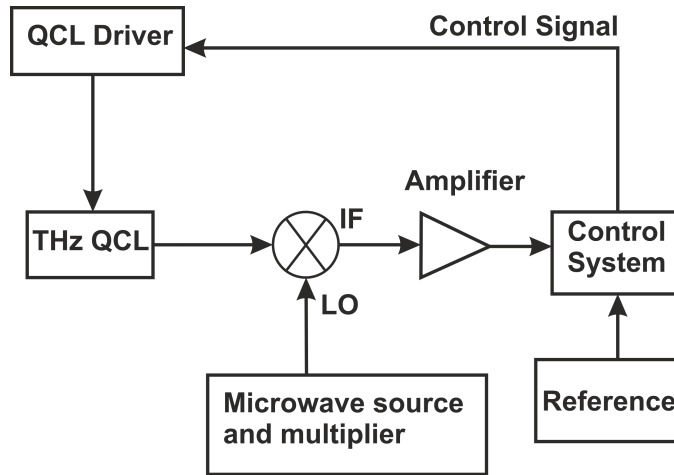


Figure 5.3: A simple block diagram of a Phase Lock Loop. The microwave source and control systems have various components such as amplifiers and filters to condition the signal.

The PLL is a system with many components that uses a stable lower frequency source reference, the multiplier chains consist of amplifiers and oscillators to reach high frequencies but the output power is in the range of microwatts. Throughout a PLL, amplifiers, filters and devices monitor the signal, ensuring the lock is stable and filtering out the desired harmonic from the mixer. Any drift in the THz frequency will shift the beat note, resulting in an error signal. A control loop such as a Proportional Integral (PI) controller evaluates the error and modulates the QCL driver accordingly, correcting the phase shift.

5.1.5 Injection Lock

Injection locking is a phase synchronisation technique that uses photon interaction within a laser cavity when the external light is coupled. The system uses a master laser which is a stable reference that is similar in phase and frequency to the slave laser which is typically a laser with higher power with an unstable frequency. Like in self-mixing, the external light interacts with the optical mode within the cavity, in this operation the incoming light is frequency and phase matched to the slave laser. The slave laser will synchronise with the master and follow any drifts in phase from the more stable input radiation [170].

In THz this configuration is typically a QCL stabilised by a PLL or gas laser. An example of injection locking a QCL is using a telecommunications frequency comb. J. Freeman, et al, demonstrated this in 2017 by locking a 1.97 THz QCL to a telecommunications frequency comb. Two comb lines were selected and the difference signal was injected into the QCL facet to lock the emission. This locking method produced a stabilised QCL in the range of minutes with a linewidth < 100 Hz [171].

A QCL can also be stabilised through Near Infrared (NIR) illumination from a diode laser. This experimental system was reported by T. Alam, et al, in 2019 where an optical fibre mounted inside a cryocooler was aligned to the rear facet of a QCL and coupled radiation from a NIR laser. The role of the illumination is to provide fast frequency tuning to the QCL on the speed of GHz which exceeds modulation speeds demonstrated in temperature tuning and direct bias tuning [172]. The QCL was power and frequency locked using a MeOH absorption line and a PID control system. The locked QCL linewidth demonstrated a FWHM of 260 kHz, with a measurement noise FWHM of 200 kHz. The power and frequency lock achieved a RMS power stability 0.03% FWHM [161].

5.2 Racetrack Resonator

The external methods discussed previously in this chapter involve increasing the size of the optical system with modulators and having external optical components. The RTR is a PIC which can be used as an attenuator fabricated on the same chip, these resonators have previously been reported operating in the IR region [173]. A brief explanation of the RTR operating principles and design will be explained in this chapter, the RTR design, simulation and fabrication have been reported by Dr Iman Kundu [174]. A 3D image of the RTR device is shown in Figure 5.4.

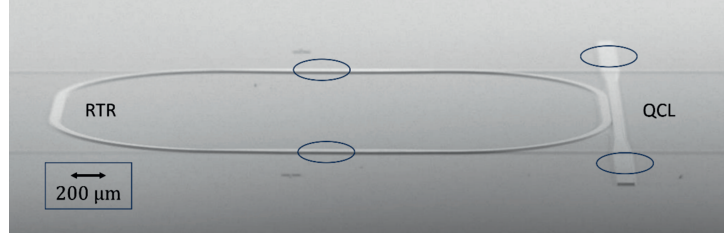


Figure 5.4: 3D image of a RTR coupled to a QCL ridge. Black rings show the bonding pads. Figure taken from [175].

The resonator is a circular circuit resembling a racetrack which is symmetrical and consists of an absorber, bonding pads and a coupler. The device was fabricated using a photolithographic method, where the mask was applied using a maskless alignment process. The mask was designed in CAD software and converted to a 2D pattern for precise patterning and vertical sidewalls in the gap, a dry etching method was used.

To match the Free Spectral Range (FSR) of the stop bands within the RTR to the modes in the QCL, the RTR diameter must be approximately twice the length of the QCL ridge (L_{Ridge}). The RTR is 9.144 mm, approximately double 4 mm L_{Ridge} . Two bonding pads on each device are shown as black rings in Figure 5.4 which are 88 μm wide and 500 μm in length. The coupler was designed to be 565 μm in length and flat to facilitate strong coupling, three waveguides

of identical length form the resonator with a corner radius of $893.52 \mu\text{m}$. The dimensions of the RTR were first found theoretically, then optimised through FEM modelling to optimise the performance while giving the smallest RTR dimensions. The air gap was chosen as $3 \mu\text{m}$ to give the best coupling between the ridge and RTR, the air gap in the fabricated design was measured at $2.54 \mu\text{m}$. Figure 5.5 shows a CAD design and microscope image of the RTR device [174].

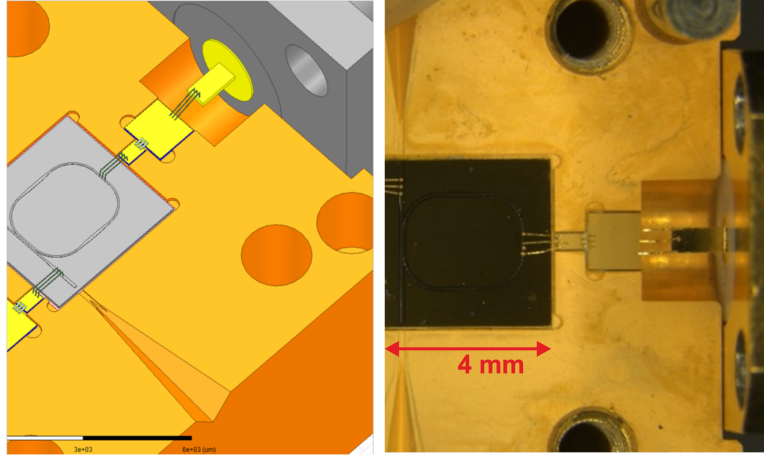
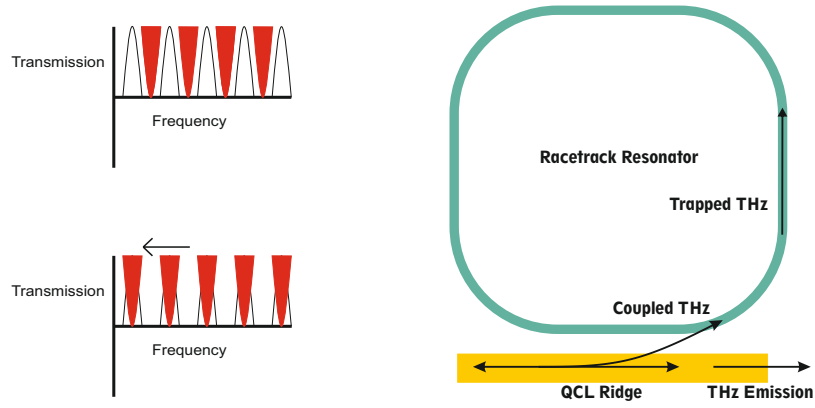


Figure 5.5: (Left) 3D model of the device integrated into a waveguide block. (Right) Microscope image showing the gap between the resonator and QCL ridge inside a waveguide block.

Phase matching these conditions in the design results in a frequency comb of stop bands close to the QCL emission frequencies. Phase matching is completed by changing the bias of the RTR. Applying a bias to the RTR stark-shifts the stop bands to overlap the QCL emission frequency, resulting in a decrease in output optical power [174]. Figure 5.6a shows a sketch of how the comb of stop bands overlap the THz emission. The top shows multi-mode emission where there is no bias applied, the bottom image is when a bias is applied to the RTR. The black arrow represents a Stark shift in the stop bands which now overlap the QCL emission and result in attenuation.



(a) QCL emission frequency (Black) vs RTR stop bands (Red). (b) Diagram of the optical mode coupling into the RTR.

Figure 5.6: Diagrams of how the QCL emission is coupled into the RTR as it is biased.

Figure 5.6b shows a simple diagram of the radiation being coupled into the RTR. As the bias on the ring is changed, it alters the refractive index of the device and couples radiation into the ring. The material of the RTR is lossy compared to the QCL ridge, resulting in the coupled radiation becoming trapped and absorbed by the resonator.

5.3 Control Loop

A range of control systems can be used to stabilise a THz QCL, in this work a RTR was controlled with a PI and PID controller. The optical output can be stabilised by using an error signal from an external set point and the RTR as a transducer. This section will discuss the experimental setup and results of controlling the power of an unmounted 3.4 THz QCL. The output power was stabilised for 600 seconds using a precise voltage source as a reference.

5.3.1 PI Lock Box

The PI controller used was a New Focus LB1005 High-Speed Servo Controller which has a 10 MHz bandwidth and a simple front panel which consists of potentiometers to alter the PI parameters. range of uses including high-speed laser stabilisation. There are three main stages in this controller:

1. **Input:** Inputs A and -B are summed with an offset using a difference amplifier, creating an error signal that can be monitored through a BNC output.

$$V_{error} = V_A - V_{-B} + V_{offset}$$

2. **PI Control:** This section converts the error signal into the control signal, which is done through a PI filter. A toggle switch is used to disable or enable the control signal for acquiring a lock, this can also be done through a TTL signal.

$$V_{Control} = [k_p + k_i \int dt] V_{Error}$$

3. **Output:** The output section is a summing amplifier that combines the control signal with other signals such as an external sweep or modulation inputs.

5.3.2 Field Programmable Gate array

The microprocessor is a device that most people use every day, handling a wide range of digital tasks by following instructions written in software and changing the software will change the function of the processor. Alternative to the serial processor architecture is a programmable logic system that allows the user to program a parallel logic system with purpose-designed architecture for the task, called a Field-Programmable Gate Array (FPGA) [176]. The internals of a FPGA comprises multiple blocks of logic gates connected with programmable interconnect. The programmable interconnect lets users design an architecture that handles tasks faster than a microprocessor [177]. Due to slower response times in computer-controlled serial systems, dedicated logic systems such as the lockbox or FPGA were used as the controller in this work.

5.4 Experimental Setup

The 3.4 THz QCL was cooled inside a Janis ST-100 helium flow cryostat with temperature stabilised at 40 K using a Lakeshore temperature controller for the experiments. LIV characteristics for the device were taken in CW mode, using a current source, two off-axis parabolics and a bolometer. The LIV was recorded using a PC running LabView.

The experimental configuration is shown in Figure 5.7. The New Focus LB1005 was used as a controller which compared the lock-in amplifier magnitude (-B) to a reference voltage (A) which was set to 0.116 V, this was obtained by

measuring the lock-in magnitude while the QCL was free running. The PI controller will only lock if the following three conditions are satisfied:

1. Acquire switch is in either Low Frequency Gain Limit (LFGL) or Lock On position. LFGL is a lock condition which limits the low-frequency gain, whereas Lock On enables the full integrator response.
2. Error signal is within ± 0.33 V.
3. Output signal voltage does not exceed 90% of full-scale voltage.

The output of an Arroyo 4302 current source was modulated through the external modulation input at a ratio of $1 \text{ V} = 200 \text{ mA}$. The maximum control signal out of the PI controller was internally limited to $\pm 1 \text{ V}$ to protect the resonator from overcurrent. Due to condition 3 in the locking requirements listed above, the control signal drifting beyond $\pm 900 \text{ mV}$ resulted in the system losing the lock. This issue was resolved using a potential divider on the lock box output, leaving the internal limits at $\pm 10 \text{ V}$.

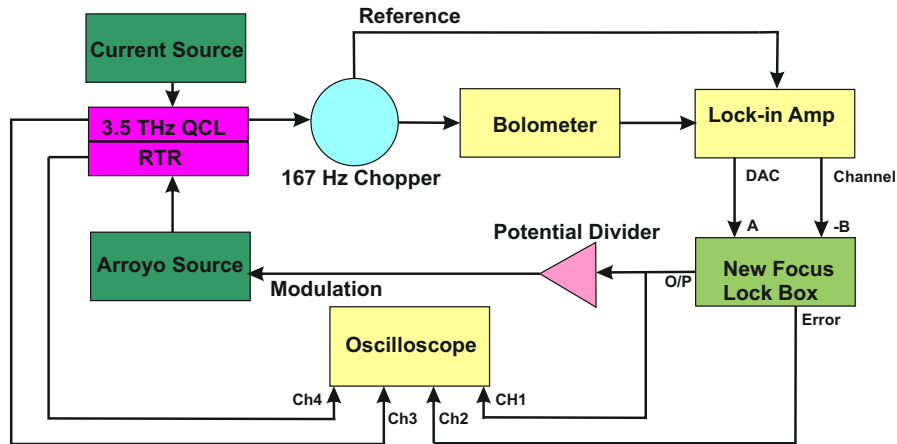


Figure 5.7: A block diagram of the power locking experimental set-up using the New Focus PI controller.

5.5 Characterisation

After fabrication, the LIV characteristics of the QCL were taken in CW mode at a range of temperatures with the RTR switched off. The QCL threshold current is at 500 mA and the peak current is 1.3 A for the QCL. The QCL was then set at the peak bias and the resonator bias was swept, a 100% modulation depth is observed at 50 K as the resonator is biased, proving the device is suitable for a power locking system. Using Figure 5.8 at 40 K, a linear relationship of the optical power out in millivolts from a lock-in amplifier (P_{QCL}) can be related to the RTR current in milliamps (I_{rtr}) can be given in Equation 5.1. At 50 K, there is a non-linear relationship between the RTR current and attenuation, but this temperature range provides a full modulation depth.

$$P_{QCL} = 500 - 0.388 \times I_{RTR} \quad (5.1)$$

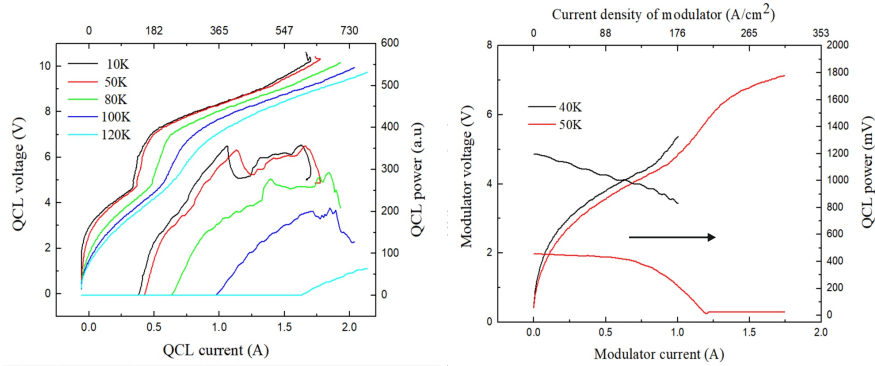


Figure 5.8: (Left) the LIV characteristics of the THz QCL. (Right) The effect of the RTR bias on the QCL power.

Figure 5.9 shows spectral characteristics of the device using a Bruker IFS/66 FTIR spectrometer. The device was investigated in continuous wave operation at a temperature of 40 K. The QCL has a tuning range in the order of GHz and operates over four lasing modes as the current is swept, these are 3.277 THz, 3.285 THz, 3.372 THz and 3.392 THz. The effect the RTR has on the QCL was investigated using the FTIR spectrometer, the QCL was biased at a constant current of 1.3 A and the RTR bias was swept.

During the RTR sweep, it can be seen that there is a small effect on the laser frequency in the range of 2 GHz. The full tuning range of the QCL as the current is swept is 3368 GHz to 3381 GHz, when the RTR is swept the tuning range is 3373 GHz to 3375 GHz. This gives a tuning range of 13 GHz for the QCL whereas the tuning range for the RTR is 2 GHz. Adjusting the RTR bias gives a frequency tuning effect 6.5 times less than adjusting the QCL.

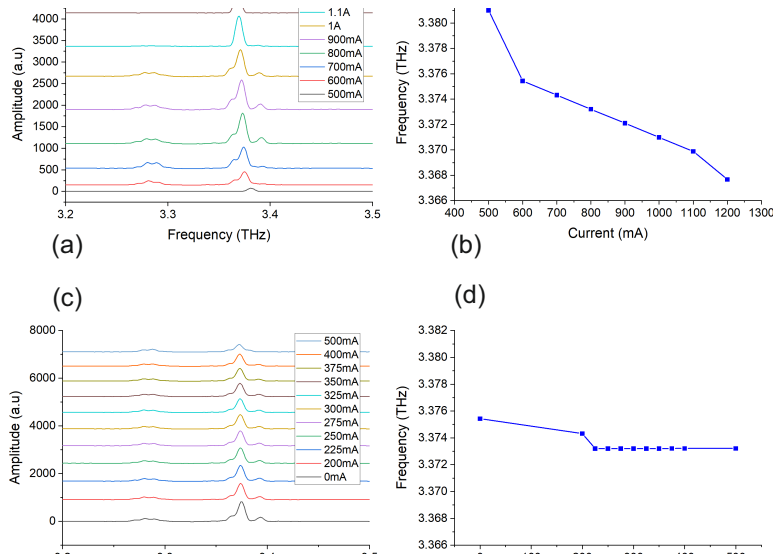


Figure 5.9: (a) RTR was off and QCL current increased. (b) Peak frequency vs bias current for QCL sweep. (c) QCL at a constant current and RTR bias increased. (d) Peak frequency vs bias current for RTR sweep.

5.6 Power Locking Results

The longest power lock was 623 seconds using a liquid helium cryostat to cool the QCL and the New Focus PI controller to lock the signal to a 116 mV reference signal from the DAC output of a lock-in amplifier. This locking time would be usable in an Earth observation instrument where integration times span 5 to 10 minutes. During measurements, the lock-in amplifier time constant was set to 50 ms and the QCL was biased at 720 mA. The RTR was set to operate in the middle of the range at 400 mA, giving a modulation range between 300 mA to 500 mA using the control signal. The controller unlocked after this time, which was suspected to be due to the pressure in the helium dewar dropping and increasing the QCL temperature. This increase in temperature resulted in a decrease of THz power which went beyond the full-scale control of the RTR.

The results of power locking with a PI controller are shown in Figure 5.10 compared to in free-running operation. A Gaussian noise shape is expected in free-running operation, but the resulting distribution is non-Gaussian due to external vibrations and thermal drift in the bolometer. In the free-running case, a baseline filter was applied to remove the bolometer noise and the standard deviation was calculated to be 2.63×10^{-3} , there is an observable change in power stability and when the control loop is active, the standard deviation is 72.3×10^{-6} . The quantisation seen in these results are due to the sensitivity of the lock-in amplifier. The helium dewar pressure was the likely cause of the unlocking. When the helium pressure drops, the heat lift from the helium flow is reduced and this causes a drop in QCL power.

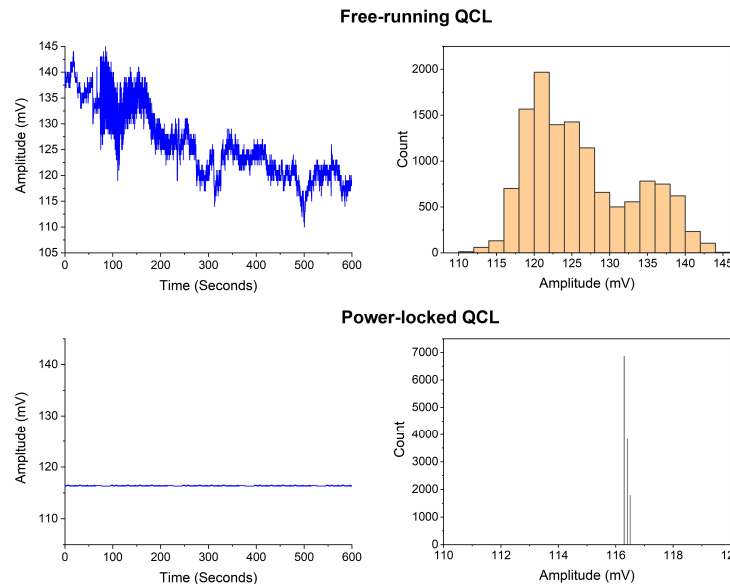


Figure 5.10: Results from the power locking experiments showing the signal detected with a lock-in amplifier. (Top) The QCL is free-running. (Bottom) The QCL signal with the control loop active, quantisation effects are due to the lock-in sensitivity.

5.6.1 PID Results

Further work on power locking included programmatically implementing a PID loop using a FPGA. Using a FPGA would allow the experiment and control system to be compiled into one program as well as reduce the system size, by combining the separate PI controller and DAQ board. For this task, a National Instruments MyRio was programmed using the PID toolkit in LabView. MyRio was chosen over a National Instruments DAQ because once the programmable interconnect has been set in the FPGA it operates as a dedicated logic system and does not require a serial connection to a PC.

Figure 5.11 shows the results from a power locking experiment using a FPGA controller.

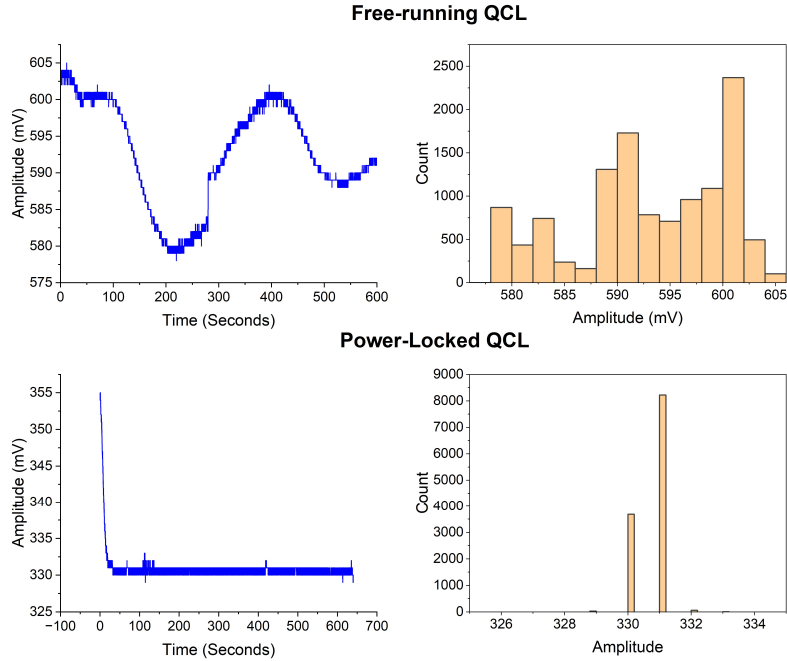


Figure 5.11: (Top) Results from the FPGA experiments showing the signal detected with a lock-in amplifier while free-running. (Bottom) Detector signal with the control loop active.

In this investigation, the lock-in amplifier time constant was set to 50 ms. The device was mounted in a Cold Edge closed cycle cryocooler with an operating temperature of 30 K. The PID controller was manually tuned using the Ziegler-Nichols method, where the proportional gain is set until the point where the output begins to oscillate and then is reduced. The integral and derivative gains are then set to optimise the response by observing the switch on transient and manually adjusting the PID gains. The reference was set at various set points, with PID gains manually tuned to Proportional Gain $K_c = 0.1$ Integral time $T_i = 0.001$ and Derivative Time $T_d = 0.0075$. Using the FPGA a lock of over 600 seconds was achieved, which would be usable in an Earth observation instrument where integration times span 5 to 10 minutes. The standard deviation of the freewheeling case is 7.6×10^{-4} and with the control loop active the standard deviation is 4.79×10^{-4} . The transient switch on period and long-term signal drift was removed from the free-running standard deviation calculation, this non-Gaussian component is due to thermal drift in the bolometer signal. The settling time can be seen at the start of the power-locked time domain signal, this settling time has been removed for the histogram and stan-

standard deviation. After the experiments in the closed cycle cryocooler, the device was damaged and it was not possible to fabricate another device in a timescale making it usable in this research.

5.7 Summary

In this chapter, the operating principle of control loops was introduced and a previously designed optical component the RTR has been investigated. The RTR is a photonic circuit commonly used in telecommunications. The operating principle of a RTR coupled to a QCL ridge was discussed and the two control systems used for this work are explained. A closed-loop control system is used to study the effectiveness of the RTR as an integrated power modulator for a 3.35 THz QCL.

The results from two power locking experiments are shown, one using a helium-cooled cryostat with a dedicated PI control box and another using a closed cycle cryocooler and a FPGA PID controller. The dependence on helium pressure while using a helium-cooled cryostat was theorised to be the limiting factor of the power-locking system resulting in a maximum power-locking time of approximately 623 seconds. Although the PI controller unlocked after this time, it would still be adequate for the integration times used in Earth observation which typically span 5 to 10 minutes.

Results from mounting the device inside of a closed-cycle cryocooler and using a FPGA as a controller showed the potential of integrating the RTR into a small package which is capable of power locking times suitable for satellite applications. Due to the device being damaged during these tests, future work would involve fabricating a new device and an investigation into the effectiveness of the constant heat draw of a cryocooler. The design of these RTR devices could also be studied further to investigate their use as an optical modulator for use in communication systems. The potential to design the stop bands of a RTR to rapidly switch the optical mode between two THz frequencies could be used for frequency-modulated signals or to rapidly change the area of a spectrum being observed in a spectroscopic measurement without disturbing the QCL bias.

Future work for power stability should investigate power locking with a TeraFET detector, the devices have modulation bandwidths up to 20 MHz compared to the 167 Hz modulation bandwidth. The low modulation bandwidth of a bolometer was sufficient to correct low-frequency temperature drift. The use of a TeraFET detector sampling at 20 MHz eliminates higher frequency noise in the THz signal. When a fast power locking scheme is implemented, a controller such as an FPGA can introduce automation to the system and automatically tune the controller to the transfer function of the system. With power stabilised, frequency locking can be realised with a calibration gas. The combination of power and frequency stabilised QCLs will enable the system to target the absorption of an intermediate state in a reaction and monitor the kinetics of a chemical reaction.

Chapter 6

Conclusion

The overall aim of this work was to develop a THz gas spectrometer which used a QCL as the radiation source to examine low-concentration gas species, with a future goal to emulate atmospheric chemistry within the lab. The motivation to develop such a spectrometer also brought further knowledge into QCL stability and detector noise as well as assisting in the Interest collaboration between the University of Leeds and Goethe University Frankfurt to characterise new room temperature FET detectors to be used for spectroscopy.

The first experimental chapter is Chapter 2 which discusses QCL cooling methods and shows the closed cycle cryocooler used throughout the project. The cryocooler was an important step in this spectrometer as moving away from cryogenics and to closed-loop systems and a room temperature THz detector increases the portability of the system, progressing towards instrumentation which can be deployed in the field. The QCL was characterised through the LI characteristics and beam profiles using a scanning detector. Spectral data using FTIR data and calibration gasses were presented, plus the difficulties in frequency calibration were discussed. The FTIR data was only valid for the first experimental system with a bolometer detector. Once the new detectors were used, the spectrometer was realigned making the previous data invalid. Although the data was invalid for future alignments, it proved valuable as a method for FTIR with a QCL was developed, frequencies given could still be applied and help in gas calibration by providing an initial guess of the mode frequency. The TeraFET detectors are fast, room temperature and electronic detectors, which overcame a problem when using the bolometers. The thermal detectors proved to be too sensitive to environmental noise giving long-term power errors, this was solved by fabricating a thermal housing over the bolometer windows until the TeraFET detectors were used. The chapter shows how a TeraFET works and presents the characterisation done on the detectors, this data contributed to three presentations at IRMMW-THz and a publication written on the TeraFET characterisation by Jakob Holstein and a publication on THz gas spectroscopy written by Dr Michael Horbury. The characterisation results for the array-type devices did not reach the theoretical noise performance,

but this is due to high experimental noise. The rapid-scan work worked as a proof of concept to examine the switching dynamics of multi-mode QCL but was ineffective due to the spectrometer speed and errors in the experimental system during the test. This experiment showed the possibility of using the TeraFET in more applications than direct absorption and the benefit provided by THz detection in the MHz range of modulation bandwidths.

Chapter 3 presents all of the gas spectroscopy done in this work. The chapter shows calibration gasses which were MeOH and D₂O. The method of extracting spectral data uses the Beer-Lambert law and compares the results to the JPL catalogue to compare experimental numbers to the simulated catalogue. The static measurements discuss many MeOH measurements taken throughout this work and show the errors which arise when using FTIR spectrometer with no stage distance calibration. The uncertainties in a QCL active region lead to drifts in frequencies between experiments and indicate the importance of a frequency-referenced measurement or frequency stabilisation. Gas spectra in this work are presented in both a frequency and QCL bias along the X-axis, this is because the length of time it can take to construct a frequency axis outweighs the need for a frequency axis. For example in the sensitivity experiments, the absorption frequency is irrelevant to the minimum absorption. Before purchasing and testing MeOD, a mixture test was conducted at various pressures and sample ratios, to see if MeOD was visible in the QCL emission. These experiments used the time-resolved gas manifold and successfully showed new peaks when D₂O and MeOH were sampled. These peaks could have been one of the many isotopologues which arise when this reaction takes place, to ensure this was not the case, MeOD was purchased and sampled which contributed to a IRMMW-THz and publication by Dr Michael Horbury. A small test in sampling cider was undertaken to see if there are possibilities for using the spectrometer in food analysis. The result showed methanol peaks and no ethanol peaks as they're not visible in this THz region. Although this experiment was simple, it opened the possibility of further investigating real-world applications and collaborations within the university.

The Herriott cell development and fabrication are shown in Chapter 4 where the different designs and justifications for alterations in the design are made. This multi-pass cell was intended to be a small project but turned into a section of this work as the difficulties in working with large optics in the THz region and using non-Gaussian sources became present. The Herriott cell was developed and processed throughout the three years of this work until the final year when the fabricated parts arrived. The Herriott cell is intended to be operated in four passes until QCL and THz technology can produce better beam qualities at higher powers, such as surface emission QCLs. The design process has also led to a method of changing experimental or simulated beam profiles into a ZBF file which is attractive for future work within the group at designing THz optics.

The final experimental chapter is Chapter 5, which presents the power stabilisation work which was done to help reduce drift in a QCL. The RTR was developed and fabricated by Dr Iman Kundu before the start of this work and was able to modulate the QCL power without external optical components.

The RTR project implemented a control loop to successfully power lock a QCL for approximately 10 minutes, which is suitable for the integration times in satellite observations. This power stability could be improved further through the use of a FPGA controller which can automatically lock or unlock depending on the experimental conditions and if an alternate cooling method was used such as a cryocooler, the helium pressure would not have caused unlocking after minutes of operation.

To summarise, this work has developed a THz gas spectrometer capable of observing absorptions of MeOH to a concentration of 1.62×10^{15} particles/cm³ and developed a multi-pass absorption cell to be used with THz QCLs. It has proved that QCL based gas spectrometers can provide access to previously unexplored areas of the THz region and have observed previously unknown gas absorptions. This work has also assisted in the development of the TeraFET detectors which are fast room temperature THz detectors which aid in reducing system footprints and increase the modulation bandwidth of THz detection.

6.1 Future Work

The improvements in QCL technology have reached a point where gas spectrometers in the THz region using these sources are benefiting from narrow linewidths and milliwatt optical powers. Further improvements will progress the field of THz spectroscopy. The quality of a beam source is important in spectroscopy and throughout this work, a single metal QCL was used which has lower power but a better beam profile when compared to a double metal waveguide. Surface emission devices may be the answer to improved output power and beam quality as these QCL devices have a comparable output power to a double metal device with a beam profile similar to the single metal waveguides [178] [179]. Such a QCL would improve the output power, reduce propagation losses through long path lengths and better couple into a detector.

The TeraFET detectors proved to be a valuable tool which removed the detector drift observed with thermal detectors as well as improved readout speeds, allowing for higher averaging in an experiment. Recently the modulation bandwidth increased on these devices, the possibility for sampling fast reactions becomes possible and the future progress should find a suitable photolysis reaction to begin sampling rapid photochemical reactions. The modulation bandwidth increases have also made heterodyne mixing on the TeraFET antenna a possibility. Once bandwidths exceed 1 GHz a multi-mode QCL with close mode spacing could be used to show the possibility of a heterodyne receiver using TeraFET mixing as an alternative to Schottky diode mixers.

The gas spectroscopy work has mostly focused on catalogued species to characterise the spectrometer, but now the sensitivity is improving, new species should be examined. To target atomic oxygen, the QCL would need swapping to a new device which emits at 4.74 THz. To calibrate this new QCL methanol can be used as well as ammonia which is a common pollutant in the agricultural field. The ammonia study could demonstrate the use for a THz gas spectrome-

ter which can be deployed in the field, by using a room temperature TeraFET detector and QCL which disperses low thermal power, a portable system could be demonstrated for in-situ measurements of ammonia in the field. The results from an ammonia study can be used as a calibration gas for a 4.74 THz QCL as there are two absorption features which surround the atomic oxygen line at 4.74 THz. This method of frequency calibration to observe the atomic oxygen transition has already been demonstrated [97].

The Herriott cell will allow long-length observations of gas species in the THz region with a QCL source. Future work will need to finish the alignment, as due to moving the spectrometer between labs this was unable to be completed in the time scale of this work. The device is set up for an alignment IR laser to pass through the Herriott cell which will allow users of the system to align the THz radiation. The alignment could become easier as THz technology evolves, with the invention of a detector card analogous to mid IR detector cards, the radiation could be easily traced passing through the multi-pass optical. An alternative is to use a THz camera and raise it into the beam path on a platform.

Photolysis experiments will be possible to take place inside the multi-pass cell, but an appropriate UV source will need to be chosen to maximise crossover between generated species and THz emission. A flash lamp could be used and fixed around the middle section, this would require the steel middle section removing and using a UV transparent section replacement. The alternative is a UV laser which passes through the middle of the Herriott mirror or coupling hole. A colinear UV beam would yield the highest crossover path but need mirrors which can reflect both THz and UV as well as a window material which can withstand atmospheric pressure and is transparent in both wavelengths.

The power lock demonstrated in Chapter 5 shows a way to overcome instabilities in the QCL without additional optics. Frequency locking the QCL and stabilising the power through a RTR power lock will overcome problems presented with uncertain active region temperatures. This method in particular will help in targeting absorption lines as they change in concentrations during a concentration. An example of this would be to use a stabilised 4.7 THz QCL where emission from both facets is collected. One direction is passed through an ammonia gas cell which frequency locks the QCL while the second direction monitors atomic oxygen concentrations within a gas cell. As well as the RTR, liquid crystals are becoming more accessible within the research group and publications from Aniella Dunn [110] [160] showed liquid crystal power modulators. Additionally, Harry Godden has been investigating the use of liquid crystals in THz adaptive optics, which could improve the beam quality as well as power stability in the spectrometer.

Chapter 7

Bibliography

- [1] M. G. Mlynczak and S. Solomon, “A detailed evaluation of the heating efficiency in the middle atmosphere,” *Journal of Geophysical Research*, vol. 98, 1993.
- [2] H. Richter, M. Wienold, L. Schrottke, K. Biermann, H. T. Grahn, and H. W. Hubers, “4.7-THz local oscillator for the great heterodyne spectrometer on SOFIA,” *IEEE Transactions on Terahertz Science and Technology*, vol. 5, pp. 539–545, 2015.
- [3] H. Richter, C. Buchbender, R. Güsten, R. Higgins, B. Klein, J. Stutzki, H. Wiesemeyer, and H. W. Hübers, “Direct measurements of atomic oxygen in the mesosphere and lower thermosphere using terahertz heterodyne spectroscopy,” *Communications Earth and Environment*, vol. 2, pp. 1–9, 2021.
- [4] G. G. Matvienko, B. D. Belan, M. V. Panchenko, and S. M. Sakerin, “Instrumentation complex for comprehensive study of atmospheric parameters,” *International Journal of Remote Sensing*, vol. 35, pp. 5651–5676, 2014.
- [5] S. Kim, M. I. W. Khan, D. W. Park, S. G. Lee, and K. R. Kim, “Effects of parasitic source/drain junction area on terahertz responsivity of MOSFET detector,” *IEEE Transactions on Terahertz Science and Technology*, vol. 8, pp. 681–687, 2018.
- [6] Q. Hu, B. S. Williams, S. Kumar, H. Callebaut, S. Kohen, and J. L. Reno, “Resonant-phonon-assisted THz quantum-cascade lasers with metal-metal waveguides,” *Semiconductor Science and Technology*, vol. 20, 2005.
- [7] T. S. Hartwick, D. T. Hodges, D. H. Barker, and F. B. Foote, “Far infrared imagery,” *Appl. Opt.*, vol. 15, pp. 1919–1922, 1976.
- [8] D. M. Mittleman, “Twenty years of terahertz imaging [invited],” *Optics Express*, vol. 26, pp. 9417–9431, 4 2018.

- [9] G. Valušis, A. Lisauskas, H. Yuan, W. Knap, and H. G. Roskos, “Roadmap of terahertz imaging 2021,” *Sensors*, vol. 21, 6 2021.
- [10] W. L. Chan, J. Deibel, and D. M. Mittleman, “Imaging with terahertz radiation,” *Reports on Progress in Physics*, vol. 70, pp. 1325–1379, 8 2007.
- [11] C. Jansen, S. Wietzke, O. Peters, M. Scheller, N. Vieweg, M. Salhi, N. Krumbholz, C. Jördens, T. Hochrein, and M. Koch, “Terahertz imaging: applications and perspectives,” *Appl. Opt.*, vol. 49, pp. 48–57, 7 2010.
- [12] D. M. Mittleman, R. H. Jacobsen, and M. C. Nuss, “T-ray imaging,” *IEEE Journal of Selected Topics in Quantum Electronics*, vol. 2, pp. 679–692, 1996.
- [13] B. B. Hu and M. C. Nuss, “Imaging with terahertz waves,” *Optics Letters*, vol. 20, pp. 1716–1718, 1995.
- [14] A. J. Fitzgerald, E. Berry, N. N. Zinovev, G. C. Walker, M. A. Smith, and J. M. Chamberlain, “An introduction to medical imaging with coherent terahertz frequency radiation,” *Physics in Medicine and Biology*, vol. 47, pp. 67–84, 2002.
- [15] Z. D. Taylor, R. S. Singh, D. B. Bennett, P. Tewari, C. P. Kealey, N. Bajwa, M. O. Culjat, A. Stojadinovic, H. Lee, J. P. Hubschman, E. R. Brown, and W. S. Grundfest, “THz medical imaging: In vivo hydration sensing,” *IEEE Transactions on Terahertz Science and Technology*, vol. 1, pp. 201–219, 2011.
- [16] H. Kasban, M. El-Bendary, and D. Salama, “A comparative study of medical imaging techniques,” *International Journal of Information Science and Intelligent System*, vol. 4, pp. 37–58, 2015.
- [17] Z. D. Taylor, R. S. Singh, M. O. Culjat, J. Y. Suen, W. S. Grundfest, and E. R. Brown, “THz imaging based on water-concentration contrast,” *Terahertz for Military and Security Applications VI*, vol. 6949, p. 69490D, 2008.
- [18] T. Cisco, “Cisco: 2020 ciso benchmark report,” *Computer Fraud Security*, vol. 2020, pp. 4–4, 2020.
- [19] T. Nagatsuma, K. Oogimoto, Y. Inubushi, and J. Hirokawa, “Practical considerations of terahertz communications for short distance applications,” *Nano Communication Networks*, vol. 10, pp. 1–12, 12 2016.
- [20] T. Schneider, “Ultrahigh-bitrate wireless data communications via THz-links; possibilities and challenges,” *Journal of Infrared, Millimeter, and Terahertz Waves*, vol. 36, pp. 159–179, 2015.
- [21] E. G. Turitsyna and S. Webb, “Simple design of fbg-based VSB filters for ultra-dense wdm transmission electronics letters 20th january 2005,” *Electronics letters*, vol. 41, pp. 40–41, 2005.

- [22] X. Li, J. Yu, L. Zhao, K. Wang, C. Wang, M. Zhao, W. Zhou, and J. Xiao, "1-Tb/s millimeter-wave signal wireless delivery at D-band," *Journal of Lightwave Technology*, vol. 37, pp. 196–204, 2019.
- [23] T. Hoffmann, "Atmospheric analytical chemistry," *Analytical and Bioanalytical Chemistry*, vol. 385, pp. 16–17, 5 2006.
- [24] I. E. Gordon, L. S. Rothman, C. Hill, and V. Boudon, "The HITRAN 2016 molecular spectroscopic database," *Journal of Quantitative Spectroscopy and Radiative Transfer*, vol. 203, pp. 3–69, 12 2017.
- [25] D. K. Farmer and J. L. Jimenez, "Real-time atmospheric chemistry field instrumentation," *Analytical Chemistry*, vol. 82, pp. 7879–7884, 10 2010.
- [26] M. R. Capella, P. J. Yoo, D. E. Cunningham, and C. Y. Wakayama, "Mission assurance framework for small satellite missions," *Annual AIAA/USU Conference on Small Satellites Proceedings*, 2017.
- [27] M. Riese, D. Offermann, and G. Brasseur, "Energy released by recombination of atomic oxygen and related species at mesopause heights," *Journal of Geophysical Research*, vol. 99, 1994.
- [28] K. U. Grossmann and K. Vollmann, "Thermal infrared measurements in the middle and upper atmosphere," *Advances in Space Research*, vol. 19, pp. 631–638, 1997.
- [29] J.-H. Yee, "TIMED mission science overview," *Johns Hopkins APL Technical Digest*, vol. 24, pp. 136–141, 2003.
- [30] M. G. Mlynczak, L. A. Hunt, J. M. Russell, and B. T. Marshall, "Updated SABER night atomic oxygen and implications for SABER ozone and atomic hydrogen," *Geophysical Research Letters*, vol. 45, pp. 5735–5741, 6 2018.
- [31] P. D. Maagt, "Terahertz technology for space and earth applications," *Conference Proceedings - 2007 IEEE International Workshop on Antenna Technology: Small and Smart Antennas Metamaterials and Applications, iWAT 2007*, pp. 111–115, 2007.
- [32] C. Walker, C. Kulesa, P. Bernasconi, and H. Eaton, "The stratospheric THz observatory (STO)," *Ground-based and Airborne Telescopes III*, vol. 7733, p. 77330N, 2010.
- [33] A. Krabbe, D. Mehlert, H. P. Röser, and C. Scorza, "SOFIA, an airborne observatory for infrared astronomy," *European Journal of Physics*, vol. 34, 11 2013.
- [34] A. Valavanis, O. Auriacombe, T. Rawlings, Y. Han, and S. Rea, "Waveguide-integrated THz quantum-cascade lasers for atmospheric-research satellite payloads," in *2019 IEEE MTT-S International Wireless*

Symposium, IWS 2019 - Proceedings, Institute of Electrical and Electronics Engineers Inc., 5 2019.

- [35] S. P. Rea, B. N. Ellison, B. Swinyard, A. Valavanis, Y. Han, and E. H. Linfield, "The low-cost upper-atmosphere sounder (LOCUS)," *26th International Symposium on Space Terahertz Technology, ISSTT 2015*, 2015.
- [36] W. G. Read, J. W. Waters, D. L. Wu, and E. M. Stone, "UARS microwave limb sounder upper tropospheric humidity measurement: Method and validation," *Journal of Geophysical Research Atmospheres*, vol. 106, pp. 32207–32258, 12 2001.
- [37] D. T. Shindell and V. Grewe, "Separating the influence of halogen and climate changes on ozone recovery in the upper stratosphere," *Journal of Geophysical Research: Atmospheres*, vol. 107, 6 2002.
- [38] M. Wienold, A. Semenov, E. Dietz, S. Frohmann, and P. Dern, "OSAS-B: A balloon-borne terahertz spectrometer for atomic oxygen in the upper atmosphere," *IEEE Transactions on Terahertz Science and Technology*, 2024.
- [39] P. Collaboration, "Planck 2018 results. I. overview and the cosmological legacy of planck," *Astronomy and Astrophysics*, vol. 641, 7 2020.
- [40] J. M. Lamarre, J. L. Puget, and P. A. Ade, "Planck pre-launch status: The HFI instrument, from specification to actual performance," *Astronomy and Astrophysics*, vol. 520, 9 2010.
- [41] V. Saptari, *Fourier Transform Spectroscopy Instrumentation Engineering*. SPIE Optical Engineering Press, 2004.
- [42] A. Albert Michelson and W. Edward Morley, "The relative motion of the earth and the luminiferous ether," *American Journal of Science*, vol. 34, pp. 333–345, 1887.
- [43] R. Rammelsberg, S. Boulas, H. Chorongiewski, and K. Gerwert, "Set-up for time-resolved step-scan FTIR spectroscopy of noncyclic reactions," *Vibrational Spectroscopy*, vol. 19, pp. 143–149, 1999.
- [44] J. Neu and C. A. Schmuttenmaer, "Tutorial: An introduction to terahertz time domain spectroscopy (THz-TDS)," *Journal of Applied Physics*, vol. 124, 12 2018.
- [45] M. Hangyo, M. Tani, and T. Nagashima, "Terahertz time-domain spectroscopy of solids: A review," *International Journal of Infrared and Millimeter Waves*, vol. 26, pp. 1661–1690, 12 2005.
- [46] R. E. Miles, P. Harrison, and D. Lippens, *Terahertz Sources and Systems*. Springer Netherlands, 2012.

- [47] A. A. Borisov, U. A. Budzinsky, and S. V. Bykovsky, "The development of vacuum microwave devices in istok," *2011 IEEE International Vacuum Electronics Conference, IVEC-2011*, pp. 437–438, 2011.
- [48] A. Dobroiu, M. Yamashita, and Y. N. Ohshima, "Terahertz imaging system based on a backward-wave oscillator," *Applied Optics*, vol. 43, pp. 5637–5646, 2004.
- [49] A. Maestrini, B. Thomas, H. Wang, and C. Jung, "Schottky diode-based terahertz frequency multipliers and mixers," *Comptes Rendus Physique*, vol. 11, pp. 480–495, 2010.
- [50] I. Mehdi, G. Chattopadhyay, E. Schlecht, and J. Ward, "Terahertz multiplier circuits," *IEEE MTT-S International Microwave Symposium Digest*, pp. 341–344, 2006.
- [51] Y. Zhang, C. Wu, X. Liu, L. Wang, C. Dai, J. Cui, Y. Li, and N. Kinar, "The development of frequency multipliers for terahertz remote sensing system," *Remote Sensing*, vol. 14, 2022.
- [52] A. S. Hajo, O. Yilmazoglu, A. Dadgar, F. Kuppers, and T. Kusserow, "Fabrication and characterization of high power gallium nitride based terahertz gunn diodes," in *International Conference on Infrared, Millimeter, and Terahertz Waves, IRMMW-THz*, vol. 2020-November, pp. 773–774, IEEE Computer Society, 11 2020.
- [53] D. Cimbri, J. Wang, A. Al-Khalidi, and E. Wasige, "Resonant tunneling diodes high-speed terahertz wireless communications a review," *IEEE Transactions on Terahertz Science and Technology*, vol. 12, pp. 226–244, 5 2022.
- [54] A. Acharyya, J. Chakraborty, K. Das, and S. J. Mukhopadhyay, "Influence of self-heating on the millimeter-wave and terahertz performance of MBE grown silicon IMPATT diodes," *J. Semicond*, vol. 41, 2020.
- [55] P. R. Smith, D. H. Auston, and M. C. Nuss, "Subpicosecond photoconducting dipole antennas," *IEEE Journal of Quantum Electronics*, vol. 24, 1988.
- [56] S. Lepeshov, A. Gorodetsky, A. Krasnok, E. Rafailov, and P. Belov, "Enhancement of terahertz photoconductive antenna operation by optical nanoantennas," *Laser and Photonics Reviews*, vol. 11, 1 2017.
- [57] E. Isgandarov, X. Ropagnol, M. Singh, and T. Ozaki, "Intense terahertz generation from photoconductive antennas," *Frontiers of Optoelectronics*, vol. 14, pp. 64–93, 3 2021.
- [58] E. Moreno, M. F. Pantoja, A. R. Bretones, M. Ruiz-Cabello, and S. G. Garcia, "A comparison of the performance of THz photoconductive antennas," *IEEE Antennas and Wireless Propagation Letters*, vol. 13, pp. 682–685, 2014.

- [59] E. F. Pliński, “Terahertz photomixer,” *Bulletin of the Polish Academy of Sciences: Technical Sciences*, vol. 58, pp. 463–470, 12 2010.
- [60] X. Li, W. Yin, and S. Khamas, “An efficient photomixer based slot fed terahertz dielectric resonator antenna,” *Sensors*, vol. 21, pp. 1–13, 2 2021.
- [61] E. R. Brown, K. A. McIntosh, K. B. Nichols, and C. L. Dennis, “Photomixing up to 3.8 thz in low-temperature-grown GaAs,” *Applied Physics Letters*, p. 285–287, 1995.
- [62] S. O. Kasap, *Optoelectronics and Photonics: Principles and Practices: International Edition*. Pearson Education, 2013.
- [63] P. Werle, “A review of recent advances in semiconductor laser based gas monitors,” *Spectrochimica Acta Part A: Molecular and Biomolecular Spectroscopy*, vol. 54, pp. 197–236, 1998.
- [64] P. Harrison and A. Valavanis, *Quantum Wells Wires and Dots*. Wiley, fourth ed., 2016.
- [65] J. Faist, F. Capasso, D. L. Sivco, C. Sirtori, A. L. Hutchinson, and A. Y. Cho, “Quantum cascade laser,” *Science*, vol. 264, pp. 553–556, 1994.
- [66] A. Tredicucci and F. Beltram, “Terahertz semiconductor-heterostructure laser,” *Nature*, vol. 417, p. 156–159, 2002.
- [67] M. I. Amanti, G. Scalari, R. Terazzi, M. Fischer, M. Beck, J. Faist, A. Rudra, P. Gallo, and E. Kapon, “Bound-to-continuum terahertz quantum cascade laser with a single-quantum-well phonon extraction/injection stage,” *New Journal of Physics*, vol. 11, 2009.
- [68] B. S. Williams, S. Kumar, H. Callebaut, Q. Hu, and J. L. Reno, “Terahertz quantum-cascade laser operating up to 137 K,” *Applied Physics Letters*, vol. 83, pp. 5142–5144, 2003.
- [69] B. S. Williams, “Terahertz quantum-cascade lasers,” *Nature Photonics*, pp. 517–525, 2007.
- [70] A. Rostami, H. Rasooli, and H. Baghban, *Terahertz Technology: Fundamentals and Applications*. Springer Berlin Heidelberg, 2010.
- [71] L. H. Li, K. Garrasi, I. Kundu, Y. J. Han, M. Salih, M. S. Vitiello, A. G. Davies, and E. H. Linfield, “Broadband heterogeneous terahertz frequency quantum cascade laser,” *Electronics Letters*, vol. 54, pp. 1229–1231, 10 2018.
- [72] C. A. Curwen, J. L. Reno, and B. S. Williams, “Broadband continuous single-mode tuning of a short-cavity quantum-cascade vecsel,” *Nature Photonics*, vol. 13, pp. 855–859, 12 2019.

- [73] M. S. Vitiello, L. Consolino, S. Bartalini, A. Taschin, A. Tredicucci, M. Inguscio, and P. D. Natale, “Quantum-limited frequency fluctuations in a terahertz laser,” *Nature Photonics*, vol. 6, pp. 525–528, 8 2012.
- [74] A. Khalatpour, A. K. Paulsen, C. Deimert, Z. R. Wasilewski, and Q. Hu, “High-power portable terahertz laser systems,” *Nature Photonics*, vol. 15, pp. 16–20, 1 2021.
- [75] M. A. Belkin, Q. J. Wang, C. Pfügl, A. Belyanin, S. P. Khanna, A. G. Davies, E. H. Linfield, and F. Capasso, “High-temperature operation of terahertz quantum cascade laser sources,” *IEEE Journal on Selected Topics in Quantum Electronics*, vol. 15, pp. 952–967, 5 2009.
- [76] E. Pruszyńska-Karbownik, P. Gutowski, I. Sankowska, P. Karbownik, and M. Bugajski, “Field distribution in waveguide of mid-infrared strain-compensated InAlAs/InGaAs/InP quantum cascade laser,” *Optical and Quantum Electronics*, vol. 49, 2 2017.
- [77] R. Sachs and H. G. Roskos, “Mode calculations for a terahertz quantum cascade laser,” *Optics Express*, vol. 264, pp. 2062–2069, 2004.
- [78] C. Sirtori, C. Gmachl, F. Capasso, J. Faist, D. L. Sivco, A. L. Hutchinson, and A. Y. Cho, “Long-wavelength 8–115 μ m semiconductor lasers with waveguides based on surface plasmons,” *Optics Letters*, vol. 23, p. 1366, 1998.
- [79] K. Unterrainer, R. Colombelli, C. Gmachl, F. Capasso, H. Y. Hwang, A. M. Sergent, D. L. Sivco, and A. Y. Cho, “Quantum cascade lasers with double metal-semiconductor waveguide resonators,” *Applied Physics Letters*, vol. 80, pp. 3060–3062, 2002.
- [80] A. Rogalski, “Progress in performance development of room temperature direct terahertz detectors,” *Journal of Infrared, Millimeter, and Terahertz Waves*, vol. 43, pp. 709–727, 9 2022.
- [81] T. M. Klapwijk and A. V. Semenov, “Engineering physics of superconducting hot-electron bolometer mixers,” *IEEE Transactions on Terahertz Science and Technology*, vol. 7, pp. 627–648, 2017.
- [82] D. Hayton, J. Treuttel, J.-V. Siles, C. P. Chen, and R. Lin, “A compact schottky heterodyne receiver for 2.06 THz neutral oxygen [OI],” *2018 43rd International Conference on Infrared, Millimeter, and Terahertz Waves (IRMMW-THz)*, pp. 1–2, 2010.
- [83] U. U. Graf, C. E. Honingh, K. Jacobs, and J. Stutzki, “Terahertz heterodyne array receivers for astronomy,” *Journal of Infrared, Millimeter, and Terahertz Waves*, vol. 36, pp. 896–921, 10 2015.

- [84] V. K. Khanna, “Bolometers, golay cells and pyroelectric detectors,” *Practical Terahertz Electronics: Devices and Applications, Volume 2*, pp. 1–1 to 1–29, 2021.
- [85] L. Angrisani, G. Cavallo, A. Liccardo, G. P. Papari, and A. Andreone, “Thz measurement systems,” *New Trends and Developments in Metrology*, 7 2016.
- [86] P. Atkins and J. Paula, *Atkins Physical Chemistry*. Oxford University Press, 2010.
- [87] E. Nuttall, “Spectroscopy of atmospheric processes using a terahertz quantum cascade laser,” 2023.
- [88] H. M. Mcnair and J. M. Miller, *Introduction*. John Wiley Sons, Ltd, 2009.
- [89] C. A. Cramers, H.-G. Janssen, M. M. V. Deursen, and P. A. Leclercq, “High-speed gas chromatography: an overview of various concepts,” *Journal of Chromatography A*, vol. 856, pp. 315–329, 1999.
- [90] F. Bovey and P. Mirau, *Nuclear Magnetic Resonance Spectroscopy*. 2 ed., 1998.
- [91] P. Giraudeau and F. X. Felpin, “Flow reactors integrated with in-line monitoring using benchtop NMR spectroscopy,” *Reaction Chemistry and Engineering*, vol. 3, pp. 399–413, 8 2018.
- [92] A. Webb, “Increasing the sensitivity of magnetic resonance spectroscopy and imaging,” *Analytical Chemistry*, vol. 84, pp. 9–16, 1 2012.
- [93] Y. Ben-Tal, P. J. Boaler, H. J. Dale, and R. E. Dooley, “Mechanistic analysis by NMR spectroscopy: A users guide,” *Progress in Nuclear Magnetic Resonance Spectroscopy*, vol. 129, pp. 28–106, 4 2022.
- [94] R. R. Jones, D. C. Hooper, L. Zhang, D. Wolverson, and V. K. Valev, “Raman techniques: Fundamentals and frontiers,” *Nanoscale Research Letters*, vol. 14, 12 2019.
- [95] L. Cocola, G. Tondello, and L. Poletto, “A non-dispersive approach for a raman gas sensor,” *SN Applied Sciences*, vol. 2, 5 2020.
- [96] H. W. Hübers, S. G. Pavlov, H. Richter, A. D. Semenov, L. Mahler, A. Tredicucci, H. E. Beere, and D. A. Ritchie, “High-resolution gas phase spectroscopy with a distributed feedback terahertz quantum cascade laser,” *Applied Physics Letters*, vol. 89, pp. 88–91, 2006.
- [97] J. R. Wubs, U. Macherius, K. D. Weltmann, X. Lü, B. Röben, K. Biermann, L. Schrottke, H. T. Grahn, and J. H. van Helden, “Terahertz absorption spectroscopy for measuring atomic oxygen densities in plasmas,” *Plasma Sources Science and Technology*, vol. 32, 2 2023.

- [98] T. Hagelschuer, M. Wienold, H. Richter, L. Schrottke, K. Biermann, H. T. Grahn, and H. W. Hübers, “Terahertz gas spectroscopy through self-mixing in a quantum-cascade laser,” *Applied Physics Letters*, vol. 109, 11 2016.
- [99] P. Kilcullen, I. D. Hartley, E. T. Jensen, and M. Reid, “Terahertz time domain gas-phase spectroscopy of carbon monoxide,” *Journal of Infrared, Millimeter, and Terahertz Waves*, vol. 36, pp. 380–389, 4 2015.
- [100] D. M. Middleman, R. H. Jacobsen, R. Neelamani, R. G. Baraniuk, and M. C. Nuss, “Gas sensing using terahertz time-domain spectroscopy,” *Applied Physics B: Lasers and Optics*, vol. 67, pp. 379–390, 1998.
- [101] L. S. Rothman, “History of the HITRAN database,” *Nature Reviews Physics*, vol. 3, pp. 302–304, 2021.
- [102] H. M. Pickett, R. L. Poynter, E. A. Cohen, M. L. Delintsky, J. C. Pearson, and H. S. P. Müller, “Submillimeter, millimeter, and microwave spectral line catalog,” *Journal of Quantitative Spectroscopy and Radiative Transfer*, vol. 60, pp. 883–890, 1998.
- [103] R. L. Poynter and H. M. Pickett, “Submillimeter, millimeter, and microwave spectral line catalog,” *Applied Optics*, 1985.
- [104] H. M. Pickett, “The fitting and prediction of vibration-rotation spectra with spin interactions,” *Journal of Molecular Spectroscopy*, vol. 148, pp. 371–377, 1991.
- [105] H. M. Pickett, E. A. Cohen, B. J. Drouin, and J. C. Pearson, “Submillimeter, millimeter, and microwave spectral line catalog,” *Journal of Quantitative Spectroscopy and Radiative Transfer*, vol. 60, pp. 883–890, 2003.
- [106] B. Wen and D. Ban, “High-temperature terahertz quantum cascade lasers,” *Progress in Quantum Electronics*, vol. 80, 11 2021.
- [107] M. S. Vitiello, G. Scamarcio, V. Spagnolo, A. Lops, Q. Yang, C. Manz, and J. Wagner, “Experimental investigation of the lattice and electronic temperatures in Ga_{0.47}In_{0.53}As/Al_{0.62}Ga_{0.38}As_{1-x}Sb_x quantum-cascade lasers,” *Applied Physics Letters*, vol. 90, 2007.
- [108] M. S. Vitiello, G. Scamarcio, and V. Spagnolo, “Time-resolved measurement of the local lattice temperature in terahertz quantum cascade lasers,” *Applied Physics Letters*, vol. 92, 2008.
- [109] P. Gellie, S. Barbieri, J. F. Lampin, P. Filloux, C. Manquest, C. Sirtori, I. Sagnes, S. P. Khanna, E. H. Linfield, H. E. Beere, and D. A. Ritchie, “Injection-locking of terahertz quantum cascade lasers up to 35GHz via RF amplitude modulation,” *IRMMW-THz 2010 - 35th International Conference on Infrared, Millimeter, and Terahertz Waves, Conference Guide*, vol. 18, pp. 20799–20816, 2010.

- [110] A. Dunn, C. Poyser, P. Dean, A. Demić, A. Valavanis, D. Indjin, M. Salih, I. Kundu, L. Li, A. Akimov, A. G. Davies, E. Linfield, J. Cunningham, and A. Kent, “High-speed modulation of a terahertz quantum cascade laser by coherent acoustic phonon pulses,” *Nature Communications*, vol. 11, 12 2020.
- [111] S. J. Kindness, D. S. Jessop, B. Wei, R. Wallis, and V. S. Kamboj, “External amplitude and frequency modulation of a terahertz quantum cascade laser using metamaterial/graphene devices,” *Scientific Reports*, vol. 7, pp. 1–10, 2017.
- [112] S. Barbieri, W. Maineult, S. S. Dhillon, C. Sirtori, J. Alton, N. Breuil, H. E. Beere, and D. A. Ritchie, “13 GHz direct modulation of terahertz quantum cascade lasers,” *Applied Physics Letters*, vol. 91, 2007.
- [113] X. Gao, “Monte carlo simulation of electron dynamics in quantum cascade lasers,” *Applied Physics Letters*, vol. 80, p. 920–922, 2008.
- [114] W. Maineult, L. Ding, P. Gellie, P. Filloux, C. Sirtori, S. Barbieri, T. Akalin, J. F. Lampin, I. Sagnes, H. E. Beere, and D. A. Ritchie, “Microwave modulation of terahertz quantum cascade lasers: A transmission-line approach,” *Applied Physics Letters*, vol. 96, 2010.
- [115] E. Nuttall, Y. J. Han, M. D. Horbury, N. Brewster, M. Oldfield, and L. H. Li, “Spectral analysis of a gas-phase reaction using self-mixing in a terahertz quantum cascade laser,” *International Conference on Infrared, Millimeter, and Terahertz Waves, IRMMW-THz*, pp. 363–364, 2020.
- [116] Y. J. Han, J. Partington, R. Chhantyal-Pun, M. Henry, and O. Auriacombe, “Gas spectroscopy through multimode self-mixing in a double-metal terahertz quantum cascade laser,” *Optics Letters*, vol. 43, p. 5933, 2018.
- [117] M. Dyakonov and M. Shur, “Shallow water analogy for a ballistic field effect transistor: New mechanism of plasma wave generation by dc current,” *Physical Review Letters*, vol. 71, pp. 2465–2468, 1993.
- [118] M. Dyakonov and M. Shur, “Detection, mixing, and frequency multiplication of terahertz radiation by two-dimensional electronic fluid,” *IEEE Transactions on Electron Devices*, vol. 43, pp. 380–387, 1996.
- [119] M. Bauer, “Hydrodynamic modeling and experimental characterization of the plasmonic and thermoelectric terahertz response of field-effect transistors with integrated broadband antennas in AlGaIn/GaN HEMTs and CVD-grown graphene,” 2017.
- [120] W. Knap, M. Dyakonov, D. Coquillat, F. Teppe, N. Dyakonova, and J. Lusakowski, “Field effect transistors for terahertz detection: Physics and first imaging applications,” in *Journal of Infrared, Millimeter, and Terahertz Waves*, vol. 30, pp. 1319–1337, 2009.

- [121] L. Vicarelli, M. S. Vitiello, D. Coquillat, A. Lombardo, A. C. Ferrari, W. Knap, M. Polini, V. Pellegrini, and A. Tredicucci, “Graphene field-effect transistors as room-temperature terahertz detectors,” *Nature Materials*, vol. 11, pp. 865–871, 2012.
- [122] M. Khatib and M. Perenzoni, “A low-noise direct incremental A/D converter for FET-based THz imaging detectors,” *Sensors (Switzerland)*, vol. 18, 6 2018.
- [123] J. Holstein, N. K. North, M. D. Horbury, S. Kondawar, I. Kundu, M. Salih, A. Krysl, L. Li, E. H. Linfield, J. R. Freeman, A. Valavanis, A. Lisauskas, and H. G. Roskos, “8x8 patch-antenna-coupled TeraFET detector array for terahertz quantum-cascade-laser applications,” *IEEE Transactions on Terahertz Science and Technology*, vol. 14, pp. 799–807, 2024.
- [124] N. K. North, J. Holstein, M. D. Horbury, H. Godden, L. H. Li, J. R. Freeman, E. H. Linfield, H. Roskos, A. Lisauskas, and A. Valavanis, “Real-time analysis of THz quantum-cascade laser signals using a Field Effect Transistor array,” in *International Conference on Infrared, Millimeter, and Terahertz Waves, IRMMW-THz*, IEEE Computer Society, 2023.
- [125] J. Holstein, M. Horbury, N. North, H. Godden, A. Krysl, A. Lisauskas, L. H. Li, A. Valavanis, J. R. Freeman, E. H. Linfield, and H. G. Roskos, “Implementation of a multi-element detector consisting of an 8x8 network of patch-antenna-coupled TeraFETs for gas spectroscopy with THz-QCLs,” in *2023 48th International Conference on Infrared, Millimeter, and Terahertz Waves (IRMMW-THz)*, pp. 1–2, 2023.
- [126] C. Banwell and E. McCash, “Fundamentals of molecular spectroscopy,” *The Astrophysical Journal*, vol. 464, pp. 83–86, 1994.
- [127] C. P. Koch, M. Lemeshko, and D. Sugny, “Quantum control of molecular rotation,” *Reviews of Modern Physics*, vol. 91, 9 2019.
- [128] S. Flescher, Y. Khodorkovsky, Y. Prlor, and I. S. Averbukh, “Controlling the sense of molecular rotation,” *New Journal of Physics*, vol. 11, 10 2009.
- [129] H. Richter, N. Rothbart, M. Wienold, X. Lü, L. Schrottke, and H. T. Grahn, “Phase locking of 3.5-THz and 4.7-THz quantum-cascade lasers using a schottky diode harmonic mixer,” *International Conference on Infrared, Millimeter, and Terahertz Waves, IRMMW-THz*, vol. 2021-Augus, pp. 9–10, 2021.
- [130] R. C. W. Gordy, *Microwave Molecular Spectra*. Interscience Publishers, 1970.
- [131] A. Faure, M. Faure, P. Theule, E. Quirico, and B. Schmitt, “Hydrogen isotope exchanges between water and methanol in interstellar ices,” *Astronomy and Astrophysics*, vol. 584, 12 2015.

- [132] Y. D. Hang and E. E. Woodams, “Influence of apple cultivar and juice pasteurization on hard cider and eau-de-vie methanol content,” *Bioresource Technology*, vol. 101, pp. 1396–1398, 2 2010.
- [133] M. D. Horbury, N. K. North, J. Holstein, H. Godden, L. H. Li, J. R. Freeman, E. H. Linfield, H. Roskos, A. Lisauskas, and A. Valavanis, “Real-time terahertz absorption spectroscopy of methanol and deuterated-methanol vapour, using a TeraFET detector array,” in *2023 48th International Conference on Infrared, Millimeter, and Terahertz Waves (IRMMW-THz)*, pp. 1–2, 2023.
- [134] J. U. White, “Long optical paths of large aperture,” *Journal of the Optical Society of America*, pp. 285–288, 1942.
- [135] A. Cuisset, F. Hindle, G. Mouret, R. Bocquet, J. Bruckhuisen, J. Decker, A. Pienkina, C. Bray, Éric Fertein, and V. Boudon, “Terahertz rotational spectroscopy of greenhouse gases using long interaction path-lengths,” *Applied Sciences (Switzerland)*, vol. 11, pp. 1–13, 2 2021.
- [136] J. C. M. Antón and M. Silva-López, “Optical cavity for auto-referenced gas detection,” *Optics Express*, vol. 19, p. 26079, 2011.
- [137] D. Herriott, H. Kogelnik, and R. Kompfner, “Off-axis paths in spherical mirror interferometers,” *Applied Optics*, vol. 3, p. 523, 1964.
- [138] D. R. Herriott and H. J. Schulte, “Folded optical delay lines,” *Applied Optics*, vol. 4, p. 883, 1965.
- [139] J. B. McManus, P. L. Keabian, and M. S. Zahniser, “Astigmatic mirror multipass absorption cells for long-path-length spectroscopy,” *Applied Optics*, vol. 34, p. 3336, 1995.
- [140] J. Altmann, R. Baumgart, and C. Weitkamp, “Two-mirror multipass absorption cell,” *Applied Optics*, vol. 20, p. 995, 1981.
- [141] A. Fried, J. R. Drummond, and B. Henry, “Reduction of interference fringes in small multipass absorption cells by pressure modulation alan,” *Optical Society of America.*, vol. 29, pp. 900–902, 1989.
- [142] J. Reid, M. El-Sherbiny, B. K. Garside, and E. A. Ballik, “Sensitivity limits of a tunable diode laser spectrometer, with application to the detection of no 2 at the 100-ppt level,” *Applied Optics*, vol. 19, pp. 3349–3354, 1980.
- [143] J. B. McManus and P. L. Keabian, “Narrow optical interference fringes for certain setup conditions in multipass absorption cells of the herriott type,” *Applied Optics*, vol. 29, p. 898, 1990.
- [144] J. Pearson, A. J. Orr-Ewing, M. N. Ashfold, and R. N. Dixon, “Spectroscopy and predissociation dynamics of the \tilde{A} 1A state of HNO,” *Journal of Chemical Physics*, vol. 106, pp. 5850–5873, 4 1997.

- [145] A. O’Keefe and D. A. Deacon, “Cavity ring-down optical spectrometer for absorption measurements using pulsed laser sources,” *Review of Scientific Instruments*, vol. 59, pp. 2544–2551, 1988.
- [146] G. Berden and R. Engeln, *Cavity ring-down spectroscopy : techniques and applications*. Wiley, 2009.
- [147] C. Elmaleh, F. Simon, J. Decker, J. Dumont, F. Cazier, M. Fourmentin, R. Bocquet, A. Cuisset, G. Mouret, and F. Hindle, “THz cavity ring-down quantitative gas phase spectroscopy,” *Talanta*, vol. 253, p. 124097, 2023.
- [148] G. H. Spencer and M. V. R. K. Murty, “General ray-tracing procedure,” *Journal of The Optical Society of America*, vol. 52, pp. 672–678, 1961.
- [149] P. H. Corporation, “Parker O-ring handbook,” 2007.
- [150] Y. L. Lim, P. Dean, M. Nikoli, R. Kliese, S. P. Khanna, M. Lachab, A. Valavanis, D. Indjin, Z. Ikoni, P. Harrison, E. H. Linfield, A. G. Davies, S. J. Wilson, and A. D. Raki, “Demonstration of a self-mixing displacement sensor based on terahertz quantum cascade lasers,” *Applied Physics Letters*, vol. 99, 8 2011.
- [151] C. Liu, Z. Yue, Z. Xu, M. Ding, and Y. Zhai, “Far off-resonance laser frequency stabilization technology,” *Applied Sciences (Switzerland)*, vol. 10, pp. 1–14, 2020.
- [152] C. A. Evans, V. D. Jovanović, D. Indjin, Z. Ikonić, and P. Harrison, “Investigation of thermal effects in quantum-cascade lasers,” *IEEE Journal of Quantum Electronics*, vol. 42, pp. 859–867, 2006.
- [153] B. Argence, B. Chanteau, and O. Lopez, “Quantum cascade laser frequency stabilization at the sub-Hz level,” *Nature Photonics*, vol. 9, pp. 456–460, 2015.
- [154] R. P. Borase, D. K. Maghade, S. Y. Sondkar, and S. N. Pawar, “A review of PID control, tuning methods and applications,” *International Journal of Dynamics and Control*, vol. 9, pp. 818–827, 6 2021.
- [155] N. S. Nise, *Control System Engineering*. Wiley, third ed., 2000.
- [156] M. A. Johnson, M. Moradi, J. Crowe, K. K. Tan, T. H. Lee, and R. Ferdous, *PID control: New identification and design methods*. Springer, 2005.
- [157] X. G. Peralta, I. Brener, W. J. Padilla, and E. W. Young, “External modulators for terahertz quantum cascade lasers based on electrically-driven active metamaterials,” *Metamaterials*, vol. 4, pp. 83–88, 2010.
- [158] D. S. Jessop, S. J. Kindness, L. Xiao, P. Braeuninger-Weimer, H. Lin, Y. Ren, and C. X. Ren, “Graphene based plasmonic terahertz amplitude modulator operating above 100 MHz,” *Applied Physics Letters*, vol. 108, 4 2016.

- [159] S. Savo, D. Shrekenhamer, and W. J. Padilla, “Liquid crystal metamaterial absorber spatial light modulator for THz applications,” *Advanced Optical Materials*, vol. 2, pp. 275–279, 2014.
- [160] A. Dunn, Z. Zhang, M. D. Horbury, E. Nuttall, Y. Han, M. Salih, L. Li, A. Bond, E. Saleh, R. Harris, D. Pardo, B. Ellison, A. D. Burnett, H. F. Gleeson, and A. Valavanis, “Extracting material properties from a liquid crystal cell using terahertz spectroscopy,” in *International Conference on Infrared, Millimeter, and Terahertz Waves, IRMMW-THz*, vol. 2022-August, IEEE Computer Society, 2022.
- [161] T. Alam, M. Wienold, X. Lü, K. Biermann, L. Schrottke, H. T. Grahn, and H.-W. Hübers, “Wideband, high-resolution terahertz spectroscopy by light-induced frequency tuning of quantum-cascade lasers,” *Optics Express*, vol. 27, p. 5420, 2019.
- [162] A. Forrer, L. Bosco, M. Beck, J. Faist, and G. Scalari, “RF injection of THz QCL combs at 80 K emitting over 700 GHz spectral bandwidth,” *Photonics*, vol. 7, 2020.
- [163] A. L. Betz and R. T. Boreiko, “Frequency and phase-lock control of a 3 THz quantum cascade laser,” *Optics Letters*, vol. 30, pp. 1837–1839, 2005.
- [164] M. Ravaro, C. Manquest, C. Sirtori, S. Barbieri, G. Santarelli, K. Blary, J.-F. Lampin, S. P. Khanna, and E. H. Linfield, “Phase-locking of a 2.5 THz quantum cascade laser to a frequency comb using a GaAs photomixer,” *Optics Letters*, vol. 36, p. 3969, 2011.
- [165] A. Barkan, F. K. Tittel, D. M. Mittleman, R. Dengler, P. H. Siegel, G. Scalari, L. Ajili, J. Faist, H. E. Beere, E. H. Linfield, A. G. Davies, and D. A. Ritchie, “Linewidth and tuning characteristics of terahertz quantum cascade lasers,” *Optics Letters*, vol. 29, p. 575, 2004.
- [166] Y. Ren, D. J. Hayton, J. N. Hovenier, M. Cui, J. R. Gao, T. M. Klapwijk, S. C. Shi, T. Y. Kao, Q. Hu, and J. L. Reno, “Frequency and amplitude stabilized terahertz quantum cascade laser as local oscillator,” *Applied Physics Letters*, vol. 101, 9 2012.
- [167] A. V. Khudchenko, D. J. Hayton, D. G. Pavelyev, A. M. Baryshev, J. R. Gao, T. Y. Kao, Q. Hu, J. L. Reno, and V. L. Vaks, “Phase locking a 4.7 THz quantum cascade laser using a super-lattice diode as harmonic mixer,” *International Conference on Infrared, Millimeter, and Terahertz Waves, IRMMW-THz*, pp. 4–6, 2014.
- [168] A. Danylov, N. Erickson, A. Light, and J. Waldman, “Phase locking of 2.324 and 2.959 terahertz quantum cascade lasers using a schottky diode harmonic mixer,” *Opt. Lett.*, vol. 40, pp. 5090–5092, 2015.

- [169] N. Daghestani, K. Parow-Souchon, D. Pardo, H. Liu, N. Brewster, M. Frogley, G. Cinque, B. Alderman, and P. G. Huggard, “Room temperature ultrafast ingaas schottky diode based detectors for terahertz spectroscopy,” *Infrared Physics and Technology*, vol. 99, pp. 240–247, 6 2019.
- [170] Z. Liu and R. Slavik, “Optical injection locking: From principle to applications,” *Journal of Lightwave Technology*, vol. 38, pp. 43–59, 2020.
- [171] J. R. Freeman, L. Ponnampalam, H. Shams, R. A. Mohandas, C. C. Renaud, P. Dean, L. Li, A. G. Davies, A. J. Seeds, and E. H. Linfield, “Injection locking of a terahertz quantum cascade laser to a telecommunications wavelength frequency comb,” *Optica*, vol. 4, p. 1059, 2017.
- [172] M. Hempel, B. Röben, L. Schrottke, H. W. Hübers, and H. T. Grahn, “Fast continuous tuning of terahertz quantum-cascade lasers by rear-facet illumination,” *Applied Physics Letters*, vol. 108, 2016.
- [173] W. Bogaerts, P. de Heyn, T. van Vaerenbergh, K. de Vos, S. K. Selvaraja, T. Claes, P. Dumon, P. Bienstman, D. van Thourhout, and R. Baets, “Silicon microring resonators,” *Laser and Photonics Reviews*, vol. 6, pp. 47–73, 2012.
- [174] I. Kundu, J. R. Freeman, P. Dean, L. H. Li, E. H. Linfield, and A. G. Davies, “Terahertz photonic integrated circuit for frequency tuning and power modulation,” *Optics Express*, vol. 28, p. 4374, 2 2020.
- [175] S. S. Kondawar, N. K. North, Y. Han, and D. Pardo, “Power stabilization of a terahertz-frequency quantum-cascade laser using a photonic-integrated modulator,” *Optics Express*, vol. 32, p. 30017, 8 2024.
- [176] J. Ruiz-Rosero, G. Ramirez-Gonzalez, and R. Khanna, “Field programmable gate array applications-a scientometric review,” *Computation*, vol. 7, pp. 1–111, 2019.
- [177] S. M. Trimberger, D. McCarty, and T. Whitney, *Field-Programmable Gate Array Technology*, vol. 1. Springer US, 1 ed., 1994.
- [178] G. Xu, L. Li, N. Isac, Y. Halioua, A. G. Davies, E. H. Linfield, and R. Colombelli, “Surface-emitting terahertz quantum cascade lasers with continuous-wave power in the tens of milliwatt range,” *Applied Physics Letters*, vol. 104, 3 2014.
- [179] J. A. Fan, M. A. Belkin, F. Capasso, S. Khanna, M. Lachab, A. G. Davies, and E. H. Linfield, “Surface emitting terahertz quantum cascade laser with a double-metal waveguide,” *Optics Express*, vol. 14, p. 156, 2006.